Computational Investigations of Mechanisms, Pathway Complexity and Dipole Dynamics in Supramolecular Polymers

A Thesis
Submitted For the Degree of
DOCTOR OF PHILOSOPHY
in the Faculty of Science

by

Korlepara Divya Bharathi

CHEMISTRY AND PHYSICS OF MATERIALS UNIT
JAWAHARLAL NEHRU CENTRE FOR ADVANCED SCIENTIFIC RESEARCH
Bangalore – 560 064, India

JULY 2020

To My Family

DECLARATION

I hereby declare that the matter embodied in the thesis entitled "**Computational Investigations of Mechanisms, Pathway Complexity and Dipole Dynamics in Supramolecular Polymers**" is the result of investigations carried out by me at the Chemistry and Physics of Materials Unit, Jawaharlal Nehru Centre for Advanced Scientific Research, Bangalore, India under the supervision of Prof. S. Balasubramanian and that it has not been submitted elsewhere for the award of any degree or diploma.

In keeping with the general practice in reporting scientific observations, due acknowledgement has been made whenever the work described is based on the findings of other investigators. Any omission that might have occurred by oversight or error of judgement is regretted.

Korlepara Divya Bharathi

CERTIFICATE

I hereby certify that the matter embodied in this thesis entitled "**Computational Investigations of Mechanisms, Pathway Complexity and Dipole Dynamics in Supramolecular Polymers**" has been carried out by Ms. Korlepara Divya Bharathi at the Chemistry and Physics of Materials Unit, Jawaharlal Nehru Centre for Advanced Scientific Research, Bangalore, India under my supervision and that it has not been submitted elsewhere for the award of any degree or diploma.

Prof. S. Balasubramanian
(Research Supervisor)

Acknowledgements

It is my immense pleasure to thank my research supervisor, Prof. S. Balasubramanian for giving me an opportunity to explore the interesting area of research on computational materials science. I am extremely thankful to him for his guidance, support, and encouragement throughout the journey of my Ph.D. career. I am greatly thankful to him for providing me with excellent computing resources without which the projects would not be successful.

I thank the Jawaharlal Nehru Centre for Advanced Scientific Research (JNCASR) for providing excellent research facilities. I would like to thank the faculty members of CPMU, TSU, NCU and Prabal Maiti at IISC for the courses they offered. I also thank my collaborators Prof. Subi J. George, Prof. Ronald K. Castellano, Dr. Ananya Mishra and Will R. Henderson.

I acknowledge JNCASR, TUE-CMS for computational facilities. I also thank CSIR for the fellowship and DST for the funding. I thank all the academic and non-academic staff of JNCASR.

I am thankful to the open-source community for their services in providing useful softwares and operating systems. I thank the developers of LAMMPS, CP2K, GROMACS and PLUMED and their mailing list for the support.

I have enjoyed the company and friendship of my present and past lab mates: Dr. Rajdeep, Dr. Anurag, Dr. Satyanarayana, Dr. Tarak, Dr. Karteek, Dr. Anirban, Dr. Saibal, Dr. Sourav Palchowdary, Dr. Abhishek, Dr. Anwesa, Dr. Promit, Sudip, Nimish, Nikhil, Srinath, Anjali Gaur, Srimayee and Oishika. I thank all of them for useful and healthy discussions.

Finally, I am thankful to my family members, who have been a source of constant support and strength for years. I thank my mother, sister and my husband for their patience and encouragement.

Preface

The thesis presents the results of investigations on supramolecular polymers using computational methods, including classical molecular dynamics (MD) simulations, enhanced sampling methods, and density functional theory (DFT) based quantum chemical calculations. Wherever possible, results obtained from simulations have been validated against experimental measurements from the literature.

Chapter 1 presents a general introduction to supramolecular polymers and describes the types of interactions involved in the process of self-assembly. An overview of the mechanisms of self-assembly leading to supramolecular polymers is presented along with the wide range of phenomena they exhibit, and their applications. Prior research on computer simulations and experimental findings on supramolecular polymers is also presented. A brief description of the theoretical methods adopted in this thesis is provided. This chapter ends with a section on 'Scope of the thesis'.

The rest of the thesis is divided into two parts: **Part I** discusses the mechanisms of self-assembly **(Chapter 2)**, molecular dipole relaxations **(Chapter 3)**, and polarisation retention times in liquid crystalline phases **(Chapter 4)**, while **Part II** studies lag times associated with self-assembly processes. The fuel-driven self-assembly of oligo(p-phenylenevinylene) (OPV) functionalised with the phosphate receptor dipicolylethylenediamine-zinc complex (DPA-Zn) — OPV-DPA and naphthalene diimide appended with guanidinium receptor (**Amph-NDG**) were examined in **Chapters 5A and 5B**. The role of intramolecular hydrogen bonding in giving rise to lag times and lag phases during oligomerisation was investigated in **Chapter 6**.

Chapter 2 Free energy calculations based on atomistic MD simulations were performed on N,N′,N″-trialkylbenzene-1,3,5-tricarboxamide (BTA) and [2.2]paracyclophane-4,7,12,15-tetracarboxamide (pCpTA) to investigate the mechanism of self-assembly in non-polar solvents at ambient conditions. While the former polymerises via the cooperative pathway, the latter does so via an isodesmic mechanism. Free energy calculations at ambient conditions have been carried out for both systems, and these experimentally observed mechanisms have been ascertained through these simulations. An asymmetric pattern of dipole arrangement (anti) in pCpTA molecule is favoured over the symmetric one (syn) due to dipole-dipole interactions. The free energy barrier associated with the change from anti to syn conformation of pCpTA is estimated.

Chapter 3 N,N′,N″,N‴-tetra-(Tetradecyl)-1,3,6,8-pyrenetetracarboxamide (PCA) molecule was modelled in all-atom representation with an aim to understand its behaviour in ferroelectric thin films. Possible configurations (depending on the relative amide dipole orientations) of PCA molecule were studied through gas-phase quantum calculations. Dipole relaxation in its liquid crystalline (LC) phase has been investigated and contrasted against that in the well-established N,N′,N″-trialkylbenzene-1,3,5-tricarboxamide (BTA) family. Furthermore, torsional barriers related to the amide dipole flip in both BTA and PCA are estimated from relaxed dihedral scan runs at M06-2x/6-311+g(d,p) level of theory. The mechanism underlying the polarisation switching in the LC phase on the application of an external electric field is investigated.

Chapter 4 To understand the origin and parameters governing the ferroelectric character of supramolecular polymeric thin films, derivatives of benzenecarboxamide **(BC)** bearing multiple $-\mathrm{CONHC}_{14}\mathrm{H}_{29}$ chains — N,N′-bis(tetradecyl)-1,4-benzenedicarboxamide **(2BC)**, N,N′,N″-tri(tetradecyl)-1,3,5-benzenetricarboxamide **(3BC)**, N,N′,N″,N‴-tetra(tetradecyl)-1,2,4,5-benzenetetracarboxamide **(4BC)**, N,N′,-N″,N‴,N⁗-penta(tetradecyl)benzenepentacarboxamide **(5BC)**, and N,N′,N″,N‴,N⁗,-N′′′′′-hexa(tetradecyl)benzenehexacarboxamide **(6BC)** — were examined in solution and LC phases. Various geometrical quantities have been compared against experimental findings for the LC phase. The homologues of 3BC molecule with different alkyl chain lengths — hexyl **(3BC-C6)**, decyl **(3BC-C10)**, and tetradecyl **(3BC-C14)** were examined in their liquid crystalline (LC) phases with an aim to identify molecular-level reasons for variations in dipole relaxation and thus the time scales for depolarisation in thin film samples. Methods to improve the retention times and the magnitude of remnant polarisation are suggested via studies of **(5BC-C14)** in its LC phase.

Chapter 5 is divided into two parts. **Chapter 5A** and **Chapter 5B** presents molecular-level insights into structural changes which take place during the process of self-assembly.

Chapter 5A ATP-selective and ATP-fuelled controlled supramolecular polymerisation of oligo(p-phenylenevinylene) (OPV) functionalised with the phosphate receptor dipicolylethylenediamine-zinc complex (DPA-Zn) — referred to as OPV-DPA — was studied experimentally by our collaborators, George and co-workers. While a time-delayed self-assembly was observed in absorption spectroscopy, the circular dichroism (CD) signal appeared with an additional delay. MD simulations presented in this thesis provide molecular level information for selective self-assembly along with the reasons for the observed lag times. The experimentally observed ATP selectivity is attributed to the formation of intermolecular hydrogen bonds between the ATP molecules in the stack. The structural rearrangement in the OPV-DPA molecules in the presence of ATP is responsible for the lag time in the formation of short oligomers. Chirality in the stack is induced with progress in oligomerisation.

Chapter 5B The fuel-driven self-assembly of **Amph-NDG** and the associated lag time were studied using UV-Vis absorption spectroscopy by George and co-workers. MD simulations provide possible model structures for NDG-ATP and NDG-GTP systems which were substantiated with height profiles of NDG-ATP obtained from atomic force microscopy and the monomer to ATP molar ratio in the self-assembly. Zero Kelvin DFT calculations have been performed to identify viable changes in the self-assembled structures. The dormant state of **Amph-NDG** monomer was found to possess an intramolecular hydrogen bond between the guanidinium N−H and C−O group. The existence of the dormant state precludes self-assembly. Upon addition of triphosphates (either ATP or GTP), the interaction between the imide group of guanidinium and phosphate group of triphosphate (from either ATP or GTP) triggers the dihedral rotation in **Amph-NDG**, as a consequence of which the intramolecular hydrogen bond breaks. The time spent in undergoing this structural rearrangement has been ascribed to cause the experimentally observed lag time.

Chapter 6 A prototypical molecule, N1,N1- (n-alkane-1,n-diyl)bis(N3,N5-dialkyl benzene-1,3,5-tricarboxamide), BNB, (N=6,9) has been considered to obtain generic insights into pathway complexity in supramolecular oligomerisation. Two molecules varying in their linker lengths have been studied. Conformational and configurational isomers of the monomer and dimer species have been identified; the free energy differences between these states as well as the pathways connecting them have been determined at ambient conditions, in their solution phase. The free energy barriers associated with these transitions obtained from the MD simulations match well with experimental estimates of the same obtained from lag times. The thesis ends with **Chapter 7**, providing a brief summary of the thesis and a future outlook.

Contents

Acknowledgements v

Preface vii

List of Figures xv

List of Tables xxix

1 Introduction 1

1.1 Historical Background . . . 1
1.2 Types of Self Assembly . . . 2
  1.2.1 Static Self Assembly (SSA) . . . 2
  1.2.2 Dynamic Self Assembly (DySA) . . . 2
1.3 Types of Interactions . . . 2
  1.3.1 van der Waals (vdW) Interactions . . . 2
  1.3.2 Dipole-Dipole Interactions . . . 2
  1.3.3 Hydrogen Bonding . . . 3
  1.3.4 π-π Interactions . . . 3
  1.3.5 Host-guest Interactions . . . 3
1.4 Mechanism of Supramolecular Polymerisation . . . 3
  1.4.1 Isodesmic Mechanism . . . 4
  1.4.2 Cooperative Mechanism . . . 5
1.5 Thermodynamics and Kinetics of Supramolecular Polymerisation . . . 7
1.6 Types of Aggregates . . . 8
1.7 Supramolecular Polymers in Aqueous Media . . . 9
1.8 Supramolecular Polymers in non-polar solvents . . . 9
1.9 Supramolecular Polymerisation at Interface . . . 10
1.10 Morphology of Supramolecular Polymers . . . 10
1.11 Applications . . . 10
  1.11.1 Self-Healing Materials . . . 10

1.11.2 Drug Delivery 12
1.11.3 Ferroelectrics 12
1.11.4 Sensors 13
1.12 Methodology 13
1.12.1 Quantum Chemical Calculations 13
1.12.2 Molecular Dynamics Simulations 14
1.12.3 Free Energy Calculations 17
1.12.4 Free Energy Methods 19
1.13 Molecules Under Study in the Present Thesis 22
1.13.1 Benzenecarboxamide (BC) 23
1.13.2 N,N′,N″,N‴-tetra-(Tetradecyl)-1,3,6,8-pyrenetetracarboxamide 27
1.13.3 [2.2]paracyclophane-4,7,12,15-tetracarboxamide (pCpTA) . . 28
1.13.4 Oligo(*p*-phenylenevinylene) (OPV) Derivatives 29
1.13.5 Naphthalene diimide (NDI) Derivatives 29
1.14 Softwares Used 30
1.15 Codes and Scripts for Analysis Written In-house: 30
1.16 Scope of the Thesis 30
Bibliography 33

2 Differentiating the mechanism of self-assembly in supramolecular polymers through computation 59
2.1 Introduction 60
2.2 Computational Details 62
2.2.1 Gas-Phase calculations 62
2.2.2 Solution Phase 62
2.2.3 Free energy Simulations 62
2.3 Results and Discussion 64
2.3.1 Conformations of Molecules 64
2.3.2 MD simulations to determine the self diffusion coefficient of [2.2]pCpTA-hex in chloroform 67
2.3.3 MD simulations of preformed decamer ([2.2]pCpTA-hex) in chloroform 69
2.3.4 Mechanism of Self-assembly 70
2.3.5 Conformational free energy difference in [2.2]pCpTA-hex . . 74
2.3.6 Conclusions 75
Bibliography 77

3 Supramolecular Polymerization of N,N′,N″,N‴ -tetra-(tetradecyl)-1,3,6,8-pyrenetetracarboxamide: A Computational Study 83
3.1 Introduction 84
3.2 Computational Details 84
3.3 Results and Discussion 86
    3.3.1 Monomer configurations 86
    3.3.2 Oligomers: Quantum calculations 87
    3.3.3 Comparison between force field and quantum approaches . . . 90
    3.3.4 Modelling stack stability in solution 90
    3.3.5 Self-assembly of PCA in solution 93
    3.3.6 Liquid Crystalline Phase 93
3.4 Conclusions 103
Bibliography 106

4 Dipolar Relaxation in Thin Films of Benzenecarboxamides 111
4.1 Introduction 112
4.2 Computational Details: 113
    4.2.1 Charge Calculations: 113
    4.2.2 MD simulations: 114
4.3 Results and Discussions: 115
    4.3.1 Solution Phase: 115
    4.3.2 Liquid Crystalline (LC) Phase: 117
4.4 Conclusions: 123
Bibliography 125

5 Computational Studies to Understand Self-assembly Selectively in the presence of ATP and Structural Rearrangments Therein 127

5A Modelling Biomimetic Temporal Self-assembly via Fuel-driven Controlled Supramolecular Polymerization 129
5A.1 Introduction 130
5A.2 Computational Details 132
    5A.2.1 Charge Calculations 132
    5A.2.2 MD simulations 136
5A.3 Results and Discussions 137
5A.4 Conclusions 143
Bibliography 145

5B Microscopic Insights from Quantum Chemical Calculations to Explore Lagtime in Spectroscopic Measurements 147

5B.1 Introduction 148
5B.2 Quantum Chemical Calculations 148
5B.3 Modelling of self-assembled structures 149
5B.4 Results and discussion 150
5B.5 Conclusions 153
Bibliography 154

6 Exploring the lag phase and lag times of supramolecular polymers: Free Energy Simulations 157

6.1 Introduction 158
6.2 Computational Details: 160
    6.2.1 Quantum Chemical Calculations: 160
    6.2.2 Force field based Molecular Dynamics (MD) Simulations: . . 160
6.3 Results and Discussions: 162
    6.3.1 Gas Phase: 162
    6.3.2 Free energy calculations: 164
    6.3.3 Conclusions: 176
Bibliography 177

7 Summary and Future Outlook 183

List of publications 185

List of Figures

1.1 Schematic representation of (a). Concentration-dependent and (b). Temperature-dependent degree of aggregation profiles for isodesmic and cooperative mechanisms. Adapted with permission from [28]. Copyright (2009) American Chemical Society. 4

1.2 Schematic free energy diagram describing (a) isodesmic, (b) uphill cooperative and (c) downhill cooperative mechanisms. This image is recreated with permission from [28]. Copyright (2009) American Chemical Society. 5

1.3 Schematic representation of dispersity of the polymer melt for cooperative & isodesmic mechanisms. 6

1.4 Schematic representation of the free energy landscape of different aggregation pathways: (a). Equilibrium versus non-equilibrium states, (b). Competitive pathway, (c). Consecutive pathway and (d). Kinetic pathway. The image is recreated from the minireview of Metern *et al.* [128] 8

1.5 Schematic diagram of chromophore arrangements and the corresponding spectral shifts. Adapted with permission from ref. [129]. Copyright 2014 The Royal Society of Chemistry. 8

1.6 Schematic representation of the different arrangements of chromophores in J-aggregates. (a) Ladder-type, (b) Staircase-type and (c) Brickwork type 9

1.7 Schematic representation of self-healing process in a material consisting of hierarchical hydrogen-bonding interactions. This figure has been reproduced from ref. [160] with permission from John Wiley and Sons 11

1.8 Schematic representation of several umbrella sampling windows along the reaction coordinate (ξ), & constructed free energy profile. 21

1.9 Variants of BTA (a). first BTA molecule by Curtius, (b). C=O-centered BTA and (c). N-centered BTA. 23

1.10 Schematic representation of dipole relaxation processes in liquid crystalline phase. Reprinted with permission from [41]. Copyright (2012) American Chemical Society. 25

1.11 Variants of Benzenecarboxamide; R=$C_{14}H_{29}$ (a). N,N′-bis(tetradecyl)-1,4-benzenedicarboxamide (2BC), (b). N,N′,N″,N‴tetra(tetradecyl)-1,2,4,5-benzenetetracarboxamide (4BC), (c). N,N′,N″,N‴,N⁗-penta-(tetradecyl)benzenepentacarboxamide (5BC) and (d). N,N′,N″,N‴,-N⁗,N′′′′′-hexa(tetradecyl)benzenehexacarboxamide (6BC). 27

1.12 Structure of BTA dimer in (a) 2:1 and (b). 3:0 configuration. Colour Scheme: Green- carbon, Red- Oxygen, Blue- Nitrogen, Tan- Hydrogen and the dotted lines represents the hydrogen bonds. 27

1.13 Structure of (a) Pyrene and (b). Pyrene tetracarboxamide, R=$C_{14}H_{29}$. 28

1.14 Structure of (a) [2.2]paracyclophane and (b). [2.2]paracyclophane-4,7,12,15-tetracarboxamide (pCpTA), R=C_6H_{13} 28

1.15 Structure of oligo(*p*-phenylenevinylene). 29

1.16 Structure of Naphthalene diimide. 29

2.1 Structure of **(a)** [2.2]Paracyclophane-tetracarboxamide ([2.2]pCpTA) (S_p enantiomer) and **(b)** benzene-1,3,5-tricarboxamide (BTA) and their associated supramolecular assemblies. Only the anti conformation of the monomer is shown in each case. 61

2.2 Structures of [2.2]pCpTA-met and BTA-met molecules. (a) anti conformer of [2.2]pCpTA-met (b) syn conformer of [2.2]pCpTA-met and (c) 2:1 conformer of BTA-met. Colour scheme: Green-Carbon, Red-Oxygen, Blue-Nitrogen, Tan-Hydrogen and dashed lines represent hydrogen bonds. The hydrogen bonds are Coloured in red and black depending on their dipole directions. The arrows shows the direction of the dipoles. 65

2.3 Dimer structures of [2.2]pCpTA-met and BTA-met molecules. (a) constructed out of anti conformers of [2.2]pCpTA-met (b) constructed out of syn conformers of [2.2]pCpTA-met and (c) 2:1 of BTA-met. See Figure. 2.2 for the Colour scheme. 65

2.4 (a). Evolution of total electric dipole moment of [2.2]pCpTA-met oligomers in anti & syn conformations and of oligomers of BTA-met in their 2:1 conformation. Structures of dimer of these two molecules are shown in Figure. 2.3 and (b). Energy difference (ΔE_N) of oligomers of anti and syn conformations of [2.2]pCpTA-met. Where, $\Delta E_N = E_{anti} - E_{syn}$. The structures were optimised using density functional theory at PBE-D3 level of theory. 67

2.5 Structures of [2.2]pCpTA-met and BTA-met oligomers were optimised at PBE-D3 level of density functional theory. **(a)** Binding energy as a function of oligomer size (N), **(b)** Normalized macrodipole moment of an oligomer (DP_N) [53] along the stacking direction and its running average. The solid line is DP_N and the dotted line represents its running average. 67

2.6 Results for oligomers of [2.2]pCpTA-met and BTA-met optimised using force field in gas phase. **(a)** Binding energy as a function of oligomer size, [54] **(a)** Normalized macrodipole moment (DP_N) [53] of the stack along the stacking direction and its running average. . . 68

2.7 Mean squared displacment of [2.2]pCpTA-hex molecule in chloroform obtained from three independent simulations. 69

2.8 Twist angle between successive molecules in a stack **(a)** Side view **(b)** Top view. The Colour scheme: Green-Carbon, Red-Oxygen, Blue-Nitrogen, Tan-Hydrogen and dotted lines represents the hydrogen bonds (Red-Inter, Black-Intra) and the angle between $\vec{A}$ and $\vec{B}$ is defined as twist angle. Alkyl tails are not shown for clarity. 70

2.9 Structural properties of a preformed decamer of [2.2]pCpTA-hex in chloroform solvent at ambient conditions: **(a)** Intermolecular distance (Inset: Twist angle), **(b)** Radial distribution function (black) and running coordination number (red) between oxygen of amide group and chlorine atom of the chloroform. Colour Scheme: Green-Carbon, Red-Oxygen, Blue-Nitrogen, Tan-Hydrogen and Magenta-Chlorine. 70

2.10 Free energy calculations: **(a)** Snapshot from MD simulations of dimer in chloroform, **(b)** Zoomed in portion of [2.2]pCpTA-hex dimer, the alkyl tails are not shown for clarity, "d" represents the distance between the centre of mass of the two molecules, d$_Z$ is the distance component along the stacking direction (z-direction). The Colour scheme is as described in Figure. 2.8; in addition, magenta represents the pseudoatom to refer to the centre of mass of the core in the [2.2]pCpTA-hex molecule. 71

2.11 Free energy profiles: (a). [2.2]pCpTA-hex oligomers solvated in chloroform and (b) BTA-hex oligomers solvated in *n*-nonane. The projection of distance between the top molecule in the oligomer and the dissociating monomer along the stacking direction is the collective variable. Inset shows the same data, near the free-energy minimum. 71

2.12 (a) Free energy difference, ΔF_N (see text for definition) of [2.2]pCpTA-hex and BTA-hex oligomers, (b) Deviations in free-energy difference from the dimerisation free energy obtained from MD simulations using the adaptive biased force (ABF) method. The solid line is a guide to the eye 72

2.13 Free-energy of formation. The solid line represents a linear fit for the raw data shown as points. 73

2.14 **(a)**. Definition of the dihedrals Φ and Ψ in [2.2]pCpTA-hex molecule, as used in the well-tempered metadynamics simulations. The atoms which form the dihedral are shown in CPK representation. The Colour scheme is same as in Figure. 2.10 **(b)**. The time evolution of the dihedrals **(c)**. Contour maps of free-energy (kcal/mol) for dihedrals Φ and Ψ. The yellow dotted line serves as a guide to the eye showing the minimum free energy path followed by the [2.2]pCpTA-hex molecule to convert from its anti to syn conformation. **(d)**. Time evolution of free-energy difference (ΔF$_{AS}$). Anti and syn regions are labelled for clarity. 74

2.15 The error in free-energy calculations: Block analysis of a biased potential from well-tempered metadynamics simulation using Φ and Ψ as collective variables. 75

3.1 **(a)** Pyrene derivative, N,N′,N′′,N′′′ -tetra-(tetraalkyl)-1,3,6,8-pyrenetetracarboxamide 1: R = -CH_3 (MPCA) 2: R = -$(CH_2)_{13}CH_3$ (PCA), **(b)** Schematic representation of pyrene core and the amide dipoles situated at the vertices of the rectangle. The anti-clockwise arrow illustrates the indexing convention for the dipole orientational configuration. The first dipole in the four-letter scheme is located at the tail of the arrow. 85

3.2 Structure of MPCA monomer optimised at M06-2x/6-311+d(g,p) level of theory. **(a)** Before optimisation and **(b)** After optimisation. Colour Scheme: Green-Carbon, Blue-Nitrogen, Red-oxygen and Tan-Hydrogen. 86

3.3 Structures of monomer of MPCA molecule optimised at M06-2x/6-311+g(d,p) level of theory. Methyl tail is not shown for clarity. **(a)** UDUD **(b)** UUDD **(c)** DDDU **(d)** DUUD **(e)** UUUU Colour scheme: Same as in Figure 3.2. **(f)** Energy level diagram. 87

3.4 Structures of MPCA dimer optimised at M06-2x/6-311+g(d,p) level of theory. **(a)** UDUD **(b)** UUDD **(c)** DUUD **(d)** DDDU **(e)** UUUU. and **(f)** Energy level diagram. **(g)**,**(h)** Definition of the twist angle between consecutive molecules in an oligomer. 88

3.5 Optimised structures of a trimer of molecule MPCA at M06-2x/6-311+g(d,p) level of theory. **(a)** UDUD **(b)** UUDD **(c)** DDDU **(d)** DUUD **(e)** UUUU. Colour scheme: Green-Carbon, Blue-Nitrogen, Red-Oxygen and Tan-Hydrogen. Methyl groups are not shown for clarity. **(f)** Energy level diagram. 89

3.6 **(a)** Final snapshot from a MD simulation of a decamer of PCA at 298.15 K in cyclohexane. Colour scheme: same as Figure 3.2 and black colour lines represent hydrogen bonds. **(b)** side view and **(c)** top view of zoomed shot of the stack, alkyl tails are not shown for clarity. **(d)** Normalised distribution of twist angle. **(e)** Normalised distribution of π-π distance. 92

3.7 Self-assembly of 20 PCA molecules in cyclohexane solution at 298.15 K. **(a)** Number of short oligomers of various sizes over time. Number of molecules present in dipole configuration **(b)** UDUD, **(c)** UUDD, **(d)** DUUD, **(e)** UUUD, **(f)** UUUU. 94

3.8 Progress of self-assembly of 20 PCA molecules in cyclohexane solution at 290 K **(a)** 0 ns, **(b)** 50 ns, **(c)** 100 ns. Solvent molecules are shown in Quicksurf representation. The C_{14} alkyl tail of PCA is not shown for clarity. The colour scheme is same as Figure 3.2. 94

3.9 The initial structure of the PCA system in liquid crystalline (LC) phase. Molecules in UUUU configuration. Colour Scheme: Green-Carbon, Red-Oxygen, Blue-Nitrogen, Tan-Hydrogen. Alkyl tails are not shown for clarity. The inter stack distance is shown. 95

3.10 Sequential dipole flips at zero electric field in the liquid crystalline phase of PCA in a simulation at 393 K, initiated from the UUUU configuration. Results from two arbitrarily chosen stacks are shown. **(a)** Stack1 **(b)** Stack2. The time at which the first dipole flips is taken to be zero and its molecule index is taken to be one. Corresponding simulations of BTA in its LC phase at 460 K starting from the UUU configuration. **(c)** Stack1 **(d)** Stack2 for BTA. 96

3.11 **(a)** MPCA, **(b)** BTA. Atoms which form the dihedral involved in the flip of the amide dipole are highlighted. Colour Scheme: Green-Carbon, Red-Oxygen, Blue-Nitrogen, Tan-Hydrogen. Alkyl tails are not shown for clarity. 97

3.12 Sequential dipole flips at zero electric field in the LC phase of PCA initiated from UUUU configuration. **(a)** Stack1,**(b)** Stack2 at 423 K. The time at which the first dipole flips is taken to be zero. 97

3.13 Dihedral angle ψ_1 (see Figure 3.11**(a)**) as a function of time for PCA in LC phase at 393 K at zero field. **(a)** Molecule 0, **(b)** Molecule 1, **(c)** Molecule 2, **(d)** Molecule 3, **(e)** Molecule 4, **(f)** Molecule 5, **(g)** Molecule 6, **(h)** Molecule 7, **(i)** Molecule 8, **(j)** Molecule 9 of stack 1. The abrupt change in the sign of the dihedral angle denotes a dipole flip and a consequent change in the molecular configuration from UUUU to UUUD. 98

3.14 Polarization per molecule of the system in the LC phase starting with UUUU configuration as a function of time at 393 K. The simulation attempts to capture polarisation inversion upon reversal of the direction of the applied E-field. 98

3.15 Snapshots of an arbitrarily chosen stack in the LC phase from equilibrium (zero-field) simulations. PCA at 393 K: **(a)** initial (0 ns), **(b)** & **(c)** intermediate (27 & 28 ns respectively) **(d)** final state (28.15 ns). Alkyl tails are not shown for clarity and the colour scheme is same as in Figure 3.2. Hydrogen bonds are shown in black color. 99

3.16 Non-sequential flipping of amide dipoles during simulations of PCA and BTA systems, initiated from the UUUU and symmetric (UUU) configurations in the LC phase. An external electric field is applied in a direction opposite to the amide dipoles. Events in two arbitrarily chosen stacks in each system are shown. **(a)**-**(b)**: Two stacks of PCA at 393 K. **(c)**-**(d)**: Two stacks of BTA at 460 K. 100

3.17 Potential energy surface (PES) of $\mathrm{C_{ar}}$-$\mathrm{C_{ar}}$-$\mathrm{C_{a}}$-O dihedral angle, obtained from relaxed scan at M06-2x/6-311+g(d,p) level of theory, for **(a)** MPCA **(b)** BTA. The conformation of the molecules at important points on the PES are depicted on the right panels. Alkyl groups are not shown for clarity and the colour scheme is same as in Figure 3.2. 101

3.18 Results from equilibrium MD simulations of PCA **(a-c)** and BTA **(d- f)** stacks in their respective liquid crystalline phases. Only two molecules are shown fot clarity. Alkyl groups are not shown for clarity. The rotation of an amide group in the bottom molecule (highlighted with thicker bonds) causes a dipole flip in the molecule on the top as well. **(a)**-**(c)**: Stages of dipole flip in PCA. **(d)**-**(f)**: Stages of dipole flip in BTA. The dotted lines represents hydrogen bonds. Black (left handed) and red (right handed). 102

3.19 Schematic representation of the mechanism of handedness reversal in the LC phase upon application of electric field. **(a)**-**(c)** are for PCA while **(d)**-**(f)** are for BTA. **(a)** Starting geometry, **(b)** metastable, **(c)** final structure and **(d)** starting geometry, **(e)** metastable and **(f)** final structure. Black (left handed) and red (right handed) dotted lines are hydrogen bonds. Red arrow represents the E-field. While the helical sense of the hydrogen bonds in BTA are reversed, those in PCA do not exhibit a clear sense (handedness), post the reversal of the amide dipole vector. 102

4.1 Chemical structure of molecules (a) N,N′-bis(tetradecyl)-1,4-benzenedicarboxamide (2BC), (b) N,N′,N″-tri(tetradecyl)-1,3,5-benzenetricarboxamide (3BC), (c) N,N′,N″,N‴-tetra(tetradecyl)-1,2,4,5--benzenetetracarboxamide (4BC), (d) N,N′,N″,N‴,N⁗-penta(tetradecyl)benzenepentacarboxamide (5BC), (e) N,N′,N″,N‴,N⁗,N′⁗-hexa-(tetradecyl)benzenehexacarboxamide (6BC) 113

4.2 Results from MD simulations of preformed decamer of nBCs in solution at 298.15 K (a) Normalized distribution of centroid-centroid distance and (b) Normalized distribution of twist angle. 116

4.3 Probability density of (a) lateral displacement and (b) angle between the normals of phenyl cores of successive molecules in the stack. Results are obtained from MD simulations of preformed decamers of nBCs in solution at 298.15 K 116

4.4 The initial structures of the systems in liquid crystalline (LC) phase. All amide dipoles are oriented in the same direction. (a) N,N′,-N″-tri(hexyl)-1,3,5-benzenetricarboxamide (3BC-C6), (b) N,N′,N″-tri(decyl)-1,3,5-benzenetricarboxamide (3BC-C10), (c) N,N′,N″-tri-(tetradecyl)-1,3,5-benzenetricarboxamide (3BC-C14), and (d) N,N′,-N″,N‴,N⁗-penta(tetradecyl)benzenepentacarboxamide (5BC-C14) . Color Scheme: Green - Carbon, Tan - hydrogen, Red - Oxygen, Blue - Nitrogen. 117

4.5 The final structure of 3BC-C6 from equilibrium simulations at 460 K. (a) side view and (b) top view. The colour scheme is same as in Figure. 4.4. 119

4.6 The final structure of 3BC-C10 from equilibrium simulations at 460 K. (a) side view and (b) top view. The colour scheme is same as in Figure. 4.4. 119

4.7 The final structure of 3BC-C14 from equilibrium simulations at 460 K. (a) side view and (b) top view. The colour scheme is same as in Figure. 4.4. 119

4.8 The configurations of each stack after 25 ns of equilibration in the NPT ensemble for (a) 3BC-C6, (b) 3BC-C10, and (c) 3BC-C14. The dipole configuration of each stack is labeled. 120

4.9 Depolarisation curves of 3BC homologues at 460 K. The inset shows the faster decay of polarisation in 3BC-C10 and 3BC-C14. P_0 is the polarisation of the sample in the fully poled state. 120

4.10 Potential energy surface (PES) of C$_{ar}$−C$_{ar}$−C$_a$−O dihedral angle, obtained from relaxed scan at M06-2x/6-311+g(d,p) level of theory. The dihedral definitions are given in Figure. 4.11. 121

4.11 Atoms considered for relaxed dihedral scan runs are highlighted in magneta (a) N,N$'$,N$''$-tri(methyl)-1,3,5-benzenetricarboxamide (M-3BC), (b) Asymmetric dihedral of N,N$'$,N$''$,N$'''$,N$''''$-penta(methyl)-benzenepentacarboxamide (M-5BC), and (c) Symmetric dihedral of N,N$'$,N$''$,N$'''$,N$''''$-penta(methyl)benzenepentacarboxamide (M-5BC). Color Scheme is same as in Figure. 4.4. 122

4.12 Depolarisation curve of 5BC system in its LC phase at 460 K. P$_0$ is the polarisation of the sample in fully poled state. 122

4.13 The final structure of 5BC-C14 from equilibrium simulations at 460 K. (a) side view and (b) top view. The colour scheme is same as in Figure. 4.4. 123

5A.1 Structure of **(a)** oligo(*p*-phenylenevinylene) (OPV) functionalized with dipicolylethylenediamine-zinc complex (DPA-Zn) (OPV-DPA) , **(b)** adenosine triphosphate (ATP). 130

5A.2 Experimentally determined, growth kinetics and lag phases of ATP-driven nucleation growth of **1** monitored by CD (mdeg), absorbance, scattering in kcps (kilo counts per second), size (nm) obtained from dynamic light scattering (DLS) and fluorescence. Absorbance, CD, and emission were monitored at 500 nm (c=2X10^{-5}M, HEPES/CH$_3$CN, 90/10, v/v, 0.9 equiv. ATP, 30 °C). Data from experimental collaborators. 131

5A.3 Schematic model of ATP-**1** employed in MD simulations. 132

5A.4 Gas phase DFT calculations of the ATP-**1** dimer, **(a)** Initial and **(b)** final configurations of ATP-1 dimer. Colour Scheme: Green - OPV, Blue - DPA, Red - ATP/GTP. Zinc atoms are represented as spheres in two different colours (yellow and magenta) to emphasize helicity and the counter ions (Cl$^-$) shown in tan colour. 132

5A.5 Atom mapping scheme in the ATP-**1** dimer. 133

5A.6 Segment-wise representaion of ATP-**1** oligomers. (a). Dimer, (b). trimer and (c). hexamer. Segments with the same colour code have the same atomic site charges across different oligomers. The site charges themselves are determined for the dimer via gas phase DFT calculations. 134

5A.7 Snapshots of initial structures of preformed (a). ATP-**1** and (b). GTP-**1** 25-mer. Zinc atoms have been depicted as spheres of two different colours (magenta and yellow) to demonstrate the helicity in the oligomers of the initial configurations in either of the stacks. Molecules of **1** are depicted in gray sticks (in a and b) and ATP and GTP have been shown in red. 137

5A.8 Snapshots of final structures of 25-mer (a). ATP-**1** and (b). GTP-**1** obatined from MD simulations. Zoomed images in (a) and (b) show intermolecular H-bonding between the triphosphates. Zinc atoms have been depicted as balls of two different colours (magenta and yellow) for easy identification of the helicity in the oligomer. Molecules of **1** are depicted as grey sticks (in (a) and (b)), while ATP and GTP are in red. In zoomed images of (a) and (b), intermolecular H-bonds are shown as dashed light blue lines. Each ATP/GTP molecule is depicted in a distinct colour to make it obvious that the hydrogen bonds are intermolecular in character. Comparison between (c). intramolecular H-bonds, (d). intermolecular H-bonds and (e). π-π distance between two adjacent molecules of **1** in ATP-**1** and GTP-**1** simulated assemblies. 138

5A.9 (a). Molecular structure of **1** and schematic depicting its A-D-A electronic configuration and (b). schematic showing inactive slipped supramolecular conformation of **1** in the absence of ATP. 140

5A.10 Simulated Dimer (a). Initial configuration, (b). Final snapshot and (c). Definition of slip distance. The colour scheme is same as Figure. 5A.4 140

5A.11 (a). Slip distance distribution, (b). inverse order parameter (blue curve) and intermolecular H-bonds (green curve) per ATP for various oligomers extracted from MD simulations of ATP-**1** stacks and (c). Snapshots from MD simulations of ATP-1 oligomers showing decrease in slip distance with extent of polymerisation. The colour scheme is same as Figure. 5A.4 141

5A.12 Inverse order parameter (IOP) of various oligomers of ATP-**1** stacks with reference frame chosen for the calculation of RMSD. (a). 28 ns and (b). 29 ns. 142

5A.13 Final snapshots of the simulated oligomers of (a) dimer, (b) trimer, (c) tetramer, (d) hexamer, (e) decamer and (f) pentadecamer. OPV core is depicted by thick green sticks, DPA and ATP have been represented by thin blue and red sticks, Zn atoms are depicted in spheres, with yellow on one side and magenta on the opposite, to clearly bring about the chirality of the assembly. 142

5A.14 RMSD of various oligomers of ATP-**1** with different reference frame chosen for the calculation of RMSD: (a). 28 ns, (b). 29 ns and (c). 30 ns. The error bars were calculated using the standard error formalism, by considering the RMSD data over time as blocks. 143

5B.1 Molecular structures (a) **Amph-NDG**, (b) adenosine triphosphate (ATP) and (c) guanosine triphosphate (GTP) 149

5B.2 Experimentally determined, growth kinetics and lag phases of (a) ATP-driven, and (b) GTP-driven nucleation growth of **Amph-NDG** monitored by absorbance spectra. Data from experimental collaborators. 149

5B.3 Model structures of **Amph-NDG** bound to (a) adenosine triphosphate (ATP) and (b) guanosine triphosphate (GTP). Colour scheme: Green and orange - Carbon, Red - oxygen, Blue - Nitrogen, Tan - Hydrogen and the dotted lines (Magenta - inter and black -intra) represent hydrogen bonds. 150

5B.4 Quantum chemical calculations at M06-2x/6-311g level of theory (a) Initial, (b) final conformation of **Amph-NDG**, the intramolecular hydrogen bond distance is shown in magenta and the O−H−N (acceptor-hydrogen-donor) angle is shown in blue. (c) structure of **Amph-NDG** at global minimum on the potential energy surface for N−C−C−N dihedral angle, and the atoms corresponding to dihedral scan are shown in orange and (d) potential energy surface. Colour scheme is same as Figure. 5B.3. 151

5B.5 Initial configurations of a trimer of (a) NDG-ATP and (b) NDG-GTP. The intramolecular hydrogen bond distance is shown in red and the O−H−N (acceptor-hydrogen-donor) angle is shown in blue. Colour scheme is same as Figure. 5B.3 151

5B.6 Final configurations of trimer of (a) NDG-ATP and (b) NDG-GTP from geometry optimisations performed at PBE-D3 level of theory. The intramolecular hydrogen bond distance is shown in red and the O−H−N (acceptor-hydrogen-donor) angle is shown in blue. Colour scheme is same as Figure. 5B.3 152

6.1 Schematic representation of the free-energy landscape of pathway complexity in supramolecular polymer. 159

6.2 Structure of the molecules studied here. (a) N1,N1-(n-alkane-1,n-diyl)bis(N3,N5-dialkylbenzene-1,3,5-tricarboxamide), R=$C_{12}H_{25}$ — BnB and (b) N,N′,N″-1,3,5,benzene tricarboxamide (BTA). 159

6.3 Schematic representation of possible monomer conformations and dimer configurations. Each configuration is labelled with a number for easy readability. 162

6.4 Optimized geometries of monomers from quantum chemical calculations. (a) M-B6B, and (b) M-B9B. Color Scheme: Green - Carbon, Red - Oxygen, Blue - Nitrogen and Tan - Hydrogen. The dotted lines represent the hydrogen bonds: Red - dipoles pointing above the phenyl core, Black - dipoles pointing down the phenyl core. The hydrogens which are not part of hydrogen bonding are not shown for clarity. 163

6.5 Probability distributions of reaction coordinate (RG) for all the windows from umbrella sampling simulations at 298.15 K. (a) for B6B and (b) for B9B. 165

6.6 Free energy profiles of monomers in *n*-nonane. (a). For BnB molecules at 298.15 K, the schematics of structures contributing to various regions are shown. (b) for B6B, (c) for B9B with structures at 298.15 K and (d) for B6B at 50 K. The structures representing the different minima in the free energy profiles were obtained using cluster analysis as implemented in Gromacs *cluster* module. 166

6.7 Probability distributions of reaction coordinate (RG) for all the windows of B6B free energy simulations at 50 K. 166

6.8 Time evolution of free-energy of various dimer configurations of (a) B6B, and (b) B9B. (c) Free energies of configurations **1**,**3**,**4** relative to the global minimum configuration **2**. The values were obtained from WTM simulations in solution at 298.15 K. 168

6.9 (a), (c) Network diagram of dimer configurations connecting the thermodynamically stable configuration (configuration 2) to the other configurations of B6B and B9B respectively. The arrows are drawn from low energy configurations to high energy configurations. The values on the arrows are the free energy differences between the connected nodes. The central node represents the global minimum. (b) and (d) The free energy landscape of B6B and B9B dimer respectively. Chemical structures shown in (b) and (d) are the most dominant clusters obtained from a cluster analysis of configurations contributing to the respective position in collective variable space. . 169

6.10 Minimum free energy path enroute configuration **2** from (a) **1**, (b) **3**, (c) **4** of B6B dimer and (d) **1**, (e) **3**, (f) **4** of B9B dimer. Structures corresponding to transition state and intermediate structures along the reaction pathway are shown via schematic representation. . . . 170

6.11 The representative structures (most probable ones from cluster analysis) of B6B dimer in configuration **1**. The colour scheme is same as in Figure. 6.4. The linkers are shown in magenta and ochre to differentiate the molecules. 170

6.12 The representative structures (most probable ones from cluster analysis) of B6B dimer in configuration **2**. The colour scheme is same as in Figure. 6.4. The linkers are shown in magenta and ochre to differentiate the molecules. 171

6.13 The representative structures (most probable ones from cluster analysis) of B6B dimer in configuration **3**. The colour scheme is same as in Figure. 6.4. The linkers are shown in magenta and ochre to differentiate the molecules. 171

6.14 The representative structures (most probable ones from cluster analysis) of B6B dimer in configuration **4**. The colour scheme is same as in Figure. 6.4. The linkers are shown in magenta and ochre to differentiate the molecules. 172

6.15 The representative structures (most probable ones from cluster analysis) of B9B dimer in configuration **1**. The colour scheme is same as in Figure. 6.4. The linkers are shown in magenta and ochre to differentiate the molecules. 174

6.16 The representative structures (most probable ones from cluster analysis) of B9B dimer in configuration **2**. The colour scheme is same as in Figure. 6.4. The linkers are shown in magenta and ochre to differentiate the molecules. 174
6.17 The representative structures (most probable ones from cluster analysis) of B9B dimer in configuration **3**. The colour scheme is same as in Figure. 6.4. The linkers are shown in magenta and ochre to differentiate the molecules. 175
6.18 The representative structures (most probable ones from cluster analysis) of B9B dimer in configuration **4**. The colour scheme is same as in Figure. 6.4. The linkers are shown in magenta and ochre to differentiate the molecules. 175

List of Tables

1.1 Representative molecules and the mechanism of self-assembly . . . 6

2.1 System sizes of BTA-hex in *n*-nonane for ABF simulations. 64
2.2 Windows setup in free-energy calculations performed using the ABF method 64
2.3 Mean values of intermolecular π-π distance and electric dipole moment of oligomers of [2.2]pCpTA-met optimised using force field in gas phase. 66
2.4 Mean values of intermolecular π-π distances (distance between centroids of closest phenyl rings of adjacent molecules in a stack) (in Å) and intermolecular hydrogen bond (N - - - O) distance (in Å) in oligomers of [2.2]pCpTA-met and BTA-met obtained from gas phase DFT calculations.[a] 68
2.5 Calculated free-energy difference ΔF_N using the ABF method.[a] . . 72

3.1 Energies of MPCA monomer optimised in gas phase using quantum chemical calculations for all amide configurations at M06-2x/6-311+g(d,p) level of theory. (see Figure 3.3). 87
3.2 Energies of MPCA oligomers for all configurations, relative to that of the UDUD configuration. Slip distance and twist angle for ground state. Data is from DFT calculations at M06-2x/6-311+g(d,p) level of theory. 88
3.3 Mean π-π distance and Dipole moment for oligomers of MPCA in all configurations, optimised at M06-2x/6-311+g(d,p) level of theory. 89
3.4 Comparison of dipole moment and energy difference obtained from force field and quantum chemical calculations for geometry optimised MPCA monomer. While the quantum calculations were performed at M06-2x/6-311g+(d,p) level of theory, the classical ones were done using DREIDING force field with DDEC/c3 charges. 91

3.5 Dipole moment and π-π distance for dimers of MPCA in all configurations, optimised at M06-2x/6-311+g(d,p) level of theory. 91
3.6 Simulation cell parameters for PCA in the liquid crystalline (LC) phase wherein the molecules are either in UDUD or UUUU configurations. 94

4.1 Geometry parameters of equilibrated structures of decamer 115
4.2 Initial (at 50 K) and final (at 460 K) dimensions of the simulation box of nBC compounds in their LC phases, all the dipoles were oriented in the same direction with respect to the π plane in the initial configurations. 117
4.3 Saturation polarisation values for 3BCs and 5BC compounds. 118

5A.1 Partial charges on atoms coloured green (Segment 1). 135
5A.2 Partial charges on atoms coloured blue (Segment 2). 135
5A.3 Partial charges on atoms coloured brown (Segment 3). 135
5A.4 Partial charges on atoms coloured orange (Segment 4). 136
5A.5 Partial charges on atoms coloured black (Segment 5). 136
5A.6 Partial charges on counter ion (Cl^-). 136
5A.7 System information over the oligomers of MD simulations. 139
5A.8 Slip distances in various oligomers 140

5B.1 Structural properties of optimised geometries of trimers of NDG-ATP and NDG-GTP at PBE-D3 level of theory 152

6.1 Energy difference between conformations of M-B*n*B monomer . . . 163
6.2 Energy difference between configurations of M-B*n*B dimer 164
6.3 Values of reaction coordinates to identify the configurations in the dimers. 167
6.4 Percentage population of the most probable structures (obtained from cluster analysis) along with their figure indices of the four dimer configurations of B6B. 172
6.5 Percentage population of the most probable structures (obtained from cluster analysis) along with their figure indices of the four dimer configurations of B9B. 173

Chapter 1

Introduction

1.1 Historical Background

Supramolecular chemistry is coined as ’chemistry beyond a molecule’ as it is based on interactions between molecules, contrary to traditional chemistry focusing on the formation of covalent bonding within a molecule. [1] The term ’supramolecule’ was introduced by Karl Lothar Wolf *et al.* in 1937. [2] The interactions between the molecules are non-covalent and weak. They include dipole-dipole, [3–8] van der Waals, electrostatic, [9–11] π-π, [12] hydrogen bonding, [13] hydrophobic, [14–16] metal-ligand coordination, [17–19] charge-transfer, [20, 21] integrated non-covalent interactions such as host-guest interactions [22, 23] and so forth. Although these interactions are weak, their combined effect can produce structurally and chemically stable structures of various architectures such as spheres, rods, cylinders, sheets etc. [24–26]

Non-covalent interactions, such as hydrogen bonds are highly directional and reversible in nature. Thus, materials formed through these interactions retain their polymeric properties in solution. [27, 28] Owing to the directionality and reversibility of these secondary interactions, these polymers have good material properties with low viscosity, which makes them easily processible. Besides, they possess some fascinating functionalities such as recyclability, ability to self-heal, and can be stimuli-responsive. [29] The characterisation of the supramolecular polymers is a daunting task due to their dynamic nature and cannot be done using standard techniques used for conventional polymers. A combination of several techniques including size exclusion chromatography, light scattering techniques, viscometry, fluorescence, circular dichroism (CD), ultraviolet-visible (UV/Vis), mass spectrometry, NMR spectroscopy, scanning probe microscopy, vapour pressure osmometry and electron microscopy can characterise supramolecular polymerisation. [30]

1.2 Types of Self Assembly

The process of self-assembly is guided by "instructions" of how to assemble into larger entities which are "coded" in the monomer units. [31–34] The self-assembly process uses many discrete components to form organised structures. These components interact with each other directly (through non-covalent interactions) or indirectly (through the environment). [35, 36]

1.2.1 Static Self Assembly (SSA)

Static self-assembly is a subclass of self-assembly processes that lead to structures in local or global equilibrium. To form stable structures, SSA may require energy (for example, stirring), but once it is formed, it is stable. SSA does not dissipate energy and structures are formed via free energy minimisation process. [37, 38] SSA can be due to either enthalpic effects, entropic effects, [39] or both. The classic examples are nanorods, [40] liquid crystals, [41] nanoparticles, [42] and block copolymers. [43]

1.2.2 Dynamic Self Assembly (DySA)

Dynamic self-assembly refers to stable non-equilibrium structures that persist only as long as the system is dissipating energy. [44–48] Free from the constraints of entropy maximization, these systems can reside in low entropic states. To obtain DySA structures, one must drive the system away from the thermodynamic equilibrium by supplying energy, which alters the interactions between the monomer units and the environment. DySA is very common in nature, such as schooling fish, starling flocks, and bacterial swarms.

1.3 Types of Interactions

1.3.1 van der Waals (vdW) Interactions

van der Waals interactions or dispersion forces are ubiquitous in nature. These are the weakest among the non-covalent interactions with a strength of 1-5 kJ/mol. Despite being weak, vdW interactions influence the structure, dynamics, stability, and function of the self-assembled structures. [49–51]

1.3.2 Dipole-Dipole Interactions

Proximal dipoles align in specific directions to stabilise their configuration, and such interactions can be additive to impart a macrodipole to the macromolecule. By taking advantage of dipole-dipole interactions, supramolecular chemists have synthesised molecules to self-assemble through these interactions. [4, 52–55] Dielectric properties of the materials formed through these interactions demonstrated the existence of a macrodipole moment.

1.3.3 Hydrogen Bonding

Hydrogen bonding is a pervasive interaction that drives self-assembly in both natural and synthetic systems. The strength of the hydrogen bond ranges from 1 to 170 kJ/mol depending on the type of donor and acceptor atoms. [56] Hydrogen bonds are individually weak. However, the combined effect of several hydrogen bonds between monomer units with multiple hydrogen bonding sites can result in stable ordered structures. [57–62] Hydrogen bonds are short-ranged, highly directional, and reversible. These properties of hydrogen bonds are utilised by synthetic chemists to design self-healable materials. [63–67]

1.3.4 π-π Interactions

π-π stacking interactions occur between the unsaturated cyclic compounds. They interactions are of two types, face-to-face, and face-to-edge. [68] The interaction strength ranges from 0-12 kJ/mol. [69] π-π interactions between monomers alone may be too weak and less directional to drive supramolecular polymerisation. However, the introduction of directionality on the periphery of the aromatic core promotes the directionality in supramolecular polymerisation. [69–72] π conjugated polymers have promising functionalities in view of flexible electronic devices. In the recent past, many research groups have focused on supramolecular electronics. [73, 74]

1.3.5 Host-guest Interactions

Host-guest complexes are formed through the cooperative effect of many non-covalent interactions between the host and guest molecules. Usually, the host molecules have a large volume or pocket to accommodate the guest molecules. A plethora of host-guest complexes have been reported, of which the most common ones are cyclodextrins (CD), [75–77] cucurbiturils (CB), [78–81] pillar[*n*]arenes, [82–84] crown ethers, [85–89] and calixarenes. [90, 91] The guest molecules are small organic molecules that have complementary shape and interactions with the host. The host-guest chemistry has several properties such as molecular recognition, transport, regulation, and catalysis, [92, 93] with a wide range of biomedical applications such as targeted delivery, [94–97] co-delivery, [98] and controlled release. [75, 99–104]

1.4 Mechanism of Supramolecular Polymerisation

The mechanism of self-assembly of supramolecular polymerisations can be broadly classified as isodesmic and cooperative based on the magnitude of equilibrium constant between the molecules and its variation with oligomer size. [28] The equilibrium constant (K_i) of the reaction (see equation. 1.1) is the ratio of rate constants of forward to backward reactions, defined as $\frac{k_i^+}{k_i^-}$.

$$\mathrm{M_i} + \mathrm{M} \underset{k_i^-}{\overset{k_i^+}{\rightleftharpoons}} \mathrm{M_{i+1}} \tag{1.1}$$

where,

M_i represents a oligomer of size i.

M denotes a monomer.

k_i^+, k_i^- are the rate constants for the forward and backward reactions.

Experimentally, the mechanism of self-assembly is determined by concentration- or temperature- dependent spectroscopic studies like Ultraviolet-visible (UV-Vis) or Circular dichroism (CD). The spectral changes indicates the formation of aggregates. In case of temperature dependent studies, the degree of aggregation (α) defined as $\alpha = \frac{\epsilon - \epsilon_{min}}{\epsilon_{max} - \epsilon_{min}}$ (ϵ_{max}, ϵ_{min}: maximum and minimum absorption at the maximum of the low energy shoulder) and α = 1 - $\frac{I_f - I_{f,min}}{I_{f,max} - I_{f,min}}$ ($I_{f,max}$, $I_{f,min}$: maximum and minimum fluorescence intensities). The sigmoidal or non-sigmoidal nature of the fraction of aggregates (α) as a function of temperature or concentration characterises the mechanism of self-assembly to be isodesmic or cooperative, respectively, as shown in Figure 1.1.

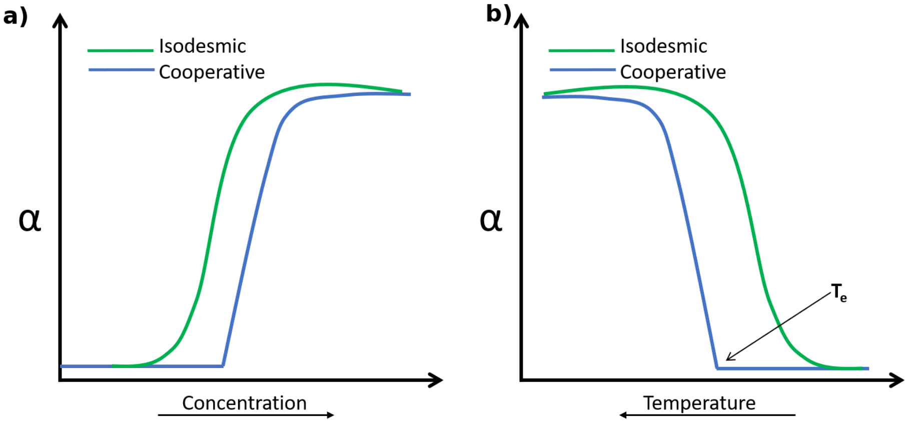

Figure 1.1: Schematic representation of (a). Concentration-dependent and (b). Temperature-dependent degree of aggregation profiles for isodesmic and cooperative mechanisms. Adapted with permission from [28]. Copyright (2009) American Chemical Society.

1.4.1 Isodesmic Mechanism

Isodesmic mechanism of supramolecular polymerisation is characterised by a single association constant (K) for each step in the assembly pathway, i.e., the association constant does not depend on the size of the oligomer. Sometimes, this mechanism is also called an equal-K model, and the free energy as a function of oligomer size is shown in Figure. 1.2(a).

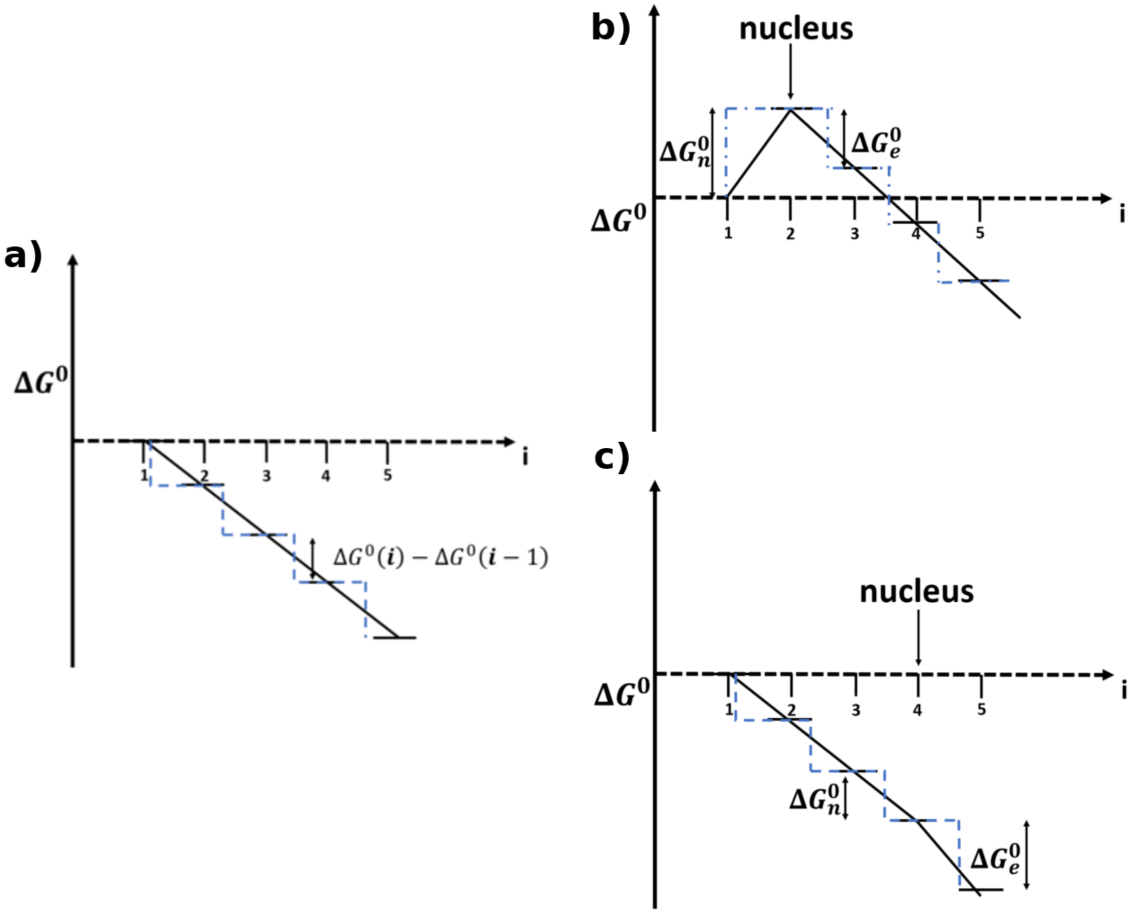

Figure 1.2: Schematic free energy diagram describing (a) isodesmic, (b) uphill cooperative and (c) downhill cooperative mechanisms. This image is recreated with permission from [28]. Copyright (2009) American Chemical Society.

1.4.2 Cooperative Mechanism

The cooperative mechanism is a two-step process: nucleation with an association constant of k_n involving the formation of a nucleus, followed by elongation with an association constant of k_e. This process is also known as the nucleation-elongation model. If the nucleation is associated with a dimer, then the model is referred to as the K_2-K model. The cooperative model is further classified into down-hill cooperative and up-hill cooperative models, the corresponding free energy diagram is shown in Figure. 1.2(b),(c). If the polymer elongates with an association constant higher than that of nucleation, the process is uphill cooperative, else it is downhill cooperative. The degree of cooperativity is described by cooperativity factor ($\sigma = \frac{k_n}{k_e}$). For the isodesmic mechanism, $\sigma = 1$, whereas for the cooperative mechanism, σ takes a value less than one. For systems with high cooperativity, the value approaches zero. Depending upon the mechanism by which the monomers self-assemble, the polymer melt would have a different degree of polydispersity and polymer length. Systems that follow the cooperative mechanism show monodispersity with long fibres, while those that follow the isodesmic mechanism result in short fibres with high polydispersity, as shown in Figure. 1.3

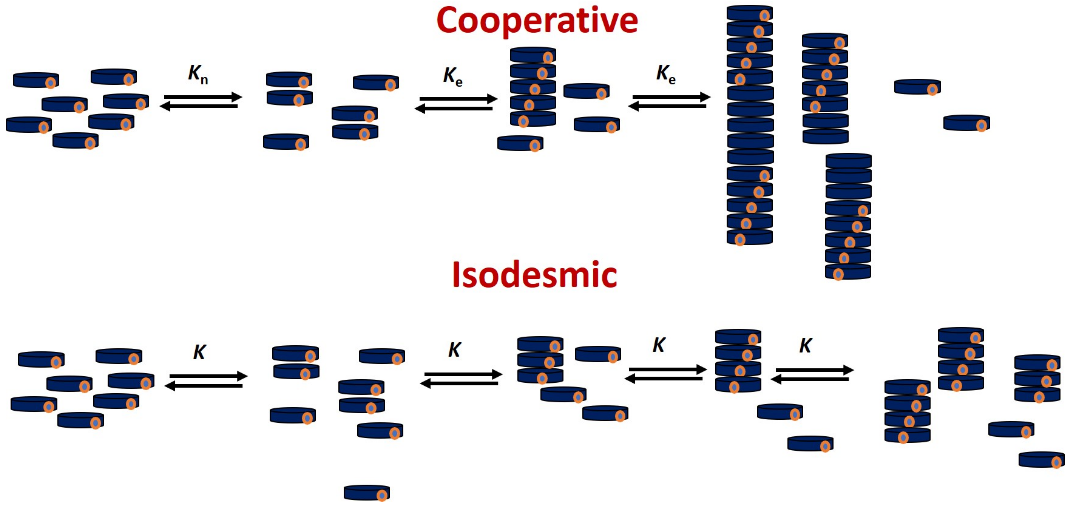

Figure 1.3: Schematic representation of dispersity of the polymer melt for cooperative & isodesmic mechanisms.

The mechanism of supramolecular polymerisation depends on the types of interaction involved in the self-assembly and may be altered by a combined effect of several interactions. For supramolecular polymers, it has been shown that minor changes in the molecular structure lead to a change in the mechanism of self-assembly. [105–110] The molecules studied till date are tabulated in Table. 1.1

Table 1.1: Representative molecules and the mechanism of self-assembly

Monomer	**Solvent**	**Mechanism of self-assembly**	**ref.**
N,N′,N″-trialkylbenzene-1,3,5-tricarboxamide (BTA)	*n*-heptane, iso-octane, and MCH	cooperative	[111]
benzotrithiophene-pentafluoro-L-phenylalanine (BTT-5F)	water	isodesmic	[105]
benzotrithiophene-L-phenylalanine (BTT-F)	water	cooperative	[105]
Perylene bisimide derivative	MCH/toulene (2:1, v/v)	cooperative	[112]

Monomer	Solvent	Mechanism of self-assembly	ref.
C_3-symmetric oligo(phenylene ethynylenes)-based trisamides	MCH	cooperative	[113]
Naphthalene-diimides-H (NDI-H)	*n*-decane	cooperative	[114]
oligo(*p*-phenylenevinylene) (OPV-x) derivative	dodecane	cooperative	[70]
pCp-4,7,12,15-tetracarboxamide (pCpTA)	$CDCl_3$	isodesmic	[115]
C_3-symmetrical acylated 3,3′-diamino-2,2′-bipyridine	MCH	isodesmic	[116]
Hexa-peri-hexabenzocoronenes (HBC)	Benzene, cyclohexane and THF	isodesmic	[117]
benzotrithiophene derivative	chloroform	isodesmic	[118]
benzotrithiophene derivative	methylcyclohexane and decalin	cooperative	[118]
terazoles and 1,3,5-tris(4,5-dihydroimidazol-2-diyl)benzene	chloroform	isodesmic	[119]

1.5 Thermodynamics and Kinetics of Supramolecular Polymerisation

In general, the mechanism of supramolecular polymerisation is studied after the thermodynamic equilibrium between the monomers and aggregates is established. At thermodynamic equilibrium, molecules in self-assembled aggregates have a specific configuration. However, during the self-assembly process, particularly in those governed by the cooperative mechanism, there can be multiple monomeric conformations and short oligomeric configurations. Therefore, kinetic contributions should also be considered while analysing the self-assembly process. [120, 121] Moreover, many naturally occurring biological self-assembly processes are kinetically controlled. [122] To mimic the functions of complex biological systems, we need to understand the self-assembly processes under kinetic control as well.

Kinetically controlled self-assembly was not understood well until 2012. For the first time, Meijer and co-workers systematically unravelled the self-assembled structures formed through kinetic and thermodynamic pathways. [123, 124] Energy landscape of a monomer in conformational space unfold different paths accessible to the monomer, as shown in Figure 1.4. Depending on the conditions (solvent composition, cooling rates, concentration) under which the self-assembly is proceeding, one can trap the monomers in the desired state to make non-equilibrium self-assembled structures with desired morphology. [124–127]

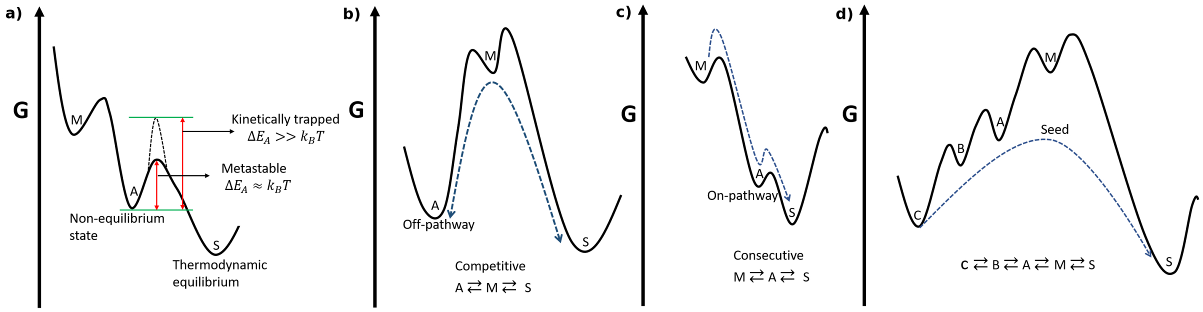
a)
G
M
A
S
Kinetically trapped
$\Delta E_A >> k_BT$
Metastable
$\Delta E_A \approx k_BT$
Non-equilibrium state
Thermodynamic equilibrium
b)
G
M
A
Off-pathway
S
Competitive
A ⇄ M ⇄ S
c)
G
M
A
On-pathway
S
Consecutive
M ⇄ A ⇄ S
d)
G
M
A
B
C
Seed
S
C ⇄ B ⇄ A ⇄ M ⇄ S

Figure 1.4: Schematic representation of the free energy landscape of different aggregation pathways: (a). Equilibrium versus non-equilibrium states, (b). Competitive pathway, (c). Consecutive pathway and (d). Kinetic pathway. The image is recreated from the minireview of Metern *et al.* [128]

1.6 Types of Aggregates

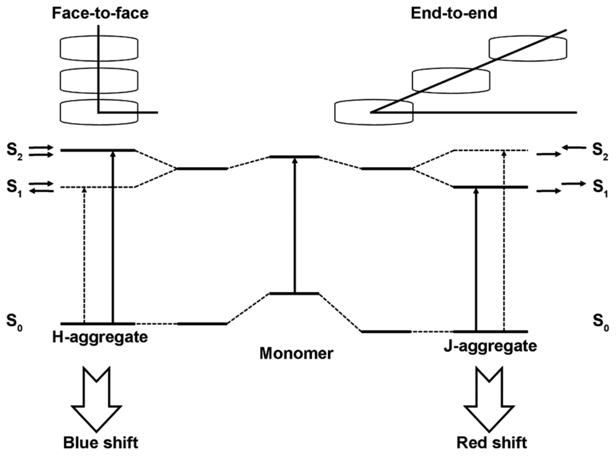
Face-to-face
End-to-end
S_2
S_1
S_0
H-aggregate
Monomer
J-aggregate
S_2
S_1
S_0
Blue shift
Red shift

Figure 1.5: Schematic diagram of chromophore arrangements and the corresponding spectral shifts. Adapted with permission from ref. [129]. Copyright 2014 The Royal Society of Chemistry.

The phenomenon of supramolecular polymerisation occurs in solution through intermolecular attractive forces between the molecules. Spectral studies reveal that upon aggregation, the aggregates exhibit distinct signature in the absorption bands as compared to the monomeric species. Based on the spectral shifts, the aggregation patterns are classified into J-aggregates and H-aggregates as shown in Figure. 1.5.

J-aggregates are identified through a shift in absorption band to a longer wavelength compared to the monomeric absorption band, whereas in H-aggregates, the absorption band shows up at a shorter wavelength. Chromophores in J-aggregates can be arranged in either of these following patterns such as brickwork, ladder, or staircase shown in Figure. 1.6. The H & J-aggregate molecules are known to show many optical properties according to their structural packing, which has many applications in major fields of science. [130–133]

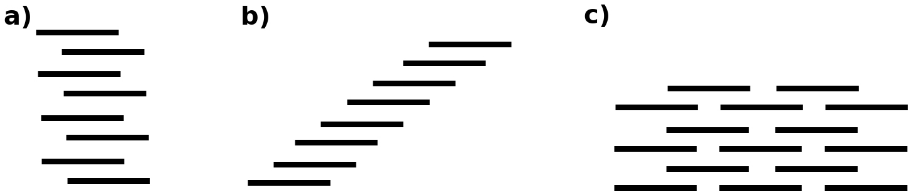

Figure 1.6: Schematic representation of the different arrangements of chromophores in J-aggregates. (a) Ladder-type, (b) Staircase-type and (c) Brickwork type

1.7 Supramolecular Polymers in Aqueous Media

Many biological systems, such as actin filament and microtubules are the inspiration for the supramolecular polymerisation process. Most of the natural processes, such as substrate binding, DNA folding, and membrane formation take place in an aqueous medium. [134] Realising the impact of the aqueous environment in the self-assembly process is pivotal for synthesising biocompatible systems. In an aqueous environment, the self-assembly of molecular building blocks is predominantly driven by hydrophobic interactions, which offer complexity, structural robustness, and adaptability. [135] The controlled pathway of self-assembly allows us to design diverse structures including spheres, tubes, vesicles, nanorods, nanofibres, and so forth. [136]

1.8 Supramolecular Polymers in non-polar solvents

In polar solvents, the strength of hydrogen bonds between the molecules in the self-assembled structures is significantly affected. [137–139] The main reason for this is the competition between the solute-solute and solute-solvent hydrogen bonds. [140, 141] Purely hydrogen-bonded self-assembled structures are rarely envisaged due to weak solute-solute hydrogen bonds in polar solvents. However, hydrogen bonds have unique advantages of directionality and versatility. Utilising these advantages, self-assemblies of molecules with hydrogen bonding functional groups in non-polar solvents were realised. [142–145]

1.9 Supramolecular Polymerisation at Interface

Supramolecular polymerisation studies are typically carried out in a homogeneous solution. The monomers should be soluble in the solvent to enable their aggregation. However, when the monomers are not soluble in the solvent, aggregation can be achieved by interfacial polymerisation. [146, 147] Through interfacial polymerisation, polymers with higher molecular weights can be achieved. Interfacial polymerisation can be used to fabricate materials with tailor-made architectures and diverse functionalities. [148–150]

1.10 Morphology of Supramolecular Polymers

Supramolecular polymerisation utilises weak non-covalent interactions to form one- or two- or three-dimensional complex ordered structures, depending on the information coded into the monomers. [151] These polymers have been shown to have different morphologies such as vesicles, fibres, ribbons, micelles, tubes, 2D-sheets. The nanostructures can be tuned by several factors such as temperature, photo-irradiation, ultrasonication, selection of solvents, external stimuli, and so on. The nanostructures have several applications such as field-effect transistors, photovoltaics, and sensors. [152–156] The properties of the device depend on size, shape, and morphologies. [40, 157, 158]

1.11 Applications

The complex supramolecular systems have fascinated material scientists, chemists, and biologists due to their unique features such as dynamic adaptivity, stimuli-responsive nature [159] that enable their use in many potential applications varying from ferroelectric materials to biomedical applications. We discuss a few such applications here.

1.11.1 Self-Healing Materials

The concept of self-healing in polymers was developed by taking cues from the natural healing processes in biological systems that extend their lifetime. Traditional polymers or polymer composites are used in several quotidian applications, which include transport vehicles, civil engineering, and electronics. However, these materials are susceptible to damage due to mechanical, chemical, UV radiation, or thermal effects. [161] The damages may be visible or invisible. To deal with invisible damages, the concept of self-healing materials was proposed. [162]

When the material undergoes damage, the reversible supramolecular network forms reactive end groups, which are named as sticky ends. Due to the formation of sticky ends, the material reaches a non-equilibrium state. To re-establish the equilibrium in the

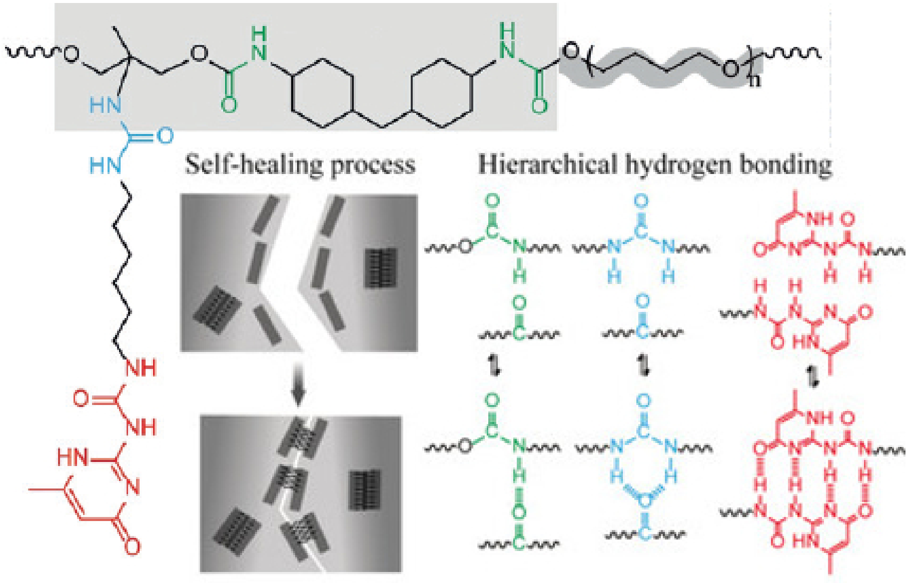

Figure 1.7: Schematic representation of self-healing process in a material consisting of hierarchical hydrogen-bonding interactions. This figure has been reproduced from ref. [160] with permission from John Wiley and Sons

polymer network, sticky ends strive to reassociate. [163] The sticky ends can interact via hydrogen bonding, [160, 164, 165] π-π interaction, [166–168] metal-mediated, [43, 169, 170] hydrophobic interactions, [16, 171, 172] ionic interactions, [173] host-guest interactions [174] or a combination of these interactions. [175]

Self-healing polymers can be classified into two categories—intrinsic and extrinsic. Extrinsic self-healing in the polymer matrix depends on two components present in a dispersed state: microcapsules or hollow fibres [176–179] and catalyst. When a material sustains mechanical damage, the microcapsules [180–182] containing the self-healing material rupture and the healing agent is released into the cracks through a capillary motion. [183, 184] The size of the microcapsules dictates the healing efficiency in the material. The larger the microcapsule, the higher the healing performance. [185] Once the healing agent comes in contact with the catalyst in the polymer matrix, the polymerisation process will be initiated at the crack sites. [186] Though the extrinsic methods allow instant self-healing, commercialization is limited by the amount of micro-containers inside the materials. To overcome this limitation, the intrinsic self-healing materials, which have the ability to heal for multiple healing cycles, are often sought.

The intrinsic self-healing materials use inherent dynamic bond breaking and making phenomenon multiple times. The dynamic bonds can be either covalent or supramolecular bonds. The intrinsic self-healing based on supramolecular interactions are convenient to introduce automatic self-healing and the self-assembling process shown in

Figure. 1.7.

1.11.2 Drug Delivery

The essential features for drug delivering systems include increased therapeutic efficiency, reduced off-site drug exposure, reduced administered dose, and patient-specific therapeutic function. The supramolecular polymers or materials can be engineered to achieve all these goals, which enable their use in therapeutic applications. In the field of drug delivery, the supramolecular host-guest interactions are widely used. The drug (guest) is carried to the target site by the macrocyclic host. The cyclodextrin macrocycles have been widely used as the host molecules so far. [187–191]

In the context of drug delivery, the aqueous environment plays a prominent role. The macrocycle host molecule has a hydrophilic outer shell and a hydrophobic cavity accommodating a hydrophobic drug molecule. The interaction between the host and guest molecules provides a molecular-level encapsulation with a steric barrier to drug deactivation. The displacement of water molecules within the cavity by the guest molecule (free from the frustrated water molecules that surrounded it) is entropically driven. In case of certain macrocyclic compounds, additional gain for stable host-guest interactions comes from enthalpic contributions such as hydrogen-bonding. [192] The cyclodextrin macrocyclic inclusion complex has the ability to mask the odour or taste of the drug molecules. It provides palatable formulation and also mitigates incompatibility or reaction between different components in a drug formulation. Other class of macrocycles such as cucurbit[*n*]urils, pillar[*n*]arenes, and calix[*n*]arenes were used in drug delivery. [193–195]

The binding affinities of the host-guest complexes can be tuned by external stimuli such as temperature, pH, light, and enzyme. [196, 197] Based on the stimulus, the host-guest complexes distinguish lesions from normal cells. Therefore, the supramolecular materials are smart enough to be used in drug delivery applications.

1.11.3 Ferroelectrics

Organic ferroelectrics have been developed in recent years with an aim to achieve environmentally friendly, low-cost devices with recyclability, mechanical flexibility, chemical stability, and biocompatibility. The ferroelectric materials are used in many applications, such as memory devices, actuators, and sensors. In ferroelectric materials, the remnant polarisation (P_r) and the coercive electric field (E_c) are the important parameters. Upon application of an external electric field, the ferroelectric materials will be able to switch between two polarisation states — "up" and "down" refer to $+P_r$, and $-P_r$. These two states represent global minima of the free energy landscape and the free energy barrier associated with these two states (W_b). The W_b is related to the dipole rotations in the self-assembled structures. This bistable states underlies the potential of ferroelectric materials to be used for memory applications. These parameters are associated with the switching events in memory devices. The polarisation in a ferroelectric material comes from dipoles in a non-centrosymmetric lattice. [41, 143, 198] The electric dipoles can be intrinsic or induced dipoles.

Hydrogen bonds and charge-transfer (CT) complexes can also produce electrical dipoles. In hydrogen bonded supramolecular structures, a dipole is created between the hydrogen-donor, which is partially negative, and the hydrogen-acceptor, which is partially positive. The CT-complex is a pair of electron-rich and electron-deficient molecules. These complexes can either form a segregated or a mixed stack. [199] The mixed stacks have the propensity to show ferroelectricity. A wide variety of organic materials have been developed through charge-transfer, hydrogen bonding, simple cation-anion exchange.

1.11.4 Sensors

The ability to detect a variety of analytes has a broad range of applications from medical to security realms. Several parameters play an important role in finding the analytes such as transducer, solvent, temperature. Sensors can be broadly classified into two categories — sensitive and selective. The selective ones are specific to an analyte, whereas the sensitive ones can identify multiple analytes. The goal in the sensor chemistry is to develop sensors that have general applicability in multiple environments, high level of selectivity even at low concentrations of the target analyte. [200]

The adaptive nature of the materials formed through supramolecular interactions facilitates sensor development. Due to the weak non-covalent interactions between the molecules, supramolecules can change their configuration in response to the external stimuli, here which is the target analyte. The configurational changes in molecules show noticeable changes in spectral properties such as fluorescence and adsorption, which can then be analysed to detect a particular analyte. Due to the reversibility of supramolecular assemblies upon removal of external stimuli, their usage in developing sensors has another advantage that the sensor can be used several times, unlike those that rely on covalent bond formation. [201]

1.12 Methodology

1.12.1 Quantum Chemical Calculations

The quantum chemical calculations in this thesis were performed for their own insights as well as to validate the force fields through comparison of binding energies and geometries. Relative stabilities of various conformations of a monomer have been studied from density functional theory (DFT) geometry optimisation calculations. In DFT, the energy of the molecules is a functional of the electron density, which is a physical characteristic of all molecules. The electron density, $\rho(\mathbf{r})$, is defined as the integral over the spin coordinates of all electrons and over all but one of the spatial variables (x $\equiv$ **r**,s) shown in equation. 1.2.

$$\rho(\mathbf{r}) = \mathbf{N} \int ... \int |\psi(\mathbf{x_1}, \mathbf{x_2}, ..., \mathbf{x_N})|^{\mathbf{2}} d\mathbf{s_1} d\mathbf{x_2} ... d\mathbf{x_N} \tag{1.2}$$

$\rho(\mathbf{r})$ determines the probability of finding any of the N electrons within volume element *d*r. The ground-state of the system can be determined through the minimisation of the total energy functional as $\langle \phi | \hat{H} | \phi \rangle = E[\rho]$. The net atomic charges (NAC) on the atoms were calculated from the Density Derived Electrostatic and Chemical (DDEC/c3) [202, 203] charge method, which uses the valence electron density as the input.

1.12.2 Molecular Dynamics Simulations

The prudent tuning of the monomer unit in supramolecular polymerisation leads to a significant difference in the properties of self-assembled structures. [204] To understand the influence of several parameters on the self-assembled structures, chemists need a microscope that can capture the atomic level information. Molecular Dynamics (MD) simulations framework — as discussed below — involves positions, momenta & forces of individual atoms/molecules at an instant of time, and also their evolution with it. Therefore, they serve the purpose as an atomic level microscope and can be utilised by the synthetic chemists to get molecular level understanding. With this motivation, we employed MD simulations in the present thesis to study the following aspects of supramolecular polymers.

a) The self-assembly mechanism.

b) The mechanism of polarisation switching in liquid crystalline phase upon application of electric field.

c) The activation barriers associated with the transition states in the free energy landscape of dimers.

d) Structural changes in response to adenosine triphosphate.

MD simulations are computer-based experiments for analysing the movements of atoms or molecules that can mimic the real-world environment. The microstate of a system of atoms or molecules is represented in terms of their positions and momenta. The trajectory of the system is determined numerically by integrating Newton's equation of motion iteratively. The forces acting on the atoms and their potential energies are calculated using force-fields.

$$\mathbf{F}_i = m_i a_i = m_i \frac{d\mathbf{r}_i^2}{dt^2} \tag{1.3}$$

The force on each atom is the negative of the derivative of its potential energy with respect to the position of the atom,

$$\mathbf{F}_i = -\nabla V_i \tag{1.4}$$

For a given set of initial coordinates and velocities, the potential energy of each atom, and thereby the force acting on it, is calculated. The new set of coordinates & velocities are obtained by discrete integration of the equation. 1.4. This procedure is repeated as many times as needed in an iterative fashion to obtain/reveal the dynamics of the system over time. The structural and dynamical properties of any system depend on the positions and velocities of its atoms. Comparison between the properties measured through simulations and experiments is valid due to the ergodic hypothesis. The ergodic hypothesis states that, over a long period of time, the time average approaches the ensemble average, as all the accessible microstates in the system are equiprobable over a long period of time.

Integrating equation 1.4 generates a trajectory in the microcanonical ensemble, however, real-life experiments are carried out in an environment that has temperature, pressure effects. To mimic the experimental conditions, additional degrees of freedom coming from temperature and pressure have to be added to equation 1.4 to generate a trajectory of the system in the isothermal-isobaric ensemble.

Furthermore, the credibility of simulations is directly related to the potential energy function used to describe the interactions between the atoms or molecules. The interaction between the atoms are typically classified into two categories — bonded and non-bonded interactions. The bonded interactions are described by the following terms:

$$V_{bond} = \sum_{i=1}^{N_b} \frac{1}{2} K_i^b (r_i - r_{0,i})^2 \tag{1.5}$$

$$V_{angle} = \sum_{i=1}^{N_\theta} \frac{1}{2} K_i^\theta (\theta_i - \theta_{0,i})^2 \tag{1.6}$$

$$V_{dihedral} = \sum_{i=1}^{N_\phi} \frac{1}{2} K_i^\phi cos(n_i(\phi_i - \phi_{0,i})) \tag{1.7}$$

$$V_{improper} = \sum_{i=1}^{N_\xi} \frac{1}{2} K_i^\xi (\xi_i - \xi_{0,i})^2 \tag{1.8}$$

Which correspond to two, three, and four body interactions among covalently linked bodies, respectively. For bond length r_i, bond angle θ_i, and for the improper dihedral (out of plane) angle ξ_i, the interactions are harmonic, and for the dihedral angle ϕ_i the interaction potential is complex. In general, these interaction potential forms varies across different force-fields. The non-bonded interactions, which correspond to interactions between the atoms separated by more than three covalent bonds are usually described by Coulomb's law

$$V_{Coulomb} = \sum_{i<j} \frac{1}{4\pi\epsilon_0\epsilon_r} \frac{q_i q_j}{r_{ij}} \tag{1.9}$$

for electrostatic interactions and by Buckingham or the Lennard-Jones potential

$$V_{lj} = Aexp(-B_{ij} r_{ij}) - \frac{C_{ij}}{r_{ij}^6} \tag{1.10}$$

$$V_{lj} = 4\epsilon[(\frac{\sigma}{r_{ij}})^{12} - (\frac{\sigma}{r_{ij}})^6] \tag{1.11}$$

for van der Waals interactions, where r_{ij} is the separation between the particles i and j. Equivalently, equation. 1.10 can be replaced by the Lennard-Jones potential (Eq. 1.11). The potential terms (1.5, 1.6, 1.7, 1.8, 1.9, 1.10) along with the complete set of force constants (k_r,k_θ,k_ϕ,k_ξ), and equilibrium bond lengths, bond angles, improper dihedral angles and dihedral angles (r_0,θ_0,ϕ_0, ξ_0) between different types of particles constitute a force field. In this thesis, we used a variety of force fields namely DRIEDING, [205] general AMBER force field (GAFF), [206] TraPPE for linear alkanes [207] and TIP3P water, [208] depending on the system of interest.

To solve the equations of motion, various numerical integrators are available. Verlet, velocity-Verlet, Leap-frog, Gear predictor-corrector algorithm to name a few. [209, 210] The velocity-Verlet algorithm is the simplest and widely used and has time-reversibility. The positions and velocities are updated as

$$\boldsymbol{p}_i(t + \frac{1}{2}\delta t) = \boldsymbol{p}_i(t) + \frac{1}{2}\delta t \boldsymbol{f}_i(t) \tag{1.12}$$

$$\boldsymbol{r}_i(t + \delta t) = \boldsymbol{r}_i(t) + \frac{\delta t}{m_i} \boldsymbol{p}_i(t + \frac{1}{2}\delta t) \tag{1.13}$$

$$\boldsymbol{p}_i(t + \delta t) = \boldsymbol{p}_i(t + \frac{1}{2}\delta t) + \frac{1}{2}\delta t \boldsymbol{f}_i(t + \delta t) \tag{1.14}$$

where δt is the simulation time step. The maximum allowed timestep used in MD simulations is dictated by the highest frequency of bond vibrations in the system. Molecular dynamics is a handy tool to obtain information about the structure and dynamics of supramolecular polymers. However, it suffers from certain limitations. In principle, a non-bonded interaction exists between every particle pair. For each integration step, calculating the non-bonded contribution requires $\mathcal{O}(\mathrm{N}^2)$ summation, where N is the number of atoms in the system, and therefore takes the bulk of the CPU time. Improving the efficiency in this part of the computation enables one to reach a large simulation timescale. Two optimisations are widely used: cut-off radius and neighbor lists. Typically, a distance cut-off of 10 to 14 Å around each particle is taken for the non-bonded calculations to enhance the computational efficiency. Since the Lennard-Jones potential decays as r^{-6}, additional forces can be neglected for larger r. However, the use of such cut-off for the Coulomb potential is known to cause severe artefacts due to its slow 1/r decay. [211–213] Such long-range artefacts are avoided by the use of Ewald summation, [214] which was originally derived to calculate electrostatic interactions in periodic crystals. If the system has similar periodicity, this method is particularly well suited. While using the Ewald summation, the electrostatic interaction is split into two contributions. The first contribution constitutes interactions within the cut-off, computed directly via equation. 1.9. The second contribution includes long-range interactions outside the cut-off, which are computed in reciprocal space. Fast Fourier transforms are used for calculating the reciprocal sum. The Particle Mesh Ewald (PME) [215] is more efficient than Ewald summation, and it scales as NlogN.

With the CPU power available at present, MD simulations performed typically involve particles in the order of 10^3 to 10^5. Systems of this size can suffer from finite-size effects. To avoid them, periodic boundary conditions are considered during simulations. This means that the simulation takes place in a computational box, which is virtually surrounded by an infinite number of identical replica of boxes packed in a space-filling way. When periodic boundary conditions are used, particles may freely cross the simulation box boundaries. For each particle leaving the box from one side at any instant of time, an identical particle from the adjacent replica box enters into the simulation box from the opposite side at the same instant of time.

1.12.3 Free Energy Calculations

Free energy is a thermodynamic function that determines the equilibrium state of a system. The free energy landscape helps to visualise the complexity in protein aggregation, [216, 217] and rate of reactions. The Helmholtz (F) & Gibbs free energies

(G) are the characteristic state functions of the isochoric-isothermal (NVT) and isobaric-isothermal (NPT) ensembles, respectively. In contrast to the potential or kinetic energy, which can be directly computed from statistical averages of an equilibrium MD trajectory, the (Gibbs or Helmholtz) free energy (G, F) cannot be computed from a statistical average. The Gibbs free energy (G) and the entropy (S) are related as

$$G = H - TS \tag{1.15}$$

and Helmholtz free energy (F) and entropy (S) are related as

$$F = U - TS \tag{1.16}$$

F, G are the properties of NVT, NPT ensemble respectively, which depend on the extent of configurational space accessible to the system. Computing the absolute free energy of a system is a challenging task. However, over the past few decades, statistical mechanical procedures have been developed for the calculation of relative free energies between states.

Let A & B be two different states of a system with the potential energy function V(R) changing continuously between them. Define classical Hamiltonian H(**p**,**R**) as a function of coupling parameter λ, such that $H_a(\mathbf{p},\mathbf{R},\lambda{=}0)$ and $H_b(\mathbf{p},\mathbf{R},\lambda{=}1)$ describe the system in states A and B, respectively, [218]

$$H(\mathbf{p}, \mathbf{R}, \lambda) = \sum_{i=1}^{N} \frac{\mathbf{P}_i^2}{2m_i(\lambda)} + V(\mathbf{R}, \lambda) \tag{1.17}$$

The free energy of state A (or state B), represented as $F_{a,b}$ is defined as

$$F_{a,b} = -\frac{1}{\beta} ln Z_{a,b} \tag{1.18}$$

where $Z_{a,b}$ is the canonical partition function,

$$Z_{a,b} = \int \exp(-\beta(H_{a,b}(\mathbf{p}, \mathbf{R})))d(\mathbf{p}, \mathbf{R}) \tag{1.19}$$

with the inverse temperature $\beta = \frac{1}{k_B T}$. The free energy difference therefore is

$$\Delta F = F_a - F_b = -\frac{1}{\beta} ln(\frac{Z_b}{Z_a}) \tag{1.20}$$

There are two classes of methods for calculating free energy differences (ΔF or ΔG) between two states A and B. The first class —equilibrium methods —include Thermodynamic Integration (TI), Free Energy Perturbation (FEP), and Particle Insertion

(PI). Advanced sampling techniques such as Adaptive Biasing Force (ABF), [219] Umbrella Sampling (US), [220] Metadynamics, [221] Well-tempered metadynamics [222] and Steered Molecular Dynamics (SMD) fall under the other class — non-equilibrium methods. [223]

1.12.4 Free Energy Methods

Adaptive Biasing Force (ABF)

The adaptive biasing force method, developed by Darve and Pohorille, [219] is based on thermodynamic integration. The average force along the reaction coordinate (ξ) is calculated directly in ABF. To start with, the entire reaction coordinate is divided into bins and the force accumulated in each bin is calculated after N_{step} steps as

$$\mathbf{F}_\xi(N_{step}, k) = \frac{1}{\mathcal{N}(N_{step}, k)} \sum_{i=1}^{\mathcal{N}(N_{step},k)} \mathbf{F}_i(t_i^k) \tag{1.21}$$

where,

$\mathcal{N}(N_{step},k)$ is the number of samples collected in the bin k after N_{step} steps of the simulation.
$\mathbf{F}_i(t_i^k)$ is the i^{th} force sample when ξ is in bin k.
t_i^k is the time at which a sample is collected.

$$\mathbf{F}_i(t_i^k) = \frac{d}{dt}(M_\xi \frac{d\xi}{dt})\bigg|_{t_i^k} \tag{1.22}$$

where M_ξ is the mass tensor.

In ABF simulations, the force $-(\nabla\xi)\mathbf{F}_\xi(N_{step},k)$ is applied to bias the dynamics of the system. For a large number of samples $\mathcal{N}(N_{step},k)$, the quantity $\mathbf{F}_\xi(N_{step},k)$ is a good approximation for the average thermodynamic force acting along ξ. Thus, the total bias acting on the system is close to zero when it enters the diffusive region along the reaction coordinate ξ. The free energy difference ($\Delta A_{a\rightarrow b}$) between state A and state B can be estimated by integrating the average biasing force $\mathbf{F}_\xi$,

$$\Delta A_{a\rightarrow b} = -\int_{\xi_a}^{\xi_b} \mathbf{F}_\xi d\xi \approx -\frac{\xi_b - \xi_a}{k_{max}} \sum_{k=1}^{k_{max}} \mathbf{F}_\xi(N_{step}, k) \tag{1.23}$$

In ABF simulations for long reaction pathways, the entire reaction coordinate (ξ) is divided into shorter consecutive windows. While constructing the free energy profiles, ABF does not require an overlap of reaction coordinate between the consecutive windows, unlike umbrella sampling.

Umbrella Sampling (US)

Umbrella sampling is a free energy technique used to improve the sampling of the system, where the ergodicity is hindered by a large barrier(s) in its free energy landscape. It was introduced by Torrie and Valleau in 1977. [220] This method is based on importance sampling in statistics. Systems with high free energy barrier(s) in their reaction pathways are poorly sampled in normal MD simulations. To overcome such difficulties in estimating the free energy differences, the potential function of the system is modified so that the unfavourable states are sampled sufficiently. For reaction coordinate (ξ), the modified potential $V^{'}(\xi)$ is written as

$$V^{'}(\xi) = V(\xi) + W(\xi) \tag{1.24}$$

where $W(\xi)$ is the biasing function, which is usually a harmonic potential with a force constant k_w, centered around the equilibrium ξ_0

$$W(\xi) = k_w(\xi - \xi_0)^2 \tag{1.25}$$

In the US simulation, the reaction coordinate (ξ) connecting the two regions of interest is divided into small windows (see Figure.1.8), and the system in each window is simulated independently with the corresponding modified potential (eq. 1.24). For each window, the probability distribution (P_ξ) of ξ centered around the reference value ξ_0 is calculated. Larger the values of k_w, narrower would be the distribution (P_ξ). The unbiased distribution $P^{'}(\xi)$ can be constructed from

$$P^{'}(\xi) = P(\xi)e^{\frac{-k_w(\xi-\xi_0)^2}{2K_BT}} \tag{1.26}$$

With adequate overlaps between the probability distributions of any two consecutive windows, the free energy as a function of ξ, calculated as the work done in undergoing the transformation from state A to state B can be obtained by means of Weighted Histogram Analysis Method (WHAM). [224] If the unbiased probability distribution of the system along ξ is,

$$Q(\xi) = \frac{\int \delta[\xi(r) - \xi]e^{[(-\beta E)d^N r]}}{\int e^{[(-\beta E)d^N r]}} \tag{1.27}$$

where $Q(\xi)\delta\xi$ is the probability of finding the system in a small interval of $\delta\xi$ around ξ, then the free energy along ξ is

$$A(\xi) = -\frac{1}{\beta}ln(Q(\xi)) \tag{1.28}$$

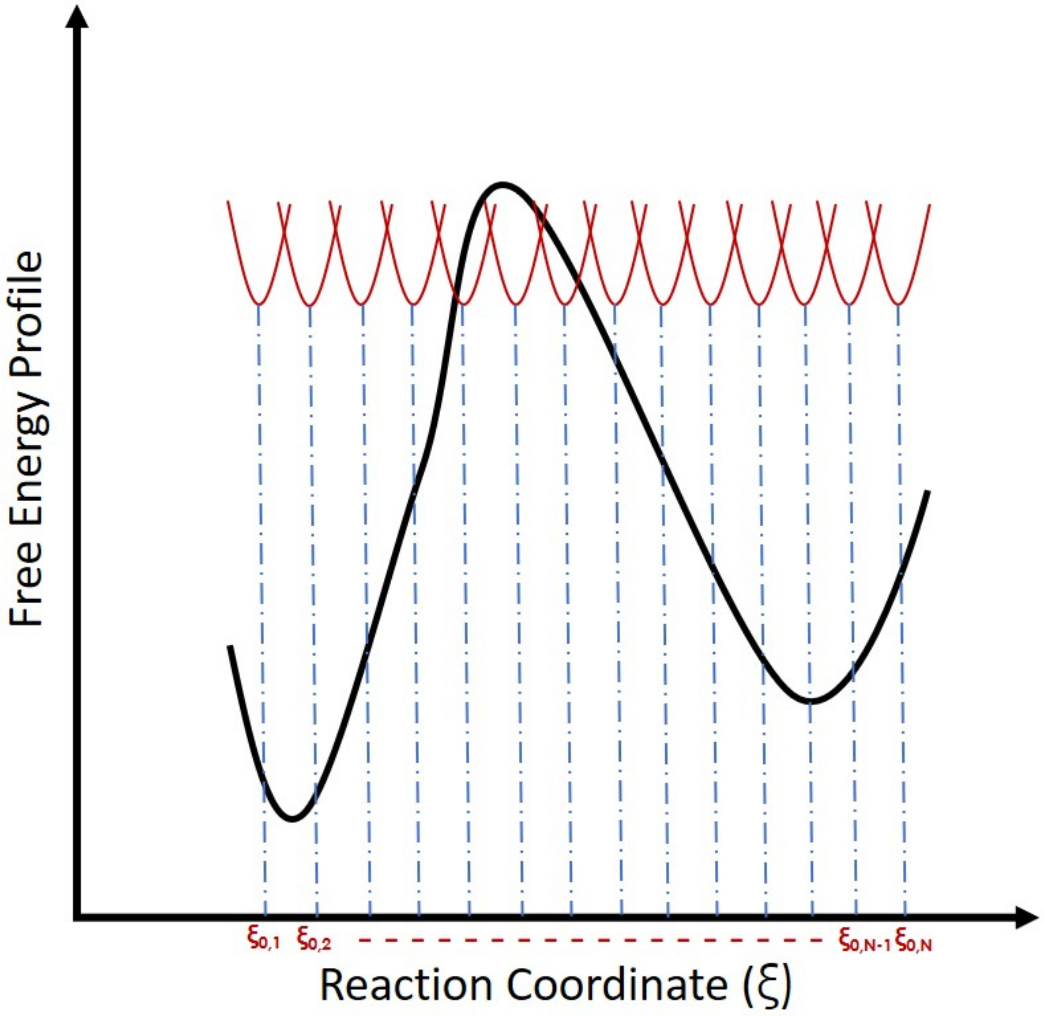

Figure 1.8: Schematic representation of several umbrella sampling windows along the reaction coordinate (ξ), & constructed free energy profile.

Well-Tempered Metadynamics (WTM)

The Well-tempered metadynamics (WTM) simulation, the system is biased by applying a history-dependent potential (V$_G$) in the space of predefined collective variables (CVs). [222] The bias potential has a gaussian form as in equation. 1.29

$$V_G(\mathbf{S},t) = \sum_{t'=0,\tau_G,2\tau_G,\ldots}^{t^1<t} dt' \omega exp(-\sum_{i=1}^{d} \frac{(S_i(R) - S_i(R(t')))^2}{2\sigma_i^2}) \tag{1.29}$$

where,

S is the set of CVs described by the coordinates **R** of the system.

σ_i is the width of the Gaussian along the ith CV.

ω is a constant energy rate that depends on the Gaussian height W and the Gaussian deposition stride τ_G as

$$\omega = \frac{W}{\tau_G} \tag{1.30}$$

The height of the Gaussian is decreased with simulation time as,

$$W = \omega \tau_G e^{\frac{V_G(\mathbf{S},t)}{k_B \Delta T}} \tag{1.31}$$

where ΔT is an input parameter with the dimension of temperature, and k_B is the Boltzmann constant. The effect of the well-tempered metadynamics bias potential is to push the system away from the local free energy minima and drive it to visit new regions of the CV space. After the free energy minima are filled up by the deposited Gaussians, the bias potential V_G flattens the underlying free energy surface F(**S**) slowly over the limit long simulation time and converges to,

$$V_G(\mathbf{S}, t \to \infty) = -\frac{\Delta T}{T + \Delta T} F(\mathbf{S}) + C \tag{1.32}$$

where T is the simulation temperature, and C is an irrelevant constant. The CVs are sampled at a temperature T+ΔT, which is higher than the system temperature T. While ΔT = 0 corresponds to standard molecular dynamics, $\Delta T \to \infty$ corresponds to metadynamics. The ratio between temperatures of CVs (T+ΔT) and the system temperature (T) is defined a bias factor in well-tempered metadynamics simulations.

$$\gamma = \frac{T + \Delta T}{T} \tag{1.33}$$

The bias factor γ should be chosen carefully for the system to cross the relevant free energy barriers efficiently.

1.13 Molecules Under Study in the Present Thesis

Self-assembled organic motifs have received attention toward the development of functional materials. Many examples using π conjugated organic molecules which organise into one-, two-, and three-dimensional structures are reported in the literature. In the present thesis, we performed computational investigations to obtain molecular level insights into the self-assembly, dipolar interactions and reorientational dynamics in supramolecular thin films and seeded polymerisation in the following systems: (a) variants of Benzenecarboxamide (BC), (b) N,N′,N″,N‴-tetra-(Tetradecyl)-1,3,6,8-pyrenetetracarboxamide, (c) oligo(*p*-phenylenevinylene) (OPV) derivative functionalized with dipicolyethylenediamine-zinc (DPA-Zn) complex, and (d) amphiphilic naphthalene diimide (AmphNDG). All these systems, barring AmphNDG, form one-dimensional supramolecular assemblies, which are amenable to explore the aforementioned aspects. Furthermore, the contrasting self-assembly mechanisms of Benzene-1,3,5-tricarboxamide (BTA) and [2.2]paracyclophane-4,7,12,15-tetracarboxamide (pCpTA) were investigated. The free energy barriers between the kinetically trapped and thermodynamically stable states of N1,N1-(n- alkane-1,4-diyl)bis(N3,N5-dialkylbenzene-1,3,5- tricarboxamide) were estimated and predictions of lag time estimated in this system have been made.

1.13.1 Benzenecarboxamide (BC)

Benzene-1,3,5-tricarboxamide (BTA)

A wide variety of molecules which form one-dimensional supramolecular polymers utilising π-π interactions, hydrogen bonding and hydrophobic interactions have been reported in the literature. Among the plethora of such molecules, BTA based molecules were widely studied through experiments and theoretical methods such as quantum chemical calculations [6, 144] and molecular dynamics simulations, both in polar and non-polar solvents. [225–240]

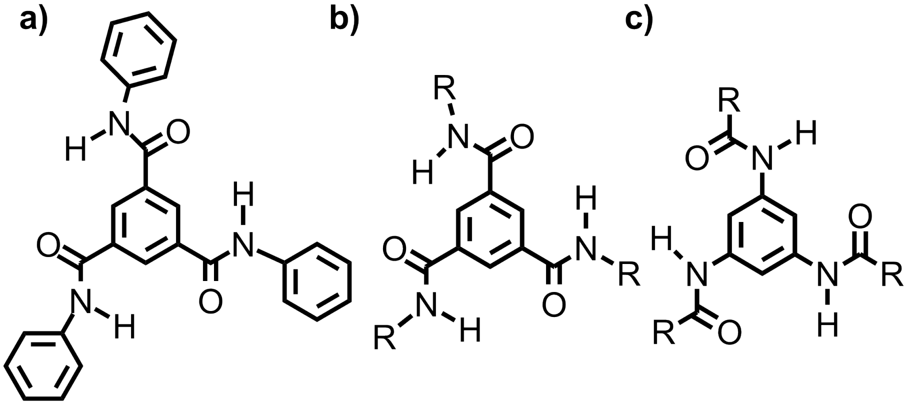

Figure 1.9: Variants of BTA (a). first BTA molecule by Curtius, (b). C=O-centered BTA and (c). N-centered BTA.

The first BTA based supramolecule (Figure. 1.9(a)), was synthesised by Curtius [241] in 1915. Later, the synthesis of well known C-centered BTA (Figure 1.9(b)) and N-centered BTA (Figure 1.9(c)) were reported by Bayer in 1975 and Gill in 1949 [242], respectively. Over the past few decades, synthesis of a broad range of BTA based molecules with various R-groups such as alkyl, [143, 144] branched-alkyl, [243, 244] aryl, [245–247] pyridyl, [248] bipyridyl, [249, 250] porphyrinyl, [251] triphenyl, [252] oligo(*p*-phenylenevinylene), [253] amino acid, [254–259] dipeptide, [260] oligopeptide, [261] oligo(ethyleneoxy), [262, 263] and benzocrown ethers [264] were reported. The side chain (R-group) influences the mechanism of self-assembly, the morphology and properties of self-assembled structures.

Crystal Structure

BTA molecules utilise their hydrogen bonding ability to self-assemble, and the organisation of hydrogen bonds in the solid state of self-assembled BTA is investigated using Infrared spectroscopy. Pyridine based BTA molecules form honeycomb like bilayer sheets and the H-bonds between the amide hydrogen and pyridine nitrogen create pores of diameter 8.2 Å, which can be used to trap solvents. [248] N,N′,N″-tris(2-methoxyethyl)benzene-1,3,5-tricarboxamide aggregates into helical supramolecular columnar structures through threefold H-bonding between the amides of consecutive molecules. [265].

The packing of BTA also depends on the nature of the side chains. N,N′,N″-trimethyl-1,3,5-benzenetricarboxamide forms monoclinic $p2_1$ lattice, in which there is one H-bond between the molecules within the same stack whereas the other two H-bonds are formed through lateral interaction between amide groups of the adjacent stacks in the crystal.

Liquid Crystalline (LC) Phase

The disc like BTA molecule with alkyl side chains is known to form columnar hexagonal liquid crystals, and its ferroelectric response was reported by Fitié *et al.* in 2010 for the first time. [266]. Liquid crystals of BTA homologues with R-groups being alkyl chains of different lengths (18 (BTA-C18), 10 (BTA-C10), and 6 (BTA-C6)) were synthesised, of which BTA-C10 and BTA-C18 were shown to exhibit extrinsic polar switching. [41]

The polar switching in ferroelectric materials is characterised by two mechanisms. In ideal ferroelectric materials, since all the dipoles are correlated inherently, their switching is coherent and named as intrinsic switching. [267] But the dipoles in real systems are not correlated, and the dipole switching involves a nucleation step. Therefore, the switching mechanism is called an extrinsic or nucleated mechanism. In the systems with nucleation limited switching (NLS), the energy barrier (W_b) associated with dipolar switching is estimated as

$$t_{sw} \cong \frac{1}{\nu_0} exp(\frac{W_b - P_S E_{app} V^*}{K_B T}) \tag{1.34}$$

Where,

t_{sw} is the switching time.

ν_0 is the attempt frequency.

E_{app} is the applied electric field.

V^* is the critical domain volume for polar switching.

T is temperarture of the system.

P_s is the saturation polarisation.

Molecular dipole relaxations are captured through dielectric relaxation spectroscopy (DRS), which operates in the frequency regime ranging from 10^{-6} to 10^{12} Hz. [268] Using the DRS method, the dynamic nature of the columnar LC phases and molecular processes responsible for polar switching can be probed over a range of temperatures. BTAs show α-relaxation at temperatures lower than 120 °C, and R-relaxation at temperatures ranging from 120-200 °C. [41] The corresponding changes in the molecular dipole orientations of these relaxation processes are shown in Figure 1.10.

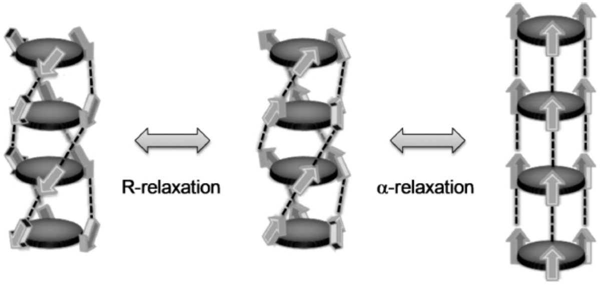

Figure 1.10: Schematic representation of dipole relaxation processes in liquid crystalline phase. Reprinted with permission from [41]. Copyright (2012) American Chemical Society.

Kemerink and co-workers have studied ferroelectric switching in these materials systematically. [269] They showed that polarisation enhances with decreasing alkyl side chain length. The side chain length also affects several parameters of the ferroelectric materials, such as the rate of depolarisation, phase transition temperature, and coercive field. [270] The physical processes responsible for the polarisation loss were also studied. [271] Tailor-made BTAs with branched alkyl tails mixed with BTAs with linear alkyl tails were shown to suppress the depolarisation, and to increase the retention times of the ferroelectric supramolecular materials. [243] Simulations on N,N′,N″-trihexyl-1,3,5-benzenetricarboxamide in its liquid crystalline phase in the presence of external electric field in a direction opposite to that of the macrodipole encourages the molecules to realign in the direction of the electric field. Since the overall rotation of the stack is impossible, instead, the intermolecular hydrogen bonds break so that the amide groups can rotate freely. The hydrogen bonds then reform to align in the direction of the applied electric field, which reverses the handedness of each helix. [272]

BTAs in Solution

The facile synthesis of a variety of BTA homologues makes it an ideal model to study the role of solvent on the self-assembly mechanism of supramolecular polymers. The C-centered BTA molecular aggregation have been studied in apolar solvents such as linear alkanes and methylcyclohexane. The crystal structure of BTA reveals the presence of threefold H-bond network to form helical columnar aggregates, the helical nature of the polymer is confirmed by introducing a chiral center into the alkyl side chains. [273–275] Changing the side chains to chromophores, the formed stacks are more stable due to secondary interactions between the chromophores. However, these interactions can alter the self-assembly mechanism. [253, 276] Water-soluble BTAs which can be used in biomedical applications are designed with amphiphilic side chains. [277]

The solubility of BTAs in polar and non-polar solvents depends on the side chains attached to their cores. The cooperative nature of BTA (R = alkyl) self-assembly in n-nonane was studied earlier employing both all-atom (AA) DREIDING force-field, [205, 225] and a coarse-grain (CG) model. [226] Along with the size of the critical nucleus, the CG study revealed that the free energy changes associated with the addition of a monomer to the terminus and the center of the BTA stack are the same.

Water-soluble BTAs have been studied extensively by Pavan and co-workers using several computational approaches. They investigated the effect of chiral center on internal ordering of the self-assembled structures, [278] the dynamic exchange of monomers in fibres with those present in the solution, [238] and the role of hydrogen bonds in stabilising the stack. [227] They developed a CG force-field to understand the sequence of events taking place during polymerisation, [228] and showed that the packing of molecules is highly dependent on the periphery chains attached to the BTA core. [204]. Their implicit solvent model study revealed the formation of highly ordered structures and large disordered clusters at dilute and high concentrations, respectively. [239]

More Benzenecarboxamides (BC)

A large number of studies on C_3 symmetric BTA molecule and its derivatives have been reported, but those by changing the number of carboxamide substituents attached to the benzene core, shown in Figure. 1.11, are still at infancy. 4BC (Figure. 1.11(b)) is shown to form organogels, [279, 280] and have the potential to form functional materials such as liquid crystals, anion sensors, drug delivery systems, and tissue engineering. [281, 282] Shishido *et al.* [283] studied the solubility of all the variants of BCs in different solvents, their phase transitions, and the ferroelectric response. 4BC, 5BC and 6BC are shown to exist in hexagonal ordered columnar (Col_{ho}) and the intercolumnar distance along with inter disc separation was measured. The inter disc separation or π-π distance increases with increasing the number of chains attached to the benzene core. The ferroelectric measurements show that while 2BC and 5BC are ferroelectric, 4BC and 6BC are paraelectric in nature. DFT calculations on all possible conformations and configurations of 2BC, 4BC, 5BC, and 6BC found that

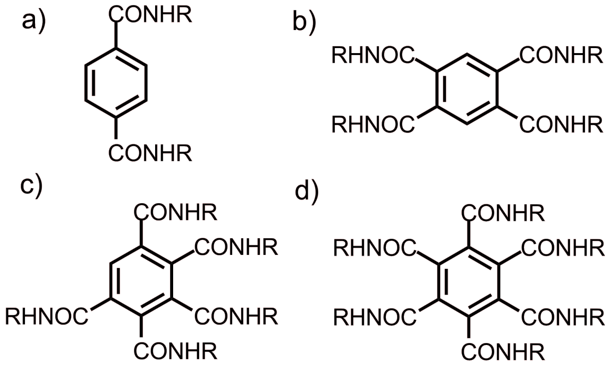

Figure 1.11: Variants of Benzenecarboxamide; R=$C_{14}H_{29}$ (a). N,N′-bis(tetradecyl)-1,4-benzenedicarboxamide (2BC), (b). N,N′,N″,N‴tetra(tetradecyl)-1,2,4,5-benzenetetracarboxamide (4BC), (c). N,N′,N″,N‴,N⁗-penta(tetradecyl)benzenepentacarboxamide (5BC) and (d). N,N′,N″,N‴,N⁗,N⁗′-hexa(tetradecyl)benzenehexacarboxamide (6BC).

alternate up-down arrangement of dipoles is energetically the most preferred. This result corroborates with the fact that the ground state of BTA is 2:1 configuration of its dipoles. A monomer of BTA exists in a planar conformation where are the dipoles stay in the same plane as benzene-core. However, to form a dimer or higher oligomers, the amide dipoles are coming out-of-the benzene plane and forms two configurations namely, 2:1 and 3:0. [225] In 2:1 configuration, two amide groups of a molecule oriented along the same direction and the third in the opposite direction whereas in 3:0 configuration, all dipoles orient in the same direction is shown in Figure. 1.12

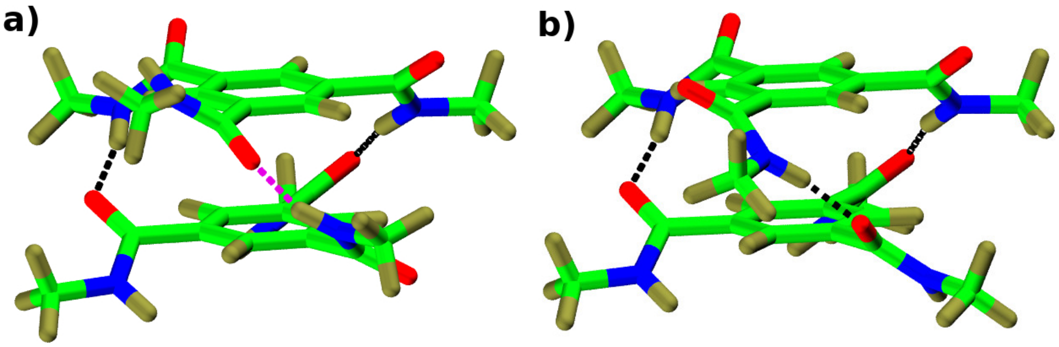

Figure 1.12: Structure of BTA dimer in (a) 2:1 and (b). 3:0 configuration. Colour Scheme: Green- carbon, Red- Oxygen, Blue- Nitrogen, Tan- Hydrogen and the dotted lines represents the hydrogen bonds.

1.13.2 N,N′,N″,N‴-tetra-(Tetradecyl)-1,3,6,8-pyrenetetracarboxamide

Pyrene molecule is shown in Figure 1.13(a) and its derivatives are used as dyes due to their high molecular extinction coefficients. The colour of the molecule can be tuned by changing the substituents on the pyrene core. Pyrene is electron-rich, which could result in a strongly bound charge transfer (CT) interaction with an electron-deficient molecule, such as naphthalene diimide. [284] These CT complexes have promising applications in organic field-effect transistors (OFETs), organic photovoltaic cells, and organic light-emitting diodes. [285] Burattini and co-workers showed the formation of a copolymer of nitroaromatic compounds (NACs) and functionalized pyrene. The copolymerisation quenches the excimer emission of pyrene, which can be used to identify the presence of volatile compounds, commonly present in many explosives. [286] Akutagawa and co-workers synthesised a pyrene derivative (Figure 1.13(b)) containing four amide groups on the 1,3,6, and 8 positions to investigate its fluorescence, ferroelectric, and electron transport properties. [287]

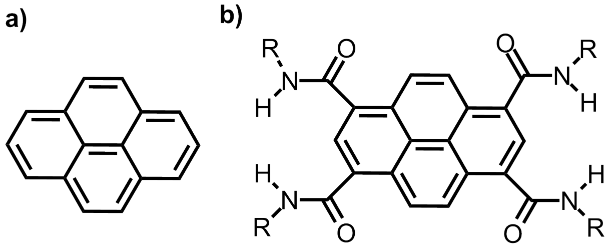

Figure 1.13: Structure of (a) Pyrene and (b). Pyrene tetracarboxamide, R=$C_{14}H_{29}$.

1.13.3 [2.2]paracyclophane-4,7,12,15-tetracarboxamide (pCpTA)

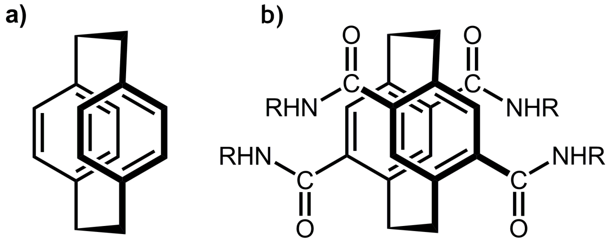

Figure 1.14: Structure of (a) [2.2]paracyclophane and (b). [2.2]paracyclophane-4,7,12,15-tetracarboxamide (pCpTA), R=C_6H_{13}

[2.2]paracyclophane (PCP) shown in Figure 1.14(a) was discovered by Brown and Farthing in 1949. [288] PCP molecule has two phenyl rings which are stacked co-facially through two ethylene bridges. The distance between the center of masses of the phenyl rings ("decks") is ∼ 3.09 Å. However, the phenyl carbons connected by ethylene bridge are separated by ∼ 2.78 Å. Therefore, the phenyl rings are non-planar and are thus frustrated. PCP has attractive reactivity, structural and physical properties. [289] The two phenyl rings present in PCP have interactions through space due to their close proximity. [290, 291] The consequences of through-space conjugation on the properties of the materials have been studied by several groups. [291–300]

Caramori and Galembeck studied the interactions in PCP molecule through Natural Bond Order (NBO) analysis, [301] and transport abilities in thin films have been studied by Hu *et* al. [302] Planar chirality introduced in PCP molecules with appropriate functionalization, is used in ligand and catalyst design. [303] Materials based on PCP remain attractive in organic optoelectronic applications. [304, 305] Castellano and co-workers synthesised pCp-4,7,12,15-tetracarboxamide (pCpTA) molecules shown in Figure 1.14(b), which can self-assemble into homochiral 1D columnar stacks. They determined the crystal structure, and the results are consistent with NMR, IR, and UV/Vis spectroscopic measurements. [115]

1.13.4 Oligo(*p*-phenylenevinylene) (OPV) Derivatives

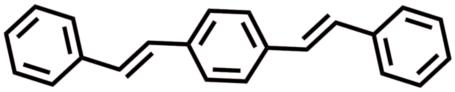

Figure 1.15: Structure of oligo(*p*-phenylenevinylene).

Conjugated polymers have an extended conjugation with outstanding optical properties. [42, 306–308] In the past few decades, π-conjugated oligomers have been investigated as advanced materials, because of their conjugation length that gives rise to defined functional properties and controlled supramolecular structures. [309, 310] One of the fascinating extended π-conjugated systems is oligo(*p*-phenylenevinylene)-OPV shown in Figure. 1.15. Electron transfer in OPV has been studied through UV-MALDI measurements. [311] OPV has several applications in the field of organic electronics. [312–316] Functionalized OPV molecules were shown to have better reactivity than OPV, [317] and they show promising biomedical applications. [318]

1.13.5 Naphthalene diimide (NDI) Derivatives

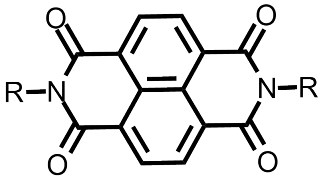

Figure 1.16: Structure of Naphthalene diimide.

Among several aromatic compounds, the naphthalenediimides (NDIs), shown in Figure 1.16, have grabbed much attention due to their tendency to form n-type and p-type semiconductor materials. [319] Due to the presence of a lipophilic naphthyl core in NDI, these are soluble in low polar solvents such as toluene, and chloroform. Their solubility in polar aprotic solvents such as acetonitrile, DMF, DMSO depends on the substituents on the imide group. NDI derivatives are popularly used as sensors, [320] and ion channels. [321] The core substituted NDIs (c-NDIs) were first studied by Vollmann, [322] but the improved properties of c-NDIs were realised by Würthner *et al.* in 2002. [323] The c-NDIs have applications ranging from biomimetic and bioinspired artificial systems, including electron and energy transfer systems. [324–326]

1.14 Softwares Used

Classical MD simulations reported in this thesis were performed using LAMMPS, [327] and GROMACS [328] packages. Enhanced sampling calculations were performed with the same packages patched with PLUMED. [329] CP2K [330] was used to perform geometry optimisations of large molecules and Gaussian 09 [331] package was employed for relaxed dihedral scan runs. DDEC/c3 [202, 203] program was used to get the atomic site charges from valence electron densities obtained from DFT calculations. The trajectories were visualised in VMD. [332]

1.15 Codes and Scripts for Analysis Written In-house:

This thesis is devoted to study one-dimensional supramolecular polymers formed through π-π interactions, hydrogen bonding between the monomers.

- ∗ A TCL script to calculate the π-π distance, centroid-centroid distance, and twist angle between neighbouring π rings in the self-assembled structures.
- ∗ A TCL script to identify the configurations of the molecules in the self-assembly simulations, and also to calculate the length of the polymers formed.
- ∗ A FORTRAN code to calculate the macrodipole and polarisation of sample in thin films.
- ∗ A TCL script to analyse the time evolution of dipole flipping events in liquid crystalline phase.

1.16 Scope of the Thesis

Chapter 1 presents a general introduction to supramolecular polymers, their polymerisation mechanism, and types of interactions involved in the self-assembly process. Applications of supramolecular polymers are discussed. For the molecules under study in this thesis, the experimental and earlier computational studies on molecules and phenomenon related to the ones present in this thesis are discussed. A concise description of the theoretical methods employed in this thesis is also provided.

Chapter 2 Free energy calculations based on atomistic MD simulations were performed on N,N′,N″-trialkylbenzene-1,3,5-tricarboxamide (BTA) and [2.2]paracyclophane-4,7,12,15-tetracarboxamide (pCpTA) to investigate the mechanism of self-assembly in non-polar solvents at 298.15 K temperature. The cooperativity factors for BTA and pCpTA molecules were calculated. An asymmetric pattern of dipole arrangement (anti) in pCpTA molecule is favoured over the symmetric one (syn) due to dipole-dipole interactions. The free energy barrier associated with a change from anti to a syn conformation change of pCpTA is estimated.

Chapter 3 N,N′,N″,N‴-tetra-(Tetradecyl)-1,3,6,8-pyrenetetracarboxamide (PCA) molecule was modelled in all-atom representation in chloroform. The possible configurations (depending on the relative amide dipole orientations) of PCA molecule were studied through gas-phase quantum chemical geometry optimisations. The dipole relaxation in liquid crystalline (LC) phase has been investigated and contrasted against that in the well-established N,N′,N″-trialkylbenzene-1,3,5-tricarboxamide (BTA) family. Furthermore, the torsional barriers related to the amide dipole flip in both BTA and PCA are estimated from relaxed dihedral scan runs using M06-2x/6-311+g(d,p) level of theory. The mechanism underlying the polarisation switching in the LC phase on the application of an external electric field is investigated.

Chapter 4 To understand the origin and various parameters governing the ferroelectric character of supramolecular polymeric thin films, derivatives of benzenecarboxamide **(BC)** bearing multiple $-\mathrm{CONHC}_{14}\mathrm{H}_{29}$ chains — N,N′-bis(tetra decyl)-1,4-benzenedicarboxamide **(2BC)**, N,N′,N″-tri(tetradecyl)-1,3,5-benzenetricarboxamide **(3BC)**, N,N′,N″,N‴-tetra(tetradecyl)-1,2,4,5-benzenetetracarboxamide **(4BC)**, N,N′ ,N″,N‴,N⁗-penta(tetradecyl)benzenepentacarboxamide **(5BC)**, and N,N′,N″,N‴,N⁗ ,N‴″-hexa(tetrad- ecyl)benzenehexacarboxamide **(6BC)** — were examined in solution and LC phases. Various geometrical quantites have been compared against experimental findings for the LC phase. The homologues of 3BC molecule with different alkyl chain lengths — hexyl **(3BC-C6)**, decyl **(3BC-C10)**, and tetradecyl **(3BC-C14)** were examined in liquid crystalline (LC) phase with an aim to identify molecular level reasons for variations in dipole relaxation and thus the time scales for depolarisation in thin film samples. Methods to improve the retention times and remnant polarisation are suggested via studies of **(5BC-C14)** in its LC phase.

Chapter 5 is divided into two parts. **Chapter 5A** and **Chapter 5B** present molecular level insights into structural changes during the process of self-assembly.

Chapter 5A ATP-selective and ATP-fuelled controlled supramolecular polymerisation of oligo(p-phenylenevinylene) (OPV) functionalized with the phosphate receptor dipicolylethylenediamine-zinc complex (DPA-Zn) — referred to as OPV-DPA — was studied experimentally by George and co-workers. The time-delayed self-assembly was observed from absorbtion spectroscopy, but the CD signal appeared with a further delay. However, molecular-level insights into the selective self-assembly and time lags in the spectroscopic measurements were not understood from experiments alone. MD simulations presented in this thesis provide molecular level information for selective self-assembly along with the reasons for the observed lag times. The experimentally observed ATP selectivity is attributed to the formation of intermolecular hydrogen bonds between the ATP molecules in the stack. The structural rearrangement in the OPV-DPA molecules in the presence of ATP is responsible for the lag time in the formation of short oligomers. Chirality in the stack is induced with progress in oligomerisation.

Chapter 5B The fuel-driven self-assembly of **Amph-NDG** and the associated lag times were studied using UV-Vis absorption spectroscopy by George and co-workers. MD simulations provide possible model structures for NDG-ATP and NDG-GTP systems which was substantiated with height profiles of NDG-ATP from atomic force microscopy and the monomer to ATP molar ratio in the self-assembly. Zero Kelvin DFT calculations have been performed to identify viable changes in the self-assembled structures. The dormant state of **Amph-NDG** monomer was found to possess an intramolecular hydrogen bond between the guanidinium N$-$H and C$-$O group. The existence of the dormant state precludes self-assembly. Upon addition of triphosphates (either ATP or GTP), the interaction between the imide group of guanidinium and phosphate group of triphosphate (from either ATP or GTP) triggers the dihedral rotation in **Amph-NDG**, as a consequence of which, the intramolecular hydrogen bond breaks. The time spent in undergoing this structural rearrangement has been ascribed to cause the experimentally observed lag time.

Chapter 6 A prototypical molecule, N1,N1- (n-alkane-1,n-diyl)bis(N3,N5-dialkyl benzene-1,3,5-tricarboxamide), BNB has been considered to obtain generic insights into pathway complexity in supramolecular oligomerization. Two molecules varying in their linker lengths have been studied. Conformational and configurational isomers of the monomer and dimer species have been identified; the free energy differences between these states as well as the pathways connecting them have been determined at ambient conditions, in their solution phase. The free energy barriers associated with these transitions obtained from the MD simulations match well with experimental estimates of the same obtained from lag times.

The thesis ends with **Chapter 7** providing a brief summary of the thesis and a future outlook.

Bibliography

[1] Lehn, J.-M. Supramolecular chemistry: receptors, catalysts, and carriers. *Science* **1985**, *227*, 849–856.

[2] Wolf, K.; Frahm, H.; Harms, H. The state of arrangement of molecules in liquids. *Z. Phys. Chem. Abt. B* **1937**, *36*, 237–287.

[3] Würthner, F. Dipole–dipole interaction driven self-assembly of merocyanine dyes: from dimers to nanoscale objects and supramolecular materials. *Acc. Chem. Res.* **2016**, *49*, 868–876.

[4] Kulkarni, C.; Bejagam, K. K.; Senanayak, S. P.; Narayan, K.; Balasubramanian, S.; George, S. J. Dipole-moment-driven cooperative supramolecular polymerization. *J. Am. Chem. Soc.* **2015**, *137*, 3924–3932.

[5] Sakamoto, A.; Ogata, D.; Shikata, T.; Hanabusa, K. Controlled Large Macrodipoles in a Supramolecular Polymer of Tri-3, 7-dimethyloctyl-cis-1, 3, 5-cyclohexanetricarboxamide in n-Decane. *Macromolecules* **2005**, *38*, 8983–8986.

[6] Kulkarni, C.; Balasubramanian, S.; George, S. J. What molecular features govern the mechanism of supramolecular polymerization? *ChemPhysChem* **2013**, *14*, 661–673.

[7] Haino, T. Molecular-recognition-directed formation of supramolecular polymers. *Polym. J.* **2013**, *45*, 363.

[8] Zhang, Y.; Li, Y.; Liu, W. Dipole–dipole and h-bonding interactions significantly enhance the multifaceted mechanical properties of thermoresponsive shape memory hydrogels. *Adv. Funct. Mater.* **2015**, *25*, 471–480.

[9] Willerich, I.; Gröhn, F. Photoswitchable Nanoassemblies by Electrostatic Self-Assembly. *Angew. Chem. Int. Ed.* **2010**, *49*, 8104–8108.

[10] Gröhn, F. Electrostatic Self-Assembly as Route to Supramolecular Structures. *Macromol. Chem. Phys.* **2008**, *209*, 2295–2301.

[11] Stavrouli, N.; Aubry, T.; Tsitsilianis, C. Rheological properties of ABA telechelic polyelectrolyte and ABA polyampholyte reversible hydrogels: A comparative study. *Polymer* **2008**, *49*, 1249–1256.

[12] Liu, K.; Yao, Y.; Wang, C.; Liu, Y.; Li, Z.; Zhang, X. From Bola-amphiphiles to Supra-amphiphiles: The Transformation from Two-Dimensional Nanosheets into One-Dimensional Nanofibers with Tunable-Packing Fashion of n-Type Chromophores. *Chem.–Eur. J.* **2012**, *18*, 8622–8628.

[13] Kieltyka, R. E.; Pape, A.; Albertazzi, L.; Nakano, Y.; Bastings, M. M.; Voets, I. K.; Dankers, P. Y.; Meijer, E. Mesoscale modulation of supramolecular ureidopyrimidinone-based poly (ethylene glycol) transient networks in water. *J. Am. Chem. Soc.* **2013**, *135*, 11159–11164.

[14] Obert, E.; Bellot, M.; Bouteiller, L.; Andrioletti, F.; Lehen-Ferrenbach, C.; Boué, F. Both water-and organo-soluble supramolecular polymer stabilized by hydrogen-bonding and hydrophobic interactions. *J. Am. Chem. Soc.* **2007**, *129*, 15601–15605.

[15] Ustinov, A.; Weissman, H.; Shirman, E.; Pinkas, I.; Zuo, X.; Rybtchinski, B. Supramolecular polymers in aqueous medium: Rational design based on directional hydrophobic interactions. *J. Am. Chem. Soc.* **2011**, *133*, 16201–16211.

[16] Tuncaboylu, D. C.; Sari, M.; Oppermann, W.; Okay, O. Tough and self-healing hydrogels formed via hydrophobic interactions. *Macromolecules* **2011**, *44*, 4997–5005.

[17] Liu, Y.; Huang, Z.; Tan, X.; Wang, Z.; Zhang, X. Cucurbit [8] uril-based supramolecular polymers: promoting supramolecular polymerization by metal-coordination. *Chem. Commun.* **2013**, *49*, 5766–5768.

[18] Noro, A.; Matsushima, S.; He, X.; Hayashi, M.; Matsushita, Y. Thermoreversible supramolecular polymer gels via metal–Ligand coordination in an ionic liquid. *Macromolecules* **2013**, *46*, 8304–8310.

[19] Wei, P.; Yan, X.; Huang, F. Supramolecular polymers constructed by orthogonal self-assembly based on host–guest and metal–ligand interactions. *Chem. Soc. Rev.* **2015**, *44*, 815–832.

[20] Das, A.; Ghosh, S. Stimuli-Responsive Self-Assembly of a Naphthalene Diimide by Orthogonal Hydrogen Bonding and Its Coassembly with a Pyrene Derivative by a Pseudo-Intramolecular Charge-Transfer Interaction. *Angew. Chem. Int. Ed.* **2014**, *53*, 1092–1097.

[21] Das, A.; Ghosh, S. Supramolecular Assemblies by Charge-Transfer Interactions between Donor and Acceptor Chromophores. *Angew. Chem. Int. Ed.* **2014**, *53*, 2038–2054.

[22] Guo, D.-S.; Liu, Y. Calixarene-based supramolecular polymerization in solution. *Chem. Soc. Rev.* **2012**, *41*, 5907–5921.

[23] Dong, S.; Zheng, B.; Wang, F.; Huang, F. Supramolecular polymers constructed from macrocycle-based host–guest molecular recognition motifs. *Acc. Chem. Res.* **2014**, *47*, 1982–1994.

[24] Hunter, C. Bigger and better synthesis: nature constructs macromolecules with a precision that chemists have struggled to achieve. So a strategy that offers simple routes to large molecules, starting from small templates, could be the next big thing in synthesis. *Nature* **2011**, *469*, 39–42.

[25] Whitesides, G. M.; Grzybowski, B. Self-assembly at all scales. *Science* **2002**, *295*, 2418–2421.

[26] Lehn, J.-M. Perspectives in chemistry —steps towards complex matter. *Angew. Chem. Int. Ed.* **2013**, *52*, 2836–2850.

[27] Brunsveld, L.; Folmer, B.; Meijer, E. W.; Sijbesma, R. Supramolecular polymers. *Chem. Rev.* **2001**, *101*, 4071–4098.

[28] De Greef, T. F.; Smulders, M. M.; Wolffs, M.; Schenning, A. P.; Sijbesma, R. P.; Meijer, E. Supramolecular polymerization. *Chem. Rev.* **2009**, *109*, 5687–5754.

[29] Huang, F.; Scherman, O. A. Supramolecular polymers. *Chem. Soc. Rev.* **2012**, *41*, 5879–5880.

[30] Liu, Y.; Wang, Z.; Zhang, X. Characterization of supramolecular polymers. *Chem. Soc. Rev.* **2012**, *41*, 5922–5932.

[31] van der Zwaag, D.; de Greef, T. F.; Meijer, E. Programmable supramolecular polymerizations. *Angew. Chem. Int. Ed.* **2015**, *54*, 8334–8336.

[32] Dhiman, S.; Jain, A.; Kumar, M.; George, S. J. Adenosine-phosphate-fueled, temporally programmed supramolecular polymers with multiple transient states. *J. Am. Chem. Soc.* **2017**, *139*, 16568–16575.

[33] Rest, C.; Kandanelli, R.; Fernández, G. Strategies to create hierarchical self-assembled structures via cooperative non-covalent interactions. *Chem. Soc. Rev.* **2015**, *44*, 2543–2572.

[34] Baram, J.; Weissman, H.; Rybtchinski, B. Supramolecular polymer transformation: a kinetic study. *J. Phys. Chem. B* **2014**, *118*, 12068–12073.

[35] Budrene, E. O.; Berg, H. C. Complex patterns formed by motile cells of Escherichia coli. *Nature* **1991**, *349*, 630.

[36] Budrene, E. O.; Berg, H. C. Dynamics of formation of symmetrical patterns by chemotactic bacteria. *Nature* **1995**, *376*, 49.

[37] Grzybowski, B. A.; Winkleman, A.; Wiles, J. A.; Brumer, Y.; Whitesides, G. M. Electrostatic self-assembly of macroscopic crystals using contact electrification. *Nat. Mater.* **2003**, *2*, 241.

[38] Grzybowski, B. A.; Wiles, J. A.; Whitesides, G. M. Dynamic self-assembly of rings of charged metallic spheres. *Phys. Rev. Lett.* **2003**, *90*, 083903.

[39] Onsager, L. The effects of shape on the interaction of colloidal particles. *Ann. N.Y. Acad. Sci.* **1949**, *51*, 627–659.

[40] others,, et al. Aligned 1-D nanorods of a π-gelator exhibit molecular orientation and excitation energy transport different from entangled fiber networks. *J. Am. Chem. Soc.* **2014**, *136*, 8548–8551.

[41] Fitié, C. F.; Roelofs, W. C.; Magusin, P. C.; Wübbenhorst, M.; Kemerink, M.; Sijbesma, R. P. Polar switching in trialkylbenzene-1, 3, 5-tricarboxamides. *J. Phys. Chem. B* **2012**, *116*, 3928–3937.

[42] Feng, L.; Zhu, C.; Yuan, H.; Liu, L.; Lv, F.; Wang, S. Conjugated polymer nanoparticles: preparation, properties, functionalization and biological applications. *Chem. Soc. Rev.* **2013**, *42*, 6620–6633.

[43] Bose, R. K.; Enke, M.; Grande, A. M.; Zechel, S.; Schacher, F. H.; Hager, M. D.; Garcia, S. J.; Schubert, U. S.; Van der Zwaag, S. Contributions of hard and soft blocks in the self-healing of metal-ligand-containing block copolymers. *Eur. Polym. J.* **2017**, *93*, 417–427.

[44] Grzybowski, B. A.; Fitzner, K.; Paczesny, J.; Granick, S. From dynamic self-assembly to networked chemical systems. *Chem. Soc. Rev.* **2017**, *46*, 5647–5678.

[45] van Rossum, S. A.; Tena-Solsona, M.; van Esch, J. H.; Eelkema, R.; Boekhoven, J. Dissipative out-of-equilibrium assembly of man-made supramolecular materials. *Chem. Soc. Rev.* **2017**, *46*, 5519–5535.

[46] Ragazzon, G.; Prins, L. J. Energy consumption in chemical fuel-driven self-assembly. *Nat. Nanotechnol.* **2018**, *13*, 882–889.

[47] Maiti, S.; Fortunati, I.; Ferrante, C.; Scrimin, P.; Prins, L. J. Dissipative self-assembly of vesicular nanoreactors. *Nat. Chem.* **2016**, *8*, 725.

[48] Fialkowski, M.; Bishop, K. J.; Klajn, R.; Smoukov, S. K.; Campbell, C. J.; Grzybowski, B. A. Principles and implementations of dissipative (dynamic) self-assembly. 2006.

[49] Ascolani, H.; Van Der Meijden, M. W.; Cristina, L. J.; Gayone, J. E.; Kellogg, R. M.; Fuhr, J. D.; Lingenfelder, M. Van der Waals interactions in the self-assembly of 5-amino [6] helicene on Cu (100) and Au (111). *Chem. Commun.* **2014**, *50*, 13907–13909.

[50] Roth, C. M.; Neal, B. L.; Lenhoff, A. M. Van der Waals interactions involving proteins. *Biophys. J.* **1996**, *70*, 977–987.

[51] Hermann, J.; DiStasio Jr, R. A.; Tkatchenko, A. First-principles models for van der Waals interactions in molecules and materials: Concepts, theory, and applications. *Chem. Rev.* **2017**, *117*, 4714–4758.

[52] Isoda, K.; Yasuda, T.; Kato, T. Dipole-driven self-assembly of redox-active mesogenic tetracyanoanthraquinodimethanes. *J. Mater. Chem.* **2008**, *18*, 4522–4528.

[53] Varón, M.; Pena, L.; Balcells, L.; Skumryev, V.; Martinez, B.; Puntes, V. Dipolar driven spontaneous self assembly of superparamagnetic Co nanoparticles into micrometric rice-grain like structures. *Langmuir* **2009**, *26*, 109–116.

[54] Yao, S.; Beginn, U.; Gress, T.; Lysetska, M.; Würthner, F. Supramolecular polymerization and gel formation of bis (merocyanine) dyes driven by dipolar aggregation. *J. Am. Chem. Soc.* **2004**, *126*, 8336–8348.

[55] Ikeda, T.; Iijima, T.; Sekiya, R.; Takahashi, O.; Haino, T. Cooperative self-assembly of carbazole derivatives driven by multiple dipole–dipole interactions. *J.Org. Chem.* **2016**, *81*, 6832–6837.

[56] Steiner, T. The hydrogen bond in the solid state. *Angew. Chem. Int. Ed.* **2002**, *41*, 48–76.

[57] Hirschberg, J. K.; Brunsveld, L.; Ramzi, A.; Vekemans, J. A.; Sijbesma, R. P.; Meijer, E. Helical self-assembled polymers from cooperative stacking of hydrogen-bonded pairs. *Nature* **2000**, *407*, 167.

[58] Yagai, S.; Monma, Y.; Kawauchi, N.; Karatsu, T.; Kitamura, A. Supramolecular nanoribbons and nanoropes generated from hydrogen-bonded supramolecular polymers containing perylene bisimide chromophores. *Org. Lett.* **2007**, *9*, 1137–1140.

[59] Peng, H.-Q.; Xu, J.-F.; Chen, Y.-Z.; Wu, L.-Z.; Tung, C.-H.; Yang, Q.-Z. Water-dispersible nanospheres of hydrogen-bonded supramolecular polymers and their application for mimicking light-harvesting systems. *Chem. Commun.* **2014**, *50*, 1334–1337.

[60] Lange, R. F.; Van Gurp, M.; Meijer, E. Hydrogen-bonded supramolecular polymer networks. *J. Polym. Sci., Part A: Polym. Chem.* **1999**, *37*, 3657–3670.

[61] Sijbesma, R. P.; Beijer, F. H.; Brunsveld, L.; Folmer, B. J.; Hirschberg, J. K.; Lange, R. F.; Lowe, J. K.; Meijer, E. Reversible polymers formed from self-complementary monomers using quadruple hydrogen bonding. *Science* **1997**, *278*, 1601–1604.

[62] Beijer, F. H.; Sijbesma, R. P.; Kooijman, H.; Spek, A. L.; Meijer, E. Strong dimerization of ureidopyrimidones via quadruple hydrogen bonding. *J. Am. Chem. Soc.* **1998**, *120*, 6761–6769.

[63] Luan, Y.-G.; Zhang, X.-a.; Jiang, S.-L.; Chen, J.-h.; Lyu, Y.-F. Self-healing supramolecular polymer composites by hydrogen bonding interactions between hyperbranched polymer and graphene oxide. *Chin. J. Polym. Sci.* **2018**, *36*, 584–591.

[64] Zhu, D.; Ye, Q.; Lu, X.; Lu, Q. Self-healing polymers with PEG oligomer side chains based on multiple H-bonding and adhesion properties. *Polym. Chem.* **2015**, *6*, 5086–5092.

[65] Faghihnejad, A.; Feldman, K. E.; Yu, J.; Tirrell, M. V.; Israelachvili, J. N.; Hawker, C. J.; Kramer, E. J.; Zeng, H. Adhesion and surface interactions of a self-healing polymer with multiple hydrogen-bonding groups. *Adv. Funct. Mater.* **2014**, *24*, 2322–2333.

[66] Wu, Y.; Wang, L.; Zhao, X.; Hou, S.; Guo, B.; Ma, P. X. Self-healing supramolecular bioelastomers with shape memory property as a multifunctional platform for biomedical applications via modular assembly. *Biomaterials* **2016**, *104*, 18–31.

[67] Qiu, T.; Wang, X.; Lin, X.; Zhu, Z.; Li, X.; Guo, L. Emulsion polymerization to synthesize self-healing films toward healing on fractures: A feasible strategy. *J. Polym. Sci., Part A: Polym. Chem.* **2016**, *54*, 3071–3078.

[68] Hunter, C. A.; Sanders, J. K. The nature of. pi.-. pi. interactions. *J. Am. Chem. Soc.* **1990**, *112*, 5525–5534.

[69] Hoeben, F. J.; Jonkheijm, P.; Meijer, E.; Schenning, A. P. About supramolecular assemblies of π-conjugated systems. *Chem. Rev.* **2005**, *105*, 1491–1546.

[70] Jonkheijm, P.; van der Schoot, P.; Schenning, A. P.; Meijer, E. Probing the solvent-assisted nucleation pathway in chemical self-assembly. *Science* **2006**, *313*, 80–83.

[71] Lee, C. C.; Grenier, C.; Meijer, E.; Schenning, A. P. Preparation and characterization of helical self-assembled nanofibers. *Chem. Soc. Rev.* **2009**, *38*, 671–683.

[72] Keizer, H. M.; Sijbesma, R. P. Hierarchical self-assembly of columnar aggregates. *Chem. Soc. Rev.* **2005**, *34*, 226–234.

[73] Zhang, W.; Jin, W.; Fukushima, T.; Saeki, A.; Seki, S.; Aida, T. Supramolecular linear heterojunction composed of graphite-like semiconducting nanotubular segments. *Science* **2011**, *334*, 340–343.

[74] Lista, M.; Areephong, J.; Sakai, N.; Matile, S. Lateral self-sorting on surfaces: a practical approach to double-channel photosystems. *J. Am. Chem. Soc.* **2011**, *133*, 15228–15231.

[75] Luo, Z.; Cai, K.; Hu, Y.; Li, J.; Ding, X.; Zhang, B.; Xu, D.; Yang, W.; Liu, P. Redox-responsive molecular nanoreservoirs for controlled intracellular anticancer drug delivery based on magnetic nanoparticles. *Adv. Mater.* **2012**, *24*, 431–435.

[76] Li, J.-M.; Wang, Y.-Y.; Zhao, M.-X.; Tan, C.-P.; Li, Y.-Q.; Le, X.-Y.; Ji, L.-N.; Mao, Z.-W. Multifunctional QD-based co-delivery of siRNA and doxorubicin to HeLa cells for reversal of multidrug resistance and real-time tracking. *Biomaterials* **2012**, *33*, 2780–2790.

[77] Zhang, J.; Ellsworth, K.; Ma, P. X. Hydrophobic pharmaceuticals mediated self-assembly of β-cyclodextrin containing hydrophilic copolymers: Novel chemical responsive nano-vehicles for drug delivery. *J. Controlled Release* **2010**, *145*, 116–123.

[78] Appel, E. A.; Biedermann, F.; Rauwald, U.; Jones, S. T.; Zayed, J. M.; Scherman, O. A. Supramolecular cross-linked networks via host- guest complexation with cucurbit [8] uril. *J. Am. Chem. Soc.* **2010**, *132*, 14251–14260.

[79] Montes-Navajas, P.; Corma, A.; Garcia, H. Supramolecular ionic liquids based on host–guest cucurbituril imidazolium complexes. *J. Mol. Catal. A: Chem.* **2008**, *279*, 165–169.

[80] Pluth, M. D.; Raymond, K. N. Reversible guest exchange mechanisms in supramolecular host–guest assemblies. *Chem. Soc. Rev.* **2007**, *36*, 161–171.

[81] Gadde, S.; Batchelor, E. K.; Weiss, J. P.; Ling, Y.; Kaifer, A. E. Control of h-and j-aggregate formation via host- guest complexation using cucurbituril hosts. *J. Am. Chem. Soc.* **2008**, *130*, 17114–17119.

[82] Li, C.; Han, K.; Li, J.; Zhang, Y.; Chen, W.; Yu, Y.; Jia, X. Supramolecular polymers based on efficient pillar [5] arene—neutral guest motifs. *Chem.–Eur. J.* **2013**, *19*, 11892–11897.

[83] Wang, P.; Li, Z.; Ji, X. Acidic microenvironment triggered release of a Cys probe from the cavity of a water-soluble pillar [5] arene. *Chem. Commun.* **2014**, *50*, 13114–13116.

[84] Ogoshi, T.; Ueshima, N.; Yamagishi, T.-a. An amphiphilic pillar [5] arene as efficient and substrate-selective phase-transfer catalyst. *Org. Lett.* **2013**, *15*, 3742–3745.

[85] Faridbod, F.; Ganjali, M.; Dinarvand, R.; Norouzi, P.; Riahi, S. Schiff's bases and crown ethers as supramolecular sensing materials in the construction of potentiometric membrane sensors. *Sensors* **2008**, *8*, 1645–1703.

[86] Gokel, G. W. Lariat ethers: from simple sidearms to supramolecular systems. *Chem. Soc. Rev.* **1992**, *21*, 39–47.

[87] others,, et al. Hydrogen-Bonded Complexes of Aromatic Crown Ethers with (9-Anthracenyl) methylammonium Derivatives. Supramolecular Photochemistry and Photophysics. pH-Controllable Supramolecular Switching. *J. Am. Chem. Soc.* **1997**, *119*, 10641–10651.

[88] Zhang, M.; Xu, D.; Yan, X.; Chen, J.; Dong, S.; Zheng, B.; Huang, F. Self-healing supramolecular gels formed by crown ether based host–guest interactions. *Angew. Chem. Int. Ed.* **2012**, *51*, 7011–7015.

[89] Huang, F.; Nagvekar, D. S.; Slebodnick, C.; Gibson, H. W. A supramolecular triarm star polymer from a homotritopic tris (crown ether) host and a complementary monotopic paraquat-terminated polystyrene guest by a supramolecular coupling method. *J. Am. Chem. Soc.* **2005**, *127*, 484–485.

[90] Ikeda, A.; Shinkai, S. Novel cavity design using calix [n] arene skeletons: toward molecular recognition and metal binding. *Chem. Rev.* **1997**, *97*, 1713–1734.

[91] Homden, D. M.; Redshaw, C. The use of calixarenes in metal-based catalysis. *Chem. Rev.* **2008**, *108*, 5086–5130.

[92] Pemberton, B. C.; Raghunathan, R.; Volla, S.; Sivaguru, J. From containers to catalysts: supramolecular catalysis within cucurbiturils. *Chem.–Eur. J.* **2012**, *18*, 12178–12190.

[93] Klöck, C.; Dsouza, R. N.; Nau, W. M. Cucurbituril-mediated supramolecular acid catalysis. *Org. Lett.* **2009**, *11*, 2595–2598.

[94] others,, et al. A rapid pathway toward a superb gene delivery system: programming structural and functional diversity into a supramolecular nanoparticle library. *ACS Nano* **2010**, *4*, 6235–6243.

[95] Davis, M. E.; Zuckerman, J. E.; Choi, C. H. J.; Seligson, D.; Tolcher, A.; Alabi, C. A.; Yen, Y.; Heidel, J. D.; Ribas, A. Evidence of RNAi in humans from systemically administered siRNA via targeted nanoparticles. *Nature* **2010**, *464*, 1067.

[96] Ping, Y.; Hu, Q.; Tang, G.; Li, J. FGFR-targeted gene delivery mediated by supramolecular assembly between β-cyclodextrin-crosslinked PEI and redox-sensitive PEG. *Biomaterials* **2013**, *34*, 6482–6494.

[97] Zhou, Q.; Guo, X.; Chen, T.; Zhang, Z.; Shao, S.; Luo, C.; Li, J.; Zhou, S. Target-specific cellular uptake of folate-decorated biodegradable polymer micelles. *J. Phys. Chem. B* **2011**, *115*, 12662–12670.

[98] Wang, Y.; Gao, S.; Ye, W.-H.; Yoon, H. S.; Yang, Y.-Y. Co-delivery of drugs and DNA from cationic core–shell nanoparticles self-assembled from a biodegradable copolymer. *Nat. Mater.* **2006**, *5*, 791.

[99] Quan, C.-Y.; Chen, J.-X.; Wang, H.-Y.; Li, C.; Chang, C.; Zhang, X.-Z.; Zhuo, R.-X. Core- shell nanosized assemblies mediated by the α- β cyclodextrin dimer with a tumor-triggered targeting property. *ACS Nano* **2010**, *4*, 4211–4219.

[100] Kulkarni, A.; DeFrees, K.; Hyun, S.-H.; Thompson, D. H. Pendant polymer: amino-β-cyclodextrin: siRNA guest: host nanoparticles as efficient vectors for gene silencing. *J. Am. Chem. Soc.* **2012**, *134*, 7596–7599.

[101] Adeli, M.; Fard, A. K.; Abedi, F.; Chegeni, B. K.; Bani, F. Thermo-and pH-sensitive dendrosomes as bi-phase drug delivery systems. *Nanomed. Nanotechnol. Biol. Med.* **2013**, *9*, 1203–1213.

[102] Liu, R.; Zhang, Y.; Feng, P. Multiresponsive supramolecular nanogated ensembles. *J. Am. Chem. Soc.* **2009**, *131*, 15128–15129.

[103] Zhang, J.; Yuan, Z.-F.; Wang, Y.; Chen, W.-H.; Luo, G.-F.; Cheng, S.-X.; Zhuo, R.-X.; Zhang, X.-Z. Multifunctional envelope-type mesoporous silica nanoparticles for tumor-triggered targeting drug delivery. *J. Am. Chem. Soc.* **2013**, *135*, 5068–5073.

[104] Tarn, D.; Ashley, C. E.; Xue, M.; Carnes, E. C.; Zink, J. I.; Brinker, C. J. Mesoporous silica nanoparticle nanocarriers: biofunctionality and biocompatibility. *Acc. Chem. Res.* **2013**, *46*, 792–801.

[105] Casellas, N. M.; Pujals, S.; Bochicchio, D.; Pavan, G. M.; Torres, T.; Albertazzi, L.; García-Iglesias, M. From isodesmic to highly cooperative: reverting the supramolecular polymerization mechanism in water by fine monomer design. *Chem. Commun.* **2018**, *54*, 4112–4115.

[106] Wackerly, J. W.; Moore, J. S. Cooperative self-assembly of oligo (m-phenyleneethynylenes) into supramolecular coordination polymers. *Macromolecules* **2006**, *39*, 7269–7276.

[107] Aparicio, F.; García, F.; Fernández, G.; Matesanz, E.; Sánchez, L. Mirror Helices and Helicity Switch at Surfaces Based on Chiral Triangular-Shape Oligo (phenylene ethynylenes). *Chem.–Eur. J.* **2011**, *17*, 2769–2776.

[108] Rudnev, A. V.; Malinovskii, V. L.; Nussbaumer, A. L.; Mishchenko, A.; HaÌĹner, R.; Wandlowski, T. Cooperative and noncooperative assembly of oligopyrenotides resolved by atomic force microscopy. *Macromolecules* **2012**, *45*, 5986–5992.

[109] Kulkarni, C.; Meijer, E.; Palmans, A. R. Cooperativity scale: a structure–mechanism correlation in the self-assembly of benzene-1, 3, 5-tricarboxamides. *Acc. Chem. Res.* **2017**, *50*, 1928–1936.

[110] Das, A.; Vantomme, G.; Markvoort, A. J.; ten Eikelder, H. M.; Garcia-Iglesias, M.; Palmans, A. R.; Meijer, E. Supramolecular copolymers: Structure and composition revealed by theoretical modeling. *J. Am. Chem. Soc.* **2017**, *139*, 7036–7044.

[111] Nakano, Y.; Hirose, T.; Stals, P. J.; Meijer, E.; Palmans, A. R. Conformational analysis of supramolecular polymerization processes of disc-like molecules. *Chem. Sci.* **2012**, *3*, 148–155.

[112] Ogi, S.; Stepanenko, V.; Sugiyasu, K.; Takeuchi, M.; WuÌĹrthner, F. Mechanism of self-assembly process and seeded supramolecular polymerization of perylene bisimide organogelator. *J. Am. Chem. Soc.* **2015**, *137*, 3300–3307.

[113] García, F.; Viruela, P. M.; Matesanz, E.; Ortí, E.; Sánchez, L. Cooperative Supramolecular Polymerization and Amplification of Chirality in C3-Symmetrical OPE-Based Trisamides. *Chem.–Eur. J.* **2011**, *17*, 7755–7759.

[114] Kar, H.; Gehrig, D. W.; Allampally, N. K.; Fernández, G.; Laquai, F.; Ghosh, S. Cooperative supramolecular polymerization of an amine-substituted naphthalene-diimide and its impact on excited state photophysical properties. *Chem. Sci.* **2016**, *7*, 1115–1120.

[115] Fagnani, D. E.; Meese Jr, M. J.; Abboud, K. A.; Castellano, R. K. Homochiral [2.2] Paracyclophane Self-Assembly Promoted by Transannular Hydrogen Bonding. *Angew. Chem. Int. Ed.* **2016**, *55*, 10726–10731.

[116] Metzroth, T.; Hoffmann, A.; Martín-Rapún, R.; Smulders, M. M.; Pieterse, K.; Palmans, A. R.; Vekemans, J. A.; Meijer, E.; Spiess, H. W.; Gauss, J. Unravelling the fine structure of stacked bipyridine diamine-derived C 3-discotics as determined by X-ray diffraction, quantum-chemical calculations, Fast-MAS NMR and CD spectroscopy. *Chem. Sci.* **2011**, *2*, 69–76.

[117] Kastler, M.; Pisula, W.; Wasserfallen, D.; Pakula, T.; Müllen, K. Influence of Alkyl Substituents on the Solution-and Surface-Organization of Hexa-p erihexabenzocoronenes. *J. Am. Chem. Soc.* **2005**, *127*, 4286–4296.

[118] Ikeda, T.; Adachi, H.; Fueno, H.; Tanaka, K.; Haino, T. Induced-Dipole-Directed, Cooperative Self-Assembly of a Benzotrithiophene. *J.Org. Chem.* **2017**, *82*, 10062–10069.

[119] Kraft, A.; Osterod, F.; Fröhlich, R. Bidirectional association of branched noncovalent complexes of tetrazoles and 1, 3, 5-tris (4, 5-dihydroimidazol-2-yl) benzene in solution. *J.Org. Chem.* **1999**, *64*, 6425–6433.

[120] Lohr, A.; Lysetska, M.; Würthner, F. Supramolecular Stereomutation in Kinetic and Thermodynamic Self-Assembly of Helical Merocyanine Dye Nanorods. *Angew. Chem. Int. Ed.* **2005**, *44*, 5071–5074.

[121] Lohr, A.; Würthner, F. Evolution of Homochiral Helical Dye Assemblies: Involvement of Autocatalysis in the “Majority-Rules” Effect. *Angew. Chem. Int. Ed.* **2008**, *47*, 1232–1236.

[122] Dobson, C. M.; Šali, A.; Karplus, M. Protein folding: a perspective from theory and experiment. *Angew. Chem. Int. Ed.* **1998**, *37*, 868–893.

[123] Korevaar, P. A.; Schaefer, C.; de Greef, T. F.; Meijer, E. Controlling chemical self-assembly by solvent-dependent dynamics. *J. Am. Chem. Soc.* **2012**, *134*, 13482–13491.

[124] Korevaar, P. A.; George, S. J.; Markvoort, A. J.; Smulders, M. M.; Hilbers, P. A.; Schenning, A. P.; De Greef, T. F.; Meijer, E. Pathway complexity in supramolecular polymerization. *Nature* **2012**, *481*, 492.

[125] Wehner, M.; Röhr, M. I. S.; Bühler, M.; Stepanenko, V.; Wagner, W.; Würthner, F. Supramolecular Polymorphism in One-Dimensional Self-Assembly by Kinetic Pathway Control. *J. Am. Chem. Soc.* **2019**, *141*, 6092–6107.

[126] Tidhar, Y.; Weissman, H.; Wolf, S. G.; Gulino, A.; Rybtchinski, B. Pathway-dependent self-assembly of perylene diimide/peptide conjugates in aqueous medium. *Chem.–Eur. J.* **2011**, *17*, 6068–6075.

[127] Mabesoone, M. F.; Meijer, E. Counterintuitive consequences of competitive pathways in supramolecular polymerizations. *J. Polym. Sci., Part A: Polym. Chem.* **2019**,

[128] Matern, J.; Dorca, Y.; Sánchez, L.; Fernandez, G. Revising complex supramolecular polymerization under kinetic and thermodynamic control. *Angew. Chem. Int. Ed.* **2019**, *58*, 16730–16740.

[129] Zhai, D.; Xu, W.; Zhang, L.; Chang, Y.-T. The role of "disaggregation" in optical probe development. *Chem. Soc. Rev.* **2014**, *43*, 2402–2411.

[130] Kometani, N.; Nakajima, H.; Asami, K.; Yonezawa, Y.; Kajimoto, O. Luminescence properties of the mixed J-aggregate of two kinds of cyanine dyes in layer-by-layer alternate assemblies. *J. Phys. Chem. B* **2000**, *104*, 9630–9637.

[131] Zhang, Q.; Atay, T.; Tischler, J. R.; Bradley, M. S.; Bulović, V.; Nurmikko, A. Highly efficient resonant coupling of optical excitations in hybrid organic/inorganic semiconductor nanostructures. *Nat. Nanotechnol.* **2007**, *2*, 555.

[132] Qiao, Y.; Polzer, F.; Kirmse, H.; Steeg, E.; Kühn, S.; Friede, S.; Kirstein, S.; Rabe, J. P. Nanotubular J-aggregates and quantum dots coupled for efficient resonance excitation energy transfer. *ACS Nano* **2015**, *9*, 1552–1560.

[133] Sorokin, A. V.; Yefimova, S. L.; Malyukin, Y. V. Polymer-Bound Supramolecular J-Aggregates: Optical Properties and Applications. *Encyclopedia of Polymer Science and Technology* **2018**, 1–33.

[134] Krieg, E.; Bastings, M. M.; Besenius, P.; Rybtchinski, B. Supramolecular polymers in aqueous media. *Chem. Rev.* **2016**, *116*, 2414–2477.

[135] Krieg, E.; Rybtchinski, B. Noncovalent Water-Based Materials: Robust yet Adaptive. *Chem.–Eur. J.* **2011**, *17*, 9016–9026.

[136] Du, X.; Zhou, J.; Shi, J.; Xu, B. Supramolecular hydrogelators and hydrogels: from soft matter to molecular biomaterials. *Chem. Rev.* **2015**, *115*, 13165–13307.

[137] Mammen, M.; Simanek, E. E.; Whitesides, G. M. Predicting the relative stabilities of multiparticle hydrogen-bonded aggregates based on the number of hydrogen bonds and the number of particles and measuring these stabilities with titrations using dimethyl sulfoxide. *J. Am. Chem. Soc.* **1996**, *118*, 12614–12623.

[138] Bisson, A. P.; Carver, F. J.; Eggleston, D. S.; Haltiwanger, R. C.; Hunter, C. A.; Livingstone, D. L.; McCabe, J. F.; Rotger, C.; Rowan, A. E. Synthesis and recognition properties of aromatic amide oligomers: molecular zippers. *J. Am. Chem. Soc.* **2000**, *122*, 8856–8868.

[139] Mes, T.; Smulders, M. M.; Palmans, A. R.; Meijer, E. Hydrogen-bond engineering in supramolecular polymers: polarity influence on the self-assembly of benzene-1, 3, 5-tricarboxamides. *Macromolecules* **2010**, *43*, 1981–1991.

[140] Rehm, T.; Schmuck, C. How to achieve self-assembly in polar solvents based on specific interactions? Some general guidelines. *Chem. Commun.* **2008**, 801–813.

[141] Cook, J. L.; Hunter, C. A.; Low, C. M.; Perez-Velasco, A.; Vinter, J. G. Solvent effects on hydrogen bonding. *Angew. Chem. Int. Ed.* **2007**, *46*, 3706–3709.

[142] Chen, Z.; Fimmel, B.; Würthner, F. Solvent and substituent effects on aggregation constants of perylene bisimide π-stacks–a linear free energy relationship analysis. *Org. Biomol. Chem.* **2012**, *10*, 5845–5855.

[143] Matsunaga, Y.; Miyajima, N.; Nakayasu, Y.; Sakai, S.; Yonenaga, M. Design of novel mesomorphic compounds: N, N′, N″-Trialkyl-1, 3, 5-benzenetricarboxamides. *Bull. Chem. Soc. Jpn.* **1988**, *61*, 207–210.

[144] Stals, P. J.; Everts, J. C.; de Bruijn, R.; Filot, I. A.; Smulders, M. M.; Martín-Rapún, R.; Pidko, E. A.; de Greef, T. F.; Palmans, A. R.; Meijer, E. Dynamic Supramolecular Polymers Based on Benzene-1, 3, 5-tricarboxamides: The Influence of Amide Connectivity on Aggregate Stability and Amplification of Chirality. *Chem.–Eur. J.* **2010**, *16*, 810–821.

[145] Hanabusa, K.; Koto, C.; Kimura, M.; Shirai, H.; Kakehi, A. Remarkable viscoelasticity of organic solvents containing trialkyl-1, 3, 5-benzenetricarboxamides and their intermolecular hydrogen bonding. *Chem. Lett.* **1997**, *26*, 429–430.

[146] Qin, B.; Zhang, S.; Song, Q.; Huang, Z.; Xu, J.-F.; Zhang, X. Supramolecular interfacial polymerization: a controllable method of fabricating supramolecular polymeric materials. *Angew. Chem. Int. Ed.* **2017**, *56*, 7639–7643.

[147] Qin, B.; Zhang, S.; Huang, Z.; Xu, J.-F.; Zhang, X. Supramolecular Interfacial Polymerization of Miscible Monomers: Fabricating Supramolecular Polymers with Tailor-Made Structures. *Macromolecules* **2018**, *51*, 1620–1625.

[148] Zhang, S.; Qin, B.; Huang, Z.; Xu, J.-F.; Zhang, X. Supramolecular Emulsion Interfacial Polymerization. *ACS Macro Lett.* **2019**, *8*, 177–182.

[149] Man, Y.; Li, S.; Diao, Q.; Lee, Y.-I.; Liu, H.-G. PS-b-PAA/Cu two-dimensional nanoflowers fabricated at the liquid/liquid interface: A highly active and robust heterogeneous catalyst. *Colloids Surf., A* **2019**, *570*, 377–385.

[150] Xu, H.; Erhardt, R.; Abetz, V.; Müller, A. H.; Goedel, W. A. Janus micelles at the air/water interface. *Langmuir* **2001**, *17*, 6787–6793.

[151] Lehn, J.-M. Supramolecular chemistry. *Science* **1993**, *260*, 1762–1764.

[152] Bairi, P.; Roy, B.; Routh, P.; Sen, K.; Nandi, A. K. Self-sustaining, fluorescent and semi-conducting co-assembled organogel of Fmoc protected phenylalanine with aromatic amines. *Soft Matter* **2012**, *8*, 7436–7445.

[153] Yang, X.; Zhang, G.; Zhang, D.; Zhu, D. A new ex-TTF-based organogelator: Formation of organogels and tuning with fullerene. *Langmuir* **2010**, *26*, 11720–11725.

[154] Che, Y.; Yang, X.; Liu, G.; Yu, C.; Ji, H.; Zuo, J.; Zhao, J.; Zang, L. Ultrathin n-type organic nanoribbons with high photoconductivity and application in optoelectronic vapor sensing of explosives. *J. Am. Chem. Soc.* **2010**, *132*, 5743–5750.

[155] Babu, S. S.; Praveen, V. K.; Ajayaghosh, A. Functional π-gelators and their applications. *Chem. Rev.* **2014**, *114*, 1973–2129.

[156] Xue, P.; Xu, Q.; Gong, P.; Qian, C.; Ren, A.; Zhang, Y.; Lu, R. Fibrous film of a two-component organogel as a sensor to detect and discriminate organic amines. *Chem. Commun.* **2013**, *49*, 5838–5840.

[157] Akutagawa, T.; Kakiuchi, K.; Hasegawa, T.; Noro, S.-i.; Nakamura, T.; Hasegawa, H.; Mashiko, S.; Becher, J. Molecularly Assembled Nanostructures of a Redox-Active Organogelator. *Angew. Chem. Int. Ed.* **2005**, *44*, 7283–7287.

[158] Zhang, L.; Wang, X.; Wang, T.; Liu, M. Tuning Soft Nanostructures in Self-assembled Supramolecular Gels: From Morphology Control to Morphology-Dependent Functions. *Small* **2015**, *11*, 1025–1038.

[159] Torchi, A.; Bochicchio, D.; Pavan, G. M. How the dynamics of a supramolecular polymer determines its dynamic adaptivity and stimuli-responsiveness: structure–dynamics–property relationships from coarse-grained simulations. *J. Phys. Chem. B* **2018**, *122*, 4169–4178.

[160] Song, Y.; Liu, Y.; Qi, T.; Li, G. L. Towards Dynamic but Supertough Healable Polymers through Biomimetic Hierarchical Hydrogen-Bonding Interactions. *Angew. Chem. Int. Ed.* **2018**, *57*, 13838–13842.

[161] Osswald, T.; Menges, G. Material Science of Polymers for Engineers. Hanser Gardner Publication. *Inc., OH* **2003**,

[162] Jud, K.; Kausch, H.; Williams, J. Fracture mechanics studies of crack healing and welding of polymers. *J. Mater. Sci.* **1981**, *16*, 204–210.

[163] Stukalin, E. B.; Cai, L.-H.; Kumar, N. A.; Leibler, L.; Rubinstein, M. Self-healing of unentangled polymer networks with reversible bonds. *Macromolecules* **2013**, *46*, 7525–7541.

[164] Chang, R.; Huang, Y.; Shan, G.; Bao, Y.; Yun, X.; Dong, T.; Pan, P. Alternating poly (lactic acid)/poly (ethylene-co-butylene) supramolecular multiblock copolymers with tunable shape memory and self-healing properties. *Polym. Chem.* **2015**, *6*, 5899–5910.

[165] Cheng, C.-C.; Chang, F.-C.; Chen, J.-K.; Wang, T.-Y.; Lee, D.-J. High-efficiency self-healing materials based on supramolecular polymer networks. *RSC Adv.* **2015**, *5*, 101148–101154.

[166] Greenland, B. W.; Burattini, S.; Hayes, W.; Colquhoun, H. M. Design, synthesis and computational modelling of aromatic tweezer-molecules as models for chain-folding polymer blends. *Tetrahedron* **2008**, *64*, 8346–8354.

[167] Hart, L. R.; Hunter, J. H.; Nguyen, N. A.; Harries, J. L.; Greenland, B. W.; Mackay, M. E.; Colquhoun, H. M.; Hayes, W. Multivalency in healable supramolecular polymers: the effect of supramolecular cross-link density on the mechanical properties and healing of non-covalent polymer networks. *Polym. Chem.* **2014**, *5*, 3680–3688.

[168] Hart, L. R.; Nguyen, N. A.; Harries, J. L.; Mackay, M. E.; Colquhoun, H. M.; Hayes, W. Perylene as an electron-rich moiety in healable, complementary π–π stacked, supramolecular polymer systems. *Polymer* **2015**, *69*, 293–300.

[169] Schmidt, S.; Reinecke, A.; Wojcik, F.; Pussak, D.; Hartmann, L.; Harrington, M. J. Metal-mediated molecular self-healing in histidine-rich mussel peptides. *Biomacromolecules* **2014**, *15*, 1644–1652.

[170] Schmitt, C. N.; Politi, Y.; Reinecke, A.; Harrington, M. J. Role of sacrificial protein–metal bond exchange in mussel byssal thread self-healing. *Biomacromolecules* **2015**, *16*, 2852–2861.

[171] Li, Y.; Li, L.; Sun, J. Bioinspired self-healing superhydrophobic coatings. *Angew. Chem. Int. Ed.* **2010**, *49*, 6129–6133.

[172] Jeon, I.; Cui, J.; Illeperuma, W. R.; Aizenberg, J.; Vlassak, J. J. Extremely stretchable and fast self-healing hydrogels. *Adv. Mater.* **2016**, *28*, 4678–4683.

[173] Das, A.; Sallat, A.; BoÌĹhme, F.; Suckow, M.; Basu, D.; Wießner, S.; StoÌĹckelhuber, K. W.; Voit, B.; Heinrich, G. Ionic modification turns commercial rubber into a self-healing material. *ACS Appl. Mater. Interfaces* **2015**, *7*, 20623–20630.

[174] Nakahata, M.; Takashima, Y.; Harada, A. Highly flexible, tough, and self-healing supramolecular polymeric materials using host–guest interaction. *Macromol. Rapid Commun.* **2016**, *37*, 86–92.

[175] Mei, J.-F.; Jia, X.-Y.; Lai, J.-C.; Sun, Y.; Li, C.-H.; Wu, J.-H.; Cao, Y.; You, X.-Z.; Bao, Z. A highly stretchable and autonomous self-healing polymer based on combination of pt$\cdots$ pt and π–π interactions. *Macromol. Rapid Commun.* **2016**, *37*, 1667–1675.

[176] Trask, R.; Bond, I. Biomimetic self-healing of advanced composite structures using hollow glass fibres. *Smart Mater. Struct.* **2006**, *15*, 704.

[177] Pang, J. W.; Bond, I. P. A hollow fibre reinforced polymer composite encompassing self-healing and enhanced damage visibility. *Compos. Sci. Technol.* **2005**, *65*, 1791–1799.

[178] Sun, L.; Yu, W. Y.; Ge, Q. Experimental research on the self-healing performance of micro-cracks in concrete bridge. Advanced Materials Research. 2011; pp 28–32.

[179] Williams, G.; Trask, R.; Bond, I. A self-healing carbon fibre reinforced polymer for aerospace applications. *Composites Part A: Applied Science and Manufacturing* **2007**, *38*, 1525–1532.

[180] Blaiszik, B.; Caruso, M.; McIlroy, D.; Moore, J.; White, S.; Sottos, N. Microcapsules filled with reactive solutions for self-healing materials. *Polymer* **2009**, *50*, 990–997.

[181] Brown, E. N.; White, S. R.; Sottos, N. R. Microcapsule induced toughening in a self-healing polymer composite. *J. Mater. Sci.* **2004**, *39*, 1703–1710.

[182] Szabó, T.; Molnár-Nagy, L.; Bognár, J.; Nyikos, L.; Telegdi, J. Self-healing microcapsules and slow release microspheres in paints. *Prog. Org. Coat.* **2011**, *72*, 52–57.

[183] Gardner, D.; Herbert, D.; Jayaprakash, M.; Jefferson, A.; Paul, A. Capillary flow characteristics of an autogenic and autonomic healing agent for self-healing concrete. *J. Mater. Civ. Eng.* **2017**, *29*, 04017228.

[184] Toohey, K. S.; Sottos, N. R.; Lewis, J. A.; Moore, J. S.; White, S. R. Self-healing materials with microvascular networks. *Nat. Mater.* **2007**, *6*, 581.

[185] Rule, J. D.; Sottos, N. R.; White, S. R. Effect of microcapsule size on the performance of self-healing polymers. *Polymer* **2007**, *48*, 3520–3529.

[186] Yang, J.; Keller, M. W.; Moore, J. S.; White, S. R.; Sottos, N. R. Microencapsulation of isocyanates for self-healing polymers. *Macromolecules* **2008**, *41*, 9650–9655.

[187] Uekama, K.; Hirayama, F.; Irie, T. Cyclodextrin drug carrier systems. *Chem. Rev.* **1998**, *98*, 2045–2076.

[188] Hirayama, F.; Uekama, K. Cyclodextrin-based controlled drug release system. *Adv. Drug Delivery Rev.* **1999**, *36*, 125–141.

[189] Challa, R.; Ahuja, A.; Ali, J.; Khar, R. Cyclodextrins in drug delivery: an updated review. *Aaps Pharmscitech* **2005**, *6*, E329–E357.

[190] Kurkov, S. V.; Loftsson, T. Cyclodextrins. *Int. J. Pharm.* **2013**, *453*, 167–180.

[191] Zhang, J.; Ma, P. X. Cyclodextrin-based supramolecular systems for drug delivery: recent progress and future perspective. *Adv. Drug Delivery Rev.* **2013**, *65*, 1215–1233.

[192] Isaacs, L. The mechanism of cucurbituril formation. *Isr. J. Chem.* **2011**, *51*, 578–591.

[193] Saleh, N.; Koner, A. L.; Nau, W. M. Activation and Stabilization of Drugs by Supramolecular pKa Shifts: Drug-Delivery Applications Tailored for Cucurbiturils. *Angew. Chem. Int. Ed.* **2008**, *47*, 5398–5401.

[194] Duan, Q.; Cao, Y.; Li, Y.; Hu, X.; Xiao, T.; Lin, C.; Pan, Y.; Wang, L. pH-responsive supramolecular vesicles based on water-soluble pillar [6] arene and ferrocene derivative for drug delivery. *J. Am. Chem. Soc.* **2013**, *135*, 10542–10549.

[195] Vinicius Vieira Varejao, E.; de Fatima, A.; Antonio Fernandes, S. Calix [n] arenes as goldmines for the development of chemical entities of pharmaceutical interest. *Curr. Pharm. Des.* **2013**, *19*, 6507–6521.

[196] Marquez, C.; Nau, W. M. Two Mechanisms of Slow Host–Guest Complexation between Cucurbit [6] uril and Cyclohexylmethylamine: pH-Responsive Supramolecular Kinetics. *Angew. Chem. Int. Ed.* **2001**, *40*, 3155–3160.

[197] Zarzycki, P.; Lamparczyk, H. Evidences for temperature-dependent mechanism of host-guest complexation. *Chromatographia* **1998**, *48*, 377–382.

[198] Yasuda, Y.; Iishi, E.; Inada, H.; Shirota, Y. Novel low-molecular-weight organic gels: N, N$'$, N$''$-tristearyltrimesamide/organic solvent system. *Chem. Lett.* **1996**, *25*, 575–576.

[199] Narayan, B.; Bejagam, K. K.; Balasubramanian, S.; George, S. J. Autoresolution of Segregated and Mixed p-n Stacks by Stereoselective Supramolecular Polymerization in Solution. *Angew. Chem. Int. Ed.* **2015**, *54*, 13053–13057.

[200] Peveler, W. J.; Yazdani, M.; Rotello, V. M. Selectivity and specificity: pros and cons in sensing. *ACS sensors* **2016**, *1*, 1282–1285.

[201] Wang, Q.; Li, Z.; Tao, D.-D.; Zhang, Q.; Zhang, P.; Guo, D.-P.; Jiang, Y.-B. Supramolecular aggregates as sensory ensembles. *Chem. Commun.* **2016**, *52*, 12929–12939.

[202] Manz, T. A.; Sholl, D. S. Chemically meaningful atomic charges that reproduce the electrostatic potential in periodic and nonperiodic materials. *J. Chem. Theory Comput.* **2010**, *6*, 2455–2468.

[203] Manz, T. A.; Sholl, D. S. Improved atoms-in-molecule charge partitioning functional for simultaneously reproducing the electrostatic potential and chemical states in periodic and nonperiodic materials. *J. Chem. Theory Comput.* **2012**, *8*, 2844–2867.

[204] Schoenmakers, S. M.; Leenders, C. M.; Lafleur, R. P.; Lou, X.; Meijer, E.; Pavan, G. M.; Palmans, A. R. Impact of the water-compatible periphery on the dynamic and structural properties of benzene-1,3,5-tricarboxamide based amphiphiles. *Chem. Commun.* **2018**, *54*, 11128–11131.

[205] Mayo, S. L.; Olafson, B. D.; Goddard, W. A. DREIDING: a generic force field for molecular simulations. *J. Phys. Chem.* **1990**, *94*, 8897–8909.

[206] Wang, J.; Wolf, R. M.; Caldwell, J. W.; Kollman, P. A.; Case, D. A. Development and testing of a general amber force field. *J. Comput. Chem.* **2004**, *25*, 1157–1174.

[207] Martin, M. G.; Siepmann, J. I. Transferable potentials for phase equilibria. 1. United-atom description of n-alkanes. *J. Phys. Chem. B* **1998**, *102*, 2569–2577.

[208] Jorgensen, W. L.; Chandrasekhar, J.; Madura, J. D.; Impey, R. W.; Klein, M. L. Comparison of simple potential functions for simulating liquid water. *J. Chem. Phys.* **1983**, *79*, 926–935.

[209] Smit, B. *Understanding molecular simulation: from algorithms to applications*; Academic Press, 1996.

[210] McDonald, I. R.; Hansen, J. *Theory of simple liquids*; Academic, 1976.

[211] Bergdorf, M.; Peter, C.; Hünenberger, P. H. Influence of cut-off truncation and artificial periodicity of electrostatic interactions in molecular simulations of solvated ions: A continuum electrostatics study. *J. Chem. Phys.* **2003**, *119*, 9129–9144.

[212] Saito, M. Molecular dynamics simulations of proteins in solution: artifacts caused by the cutoff approximation. *J. Chem. Phys.* **1994**, *101*, 4055–4061.

[213] Baumketner, A.; Shea, J.-E. The influence of different treatments of electrostatic interactions on the thermodynamics of folding of peptides. *J. Phys. Chem. B* **2005**, *109*, 21322–21328.

[214] Ewald, P. P. Die Berechnung optischer und elektrostatischer Gitterpotentiale. *Ann. Phys.* **1921**, *369*, 253–287.

[215] Darden, T.; York, D.; Pedersen, L. Particle mesh Ewald: An Nlog (N) method for Ewald sums in large systems. *J. Chem. Phys.* **1993**, *98*, 10089–10092.

[216] Zhuravlev, P. I.; Reddy, G.; Straub, J. E.; Thirumalai, D. Propensity to form amyloid fibrils is encoded as excitations in the free energy landscape of monomeric proteins. *J. Mol. Biol.* **2014**, *426*, 2653–2666.

[217] Zheng, W.; Tsai, M.-Y.; Chen, M.; Wolynes, P. G. Exploring the aggregation free energy landscape of the amyloid-β protein (1–40). *Proc. Natl. Acad. Sci.* **2016**, *113*, 11835–11840.

[218] Chipot, C.; Pohorille, A. *Free energy calculations*; Springer, 2007.

[219] Darve, E.; Rodríguez-Gómez, D.; Pohorille, A. Adaptive biasing force method for scalar and vector free energy calculations. *J. Chem. Phys.* **2008**, *128*, 144120.

[220] Torrie, G. M.; Valleau, J. P. Nonphysical sampling distributions in Monte Carlo free-energy estimation: Umbrella sampling. *J. Comput. Phys.* **1977**, *23*, 187–199.

[221] Barducci, A.; Bonomi, M.; Parrinello, M. Metadynamics. *WIREs Comput Mol Sci* **2011**, *1*, 826–843.

[222] Barducci, A.; Bussi, G.; Parrinello, M. Well-tempered metadynamics: a smoothly converging and tunable free-energy method. *Phys. Rev. Lett.* **2008**, *100*, 020603.

[223] Park, S.; Khalili-Araghi, F.; Tajkhorshid, E.; Schulten, K. Free energy calculation from steered molecular dynamics simulations using Jarzynski′s equality. *J. Chem. Phys.* **2003**, *119*, 3559–3566.

[224] Kumar, S.; Rosenberg, J. M.; Bouzida, D.; Swendsen, R. H.; Kollman, P. A. The weighted histogram analysis method for free-energy calculations on biomolecules. I. The method. *J. Comput. Chem.* **1992**, *13*, 1011–1021.

[225] Bejagam, K. K.; Fiorin, G.; Klein, M. L.; Balasubramanian, S. Supramolecular polymerization of benzene-1, 3, 5-tricarboxamide: a molecular dynamics simulation study. *J. Phys. Chem. B* **2014**, *118*, 5218–5228.

[226] Bejagam, K. K.; Balasubramanian, S. Supramolecular polymerization: a coarse grained molecular dynamics study. *J. Phys. Chem. B* **2015**, *119*, 5738–5746.

[227] Garzoni, M.; Baker, M. B.; Leenders, C. M.; Voets, I. K.; Albertazzi, L.; Palmans, A. R.; Meijer, E.; Pavan, G. M. Effect of H-bonding on order amplification in the growth of a supramolecular polymer in water. *J. Am. Chem. Soc.* **2016**, *138*, 13985–13995.

[228] Bochicchio, D.; Pavan, G. M. From cooperative self-assembly to water-soluble supramolecular polymers using coarse-grained simulations. *ACS Nano* **2017**, *11*, 1000–1011.

[229] Leenders, C. M.; Baker, M. B.; Pijpers, I. A.; Lafleur, R. P.; Albertazzi, L.; Palmans, A. R.; Meijer, E. Supramolecular polymerisation in water; elucidating the role of hydrophobic and hydrogen-bond interactions. *Soft Matter* **2016**, *12*, 2887–2893.

[230] Bejagam, K. K.; Remsing, R. C.; Klein, M. L.; Balasubramanian, S. Understanding the self-assembly of amino ester-based benzene-1, 3, 5-tricarboxamides using molecular dynamics simulations. *Phys. Chem. Chem. Phys.* **2017**, *19*, 258–266.

[231] Gasparotto, P.; Bochicchio, D.; Ceriotti, M.; Pavan, G. M. Identifying and Tracking Defects in Dynamic Supramolecular Polymers. *J. Phys. Chem. B* **2019**,

[232] Lafleur, R. P.; Schoenmakers, S. M.; Madhikar, P.; Bochicchio, D.; Baumeier, B.; Palmans, A. R.; Pavan, G. M.; Meijer, E. Insights into the kinetics of supramolecular comonomer incorporation in water. *Macromolecules* **2019**, *52*, 3049–3055.

[233] others,, et al. Supramolecular Copolymerization as a Strategy to Control the Stability of Self-Assembled Nanofibers. *Angew. Chem. Int. Ed.* **2018**, *57*, 6843–6847.

[234] Bochicchio, D.; Pavan, G. M. Accelerated Atomistic Simulations of a Supramolecular Polymer in Water. *arXiv preprint arXiv:1803.10491* **2018**,

[235] Lafleur, R. P.; Lou, X.; Pavan, G. M.; Palmans, A. R.; Meijer, E. Consequences of a cosolvent on the structure and molecular dynamics of supramolecular polymers in water. *Chem. Sci.* **2018**, *9*, 6199–6209.

[236] Bochicchio, D.; Pavan, G. M. Molecular modelling of supramolecular polymers. *Advances in Physics: X* **2018**, *3*, 1436408.

[237] Korlepara, D. B.; Balasubramanian, S. Molecular modelling of supramolecular one dimensional polymers. *RSC Adv.* **2018**, *8*, 22659–22669.

[238] Bochicchio, D.; Salvalaglio, M.; Pavan, G. M. Into the dynamics of a supramolecular polymer at submolecular resolution. *Nat. Commun.* **2017**, *8*, 1–11.

[239] Bochicchio, D.; Pavan, G. M. Effect of concentration on the supramolecular polymerization mechanism via implicit-solvent coarse-grained simulations of water-soluble 1, 3, 5-benzenetricarboxamide. *J. Phys. Chem. Lett.* **2017**, *8*, 3813–3819.

[240] Arefi, H. H.; Yamamoto, T. Communication: Self-assembly of a model supramolecular polymer studied by replica exchange with solute tempering. *J. Chem. Phys.* **2017**, *147*, 211102.

[241] Curtius, T. Hydrazide und Azide organischer Säuren. XXX. Abhandlung. Bildung von Hydrazihydraziden und Hydraziaziden dreibasischer Säuren. *Journal für Praktische Chemie* **1915**, *91*, 39–102.

[242] Gill, J.; MacGillivray, R.; Munro, J. 374. The preparation of symmetrical aromatic triamines and tri iso cyanates. *J. Chem. Soc. (Resumed)* **1949**, 1753–1754.

[243] Urbanaviciute, I.; Bhattacharjee, S.; Biler, M.; Lugger, J. A.; Cornelissen, T. D.; Norman, P.; Linares, M.; Sijbesma, R. P.; Kemerink, M. Suppressing depolarization by tail substitution in an organic supramolecular ferroelectric. *Phys. Chem. Chem. Phys.* **2019**, *21*, 2069–2079.

[244] Shikata, T.; Ogata, D.; Hanabusa, K. Viscoelastic Behavior of Supramolecular Polymeric Systems Consisting of N, N$'$, N$''$-Tris (3, 7-dimethyloctyl) benzene-1, 3, 5-tricarboxamide and n-Alkanes. *J. Phys. Chem. B* **2004**, *108*, 508–514.

[245] Chang, J. Y.; Baik, J. H.; Lee, C. B.; Han, M. J.; Hong, S.-K. Liquid crystals obtained from disclike mesogenic diacetylenes and their polymerization. *J. Am. Chem. Soc.* **1997**, *119*, 3197–3198.

[246] Bernet, A.; Albuquerque, R. Q.; Behr, M.; Hoffmann, S. T.; Schmidt, H.-W. Formation of a supramolecular chromophore: a spectroscopic and theoretical study. *Soft Matter* **2012**, *8*, 66–69.

[247] van Gorp, J. J.; Vekemans, J. A.; Meijer, E. C 3-symmetrical supramolecular architectures: Fibers and organic gels from discotic trisamides and trisureas. *J. Am. Chem. Soc.* **2002**, *124*, 14759–14769.

[248] Palmans, A. R.; Vekemans, J. A.; Meijer, E.; Kooijman, H.; Spek, A. L. Hydrogen-bonded porous solid derived from trimesic amide. *Chem. Commun.* **1997**, 2247–2248.

[249] Brunsveld, L.; Zhang, H.; Glasbeek, M.; Vekemans, J.; Meijer, E. Hierarchical growth of chiral self-assembled structures in protic media. *J. Am. Chem. Soc.* **2000**, *122*, 6175–6182.

[250] Palmans, A. R.; Vekemans, J. A.; Fischer, H.; Hikmet, R. A.; Meijer, E. Extended-Core Discotic Liquid Crystals Based on the Intramolecular H-Bonding in N-Acylated 2, $'$-Bipyridine-3, 3$'$-diamine Moieties. *Chem.–Eur. J.* **1997**, *3*, 300–307.

[251] others,, et al. Macroscopic hierarchical surface patterning of porphyrin trimers via self-assembly and dewetting. *Science* **2006**, *314*, 1433–1436.

[252] Paraschiv, I.; Giesbers, M.; van Lagen, B.; Grozema, F. C.; Abellon, R. D.; Siebbeles, L. D.; Marcelis, A. T.; Zuilhof, H.; Sudhölter, E. J. H-bond-stabilized triphenylene-based columnar discotic liquid crystals. *Chem. Mater.* **2006**, *18*, 968–974.

[253] van Herrikhuyzen, J.; Jonkheijm, P.; Schenning, A. P.; Meijer, E. The influence of hydrogen bonding and π–π stacking interactions on the self-assembly properties of C 3-symmetrical oligo (p-phenylenevinylene) discs. *Org. Biomol. Chem.* **2006**, *4*, 1539–1545.

[254] Gong, B.; Zheng, C.; Yan, Y. Structure of N, N′, N″-tris (carboxymethyl)-1, 3, 5-benzenetricarboxamide trihydrate. *J. Chem. Crystallogr.* **1999**, *29*, 649–652.

[255] Bose, P. P.; Drew, M. G.; Das, A. K.; Banerjee, A. Formation of triple helical nanofibers using self-assembling chiral benzene-1, 3, 5-tricarboxamides and reversal of the nanostructure's handedness using mirror image building blocks. *Chem. Commun.* **2006**, 3196–3198.

[256] Besenius, P.; Portale, G.; Bomans, P. H.; Janssen, H. M.; Palmans, A. R.; Meijer, E. Controlling the growth and shape of chiral supramolecular polymers in water. *Proc. Natl. Acad. Sci.* **2010**, *107*, 17888–17893.

[257] Gelinsky, M.; Vogler, R.; Vahrenkamp, H. Tripodal pseudopeptides with three histidine or cysteine donors: synthesis and zinc complexation. *Inorg. Chem.* **2002**, *41*, 2560–2564.

[258] de Loos, M.; van Esch, J. H.; Kellogg, R. M.; Feringa, B. L. C3-Symmetric, amino acid based organogelators and thickeners: a systematic study of structure–property relations. *Tetrahedron* **2007**, *63*, 7285–7301.

[259] Veld, M. A.; Haveman, D.; Palmans, A. R.; Meijer, E. Sterically demanding benzene-1, 3, 5-tricarboxamides: tuning the mechanisms of supramolecular polymerization and chiral amplification. *Soft Matter* **2011**, *7*, 524–531.

[260] van den Hout, K. P.; Martín-Rapún, R.; Vekemans, J. A.; Meijer, E. e. Tuning the Stacking Properties of C3-Symmetrical Molecules by Modifying a Dipeptide Motif. *Chem.–Eur. J.* **2007**, *13*, 8111–8123.

[261] Matsuura, K.; Murasato, K.; Kimizuka, N. Artificial peptide-nanospheres self-assembled from three-way junctions of β-sheet-forming peptides. *J. Am. Chem. Soc.* **2005**, *127*, 10148–10149.

[262] Akiyama, M.; Katoh, A.; Ogawa, T. N-hydroxy amides. Part 8. Synthesis and iron (III)-holding properties of di-and tri-hydroxamic acids extending from benzene-di-and-tri-carbonyl units through oligo (ethyleneoxy) arms. *J. Chem. Soc., Perkin Trans. 2* **1989**, 1213–1218.

[263] Stals, P. J.; Haveman, J. F.; Martín-Rapún, R.; Fitié, C. F.; Palmans, A. R.; Meijer, E. The influence of oligo (ethylene glycol) side chains on the self-assembly of benzene-1, 3, 5-tricarboxamides in the solid state and in solution. *J. Mater. Chem.* **2009**, *19*, 124–130.

[264] Lee, S.; Lee, J.-S.; Lee, C. H.; Jung, Y.-S.; Kim, J.-M. Nonpolymeric thermosensitive benzenetricarboxamides. *Langmuir* **2010**, *27*, 1560–1564.

[265] Lightfoot, M. P.; Mair, F. S.; Pritchard, R. G.; Warren, J. E. New supramolecular packing motifs: π-stacked rods encased in triply-helical hydrogen bonded amide strands. *Chem. Commun.* **1999**, 1945–1946.

[266] Fitié, C. F.; Roelofs, W. C.; Kemerink, M.; Sijbesma, R. P. Remnant polarization in thin films from a columnar liquid crystal. *J. Am. Chem. Soc.* **2010**, *132*, 6892–6893.

[267] Scott, J. F. Switching of ferroelectrics without domains. *Adv. Mater.* **2010**, *22*, 5315–5317.

[268] Kremer, F.; Schönhals, A. *Broadband dielectric spectroscopy*; Springer Science & Business Media, 2012.

[269] Gorbunov, A.; Putzeys, T.; Urbanavičiūtė, I.; Janssen, R.; Wübbenhorst, M.; Sijbesma, R.; Kemerink, M. True ferroelectric switching in thin films of trialkylbenzene-1, 3, 5-tricarboxamide (BTA). *Phys. Chem. Chem. Phys.* **2016**, *18*, 23663–23672.

[270] Urbanaviciute, I.; Meng, X.; Cornelissen, T. D.; Gorbunov, A. V.; Bhattacharjee, S.; Sijbesma, R. P.; Kemerink, M. Tuning the Ferroelectric Properties of Trialkylbenzene-1, 3, 5-tricarboxamide (BTA). *Adv. Electron. Mater.* **2017**, *3*, 1600530.

[271] Gorbunov, A.; Meng, X.; Urbanaviciute, I.; Putzeys, T.; Wübbenhorst, M.; Sijbesma, R.; Kemerink, M. Polarization loss in the organic ferroelectric trialkylbenzene-1, 3, 5-tricarboxamide (BTA). *Phys. Chem. Chem. Phys.* **2017**, *19*, 3192–3200.

[272] Bejagam, K. K.; Kulkarni, C.; George, S. J.; Balasubramanian, S. External electric field reverses helical handedness of a supramolecular columnar stack. *Chem. Commun.* **2015**, *51*, 16049–16052.

[273] Brunsveld, L.; Schenning, A.; Broeren, M.; Janssen, H.; Vekemans, J.; Meijer, E. Chiral amplification in columns of self-assembled N, $'$, N$''$ -tris ((S)-3, 7-dimethyloctyl) benzene-1, 3, 5-tricarboxamide in dilute solution. *Chem. Lett.* **2000**, *29*, 292–293.

[274] Cantekin, S.; Balkenende, D. W.; Smulders, M. M.; Palmans, A. R.; Meijer, E. The effect of isotopic substitution on the chirality of a self-assembled helix. *Nat. Chem.* **2011**, *3*, 42.

[275] Smulders, M. M.; Buffeteau, T.; Cavagnat, D.; Wolffs, M.; Schenning, A. P.; Meijer, E. C3-symmetrical self-assembled structures investigated by vibrational circular dichroism. *Chirality: The Pharmacological, Biological, and Chemical Consequences of Molecular Asymmetry* **2008**, *20*, 1016–1022.

[276] Narayan, B.; Kulkarni, C.; George, S. J. Synthesis and self-assembly of a C 3-symmetric benzene-1, 3, 5-tricarboxamide (BTA) anchored naphthalene diimide disc. *J. Mater. Chem. C* **2013**, *1*, 626–629.

[277] Cantekin, S.; de Greef, T. F.; Palmans, A. R. Benzene-1, 3, 5-tricarboxamide: a versatile ordering moiety for supramolecular chemistry. *Chem. Soc. Rev.* **2012**, *41*, 6125–6137.

[278] Baker, M. B.; Albertazzi, L.; Voets, I. K.; Leenders, C. M.; Palmans, A. R.; Pavan, G. M.; Meijer, E. Consequences of chirality on the dynamics of a water-soluble supramolecular polymer. *Nat. Commun.* **2015**, *6*, 1–12.

[279] Tong, K. W.; Dehn, S.; Webb, J. E.; Nakamura, K.; Braet, F.; Thordarson, P. Pyromellitamide Gelators: Exponential Rate of Aggregation, Hierarchical Assembly, and Their Viscoelastic Response to Anions. *Langmuir* **2009**, *25*, 8586–8592.

[280] Dehn, S.; Tong, K. W.; Clady, R. G.; Owen, D. M.; Gaus, K.; Schmidt, T. W.; Braet, F.; Thordarson, P. The structure and luminescence properties of europium (III) triflate doped self-assembled pyromellitamide gels. *New J. Chem.* **2011**, *35*, 1466–1471.

[281] Xing, B.; Yu, C.-W.; Chow, K.-H.; Ho, P.-L.; Fu, D.; Xu, B. Hydrophobic interaction and hydrogen bonding cooperatively confer a vancomycin hydrogel: a potential candidate for biomaterials. *J. Am. Chem. Soc.* **2002**, *124*, 14846–14847.

[282] Rajangam, K.; Behanna, H. A.; Hui, M. J.; Han, X.; Hulvat, J. F.; Lomasney, J. W.; Stupp, S. I. Heparin binding nanostructures to promote growth of blood vessels. *Nano Lett.* **2006**, *6*, 2086–2090.

[283] Shishido, Y.; Anetai, H.; Takeda, T.; Hoshino, N.; Noro, S.-i.; Nakamura, T.; Akutagawa, T. Molecular assembly and ferroelectric response of benzenecarboxamides bearing multiple- CONHC14H29 chains. *J. Phys. Chem. C* **2014**, *118*, 21204–21214.

[284] Das, A.; Ghosh, S. H-bonding directed programmed supramolecular assembly of naphthalene-diimide (NDI) derivatives. *Chem. Commun.* **2016**, *52*, 6860–6872.

[285] Goetz, K. P.; Vermeulen, D.; Payne, M. E.; Kloc, C.; McNeil, L. E.; Jurchescu, O. D. Charge-transfer complexes: new perspectives on an old class of compounds. *J. Mater. Chem. C* **2014**, *2*, 3065–3076.

[286] Burattini, S.; Colquhoun, H. M.; Greenland, B. W.; Hayes, W.; Wade, M. Pyrene-Functionalised, Alternating Copolyimide for Sensing Nitroaromatic Compounds. *Macromol. Rapid Commun.* **2009**, *30*, 459–463.

[287] Anetai, H.; Wada, Y.; Takeda, T.; Hoshino, N.; Yamamoto, S.; Mitsuishi, M.; Takenobu, T.; Akutagawa, T. Fluorescent ferroelectrics of hydrogen-bonded pyrene derivatives. *J. Phys. Chem. Lett.* **2015**, *6*, 1813–1818.

[288] Brown, C.; Farthing, A. Preparation and structure of di-p-xylylene. *Nature* **1949**, *164*, 915.

[289] Vögtle, F. *Cyclophane chemistry: synthesis, structures, and reactions*; John Wiley & Sons Inc, 1993.

[290] Morisaki, Y.; Chujo, Y. Cyclophane-containing polymers. *Prog. Polym. Sci.* **2008**, *33*, 346–364.

[291] Bazan, G. C. Novel organic materials through control of multichromophore interactions. *J.Org. Chem.* **2007**, *72*, 8615–8635.

[292] Morisaki, Y.; Chujo, Y. Construction of benzene ring-layered polymers. *Tetrahedron Lett.* **2005**, *46*, 2533–2537.

[293] Morisaki, Y.; Murakami, T.; Chujo, Y. Synthesis and properties of [2.2] paracyclophane-layered polymers. *Macromolecules* **2008**, *41*, 5960–5963.

[294] Morisaki, Y.; Murakami, T.; Sawamura, T.; Chujo, Y. [2.2] Paracyclophane-layered polymers end-capped with fluorescence quenchers. *Macromolecules* **2009**, *42*, 3656–3660.

[295] Morisaki, Y.; Chujo, Y. Through-space conjugated polymers consisting of [2.2] paracyclophane. *Polym. Chem.* **2011**, *2*, 1249–1257.

[296] Salhi, F.; Collard, D. M. π-Stacked Conjugated Polymers: The Influence of Paracyclophane π-Stacks on the Redox and Optical Properties of a New Class of Broken Conjugated Polythiophenes. *Adv. Mater.* **2003**, *15*, 81–85.

[297] Jagtap, S. P.; Collard, D. M. Multitiered 2D π-stacked conjugated polymers based on pseudo-geminal disubstituted [2.2] paracyclophane. *J. Am. Chem. Soc.* **2010**, *132*, 12208–12209.

[298] Jagtap, S. P.; Mukhopadhyay, S.; Coropceanu, V.; Brizius, G. L.; BreÌĄdas, J.-L.; Collard, D. M. Closely stacked oligo (phenylene ethynylene) s: Effect of π-stacking on the electronic properties of conjugated chromophores. *J. Am. Chem. Soc.* **2012**, *134*, 7176–7185.

[299] Guyard, L.; Audebert, P.; Dolbier Jr, W. R.; Duan, J.-X. Synthesis and electrochemical polymerization of new oligothiophene functionalized fluorocyclophanes. *J. Electroanal. Chem.* **2002**, *537*, 189–193.

[300] Guyard, L.; Nguyen Dinh An, M.; Audebert, P. Synthesis and electrochemical polymerization of new oligothiophene functionalized cyclophanes. *Adv. Mater.* **2001**, *13*, 133–136.

[301] Caramori, G. F.; Galembeck, S. E. Computational study about through-bond and through-space interactions in [2.2] cyclophanes. *J. Phys. Chem. A* **2007**, *111*, 1705–1712.

[302] Hu, W.; Gompf, B.; Pflaum, J.; Schweitzer, D.; Dressel, M. Transport properties of [2, 2]-paracyclophane thin films. *Appl. Phys. Lett.* **2004**, *84*, 4720–4722.

[303] Paradies, J. [2.2] Paracyclophane derivatives: synthesis and application in catalysis. *Synthesis* **2011**, *2011*, 3749–3766.

[304] Bartholomew, G. P.; Rumi, M.; Pond, S. J.; Perry, J. W.; Tretiak, S.; Bazan, G. C. Two-photon absorption in three-dimensional chromophores based on [2.2]-paracyclophane. *J. Am. Chem. Soc.* **2004**, *126*, 11529–11542.

[305] Yang, Y.; Zhang, G.; Yu, C.; He, C.; Wang, J.; Chen, X.; Yao, J.; Liu, Z.; Zhang, D. New conjugated molecular scaffolds based on [2, 2] paracyclophane as electron acceptors for organic photovoltaic cells. *Chem. Commun.* **2014**, *50*, 9939–9942.

[306] Zhu, C.; Liu, L.; Yang, Q.; Lv, F.; Wang, S. Water-soluble conjugated polymers for imaging, diagnosis, and therapy. *Chem. Rev.* **2012**, *112*, 4687–4735.

[307] Thomas, S. W.; Joly, G. D.; Swager, T. M. Chemical sensors based on amplifying fluorescent conjugated polymers. *Chem. Rev.* **2007**, *107*, 1339–1386.

[308] Pu, K.-Y.; Liu, B. Fluorescent conjugated polyelectrolytes for bioimaging. *Adv. Funct. Mater.* **2011**, *21*, 3408–3423.

[309] Martin, R. E.; Diederich, F. Linear Monodisperse π-Conjugated Oligomers: Model Compounds for Polymers and More. *Angew. Chem. Int. Ed.* **1999**, *38*, 1350–1377.

[310] Mba, M.; Moretto, A.; Armelao, L.; Crisma, M.; Toniolo, C.; Maggini, M. Synthesis and Self-Assembly of Oligo (p-phenylenevinylene) Peptide Conjugates in Water. *Chem.–Eur. J.* **2011**, *17*, 2044–2047.

[311] Castellanos-García, L. J.; Agudelo, B. C.; Rosales, H. F.; Cely, M.; Ochoa-Puentes, C.; Blanco-Tirado, C.; Sierra, C. A.; Combariza, M. Y. Oligo p-Phenylenevinylene Derivatives as Electron Transfer Matrices for UV-MALDI. *J. Am. Soc. Mass. Spectrom.* **2017**, *28*, 2548–2560.

[312] Burroughes, J. H.; Bradley, D. D.; Brown, A.; Marks, R.; Mackay, K.; Friend, R. H.; Burns, P.; Holmes, A. Light-emitting diodes based on conjugated polymers. *Nature* **1990**, *347*, 539.

[313] Kraft, A.; Grimsdale, A. C.; Holmes, A. B. Electroluminescent conjugated polymers-seeing polymers in a new light. *Angew. Chem. Int. Ed.* **1998**, *37*, 402–428.

[314] Yu, G.; Gao, J.; Hummelen, J. C.; Wudl, F.; Heeger, A. J. Polymer photovoltaic cells: enhanced efficiencies via a network of internal donor-acceptor heterojunctions. *Science* **1995**, *270*, 1789–1791.

[315] Horowitz, G. Organic field-effect transistors. *Adv. Mater.* **1998**, *10*, 365–377.

[316] others,, et al. Two-dimensional charge transport in self-organized, high-mobility conjugated polymers. *Nature* **1999**, *401*, 685.

[317] Nie, C.; Li, S.; Wang, B.; Liu, L.; Hu, R.; Chen, H.; Lv, F.; Dai, Z.; Wang, S. Preparation of Reactive Oligo (p-Phenylene Vinylene) Materials for Spatial Profiling of the Chemical Reactivity of Intracellular Compartments. *Adv. Mater.* **2016**, *28*, 3749–3754.

[318] Li, M.; He, P.; Li, S.; Wang, X.; Liu, L.; Lv, F.; Wang, S. Oligo (p-phenylenevinylene) Derivative-Incorporated and Enzyme-Responsive Hybrid Hydrogel for Tumor Cell-Specific Imaging and Activatable Photodynamic Therapy. *ACS Biomater. Sci. Eng.* **2017**, *4*, 2037–2045.

[319] Katz, H.; Lovinger, A.; Johnson, J.; Kloc, C.; Siegrist, T.; Li, W.; Lin, Y.-Y.; Dodabalapur, A. A soluble and air-stable organic semiconductor with high electron mobility. *Nature* **2000**, *404*, 478–481.

[320] Takenaka, S.; Yamashita, K.; Takagi, M.; Uto, Y.; Kondo, H. DNA sensing on a DNA probe-modified electrode using ferrocenylnaphthalene diimide as the electrochemically active ligand. *Anal. Chem.* **2000**, *72*, 1334–1341.

[321] Talukdar, P.; Bollot, G.; Mareda, J.; Sakai, N.; Matile, S. Ligand-gated synthetic ion channels. *Chem.–Eur. J.* **2005**, *11*, 6525–6532.

[322] Vollmann, H.; Becker, H.; Corell, M.; Streeck, H. Beiträge zur Kenntnis des Pyrens und seiner Derivate. *Justus Liebigs Ann. Chem.* **1937**, *531*, 1–159.

[323] Würthner, F.; Ahmed, S.; Thalacker, C.; Debaerdemaeker, T. Core-Substituted Naphthalene Bisimides: New Fluorophors with Tunable Emission Wavelength for FRET Studies. *Chem.–Eur. J.* **2002**, *8*, 4742–4750.

[324] others,, et al. Photoproduction of proton gradients with π-stacked fluorophore scaffolds in lipid bilayers. *Science* **2006**, *313*, 84–86.

[325] Tanaka, H.; Litvinchuk, S.; Tran, D.-H.; Bollot, G.; Mareda, J.; Sakai, N.; Matile, S. Adhesive π-clamping within synthetic multifunctional pores. *J. Am. Chem. Soc.* **2006**, *128*, 16000–16001.

[326] Gorteau, V.; Bollot, G.; Mareda, J.; Perez-Velasco, A.; Matile, S. Rigid oligo-naphthalenediimide rods as transmembrane anion- π slides. *J. Am. Chem. Soc.* **2006**, *128*, 14788–14789.

[327] Plimpton, S. Fast parallel algorithms for short-range molecular dynamics. *J. Comput. Phys.* **1995**, *117*, 1–19.

[328] Van Der Spoel, D.; Lindahl, E.; Hess, B.; Groenhof, G.; Mark, A. E.; Berendsen, H. J. GROMACS: fast, flexible, and free. *J. Comput. Chem.* **2005**, *26*, 1701–1718.

[329] Tribello, G. A.; Bonomi, M.; Branduardi, D.; Camilloni, C.; Bussi, G. PLUMED 2: New feathers for an old bird. *Comput. Phys. Commun.* **2014**, *185*, 604–613.

[330] Hutter, J.; Iannuzzi, M.; Schiffmann, F.; VandeVondele, J. Wiley Interdiscip. *Rev.: Comput. Mol. Sci* **2014**, *4*, 15–25.

[331] others,, et al. Gaussian 09, Revision D. 01, Gaussian. *Inc.: Wallingford, CT* **2009**,

[332] Humphrey, W.; Dalke, A.; Schulten, K. VMD: visual molecular dynamics. *J. Mol. Graphics* **1996**, *14*, 33–38.

Chapter 2

Differentiating the mechanism of self-assembly in supramolecular polymers through computation

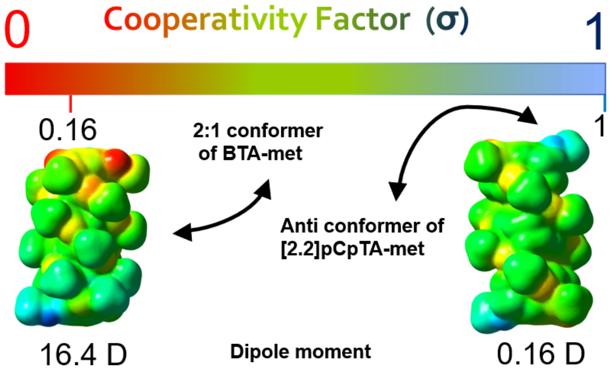

0
Cooperativity Factor (σ)
1
0.16
2:1 conformer of BTA-met
Anti conformer of [2.2]pCpTA-met
1
16.4 D
Dipole moment
0.16 D

Reprinted with permission from "Differentiating the mechanism of self-assembly in supramolecular polymers through computation" *Chem. Commun.* **2019**, *55*, 3773-3776. ⓒ 2019, Royal Society of Chemistry. http://dx.doi.org/10.1039/C9CC01058K.

2.1 Introduction

As in conventional polymers, the mechanism of polymerisation controls the molecular weight, dispersity and morphology of supramolecular polymers. [1] The assembly mechanism is determined by the dependence of the association constant for monomer addition on assembly size. When it is dependent on assembly size, the mechanism is cooperative but when it is independent of assembly size, the mechanism is isodesmic. [2–5] In terms of free energy, the isodesmic mechanism is one where the free energy gain by the addition of a monomer to an existing oligomer is independent of the latter's size. In certain cases, supramolecular polymerisation can proceed via a delicate combination of both these pathways. [6] In general, monomers assembling via the cooperative mechanism lead to larger supramolecular polymers than assemblies which follow the isodesmic mechanism. [7] The prudent tuning of the monomer design can alter the mechanism of self-assembly and also affect the morphology of resulting aggregates.[8–15]

The molecular features governing the polymerisation pathway were explored theoretically in an earlier work. [16] Based on a comparison of quantum chemical calculations of short oligomers of self-assembling molecules [16, 17] and their experimentally observed aggregation pathways, it was hypothesised that molecules possessing functional groups which impart a growing electric dipole moment for their oligomers will form supramolecular polymers via the cooperative mechanism, [11, 18–21] while those which lack such features will follow the isodesmic pathway. The same was later demonstrated within a family of molecules with a perylene bisimide core, [11] where the dipolar functionality was introduced through a carbonate linker. Along with dipole-dipole interactions, other interactions such as π-π and metal-metal can influence the degree of cooperativity in supramolecular polymerisation. [22, 23]

Experimentally, monomers self-assemble to form supramolecular polymers in an appropriate solvent below a certain temperature, but quantum chemical calculations of oligomers are carried out at 0 K in the gas phase. [21, 24–28] It is imperative that molecular computations to identify the mechanism of polymerisation take into account temperature and solvent effects as realistically as possible. Employing free energy calculations performed in solution at ambient conditions, we had shown that the classic molecule benzene-1,3,5-tricarboxamide (BTA) follows the cooperative mechanism, albeit modelled using coarse-grained molecular dynamics (CGMD). [28] Similar CGMD studies have also been carried out for water soluble BTA systems, to explore defect formation and monomer insertion. [29, 30]

The mechanism of supramolecular polymerisation can be determined experimentally using fluorescence, circular dichroism, NMR and UV-Vis spectroscopy, either as a function of temperature or concentration of solute. [10, 31–36] In computations, the free energy of oligomerisation for atomistic models of supramolecular polymers has not been examined until now. The free energy of association of chromonic molecules in water has been studied computationally earlier and was found to be quasi-isodesmic. [37]

In this Chapter, we demonstrate the free energy changes associated with the oligomerisation process for the cooperative and isodesmic classes. We consider [2.2]paracyclophane -tetracarboxamide ([2.2]pCpTA) which has recently been experimentally [38] shown to self-assemble via the isodesmic pathway and contrast its free energy of oligomerisation against that obtained for BTA. Both molecules assemble through the formation of intermolecular hydrogen bonds, but differences in the numbers and orientation of the hydrogen bonds correspond to different assembly behaviours. [19, 21, 39] Our results confirm the original hypothesis [16] that the increasing electric dipole moment of oligomers of BTA and its invariance in oligomers of [2.2]pCpTA is the underlying cause for the difference in polymerisation pathways.

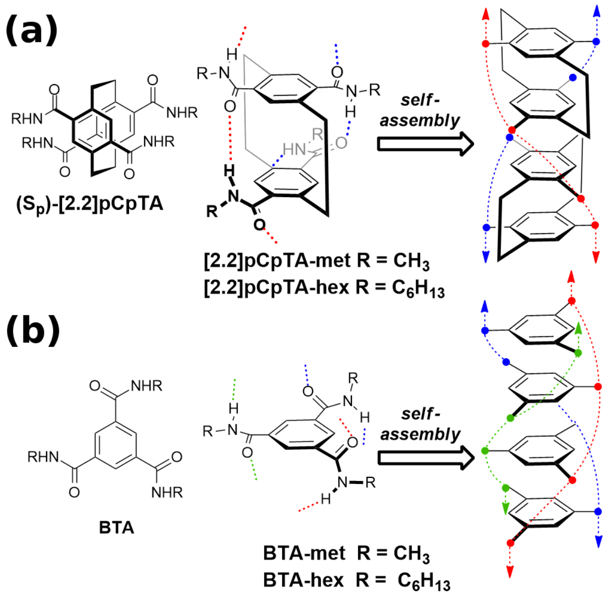

Figure 2.1: Structure of **(a)** [2.2]Paracyclophane-tetracarboxamide ([2.2]pCpTA) (S_p enantiomer) and **(b)** benzene-1,3,5-tricarboxamide (BTA) and their associated supramolecular assemblies. Only the anti conformation of the monomer is shown in each case.

Figure. 2.1 displays the two molecules studied here: (a) ([2.2]pCpTA) and (b)1,3,5-benzene tricarboxamide (BTA). The supramolecular polymerisation of the former was introduced and studied extensively by Castellano and coworkers recently. [38]

2.2 Computational Details

2.2.1 Gas-Phase calculations

Quantum Chemical Calculations

Structures of the molecules were optimised using density functional theory (DFT) using the Quickstep method (QS) in CP2K software. [40] The molecules were placed in a cubic box of edge dimension 200 Å. The Perdew-Burke-Ernzerhof (PBE) functional [41] with double ζ single polarization basis set and an energy cutoff of 280 Ry was used. The Goedecker-Tetter-Hutter (GTH) [42] pseudopotentials described the interaction of the valence electrons with the nuclei and core electrons. Empirical DFT-D3 [43] corrections were used to include the van der Waals interactions.

Charge Calculations

The partial charges on the atoms of all the molecules used in force-field calculations are calculated from the quantum optimised structures (for both [2.2]pCpTA and BTA) whose electron density cube files were analyzed using the Density Derived Electrostatic and Chemical method (DDEC/c3) [44, 45] to obtain the site charges which were used in force field based MD simulations.

Force-field based calculations

To obtain the energy differences between conformers within the force field, the geometry optimised structures of [2.2]pCpTA-met and BTA-met from the quantum chemical calculations were used as initial structures. The force-field energy calculations were carried out with LAMMPS [46] code. The dimensions of the simulation box (cubic) was taken to be 200 Å.

2.2.2 Solution Phase

Molecular modelling in MD simulations:

The atoms of [2.2]pCpTA-met (S_p), [2.2]pCpTA-hex (S_p), BTA-met (2:1) and BTA-hex (2:1) were modelled through an all-atom model. DREIDING force field [47] was used for parameterisation of bonded and non-bonded interactions. [2.2]pCpTA-hex molecule is soluble in chloroform. [38] Chloroform was modelled in all-atom representation and the parameters were taken from the DREIDING force field. [47]

2.2.3 Free energy Simulations

Adaptive biasing force method (ABF)

The adaptive biasing force (ABF) [48] method, based on the thermodynamic integration (TI) scheme to estimate the free energy profiles was used to study the dissociation free energies of oligomers in solution. The free energy (A_ξ) is estimated as a function of a collective variable (ξ), which is calculated from the average of a force F_ξ exerted on ξ.

$$A(\xi) = -\beta^{-1} \ln P(\xi) + A_0 \tag{2.1}$$

$$\nabla_\xi A(\xi) = \langle -F_\xi \rangle_\xi \tag{2.2}$$

Simulation Setup for [2.2]pCpTA-hex in chloroform

We performed free energy calculations using the Adaptive Biasing Force (ABF) [48] method for the formation of oligomers of various sizes of [2.2]pCpTA-hex in chloroform present in a cubic box of size 100 Å. The systems were prepared by inserting a preformed oligomer in such a way that stacks aligned along the z-axis in a simulation box which contains 7520 chloroform molecules. The reaction coordinate (ξ) is chosen to be the distance along the stacking direction between the Nth molecule (tip of the oligomer) and (N-1)th molecule of an oligomer size N. The same was implemented in the colvars module [49] of LAMMPS package as "distanceZ". It is worth noting that the molecule taken away from the tip of the oligomer can interact with the stack from the lateral side by its unrestricted motion throughout the simulation box. To avoid such interactions, we restricted the motion of the molecule separated from the stack in XY-plane by constructing a cylinder of radius 5 Å which can be included by the "distanceXY" [49] keyword.

The upper bound of the reaction coordinate is taken in such a way that the Nth and (N-1)th molecules do not interact with each other (22.0 Å) whereas the lower bound is considered as the centre of mass-centre of mass distance (6.0 Å) between them.

Simulation Setup for BTA-hex in *n*-nonane

The preformed BTA-hex oligomers were solvated in a cubic box which contained *n*-nonane. The free energy calculations were performed using the distanceZ & distanceXY [49] keyword in LAMMPS package, as discussed in the previous section. As the π-π distance in the BTA-hex oligomers is about 3.5 Å from our earlier reports [26, 28], we consider the lower bound of the reaction coordinate to be less than the π-π distance & is taken to be 2.5 Å and the upper boundary is taken as 19 Å. The system details are given in Table 2.1.

The details of the ABF calculations are given in Table 2.2. ABF simulations were performed under NVT ensemble at ambient conditions. Atom position and velocities are updated every 0.5 fs using velocity-Verlet algorithm. The coordinates of the atoms were saved every 2.5 ps. Each window is simulated for 25 ns.

Table 2.1: System sizes of BTA-hex in *n*-nonane for ABF simulations.

Range of oligomer size	Number of *n*-nonane molecules	Length of cubic box (Å)
2-5	215	40.00
6-10	1720	80.00

Table 2.2: Windows setup in free-energy calculations performed using the ABF method

Solute	Units	Bin width	Window 0	Window 1	Window 2	Window 3	Window 4	Window 5
[2.2]pCpTA-hex in chloroform	Å	0.1	[6.0,6.5]	[6.5,10.0]	[10.0,13.0]	[13.0,16.0]	[16.0,19.0]	[19.0,22.0]
BTA-hex in *n*-nonane	Å	0.1	[3.0,6.0]	[6.0,10.0]	[10.0,13.0]	[13.0,16.0]	[16.0,19.0]	— — —

Well-Tempered metadynamics (WTM)

Free energy surfaces arising due to conformational changes can be well sampled through the well-tempered metadynamics (WTM) simulations, due to its self-guiding nature. Gaussian hills are deposited along the trajectory of the collective variables. In WTM, the Gaussian hills height decrease with time. The effective Gaussian height is calculated by rescaling as w = $\omega e^{\frac{-V(s,t)}{\Delta T}} T_G$, where V(s,t) is the history-dependent potential, T$_G$ is the time interval at which Gaussian are deposited. The free-energy surface is estimated as $\tilde{F}$(s,t)=$-(T+\Delta T)\ln(1+\frac{\omega N(s,t)}{\Delta T})$, [50] where N(s,t) is the histogram of the collective variable 's' over the simulation time t. The simulations were performed by including PLUMED [51] to LAMMPS [46] software.

Simulation setup for WTM

One molecule of [2.2]pCpTA-hex is soaked in chloroform and is well equilibrated at ambient conditions, and later the configuration is taken for free-energy calculations. The dihedral angles (Φ & Ψ) shown in Figure. 2.14**(a)** are taken as collective variables to explore the free-energy surface (FES) which connects the anti and syn configuration of the [2.2]pCpTA-hex molecule. The simulations were performed in the NVT ensemble at 298.15 K for 400 ns & the position were updated for every 0.5 fs using the velocity-Verlet algorithm.

2.3 Results and Discussion

2.3.1 Conformations of Molecules

[2.2]pCpTA shares certain characteristics with BTA - while both contain a central phenyl ring core and amide functional group linkers, [2.2]pCpTA has two phenyl rings linked together by covalent bonds. [2.2]pCpTA can exist in two different conformations,

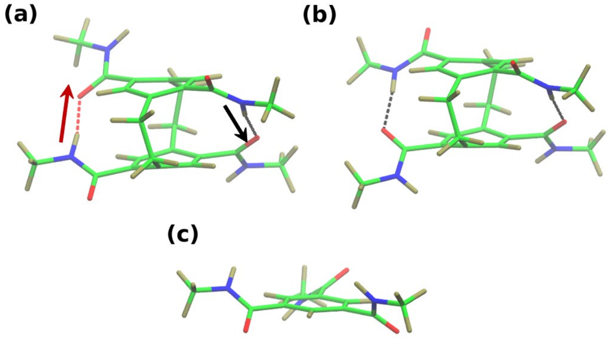

Figure 2.2: Structures of [2.2]pCpTA-met and BTA-met molecules. (a) anti conformer of [2.2]pCpTA-met (b) syn conformer of [2.2]pCpTA-met and (c) 2:1 conformer of BTA-met. Colour scheme: Green-Carbon, Red-Oxygen, Blue-Nitrogen, Tan-Hydrogen and dashed lines represent hydrogen bonds. The hydrogen bonds are Coloured in red and black depending on their dipole directions. The arrows shows the direction of the dipoles.

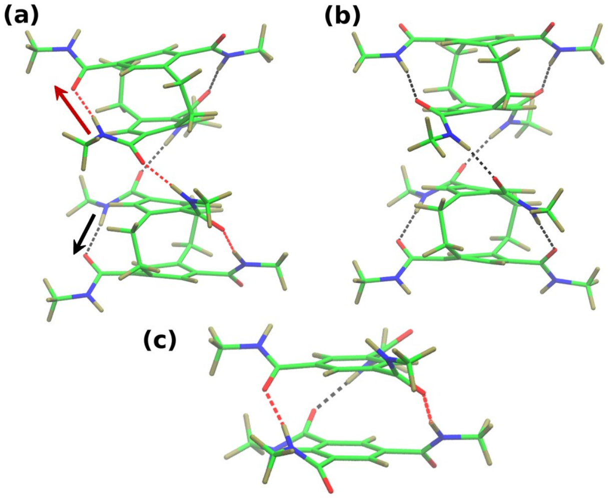

Figure 2.3: Dimer structures of [2.2]pCpTA-met and BTA-met molecules. (a) constructed out of anti conformers of [2.2]pCpTA-met (b) constructed out of syn conformers of [2.2]pCpTA-met and (c) 2:1 of BTA-met. See Figure. 2.2 for the Colour scheme.

anti and syn (Figure. 2.2(a),(b)), depending on the relative orientations of the amide groups. Figure. 2.3(a),(b) displays their oligomers. BTA has two conformers, [26, 52] and herein we consider the ground state one, i.e., the 2:1 (Two dipoles out of three amide groups of BTA are pointing up while the other pointing down with respect to the benzene plane) anti conformer (Figure. 2.2(c), 2.3(c)). Our density functional theory (DFT) calculations using the PBE-D3 [41] functional show the anti conformer of [2.2]pCpTA-met to be more stable than the syn one by 0.6 kcal/mol, which compares well against the value of 0.2 kcal/mol obtained at M06-2X/6-31g* level of theory earlier. [38] Furthermore, the anti conformer does not have an electric dipole moment component along the stacking direction, while the syn one has (Figure. 2.4(a)). Not just the monomer, but oligomers constructed out of the anti conformers too are more stable than those from the syn (Figure. 2.4(b)). The electrical dipole moments and the π-π distances of oligomers of [2.2]pCpTA-met conformers are calculated and tabulated (See Table 2.3). Given their relative stabilities, in the rest of the discussion, we focus on the anti conformer of [2.2]pCpTA and contrast its characteristics against those of BTA oligomers.

Table 2.3: Mean values of intermolecular π-π distance and electric dipole moment of oligomers of [2.2]pCpTA-met optimised using force field in gas phase.

Length of Oligomer (N)	**π-π Distance (Å)**		**Dipole moment (Debye)**	
	Anti	**Syn**	**Anti**	**Syn**
1	− − −	− − −	13.05	7.76
2	3.33	3.31	12.15	17.51
3	3.33	3.31	0.883	27.80
4	3.32	3.31	13.15	37.70
5	3.33	3.31	11.83	48.41
6	3.33	3.32	5.87	57.91
7	3.33	3.31	16.46	68.88
8	3.33	3.32	12.62	78.85
9	3.34	3.31	15.57	88.75
10	3.34	3.31	21.04	99.22

In Figure. 2.5**(a)** and Figure. 2.6**(a)** we compare the binding energy (B.E.$_\mathrm{N}$) of oligomers defined as B.E.$_\mathrm{N} = \frac{E_\mathrm{N}-\mathrm{N}E_1}{\mathrm{N}-1}$, of [2.2]pCpTA-met and BTA-met (Figure. 2.1). The data for BTA shows a strong N-dependence while that of the [2.2]pCpTA barely shows any. The former behaviour is quite similar to results reported by us earlier, [16, 26] demonstrating the cooperative behaviour of BTA oligomerisation and the isodesmic nature of that of [2.2]pCpTA. Long-range interactions such as dipole-dipole play an important role in determining the mechanism of self-assembly. [20] To examine such interactions, we calculated the normalised electric macrodipole moment (see Ref. [53] for definition) along the stacking direction of the oligomers both from MD and DFT structure optimisations, which is shown in Figure. 2.5**(b)** and Figure. 2.6**(b)**. The [2.2]pCpTA-met does not have a growing dipole; the oscillatory behaviour of the electric dipole moment of its oligomers with a period of three molecules, arises from the number of molecules required to complete a pitch (see inset to Figure. 2.9(a)). Intermolecular π-π distances in the gas phase oligomers of [2.2]pCpTA-met and BTA-met shown in Table 2.4 are in good agreement with experimental data. [38, 55]

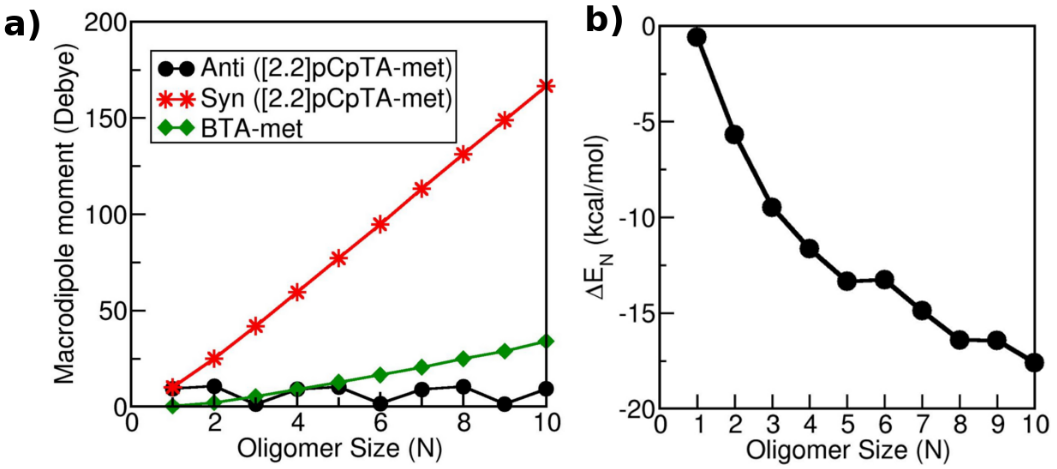

Figure 2.4: (a). Evolution of total electric dipole moment of [2.2]pCpTA-met oligomers in anti & syn conformations and of oligomers of BTA-met in their 2:1 conformation. Structures of dimer of these two molecules are shown in Figure. 2.3 and (b). Energy difference (ΔE_N) of oligomers of anti and syn conformations of [2.2]pCpTA-met. Where, ΔE_N=E_{anti}-E_{syn}. The structures were optimised using density functional theory at PBE-D3 level of theory.

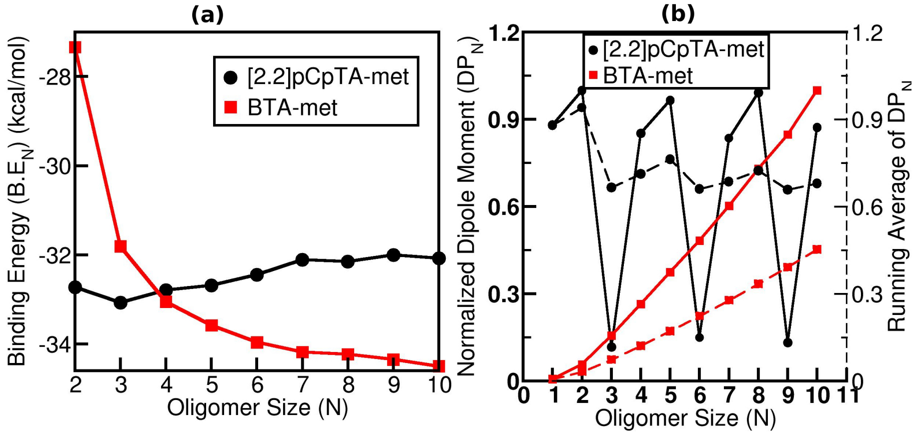

Figure 2.5: Structures of [2.2]pCpTA-met and BTA-met oligomers were optimised at PBE-D3 level of density functional theory. **(a)** Binding energy as a function of oligomer size (N), **(b)** Normalized macrodipole moment of an oligomer (DP_N) [53] along the stacking direction and its running average. The solid line is DP_N and the dotted line represents its running average.

2.3.2 MD simulations to determine the self diffusion coefficient of [2.2]pCpTA-hex in chloroform

Three independent simulations were performed to calculate the self diffusion coefficient of [2.2]pCpTA-hex in chloroform. Each system has 5 [2.2]pCpTA-hex molecules dispersed in chloroform (69613 molecules) in a cubic box of edge dimensions 212 Å. The simulations were performed at 298.15 K, the positions and velocities were updated

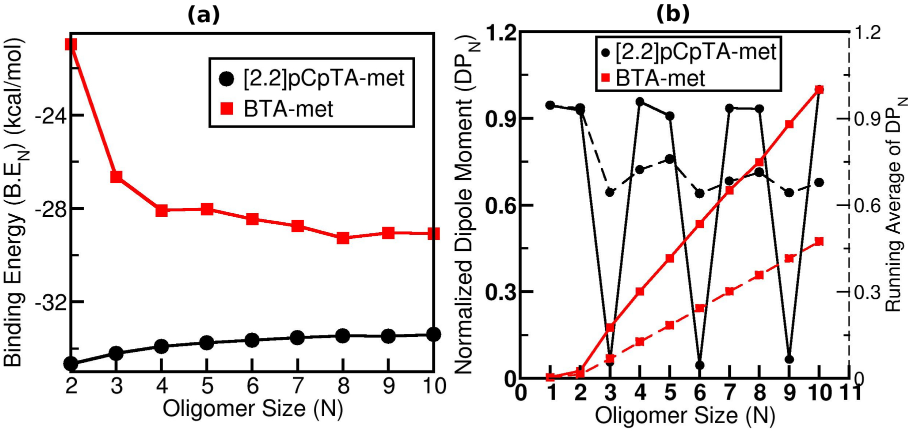

Figure 2.6: Results for oligomers of [2.2]pCpTA-met and BTA-met optimised using force field in gas phase. **(a)** Binding energy as a function of oligomer size, [54] **(a)** Normalized macrodipole moment (DP$_N$) [53] of the stack along the stacking direction and its running average.

Table 2.4: Mean values of intermolecular π-π distances (distance between centroids of closest phenyl rings of adjacent molecules in a stack) (in Å) and intermolecular hydrogen bond (N - - - O) distance (in Å) in oligomers of [2.2]pCpTA-met and BTA-met obtained from gas phase DFT calculations.[a]

Oligomer Size (N)	**π-π Distance (Å)**		**Hydrogen bond distance (Å)**	
	Anti conformer of [2.2]pCpTA-met	2:1 conformer of BTA-met	Anti conformer of [2.2]pCpTA-met	2:1 conformer of BTA-met
2	3.72	3.52	2.78	2.96
3	3.74	3.50	2.78	2.88
4	3.79	3.41	2.79	2.87
5	3.80	3.43	2.79	2.85
6	3.85	3.40	2.79	2.85
7	3.88	3.39	2.81	2.88
8	3.87	3.39	2.81	2.78
9	3.90	3.39	2.78	2.85
10	3.89	3.38	2.78	2.89

[a] Intermolecular π-π distances reported from experiments are 3.8 Å and 3.4 Å in [2.2]pCpTA crystal [38] and BTA in liquid crystalline phase [55] respectively. The hydrogen bond distance in the case of [2.2]pCpTA with propyl tail from its experimentally determined crystal structure [38] is 2.81 Å.

at every 0.5 fs using velocity-Verlet integrator. The system was equilibrated under NVT ensemble for 10 ns followed by the trajectory in the NPT ensemble. Coordinates were saved every 1 fs.

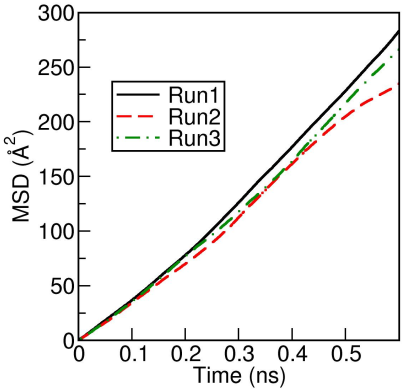

Figure 2.7: Mean squared displacment of [2.2]pCpTA-hex molecule in chloroform obtained from three independent simulations.

The diffusion coefficient is calculated from the Einstein relation via the mean square displacement (MSD). Plots of MSD from each simulation are shown in Figure. 2.7. The value obtained from simulations was 6.0×10^{-10} m^{2}s^{-1} while that from DOSY NMR experiments was 6.7×10^{-10} m^{2}s^{-1}. [38]

2.3.3 MD simulations of preformed decamer ([2.2]pCpTA-hex) in chloroform

A preformed 10-mer was soaked in a cubic box of size 100 Å filled with 7520 chloroform molecules. The system was equilibrated for 10 ns in the canonical ensemble using Nosé-Hoover thermostat [56, 57] with a damping constant of 1 ps, and the position and velocities were updated using the velocity-Verlet algorithm [58] every 0.5 fs. Atom positions were saved every 1.25 ps. Intermolecular distances and twist angles (see Figure. 2.8) between successive molecules in a stack were calculated from the last 5 ns of the trajectory. The simulations showed the stack to be stable with intact intermolecular hydrogen bonds and the equilibrated structure exhibited a mean intermolecular distance of 6.4 Å and a mean twist angle of 118°; their distributions are shown in Figure. 2.9(a). The twist angle is defined in Figure. 2.8.

In recent times, the interaction between a halogen atom and nucleophile has gained much attention [59, 60] due to its comparable strength to hydrogen bonding. [61, 62] The distribution of chlorine atom from the solvent (here, chloroform) to the oxygen of the amide group (in a preformed stack of [2.2]pCpTA-hex) is studied through the radial distribution function (RDF) shown in Figure. 2.9(b). The non-negligible first

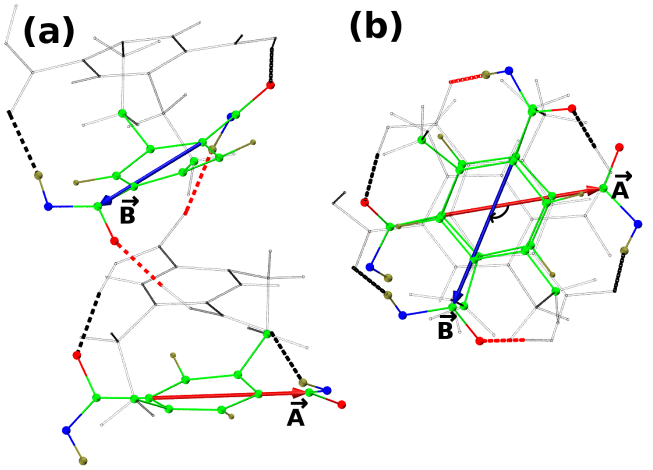

Figure 2.8: Twist angle between successive molecules in a stack **(a)** Side view **(b)** Top view. The Colour scheme: Green-Carbon, Red-Oxygen, Blue-Nitrogen, Tan-Hydrogen and dotted lines represents the hydrogen bonds (Red-Inter, Black-Intra) and the angle between $\vec{A}$ and $\vec{B}$ is defined as twist angle. Alkyl tails are not shown for clarity.

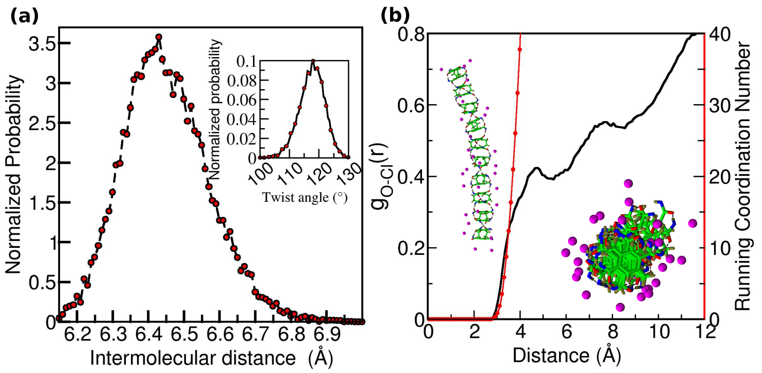

Figure 2.9: Structural properties of a preformed decamer of [2.2]pCpTA-hex in chloroform solvent at ambient conditions: **(a)** Intermolecular distance (Inset: Twist angle), **(b)** Radial distribution function (black) and running coordination number (red) between oxygen of amide group and chlorine atom of the chloroform. Colour Scheme: Green-Carbon, Red-Oxygen, Blue-Nitrogen, Tan-Hydrogen and Magenta-Chlorine.

peak in the RDF signifies reasonable ordering of the solvent chloroform molecules around the stack. The mean number of chlorine atoms within a distance of 4 Å from the amide oxygen was found to be 0.7 (see the running coordination number depicted in Figure. 2.9(b)), which once again demonstrates the stabilisation of the stack by the solvent.

2.3.4 Mechanism of Self-assembly

Towards determining the self assembly mechanism, we performed free energy calculations using the Adaptive Biasing Force (ABF) [48] method for the formation of oligomers of various sizes of [2.2]pCpTA-hex in chloroform & BTA-hex in *n*-nonane.

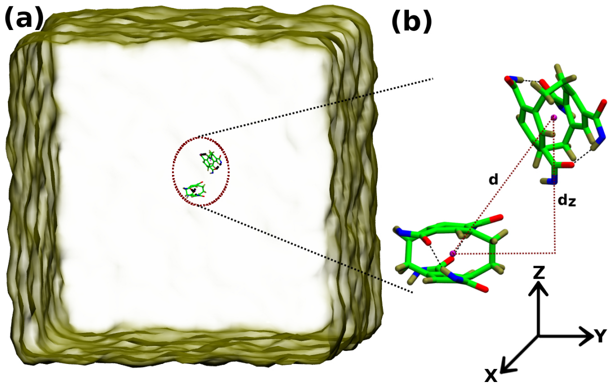

Figure 2.10: Free energy calculations: **(a)** Snapshot from MD simulations of dimer in chloroform, **(b)** Zoomed in portion of [2.2]pCpTA-hex dimer, the alkyl tails are not shown for clarity, "d" represents the distance between the centre of mass of the two molecules, d_Z is the distance component along the stacking direction (z-direction). The Colour scheme is as described in Figure. 2.8; in addition, magenta represents the pseudoatom to refer to the centre of mass of the core in the [2.2]pCpTA-hex molecule.

Oligomerisation free energy simulations were carried out by considering six windows to scan the entire ξ as shown in Table 2.2, each one sampled for 25 ns using the ABF method. The reaction coordinate for the case of a dimer is depicted in Figure. 2.10(a) and (b).

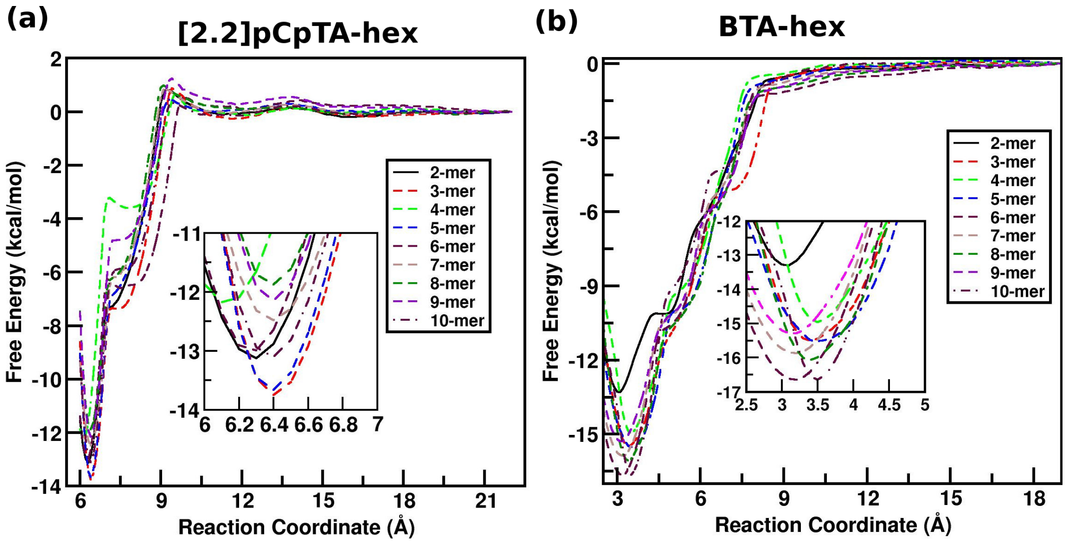

Figure 2.11: Free energy profiles: (a). [2.2]pCpTA-hex oligomers solvated in chloroform and (b) BTA-hex oligomers solvated in *n*-nonane. The projection of distance between the top molecule in the oligomer and the dissociating monomer along the stacking direction is the collective variable. Inset shows the same data, near the free-energy minimum.

The free energy profile for the dissociation of a solvated N-mer to its components (N-1)-mer and a monomer calculated using the ABF method are shown in Figure. 2.11.

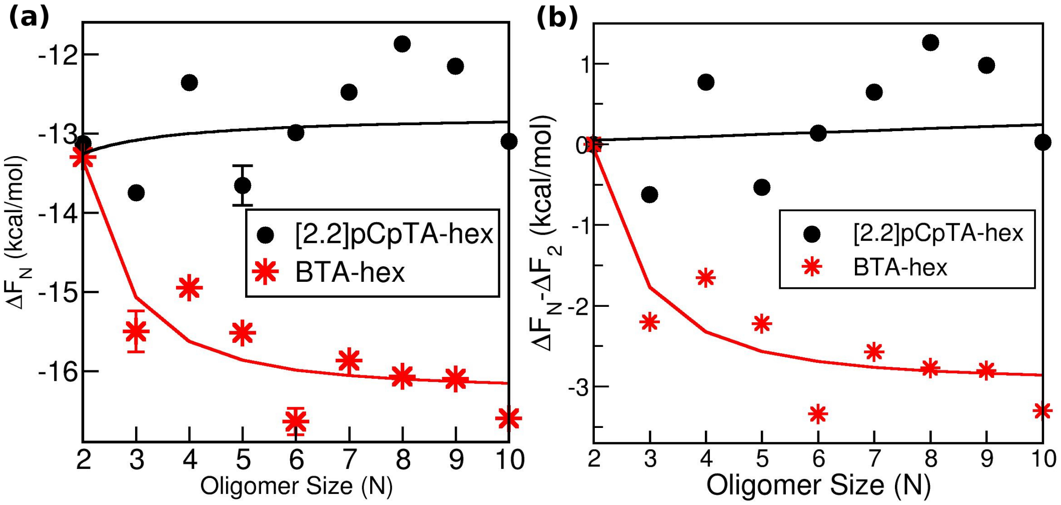

Figure 2.12: (a) Free energy difference, ΔF_N (see text for definition) of [2.2]pCpTA-hex and BTA-hex oligomers, (b) Deviations in free-energy difference from the dimerisation free energy obtained from MD simulations using the adaptive biased force (ABF) method. The solid line is a guide to the eye

ΔF_N is obtained as the difference in the free energies of the fully associated and the dissociated states; $\Delta F_N = F_N$-F_{N-1}-F_1. This free energy difference, ΔF_N for BTA-hex and [2.2]pCpTA-hex are shown in Figure. 2.12(a). The data is tabulated in Table 2.5. The free energy difference is independent of oligomer length for the [2.2]pCpTA-hex system while it exhibits a strong dependence for the BTA-hex system.

Table 2.5: Calculated free-energy difference ΔF_N using the ABF method.^{a}

Size of the oligomer (N)	**[2.2]pCpTA-hex (kcal/mol)**	**BTA-hex (kcal/mol)**
2	-13.13	-13.30
3	-13.75	-15.50
4	-12.36	-14.95
5	-13.66	-15.52
6	-12.99	-16.64
7	-12.49	-15.87
8	-11.87	-16.07
9	-12.75	-15.28
10	-13.10	-16.60

The free-energy of formation of a N-mer from N monomers, ΔF^f_N, can be obtained from a series of ΔF_N as $\Delta F^f_N = \sum_{i=2}^{N} \Delta F_N$. In the isodesmic mechanism, ΔF^f_N continues to decrease with oligomer size with a constant slope, whereas in the downhill cooperative mechanism, at least two different slopes can be distinguished – the first corresponding to the nucleation step and the second to the elongation step

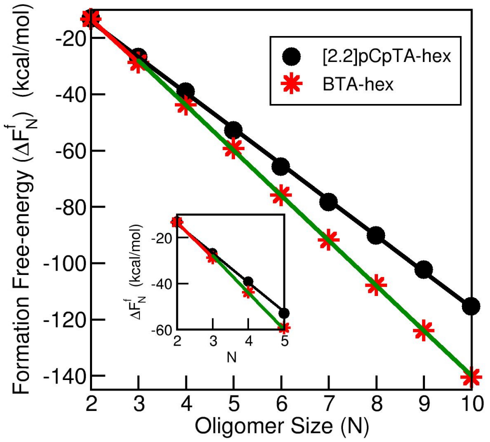

Figure 2.13: Free-energy of formation. The solid line represents a linear fit for the raw data shown as points.

(Figure. 2.13). [7] The deviation in the free-energy difference of each oligomer from the dimerisation free-energy is shown in Figure. 2.12(b); it reveals the near-independence in the case of [2.2]pCpTA-hex, and a strong dependence for the BTA-hex. The former, in particular, hugs the zero baseline which is a signature of isodesmicity or the equal-K (association constant) model.

The extent of cooperativity in self-assembly can be assessed using the cooperativity factor (σ), defined as the ratio of equilibrium constants during the nucleation and the elongation phases. Thus, in terms of the corresponding free energy changes σ = e$^{-\beta(\Delta F_{nuc}-\Delta F_{elo})}$, where $\beta = \frac{1}{k_B T}$.

It was shown by us earlier that the size of the nucleus in the case of BTA-hex is three. [28] Considering the mean value of ΔF_N beyond the nucleation step as ΔF_{elo}, we obtain σ for BTA-hex to be 0.16. The value for [2.2]pCpTA-hex is difficult to determine precisely due to the magnitude of error bars being comparable to values of ΔF_N; hence, the slope of its curve is taken to be zero which yields a σ value of unity.

2.3.5 Conformational free energy difference in [2.2]pCpTA-hex

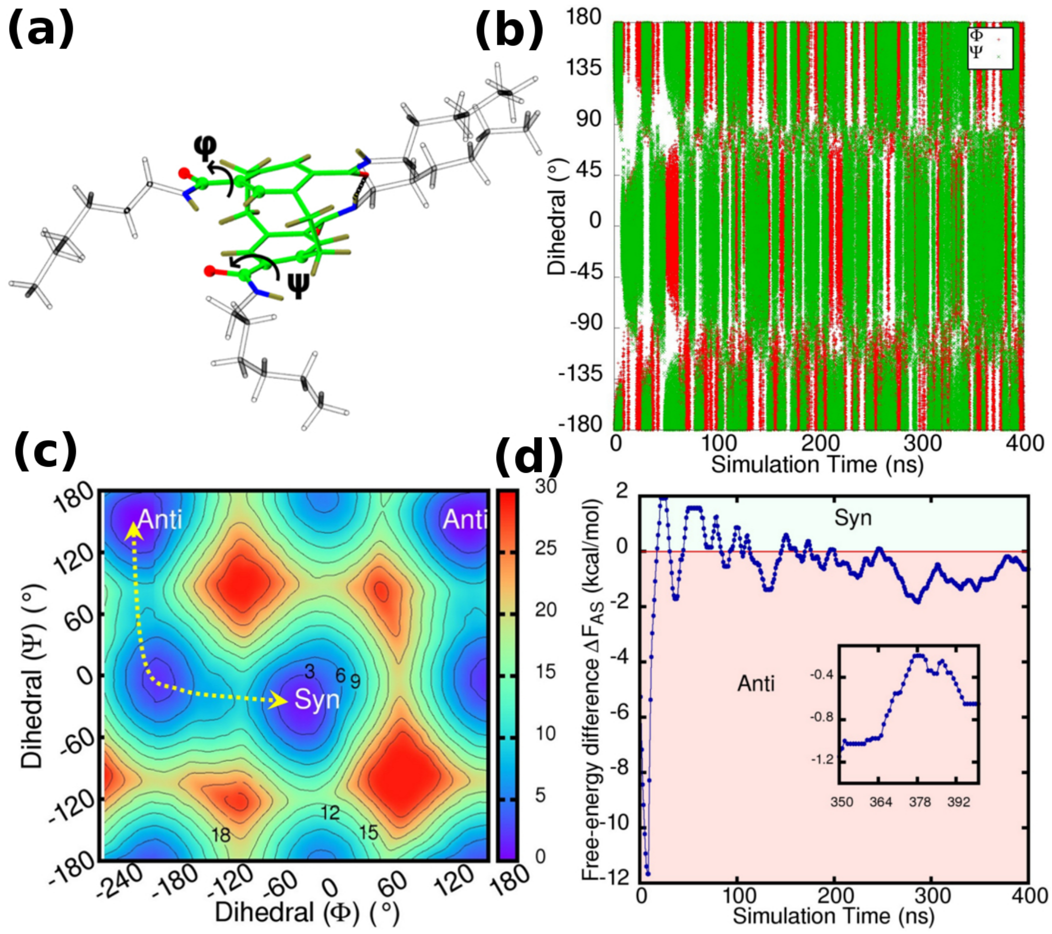

Figure 2.14: **(a)**. Definition of the dihedrals Φ and Ψ in [2.2]pCpTA-hex molecule, as used in the well-tempered metadynamics simulations. The atoms which form the dihedral are shown in CPK representation. The Colour scheme is same as in Figure. 2.10 **(b)**. The time evolution of the dihedrals **(c)**. Contour maps of free-energy (kcal/mol) for dihedrals Φ and Ψ. The yellow dotted line serves as a guide to the eye showing the minimum free energy path followed by the [2.2]pCpTA-hex molecule to convert from its anti to syn conformation. **(d)**. Time evolution of free-energy difference (ΔF_{AS}). Anti and syn regions are labelled for clarity.

The anti and syn conformations of [2.2]pCpTA-met differ in their total energies by just 0.6 kcal/mol, with the anti one being more stable. However, the syn conformation was not observed in the ABF simulations for the monomer which dissociated from the N-mer. This observation can be rationalized through an estimation of the barrier for the conformational change. In order to obtain this quantity, we performed free-energy calculations using the well-tempered metadynamics (WTM) method [50] with two dihedrals as the collective variables shown in Figure. 2.14(a).

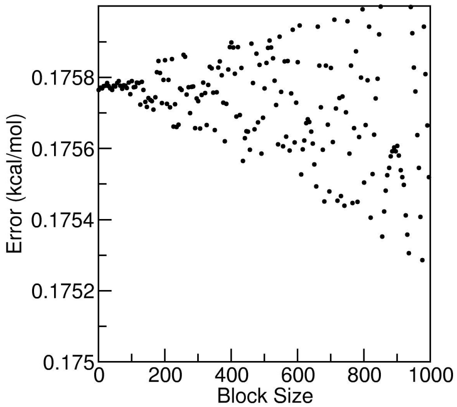

Figure 2.15: The error in free-energy calculations: Block analysis of a biased potential from well-tempered metadynamics simulation using Φ and Ψ as collective variables.

The evolution of the dihedral angles over the WTM trajectory are shown in Figure. 2.14(**b**) which indicates good sampling of the collective variables. The contour plot of dihedral angles is shown Figure. 2.14(**c**). The estimated barrier height for the anti to syn conversion is 10.2 kcal/mol, this estimate of the barrier is consistent with recent estimation of the same from NMR spectroscopy. [63] and the free-energy difference (ΔF_{AS}=F_{anti}-F_{syn}) between the conformations is 0.6±0.2 kcal/mol, favouring the anti conformer. The results of a convergence test are shown in Figure. 2.14(**d**). The error is calculated from the block-analysis shown in Figure. 2.15. The high barrier in the FES prevents the molecule to explore the syn conformation in a normal MD simulation, although the free energy difference between the conformers is low.

2.3.6 Conclusions

Employing large scale all-atom MD simulations, the free energy change associated with the oligomerisation of two molecules [2.2]pCpTA-hex and BTA-hex in solution has been determined. These molecules are representative of the two distinct categories of pathways of supramolecular polymerisation – the isodesmic and the cooperative. [2.2]pCpTA polymerises in a manner where the free energy change is independent of oligomer size while BTA does so in a manner where the free energy change (and thus the association constant) exhibits a dependence on oligomer size. The simulations clearly distinguish these two scenarios via free energy calculations. The results are consistent with experimental observations. The molecular level calculations attribute the differences in the polymerisation pathways to the development of a macrodipole in oligomers of BTA and the lack thereof in the oligomers of the anti conformer of [2.2]pCpTA, once again confirming the original hypothesis elucidated in Ref. [16] In this context, it would be interesting to computationally study the mechanism of self-assembly of the syn conformer of [2.2]pCpTA, which is expected to be cooperative due to the presence of a growing macrodipole moment along the stacking direction; we plan to pursue this aspect in future.

Bibliography

[1] Besenius, P.; de Feijter, I.; Sommerdijk, N. A.; Bomans, P. H.; Palmans, A. R. Controlling the size, shape and stability of supramolecular polymers in water. *J. Vis. Exp* **2012**, 1–7.

[2] Smulders, M. M.; Nieuwenhuizen, M. M.; de Greef, T. F.; van der Schoot, P.; Schenning, A. P.; Meijer, E. How to distinguish isodesmic from cooperative supramolecular polymerisation. *Chem.–Eur. J.* **2010**, *16*, 362–367.

[3] Goldstein, R.; Stryer, L. Cooperative polymerization reactions. Analytical approximations, numerical examples, and experimental strategy. *Biophys. J.* **1986**, *50*, 583.

[4] Powers, E. T.; Powers, D. L. The kinetics of nucleated polymerizations at high concentrations: amyloid fibril formation near and above the "supercritical concentration". *Biophys. J.* **2006**, *91*, 122–132.

[5] Kodaka, M. Interpretation of concentration-dependence in aggregation kinetics. *Biophys. Chem.* **2004**, *109*, 325–332.

[6] Ogi, S.; Sugiyasu, K.; Manna, S.; Samitsu, S.; Takeuchi, M. Living supramolecular polymerization realized through a biomimetic approach. *Nat. Chem.* **2014**, *6*, 188.

[7] De Greef, T. F.; Smulders, M. M.; Wolffs, M.; Schenning, A. P.; Sijbesma, R. P.; Meijer, E. Supramolecular polymerization. *Chem. Rev.* **2009**, *109*, 5687–5754.

[8] El Idrissi, M.; Teat, S. J.; Corvini, P. F.-X.; Paterson, M. J.; Dalgarno, S. J.; Shahgaldian, P. Template-free hierarchical self-assembly of a pyrene derivative into supramolecular nanorods. *Chem. Commun.* **2017**, *53*, 1973–1976.

[9] Cui, L.; Jiao, Y.; Wang, A.; Zhao, L.; Dong, Q.; Yan, X.; Bai, S. Regulating morphologies and near-infrared photothermal conversion of perylene bisimide via sequence-dependent peptide self-assembly. *Chem. Commun.* **2018**, *54*, 2208–2211.

[10] Das, A.; Ghosh, S. H-bonding directed programmed supramolecular assembly of naphthalene-diimide (NDI) derivatives. *Chem. Commun.* **2016**, *52*, 6860–6872.

[11] Kulkarni, C.; Bejagam, K. K.; Senanayak, S. P.; Narayan, K.; Balasubramanian, S.; George, S. J. Dipole-moment-driven Cooperative Supramolecular Polymerization. *J. Am. Chem. Soc.* **2015**, *137*, 3924–3932.

[12] Casellas, N. M.; Pujals, S.; Bochicchio, D.; Pavan, G. M.; Torres, T.; Albertazzi, L.; García-Iglesias, M. From isodesmic to highly cooperative: reverting the supramolecular polymerization mechanism in water by fine monomer design. *Chem. Comm.* **2018**, *54*, 4112–4115.

[13] Kulkarni, C.; Meijer, E.; Palmans, A. R. Cooperativity scale: a structure–mechanism correlation in the self-assembly of benzene-1, 3, 5-tricarboxamides. *Acc. Chem. Res.* **2017**, *50*, 1928–1936.

[14] Anetai, H.; Wada, Y.; Takeda, T.; Hoshino, N.; Yamamoto, S.; Mitsuishi, M.; Takenobu, T.; Akutagawa, T. Fluorescent ferroelectrics of hydrogen-bonded pyrene derivatives. *J. Phys. Chem. Lett.* **2015**, *6*, 1813–1818.

[15] Schoenmakers, S. M.; Leenders, C. M.; Lafleur, R. P.; Lou, X.; Meijer, E.; Pavan, G. M.; Palmans, A. R. Impact of the water-compatible periphery on the dynamic and structural properties of benzene-1, 3, 5-tricarboxamide based amphiphiles. *Chem. Commun.* **2018**, *54*, 11128–11131.

[16] Kulkarni, C.; Balasubramanian, S.; George, S. J. What Molecular Features Govern the Mechanism of Supramolecular Polymerization? *ChemPhysChem* **2013**, *14*, 661–673.

[17] Buendía, J.; Calbo, J.; García, F.; Aragó, J.; Viruela, P. M.; Ortí, E.; Sánchez, L. Helical supramolecular polymerization of C 3-symmetric amides and retroamides: on the origin of cooperativity and handedness. *Chem. Commun.* **2016**, *52*, 6907–6910.

[18] Fernández, G.; Stolte, M.; Stepanenko, V.; Würthner, F. Cooperative Supramolecular Polymerization: Comparison of Different Models Applied on the Self-Assembly of Bis (merocyanine) Dyes. *Chem.–Eur. J.* **2013**, *19*, 206–217.

[19] Filot, I. A.; Palmans, A. R.; Hilbers, P. A.; van Santen, R. A.; Pidko, E. A.; de Greef, T. F. Understanding cooperativity in hydrogen-bond-induced supramolecular polymerization: a density functional theory study. *J. Phys. Chem. B* **2010**, *114*, 13667–13674.

[20] Ikeda, T.; Iijima, T.; Sekiya, R.; Takahashi, O.; Haino, T. Cooperative Self-Assembly of Carbazole Derivatives Driven by Multiple Dipole–Dipole Interactions. *J. Org. Chem.* **2016**, *81*, 6832–6837.

[21] Garzoni, M.; Baker, M. B.; Leenders, C. M.; Voets, I. K.; Albertazzi, L.; Palmans, A. R.; Meijer, E.; Pavan, G. M. Effect of H-bonding on order amplification in the growth of a supramolecular polymer in water. *J. Am. Chem. Soc.* **2016**, *138*, 13985–13995.

[22] Mayoral, M. J.; Rest, C.; Stepanenko, V.; Schellheimer, J.; Albuquerque, R. Q.; FernaÌĄndez, G. Cooperative supramolecular polymerization driven by metallophilic Pd··· Pd interactions. *J. Am. Chem. Soc.* **2013**, *135*, 2148–2151.

[23] Gao, Z.; Han, Y.; Wang, F. Cooperative supramolecular polymers with anthracene–endoperoxide photo-switching for fluorescent anti-counterfeiting. *Nat. Commun.* **2018**, *9*, 3977.

[24] Korlepara, D. B.; Bejagam, K. K.; Balasubramanian, S. Supramolecular polymerization of N, N′, N″, N‴-tetra-(tetradecyl)-1, 3, 6, 8-pyrenetetracarboxamide: a computational study. *J. Phys. Chem. B* **2017**, *121*, 11492–11503.

[25] Kulkarni, C.; Reddy, S. K.; George, S. J.; Balasubramanian, S. Cooperativity in the stacking of benzene-1, 3, 5-tricarboxamide: the role of dispersion. *Chem. Phys. Lett.* **2011**, *515*, 226–230.

[26] Bejagam, K. K.; Fiorin, G.; Klein, M. L.; Balasubramanian, S. Supramolecular polymerization of benzene-1, 3, 5-tricarboxamide: a molecular dynamics simulation study. *J. Phys. Chem. B* **2014**, *118*, 5218–5228.

[27] Bochicchio, D.; Pavan, G. M. From cooperative self-assembly to water-soluble supramolecular polymers using coarse-grained simulations. *ACS Nano* **2017**, *11*, 1000–1011.

[28] Bejagam, K. K.; Balasubramanian, S. Supramolecular polymerization: a coarse grained molecular dynamics study. *J. Phys. Chem. B* **2015**, *119*, 5738–5746.

[29] Bochicchio, D.; Salvalaglio, M.; Pavan, G. M. Into the dynamics of a supramolecular polymer at submolecular resolution. *Nat. Commun.* **2017**, *8*, 147.

[30] Torchi, A.; Bochicchio, D.; Pavan, G. M. How the dynamics of a supramolecular polymer determines its dynamic adaptivity and stimuli-responsiveness: structure–dynamics–property relationships from coarse-grained simulations. *J. Phys. Chem. B* **2018**, *122*, 4169–4178.

[31] Wang, G.; Wang, W.; Miao, R.; Shang, C.; He, M.; Peng, H.; He, G.; Fang, Y. A perylene bisimide derivative with pyrene and cholesterol as modifying structures: synthesis and fluorescence behavior. *Phys. Chem. Chem. Phys.* **2016**, *18*, 12221–12230.

[32] Avakyan, N.; Greschner, A. A.; Aldaye, F.; Serpell, C. J.; Toader, V.; Petitjean, A.; Sleiman, H. F. Reprogramming the assembly of unmodified DNA with a small molecule. *Nat. Chem.* **2016**, *8*, 368.

[33] Jonkheijm, P.; van der Schoot, P.; Schenning, A. P.; Meijer, E. Probing the solvent-assisted nucleation pathway in chemical self-assembly. *Science* **2006**, *313*, 80–83.

[34] Das, A.; Vantomme, G.; Markvoort, A. J.; ten Eikelder, H. M.; Garcia-Iglesias, M.; Palmans, A. R.; Meijer, E. Supramolecular copolymers: structure and composition revealed by theoretical modeling. *J. Am. Chem. Soc.* **2017**, *139*, 7036–7044.

[35] Veld, M. A.; Haveman, D.; Palmans, A. R.; Meijer, E. Sterically demanding benzene-1, 3, 5-tricarboxamides: tuning the mechanisms of supramolecular polymerization and chiral amplification. *Soft Matter* **2011**, *7*, 524–531.

[36] Narayan, B.; Kulkarni, C.; George, S. J. Synthesis and self-assembly of a C 3-symmetric benzene-1, 3, 5-tricarboxamide (BTA) anchored naphthalene diimide disc. *J. Mater. Chem. C* **2013**, *1*, 626–629.

[37] Akinshina, A.; Walker, M.; Wilson, M. R.; Tiddy, G. J.; Masters, A. J.; Carbone, P. Thermodynamics of the self-assembly of non-ionic chromonic molecules using atomistic simulations. The case of TP6EO2M in aqueous solution. *Soft Matter* **2015**, *11*, 680–691.

[38] Fagnani, D. E.; Meese, M. J., Jr.; Abboud, K. A.; Castellano, R. K. Homochiral [2.2] Paracyclophane Self-Assembly Promoted by Transannular Hydrogen Bonding. *Angew. Chem. Int. Ed.* **2016**, *55*, 10726–10731.

[39] Van Ravensteijn, B. G.; Vilanova, N.; De Feijter, I.; Kegel, W. K.; Voets, I. K. Temperature-induced, selective assembly of supramolecular colloids in water. *ACS Omega* **2017**, *2*, 1720–1730.

[40] Hutter, J.; Iannuzzi, M.; Schiffmann, F.; VandeVondele, J. CP2K: Atomistic Simulations of Condensed Matter Systems. *WIREs Comput Mol Sci* **2014**, *4*, 15–25.

[41] Perdew, J. P.; Burke, K.; Ernzerhof, M. Generalized Gradient Approximation Made Simple. *Phys. Rev. Lett.* **1996**, *77*, 3865.

[42] Goedecker, S.; Teter, M.; Hutter, J. Separable Dual-Space Gaussian Pseudopotentials. *Phys. Rev. B* **1996**, *54*, 1703.

[43] Grimme, S.; Antony, J.; Ehrlich, S.; Krieg, H. A Consistent and Accurate ab initio Parametrization of Density Functional Dispersion Correction (DFT-D) for the 94 Elements H-Pu. *J. Chem. Phys.* **2010**, *132*, 154104.

[44] Manz, T. A.; Sholl, D. S. Chemically Meaningful Atomic Charges that Reproduce the Electrostatic Potential in Periodic and Nonperiodic Materials. *J. Chem. Theory Comput.* **2010**, *6*, 2455–2468.

[45] Manz, T. A.; Sholl, D. S. Improved Atoms-in-molecule Charge Partitioning Functional for Simultaneously Reproducing the Electrostatic Potential and Chemical States in Periodic and Nonperiodic Materials. *J. Chem. Theory Comput.* **2012**, *8*, 2844–2867.

[46] Plimpton, S. Fast parallel algorithms for short-range molecular dynamics. *J. Comput. Phys* **1995**, *117*, 1–19.

[47] Mayo, S. L.; Olafson, B. D.; Goddard, W. A. DREIDING: A Generic Force Field for Molecular Simulations. *J. Phys. Chem.* **1990**, *94*, 8897–8909.

[48] Darve, E.; Rodríguez-Gómez, D.; Pohorille, A. Adaptive biasing force method for scalar and vector free energy calculations. *J. Chem. Phys.* **2008**, *128*, 144120.

[49] Fiorin, G.; Klein, M.; Hénin, J. Using collective variables to drive molecular dynamics simulations. *Mol. Phys.* **2013**, doi: 10.1080/00268976.2013.813594.

[50] Barducci, A.; Bussi, G.; Parrinello, M. Well-tempered metadynamics: a smoothly converging and tunable free-energy method. *Phys. Rev. Lett.* **2008**, *100*, 020603.

[51] Tribello, G. A.; Bonomi, M.; Branduardi, D.; Camilloni, C.; Bussi, G. PLUMED 2: New feathers for an old bird. *Comput. Phys. Commun.* **2014**, *185*, 604–613.

[52] Korlepara, D. B.; Balasubramanian, S. Molecular modelling of supramolecular one dimensional polymers. *RSC Advances* **2018**, *8*, 22659–22669.

[53] DP_N, the scaled dipole moment, is the ratio of the electric dipole moment of a N-mer to the largest value of dipole moment observed in our calculations.

[54] The Binding energy of an oligomer of size (N) is defined as, $\text{B.E}_N = \frac{\text{E}_N - \text{N}\cdot\text{E}_1}{(N-1)}$.

[55] Urbanaviciute, I.; Meng, X.; Cornelissen, T. D.; Gorbunov, A. V.; Bhattacharjee, S.; Sijbesma, R. P.; Kemerink, M. Tuning the Ferroelectric Properties of Trialkylbenzene-1, 3, 5-tricarboxamide (BTA). *Adv. Electron. Mater.* **2017**, *3*, 1600530.

[56] Nosé, S. A unified formulation of the constant temperature molecular dynamics methods. *J. Chem. Phys.* **1984**, *81*, 511–519.

[57] Evans, D. J.; Holian, B. L. The nose–hoover thermostat. *J. Chem. Phys.* **1985**, *83*, 4069–4074.

[58] Swope, W. C.; Andersen, H. C.; Berens, P. H.; Wilson, K. R. A computer simulation method for the calculation of equilibrium constants for the formation of physical clusters of molecules: Application to small water clusters. *J. Chem. Phys.* **1982**, *76*, 637–649.

[59] Gilday, L. C.; Robinson, S. W.; Barendt, T. A.; Langton, M. J.; Mullaney, B. R.; Beer, P. D. Halogen bonding in supramolecular chemistry. *Chem. Rev.* **2015**, *115*, 7118–7195.

[60] Metrangolo, P.; Meyer, F.; Pilati, T.; Resnati, G.; Terraneo, G. Halogen bonding in supramolecular chemistry. *Angew. Chem. Int. Ed.* **2008**, *47*, 6114–6127.

[61] Xu, K.; Ho, D. M.; Pascal Jr, R. A. Azaaromatic chlorides: a prescription for crystal structures with extensive nitrogen-chlorine donor-acceptor interactions. *J. Am. Chem. Soc.* **1994**, *116*, 105–110.

[62] Müller, M.; Albrecht, M.; Gossen, V.; Peters, T.; Hoffmann, A.; Raabe, G.; Valkonen, A.; Rissanen, K. Anion–π Interactions in Salts with Polyhalide Anions: Trapping of I42-. *Chem.–Eur. J.* **2010**, *16*, 12446–12453.

[63] Henderson, W. R.; Zhu, Y.; Fagnani, D. E.; Liu, G.; Abboud, K. A.; Castellano, R. K. Self-Assembling [n.n] Paracyclophanes: A Structure–Property Relationship Study. *J. Org. Chem.* **2019**,

Chapter 3

Supramolecular Polymerization of N,N′,N″,N‴ -tetra-(tetradecyl)-1,3,6,8-pyrenetetracarboxamide: A Computational Study

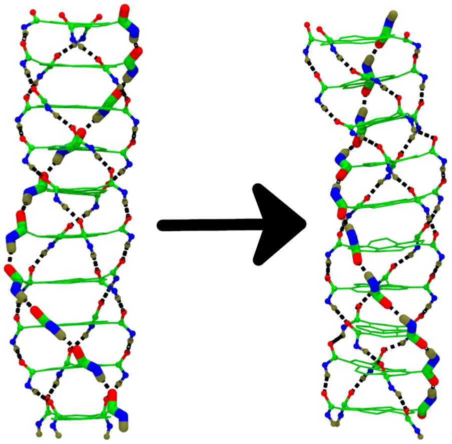

Reprinted with permission from "Supramolecular Polymerization of N,N′,N″,N‴ -tetra-(tetradecyl)-1,3,6,8-pyrenetetracarboxamide: A Computational Study" *J. Phys. Chem. B* **2017**, *121*, 11492-11503. © 2017, American Chemical Society. https://doi.org/10.1021/acs.jpcb.7b10171.

3.1 Introduction

Ferroelectrics have seen renewed interest in the recent past due to their increasing attractiveness as energy harvesting materials. [1] Although inorganic ferroelectrics continue to dominate the research landscape [2], lighter, lead-free and solution processable all-organic ferroelectrics too are being studied extensively. Working via non-covalent interactions, they can operate at room temperature and allow for wider choice of properties, given the enormous structural diversity offered by functional groups and self-assembly. [1] Significant number of molecules have been shown to form supramolecular polymers which exhibit ferroelectricity in the liquid crystalline phase. [3–5] Polarization in a supramolecular polymeric system is generated from either molecular dipoles or from intermolecular dipoles (say, the hydrogen bond). In the latter, its reversal upon the change in the direction of an applied electric field is due to the breaking and reformation of intermolecular hydrogen bonds.

Supramolecular polymers exhibit a wide range of application starting from electronics [6] to biology [7], as photoconductors, [8] capacitors, [9] molecular machines, [10, 11] non-volatile flash memory, [12] sensors, [13–15] secret documentation,[16] and biomedical applications. [17–20] A chief advantage of supramolecular polymers over covalent ones is their dynamic assembly and disassembly, which is important in processes such as mobility, and quick response to external stimuli [21, 22], dynamic exchange [23], changing environment [24, 25], drug delivery systems [26] and tunability. [27]

Among supramolecular polymers, monomers containing an amide group have been widely studied. [28–33] They possess an intrinsic ability to form intermolecular hydrogen bonds. [34, 35] One dimensional stacks constituted by such molecules exhibit large dipole moments, called a macrodipole. [36, 37] Recently, Akutagawa et al. reported the observation of ferroelectric behaviour in a supramolecular system of a pyrene derivative in its discotic hexagonal columnar liquid crystalline phase. [4] The molecule is shown in Figure 3.1**(a)**. In chapter 3 we examine the conformational and configurational landscape of the single molecule and its oligomeric forms. We also study its self-assembly in solution, the dipolar relaxation mechanism at equilibrium in its liquid crystalline (LC) phase and polarisation switching in the LC phase via an applied electric field using force field based molecular dynamics (MD) simulations. The results are contrasted against those obtained for the well-studied benzene-1,3,5-tricarboxamide supramolecular family.

3.2 Computational Details

Force field based MD simulations: Molecules of Pyrene derivative, N,N′,N″,N‴

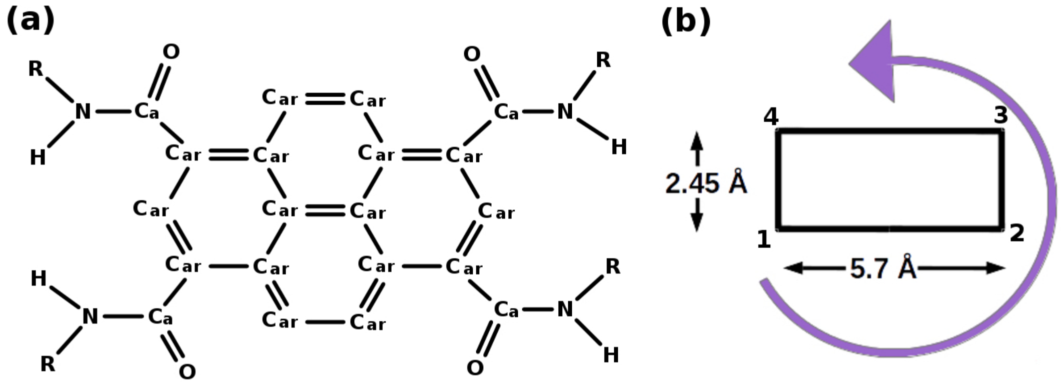

Figure 3.1: **(a)** Pyrene derivative, N,N′,N″,N‴ -tetra-(tetraalkyl)-1,3,6,8-pyrenetetracarboxamide 1: R = $-CH_3$ (MPCA) 2: R = $-(CH_2)_{13}CH_3$ (PCA), **(b)** Schematic representation of pyrene core and the amide dipoles situated at the vertices of the rectangle. The anti-clockwise arrow illustrates the indexing convention for the dipole orientational configuration. The first dipole in the four-letter scheme is located at the tail of the arrow.

-tetra-(tetradecyl)-1,3,6,8-pyrenetetracarboxamide (PCA) were modelled using the all-atom DREIDING force field [38]. Cyclohexane, considered as solvent, was modelled through the united-atom TraPPE [39] force field. Atom site charges on PCA were obtained via the DDEC/c3 method. [40, 41] The molecules were constructed using GaussView. [42] Simulations were performed using the LAMMPS package. [43] Temperature was maintained through the use of a Nóse-Hoover chain thermostat [44] with a coupling constant of 0.5 ps and the pressure was maintained through Nóse-Hoover barostat. [45]

Three-dimensional periodic boundary conditions were applied. Non-bonded interactions were truncated at 12 Å. Long range corrections to energy and pressure were applied. Full scaling of 1-4 interactions was employed for the PCA molecule. Long-range Coulombic interactions were treated using the particle-particle particle-mesh (PPPM) method with an accuracy of 0.00001. [46] The cross interactions between solute and solvent molecules were taken care through DREIDING mixing rules. The positions and velocities at each time step were updated by using velocity Verlet integration scheme with a time step of 0.5 fs. The coordinates of atoms were stored for post-processing at every 2.5 ps and the trajectory was visualized using VMD. [47] All gas phase quantum calculations of Pyrene derivative were carried out using GAUSSIAN-09 [48] with R=Me, which we denote as MPCA in this chapter.

Charge Calculation: Site charges on PCA used in the force field based simulations were derived from gas phase quantum calculations. We describe the procedure for the same here. DFT based geometry optimisation of a monomer of pyrene derivative in gas phase was performed using the QUICKSTEP module in CP2K software [49]. All valence electrons were treated in a mixed basis set with energy of cut off of 280 Ry. The short-range version of the double ζ single polarisation basis set was used. The effect of core electrons was considered through pseudopotentials of Goedecker-Tetter-Hutter (GTH) [50]. The Perdew-Burke-Ernzerhof (PBE) [51] exchange and correlation functional was employed. van der Waals interactions have been taken care through empirical DFT-D3 [52] corrections. The valence electron density of the optimised structure was used as an input to the DDEC/c3 code [40, 41] to derive the atomic charges on atoms of molecules shown in Figure 3.1(**a**).

3.3 Results and Discussion

3.3.1 Monomer configurations

While the amide group (NHCO) itself is planar, its relative orientation with respect to the aromatic pyrene core is dependent on dipole-dipole interactions between the amides in a molecule. In the following discussion, we define the amide dipole as the vector joining the amide oxygen to the amide hydrogen. The orientation of dipoles with respect to the π-plane of the molecule makes the structure either planar or non-planar. A monomer wherein the amide dipoles are in the same plane as the aromatic π-plane was considered as the initial structure (see Figure 3.2(**a**)) for gas phase DFT calculations performed at M06-2x/6-311+g(d,p) level of theory. Post geometry optimisation, the amide dipoles are oriented out of the π-plane of the pyrene, resulting in a non-planar monomer is shown in Figure 3.2(**b**).

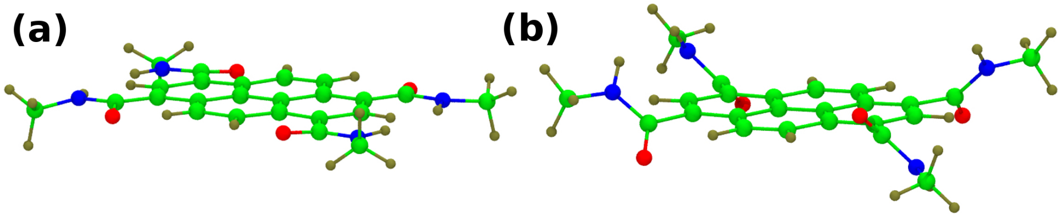

Figure 3.2: Structure of MPCA monomer optimised at M06-2x/6-311+d(g,p) level of theory. **(a)** Before optimisation and **(b)** After optimisation. Colour Scheme: Green-Carbon, Blue-Nitrogen, Red-oxygen and Tan-Hydrogen.

By varying the orientations of the four amide dipoles in a molecule with respect to the pyrene plane, different monomer configurations can be attained, as shown in Figure 3.1(**b**). Their energetics are discussed below. The core of the monomer is represented by a rectangular block and the dipoles are located at its vertices. The long and short edges of the core are 5.7 Å and 2.45 Å respectively. The energies of all optimised configurations shown in Figure 3.3, are presented in Table 3.1.

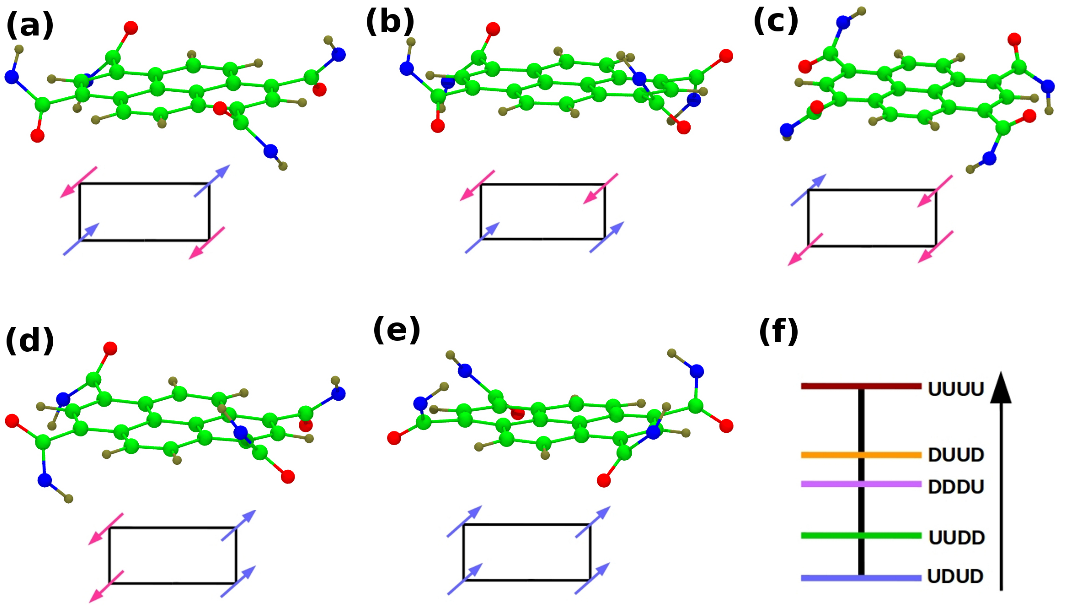

Figure 3.3: Structures of monomer of MPCA molecule optimised at M06-2x/6-311+g(d,p) level of theory. Methyl tail is not shown for clarity. **(a)** UDUD **(b)** UUDD **(c)** DDDU **(d)** DUUD **(e)** UUUU Colour scheme: Same as in Figure 3.2. **(f)** Energy level diagram.

Table 3.1: Energies of MPCA monomer optimised in gas phase using quantum chemical calculations for all amide configurations at M06-2x/6-311+g(d,p) level of theory. (see Figure 3.3).

Configurations	**Energy (kcal/mol)**	**Dipole moment (Debye)**
UDUD	0.00	0.27
UUDD	0.51	0.00
DDDU	1.11	4.75
DUUD	1.48	0.00
UUUU	2.31	9.61

3.3.2 Oligomers: Quantum calculations

Molecules of MPCA can oligomerise in a facile manner through intermolecular hydrogen bonds between amide groups. The relative stability of the UDUD configuration over other dipole configurations increases upon oligomerisation. Dimer configurations of MPCA are displayed in Figure 3.4 and their energy differences are tabulated in Table 3.2. Molecules in a MPCA dimer do not exhibit any lateral slip, similar to the case of BTA [53]. The angle between the vectors $\vec{\mathrm{A}}$ and $\vec{\mathrm{B}}$ (see Figure 3.4**(g)** and **(h)**) is defined as the twist angle. The mean slip distance and twist angle of short MPCA oligomers in ground state are tabulated in Table 3.2. An oligomer of MPCA consists of four hydrogen bonded helices whose pitch distance, assuming a twist angle of around 44° and a mean π-π distance of 3.4 Å will be around 28 Å.

Table 3.2: Energies of MPCA oligomers for all configurations, relative to that of the UDUD configuration. Slip distance and twist angle for ground state. Data is from DFT calculations at M06-2x/6-311+g(d,p) level of theory.

Energy difference (kcal/mol)	**n=2**	**n=3**
$(\mathrm{UUDD})_n$-$(\mathrm{UDUD})_n$	7.00	12.71
$(\mathrm{DDDU})_n$-$(\mathrm{UDUD})_n$	12.96	22.10
$(\mathrm{DUUD})_n$-$(\mathrm{UDUD})_n$	10.55	16.84
$(\mathrm{UUUU})_n$-$(\mathrm{UDUD})_n$	13.62	25.11
Slip distance (Å)	**n=2**	**n=3**
$(\mathrm{UDUD})_n$	0.06	0.06
Twist angle (°)	**n=2**	**n=3**
$(\mathrm{UDUD})_n$	44.20	43.95

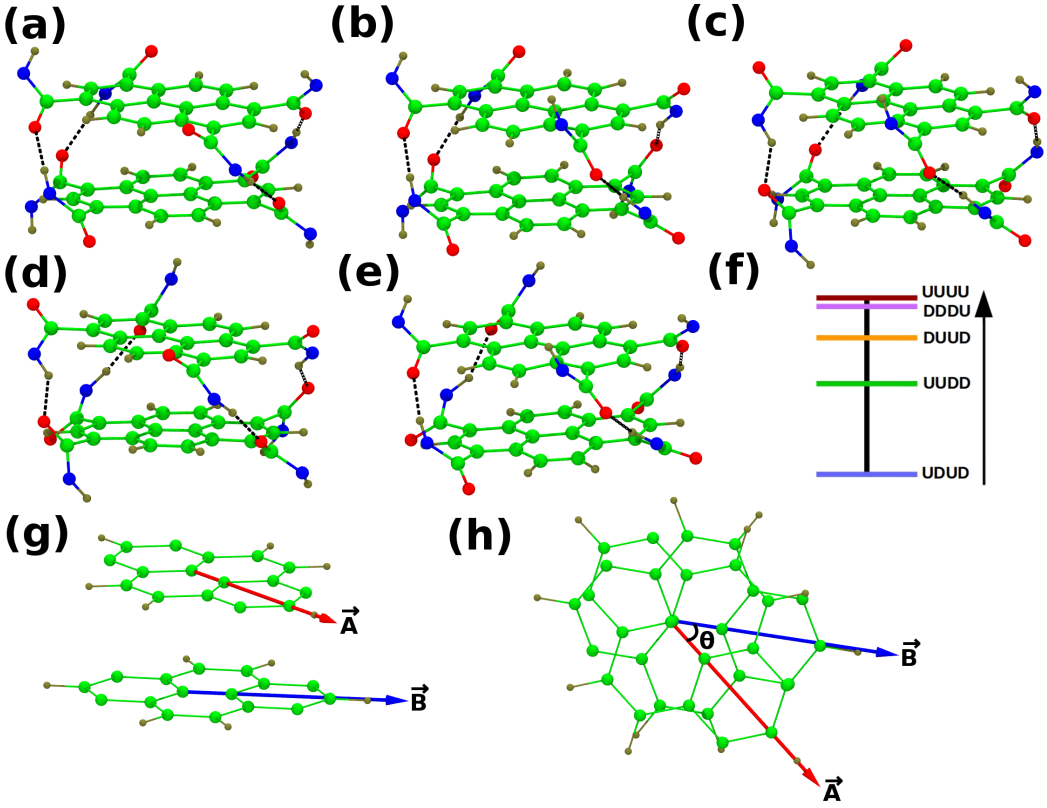

Figure 3.4: Structures of MPCA dimer optimised at M06-2x/6-311+g(d,p) level of theory. **(a)** UDUD **(b)** UUDD **(c)** DUUD **(d)** DDDU **(e)** UUUU. and **(f)** Energy level diagram. **(g)**,**(h)** Definition of the twist angle between consecutive molecules in an oligomer.

The dipole moments and π stacking distances of short oligomers of MPCA are displayed in Table 3.3. The dipole moment and π-π stacking distance of a tetramer in its ground state were calculated to be 0.098 Debye and 3.38 Å. The optimised geometries

Table 3.3: Mean π-π distance and Dipole moment for oligomers of MPCA in all configurations, optimised at M06-2x/6-311+g(d,p) level of theory.

Configurations	**Dimer**	**Trimer**
π-π distance (Å)		
UDUD	3.37	3.38
UUDD	3.42	3.44
DDDU	3.43	3.42
DUUD	3.52	3.41
UUUU	3.40	3.40
Dipole moment (Debye)		
UDUD	0.004	0.002
UUDD	12.92	17.49
DDDU	13.92	20.87
DUUD	11.17	16.18
UUUU	20.00	33.35

of a trimer are shown in Figure 3.5.

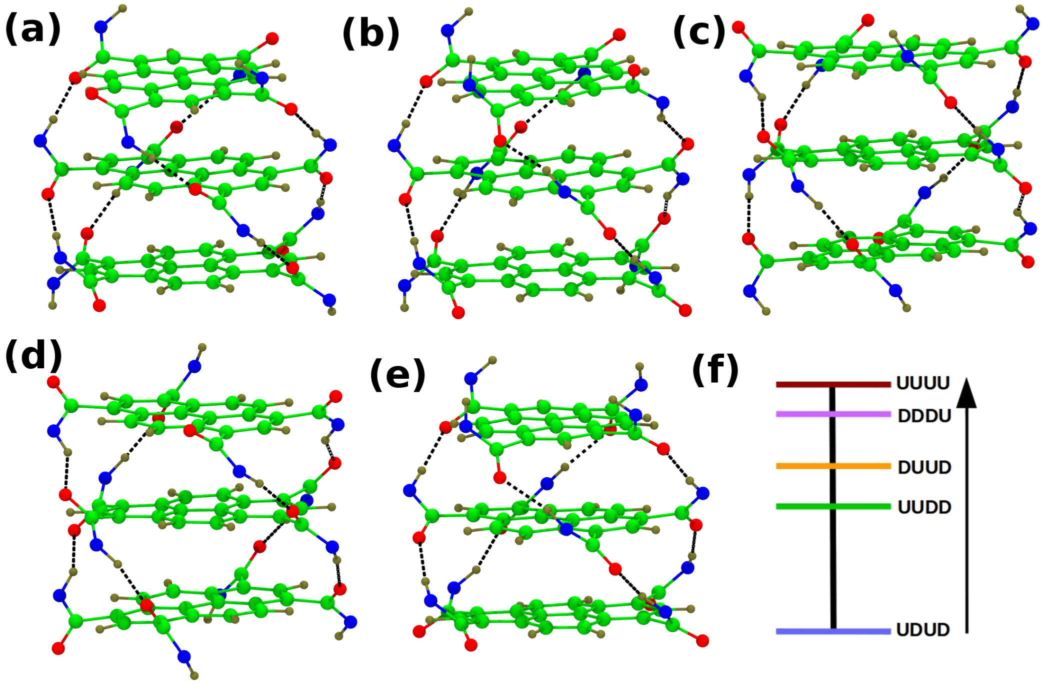

Figure 3.5: Optimised structures of a trimer of molecule MPCA at M06-2x/6-311+g(d,p) level of theory. **(a)** UDUD **(b)** UUDD **(c)** DDDU **(d)** DUUD **(e)** UUUU. Colour scheme: Green-Carbon, Blue-Nitrogen, Red-Oxygen and Tan-Hydrogen. Methyl groups are not shown for clarity. **(f)** Energy level diagram.

The dipole moment of the ground state oligomer (i.e., UDUD) is almost negligible and does not change significantly with oligomer size, unlike the case of BTA which displays a macrodipole moment that increases with oligomer size. Thus, the presence of intermolecular hydrogen bonding along the stacking direction alone does not guarantee a macrodipole moment which grows with oligomer size. The fact that the MPCA oligomer neither possesses a macrodipole nor one which increases with oligomer size suggests an isodesmic pathway of self-assembly of these monomers in solution [54, 55]. However, to our knowledge, there is no experimental report on the mechanism of its self-assembly to validate this speculation. The dipole moments of the excited state configurations ($(\mathrm{UUDD})_n$ etc.) are significantly large and grow with oligomer size. The lack of a dipole moment in the ground state oligomer and a large one in the excited state configurations can pose an interesting scenario for self-assembly in solution. Oligomers of the latter can exhibit attractive long-range dipole-dipole interactions, while those of the ground state do not. The same can result in formation of large oligomers in metastable states which will need pathways to reconfigure their dipoles to the ground state configuration.

3.3.3 Comparison between force field and quantum approaches

The characteristics of PCA in bulk can be studied only via force field based approaches, as fully quantum simulations are computationally challenging. Thus, the performance of the former has to be benchmarked against gas phase quantum chemical calculations of small oligomers presented above. Gas phase geometry optimizations of a dimer of MPCA were performed using the force field. Relative energies and dipole moment of monomer configurations obtained from the force-field are compared against quantum chemical data in Table 3.4. The ordering of energies of the different dipole configurations in the force field calculations reproduce the quantum results.

Energy differences, dipole moment, and π-π distances of oligomers are presented in Table 3.5. The dipole moment of the ground state dimer, i.e., $(\mathrm{UDUD})_2$ modelled with DDEC charges is much larger than the quantum result. In order to understand this difference, we also calculated the dipole moment of the quantum optimised dimer by assigning DDEC/c3 charges (i.e., coordinates of the quantum dimer and charges from DDEC/c3). This quantity denoted as Quantum D in Table 3.5, is quite comparable to the fully quantum data, implying that the DDEC charges are good and the differences arose from changes in the structures of the classical and quantum dimers. Thus, in the rest of the chapter, we shall discuss MD simulations using the DREIDING force field with atom charges derived from DDEC/c3.

3.3.4 Modelling stack stability in solution

A necessary but not a sufficient test of the applicability of a force field to model supramolecular assembly is the stability of a stack in solution, at finite temperatures. Herein, we describe results of the same.

Table 3.4: Comparison of dipole moment and energy difference obtained from force field and quantum chemical calculations for geometry optimised MPCA monomer. While the quantum calculations were performed at M06-2x/6-311g+(d,p) level of theory, the classical ones were done using DREIDING force field with DDEC/c3 charges.

Dipole moment (Debye)		
Configuration	**Quantum**	**Force field**
(UDUD)$_1$	0.274	0.209
(UUDD)$_1$	0.002	0.436
(DDDU)$_1$	4.747	6.442
(DUUD)$_1$	0.004	0.243
(UUUU)$_1$	9.610	6.442
ΔE = E$_*$-E$_{(\mathrm{UDUD})_1}$ **(kcal/mol)**		
*	**Quantum**	**Force field**
(UUDD)$_1$	0.51	0.61
(DDDU)$_1$	1.11	1.85
(DUUD)$_1$	1.48	2.54
(UUUU)$_1$	2.31	4.55

Table 3.5: Dipole moment and π-π distance for dimers of MPCA in all configurations, optimised at M06-2x/6-311+g(d,p) level of theory.

Dipole moment (Debye)			
Configuration	**Quantum**	**Quantum D**	**Force Field**
(UDUD)$_2$	0.0004	0.24	3.27
(UUDD)$_2$	12.92	14.47	6.18
(DDDU)$_2$	13.49	15.09	17.03
(DUUD)$_2$	11.17	13.84	9.13
(UUUU)$_2$	20.00	20.45	29.29
π-π **distance (Å)**			
Configuration	**Quantum**		**Force Field**
(UDUD)$_2$	3.37		3.73
(UUDD)$_2$	3.42		3.82
(DDDU)$_2$	3.43		3.77
(DUUD)$_2$	3.52		3.81
(UUUU)$_2$	3.40		3.84
ΔE = E$_*$-E$_{(\mathrm{UDUD})_2}$ **(kcal/mol)**			
*	**Quantum**		**Force Field**
(UUDD)$_2$	7.00		8.45
(DUUD)$_2$	12.96		22.96
(DDDU)$_2$	10.55		19.91
(UUUU)$_2$	13.62		27.54

An oligomer of size ten, in whose initial configuration the π-π distance and twist angle between adjacent π planes were set to 3.8 Å and 39° respectively was constructed

($R=(CH_2)_{13}CH_3$). All molecules in this stack were in UDUD configuration.

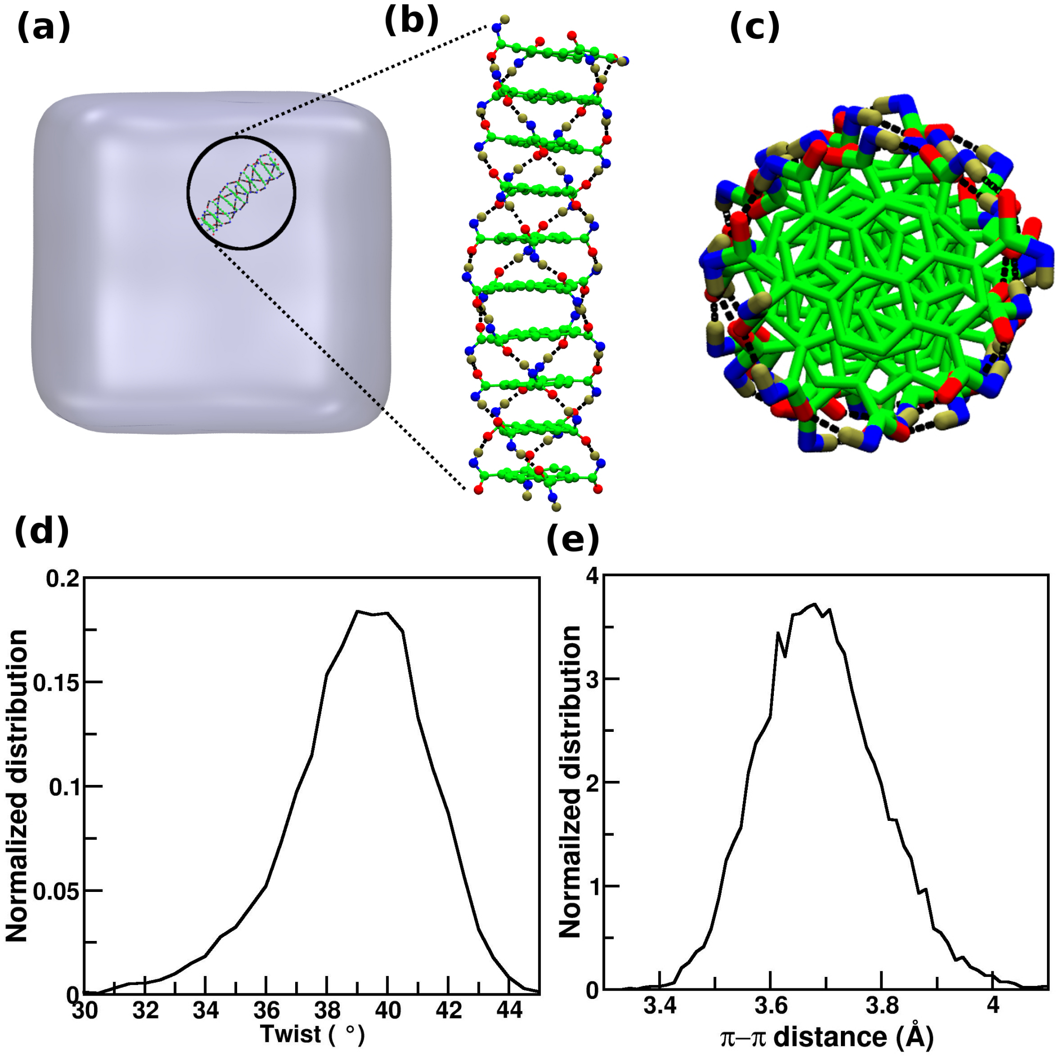

Figure 3.6: **(a)** Final snapshot from a MD simulation of a decamer of PCA at 298.15 K in cyclohexane. Colour scheme: same as Figure 3.2 and black colour lines represent hydrogen bonds. **(b)** side view and **(c)** top view of zoomed shot of the stack, alkyl tails are not shown for clarity. **(d)** Normalised distribution of twist angle. **(e)** Normalised distribution of π-π distance.

This preformed decamer was soaked in a cubic box of linear dimension 120 Å, consisting of 9623 cyclohexane molecules. Simulations were carried out at 298.15 K in the constant temperature and constant pressure ensemble with a coupling constant of 0.5 ps. The positions and velocities at each timestep were updated using the multiple timestep method, RESPA.[56] The outer time step was 1 fs, while all bond stretches were integrated with a time step of 0.5 fs. Simulations were performed for 15 ns and the coordinates were stored for every 5 ps for post processing. The last 10 ns trajectory is considered for analysing the results.

The stack and all the intermolecular hydrogen bonds were observed to be stable throughout the simulation. A final snapshot is shown in Figures 3.6**(a)**-**(c)**. The distribution of the angle of rotation between cores of adjacent molecules and π-π distances are presented in Figure 3.6**(d)**,**(e)** respectively. The mean values of these quantities were obtained as 3.7 Å and 38.75° respectively. The π-π distance obtained from simulations is close to the value of 3.65 Å reported in experiments [4]. The mean twist angle obtained from MD simulations is in reasonable agreement with the value of 44° obtained from gas phase quantum calculations of small oligomers (see Table 3.2).

3.3.5 Self-assembly of PCA in solution

A more robust test of the force field than stack stability is the observation of spontaneous assembly of monomers in solution to form a stack. Atomistic and coarse grained MD simulations have earlier been performed on a wide variety of molecules to understand the nature and mechanism of self-assembly[57, 58]. In pursuit of this aim, constant NPT, MD simulation at 290 K and at 1 atm, initiated from a configuration of 20 monomers dispersed randomly in a solution of cyclohexane, was carried out for a duration of 100 ns. The system contained 20 and 5568 numbers of solute and solvent molecules respectively. The mean box length was found to be 100 Å. In the initial configuration, generated using PACKMOL[59], all amide dipoles were coplanar with their respective pyrene cores. Atom coordinates were stored every 5 ps for post processing. In the initial phase of the trajectory, the monomers were present in all dipole configurations as shown in Figure 3.7**(b)**-**(f)**. This is to be expected, as the energy difference between them is of the order of $\mathrm{k_B T}$ and is thus thermally accessible. With time, few oligomers formed, and not all of them are of the $\mathrm{(UDUD)_n}$ (ground state) type, although the energy difference between the first excited state $\mathrm{(UUDD)_n}$ and the ground state is much larger than $\mathrm{k_B T}$. This is an indication of metastable configurations being accessed during MD simulation time scales. The free energy landscape of the dipole configurations, in solution and the paths which connect them and the respective barriers need to be estimated. This is an object of a future study. The number of molecules in the UDUD configuration increases with time, at the cost of other dipole configurations.

A final snapshot of the self-assembly simulation is shown in Figure 3.8. A pentamer formed within 100 ns. The progress of self-assembly, studied using cluster size and propensity of dipole configurations are presented in Figures 3.7**(a)**-**(f)** respectively.

3.3.6 Liquid Crystalline Phase

PCA exhibits a discotic hexagonal columnar liquid crystalline (LC) phase in the temperature range 295-480 K, [4] which is important in studies on ferroelectricity.

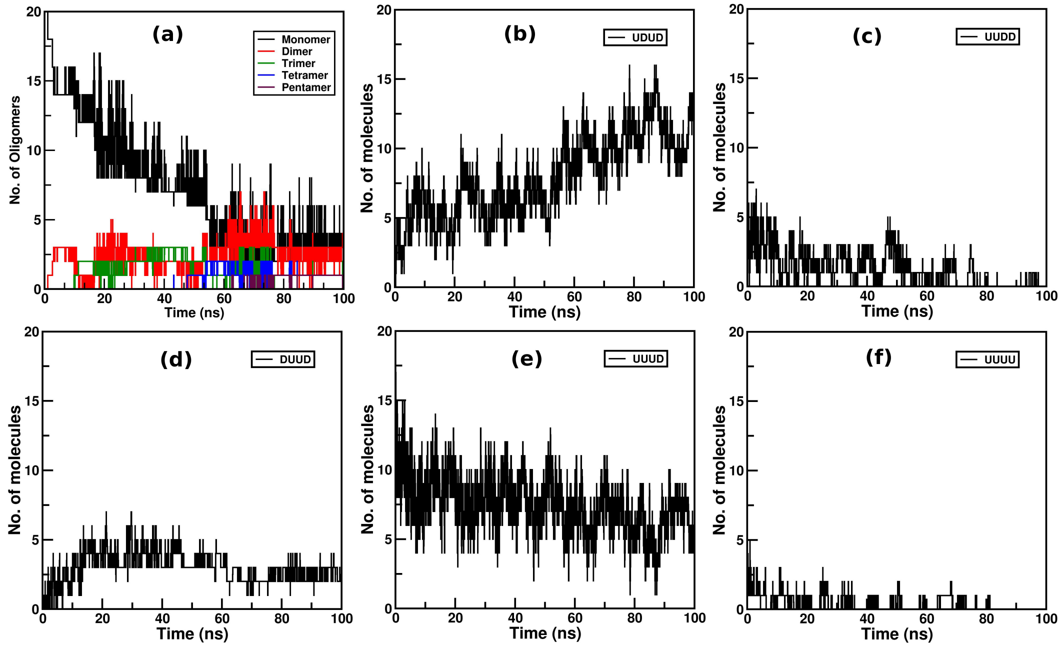

Figure 3.7: Self-assembly of 20 PCA molecules in cyclohexane solution at 298.15 K. **(a)** Number of short oligomers of various sizes over time. Number of molecules present in dipole configuration **(b)** UDUD, **(c)** UUDD, **(d)** DUUD, **(e)** UUUD, **(f)** UUUU.

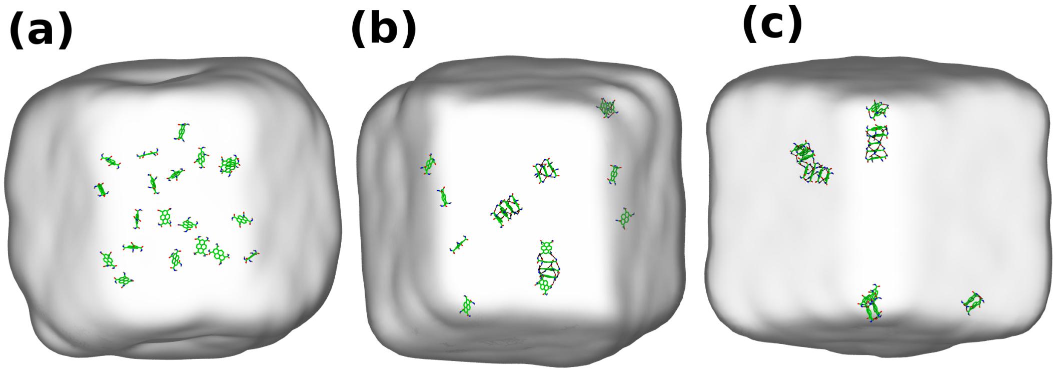

Figure 3.8: Progress of self-assembly of 20 PCA molecules in cyclohexane solution at 290 K **(a)** 0 ns, **(b)** 50 ns, **(c)** 100 ns. Solvent molecules are shown in Quicksurf representation. The C_{14} alkyl tail of PCA is not shown for clarity. The colour scheme is same as Figure 3.2.

Table 3.6: Simulation cell parameters for PCA in the liquid crystalline (LC) phase wherein the molecules are either in UDUD or UUUU configurations.

Configuration	**a (Å)**	**b (Å)**	**c (Å)**	α (°)	β (°)	γ (°)
UUUU	79.1389	80.5333	37.1229	90.0012	89.0949	119.784

For a typical ferroelectric experiment, PCA is deposited on a substrate in thin film form, [60] wherein the stacks of molecules lie with their long axes on the surface. In order to carry out the hysteresis experiments (polarisation switching), the stacks have

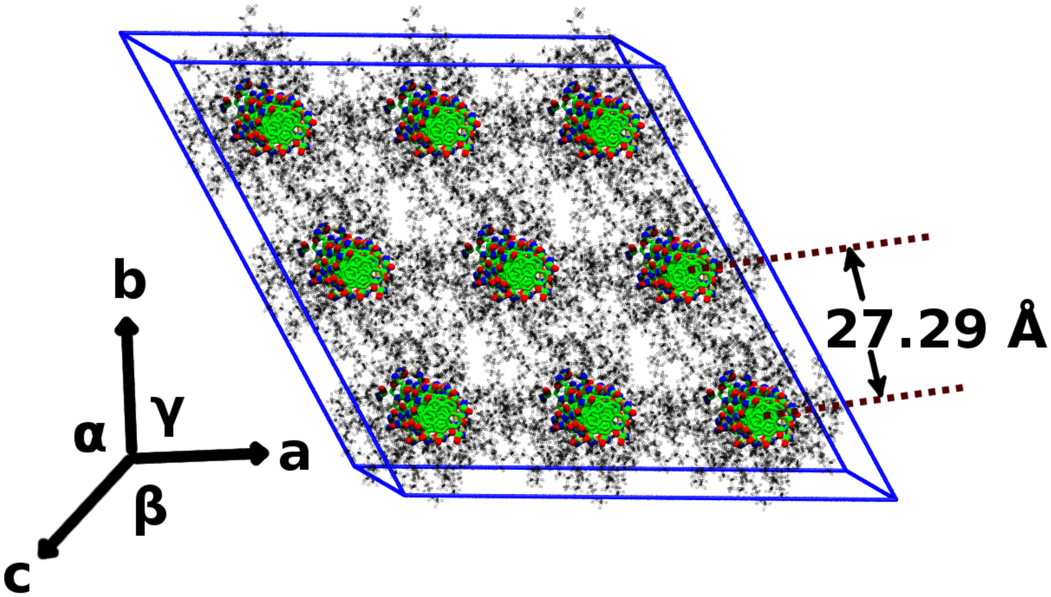

Figure 3.9: The initial structure of the PCA system in liquid crystalline (LC) phase. Molecules in UUUU configuration. Colour Scheme: Green-Carbon, Red-Oxygen, Blue-Nitrogen, Tan-Hydrogen. Alkyl tails are not shown for clarity. The inter stack distance is shown.

to be oriented in a direction perpendicular to the substrate plane. This is achieved by applying alternating electric fields at temperatures marginally above ambient and annealing the film, in cycles. [61] Despite the adoption of such a procedure, not all the stacks in a film will lie fully perpendicular to the substrate. While a majority of stacks will be oriented normal to the surface, there will always be some which are not and the quantum of latter can vary from one thin film sample to another. Thus, the value of remnant polarisation will vary across different samples of the same system. In addition, an experimental sample will also possess domains. The ferroelectric hysteresis loop observed in experiment [4] is obtained on such samples.

On the other hand, establishing an oriented thin film of stacks, although idealised, is relatively easy in simulations. Similar to our earlier studies on BTA [62], the initial configuration of PCA in the LC phase was constructed in either of UUUU and UDUD configurations in a rhombohedral simulation cell, which contained nine stacks. Each stack, oriented along the z-direction, consisted of ten PCA molecules. The initial structures are shown in Figure 3.9. As noted earlier, the UDUD configuration is the most stable one and hence it is natural to construct the thin film out of the same. However, upon application of the electric field, two of its dipoles in each molecule would flip to align themselves with the field, yielding a UUUU configuration for all the molecules. Simulations of the LC phase with an applied electric field were also carried out.

The MD simulations were performed at two temperatures – 393 K and 423 K in the constant temperature and constant pressure ensemble for 200 ns. As expected, at equilibrium (zero field), in the simulation initiated from UUUU stacks, the orientation of the dipoles changed over time. Molecules relaxed from UUUU configuration towards the more stable UDUD one. The flipping of molecular dipoles in a PCA stack takes place in a sequential manner, as depicted in Figure 3.10**(a)**,**(b)** and Figure 3.12 at 393 K and 423 K respectively. The generality of these observations made on PCA was tested against a well studied supramolecular polymer system, benzene-1,3,5-tricaboxamide (BTA) [63]. Zero-field MD simulations of the LC phase of BTA (with decyl tails) at 460 K temperature and 1 atm pressure, started from a configuration with 12 molecules in a stack, all in the 3:0 (or UUU) configuration [64], was also expected to exhibit a sequential flip of biggest amide dipoles to result in the more stable 2:1 state. Surprisingly, we observed the dipoles in the LC phase of BTA to flip in an arbitrary fashion, i.e., they were not a cascade of sequential flips as shown in Figure 3.10**(c)**,**(d)**.

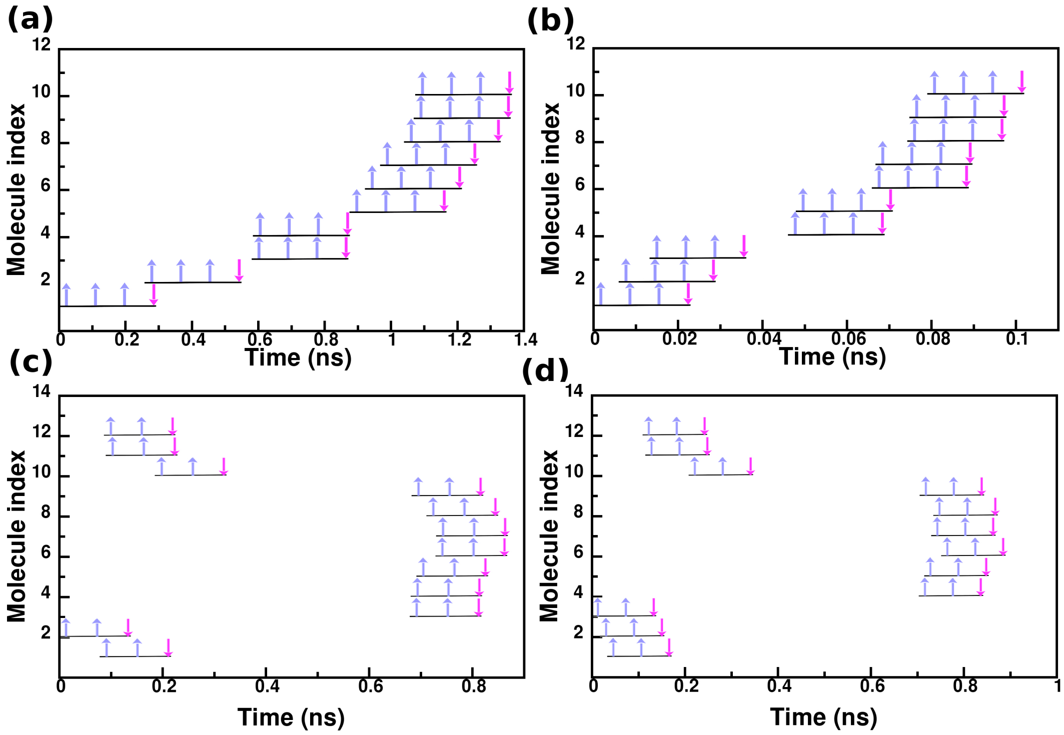

Figure 3.10: Sequential dipole flips at zero electric field in the liquid crystalline phase of PCA in a simulation at 393 K, initiated from the UUUU configuration. Results from two arbitrarily chosen stacks are shown. **(a)** Stack1 **(b)** Stack2. The time at which the first dipole flips is taken to be zero and its molecule index is taken to be one. Corresponding simulations of BTA in its LC phase at 460 K starting from the UUU configuration. **(c)** Stack1 **(d)** Stack2 for BTA.

In the figure, each dipole in a molecule is indicated by an arrow. In each graph, the time at which the first molecule in a stack flips to 'down' orientation is taken as zero.

The flip of one dipole results in a cascade of sequential dipole flips in a stack, caused due to the reformation of intermolecular amide-amide hydrogen bonds. The dihedral flipping was captured using the $\mathrm{C_{ar}}$-$\mathrm{C_{ar}}$-$\mathrm{C_a}$-O dihedral angle (see Figure 3.11(**a**) for definition). Its time evolution at 393 K is shown in Figure 3.13. A positive value of the angle represents the amide dipole orientation along the positive Z-direction and vice versa. Note that due to periodic boundary conditions, the i^{th} molecule in the stack is equivalent to $(i + 10)^{th}$ $((i + 12)^{th})$ molecule in the same stack of pyrene (BTA).

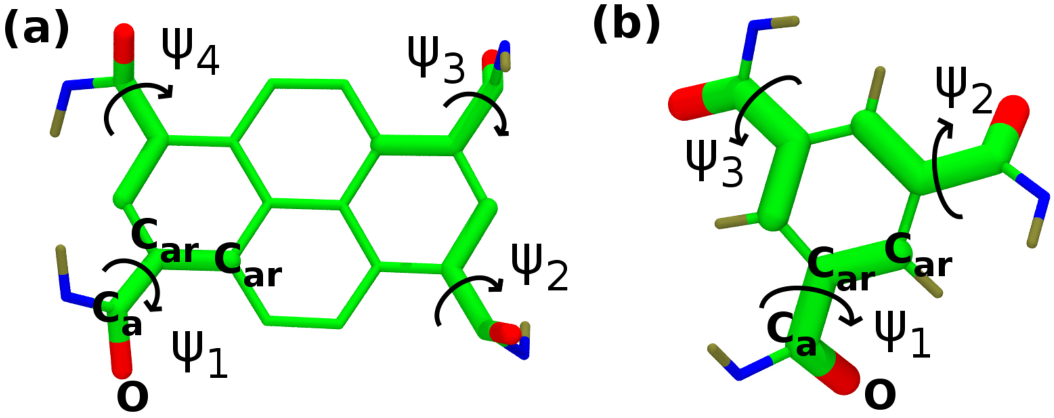

Figure 3.11: (**a**) MPCA, (**b**) BTA. Atoms which form the dihedral involved in the flip of the amide dipole are highlighted. Colour Scheme: Green-Carbon, Red-Oxygen, Blue-Nitrogen, Tan-Hydrogen. Alkyl tails are not shown for clarity.

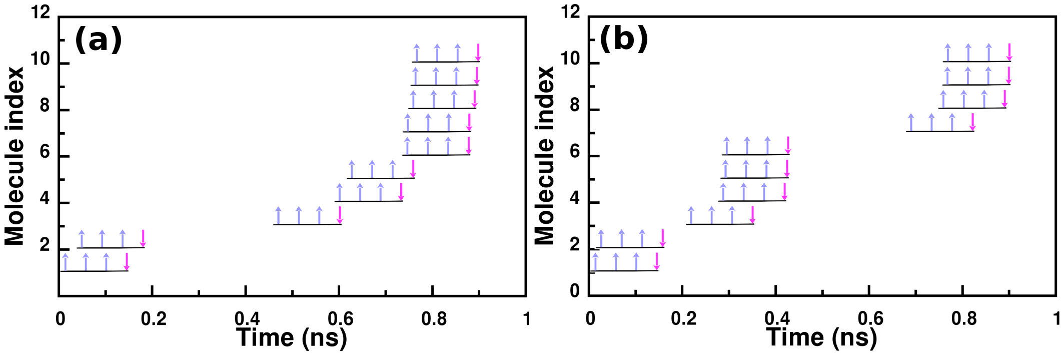

Figure 3.12: Sequential dipole flips at zero electric field in the LC phase of PCA initiated from UUUU configuration. (**a**) Stack1,(**b**) Stack2 at 423 K. The time at which the first dipole flips is taken to be zero.

The progress of dipole relaxation in the equilibrium simulations is illustrated in Figure 3.15 where an arbitrarily chosen stack in PCA is shown. The sequential flipping of amide dipoles along a PCA stack observed at zero field conditions changes its characteristic upon application of an electric field in a direction opposite to that of the amide dipole. In this case, while the amide dipoles indeed flip so as to align with the field, such flips in a stack are no longer sequential, but rather random, as

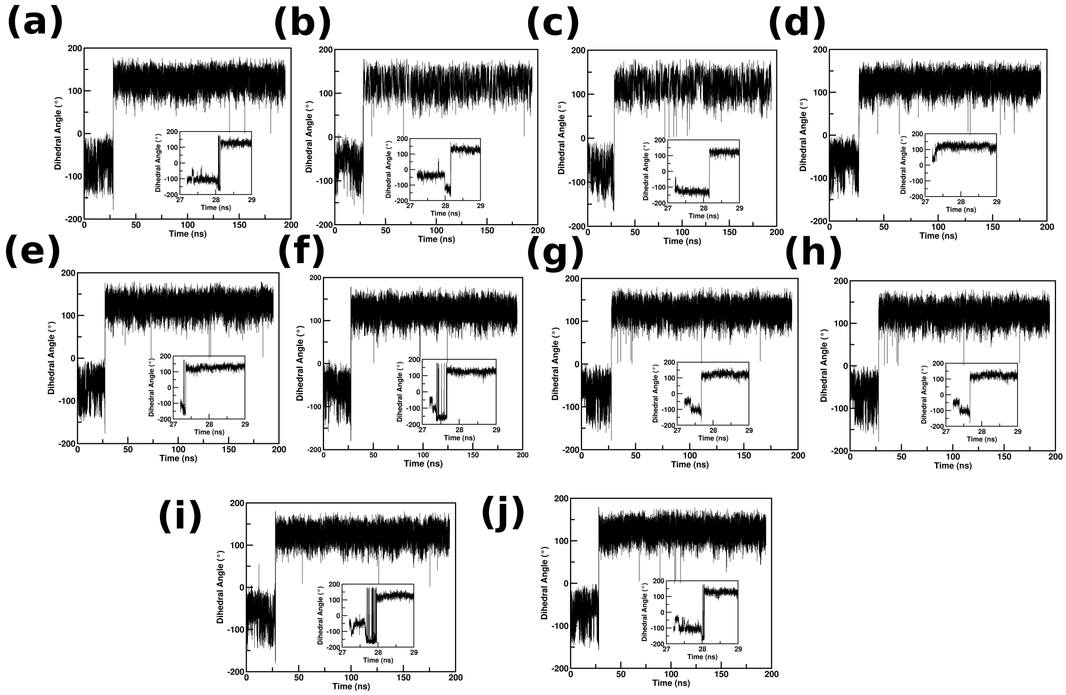

Figure 3.13: Dihedral angle ψ_1 (see Figure 3.11(**a**)) as a function of time for PCA in LC phase at 393 K at zero field. (**a**) Molecule 0, (**b**) Molecule 1, (**c**) Molecule 2, (**d**) Molecule 3, (**e**) Molecule 4, (**f**) Molecule 5, (**g**) Molecule 6, (**h**) Molecule 7, (**i**) Molecule 8, (**j**) Molecule 9 of stack 1. The abrupt change in the sign of the dihedral angle denotes a dipole flip and a consequent change in the molecular configuration from UUUU to UUUD.

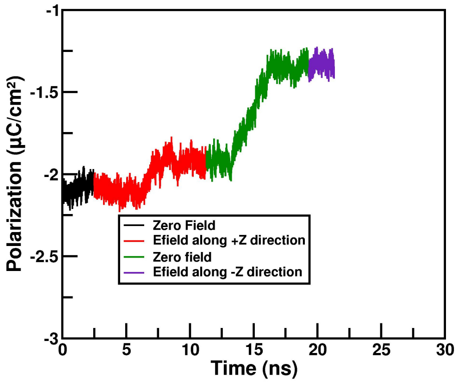

Figure 3.14: Polarization per molecule of the system in the LC phase starting with UUUU configuration as a function of time at 393 K. The simulation attempts to capture polarisation inversion upon reversal of the direction of the applied E-field.

seen in Figure 3.16(**a**),(**b**). Thus, while the formation of intermolecular amide-amide hydrogen bonding drives the sequential flip of amide dipoles in the absence of E-field, the necessity for the amide dipole to align with the field overrides the gain from such hydrogen bonding, in the presence of a field.

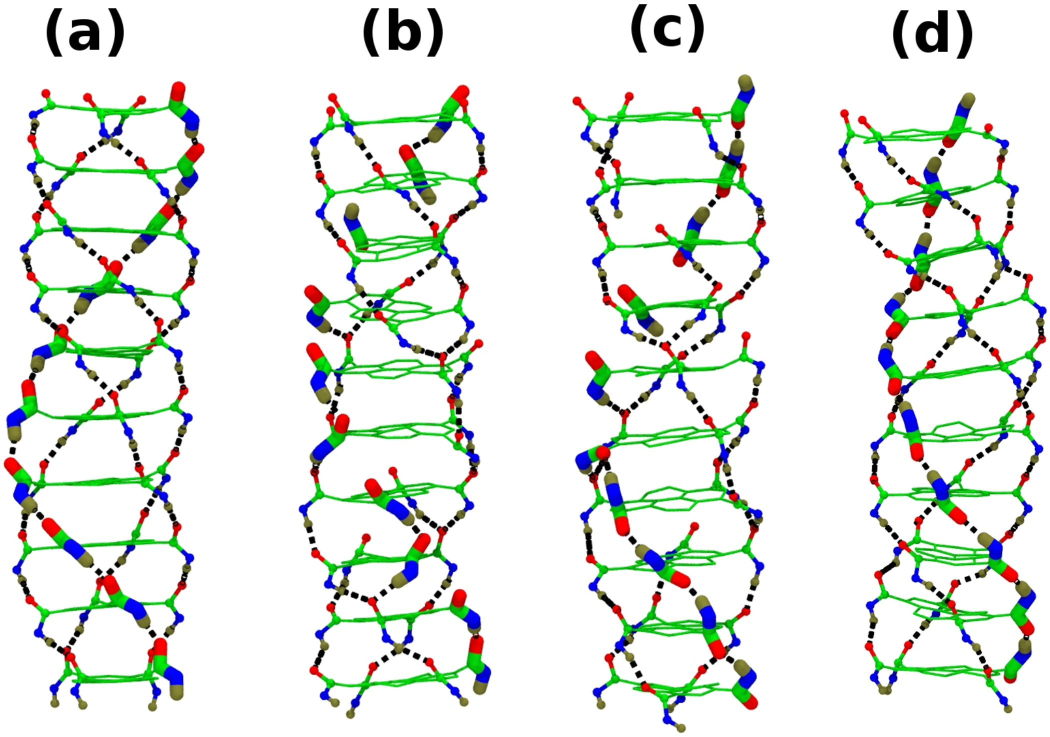

Figure 3.15: Snapshots of an arbitrarily chosen stack in the LC phase from equilibrium (zero-field) simulations. PCA at 393 K: **(a)** initial (0 ns), **(b)** & **(c)** intermediate (27 & 28 ns respectively) **(d)** final state (28.15 ns). Alkyl tails are not shown for clarity and the colour scheme is same as in Figure 3.2. Hydrogen bonds are shown in black color.

While the dipolar relaxation mechanism of BTA and PCA at equilibrium are different, the application of an E-field on BTA in a direction opposite to the amide dipoles resulted in a random flip of dipoles as shown in Figure 3.16**(c)**,**(d)**, consistent with the original observations on the pyrene system presented above (See Figure 3.16**(a)**,**(b)**).

We now examine the origin of the differences in the behaviour of dipole relaxation between PCA and BTA stacks at zero field. All the three hydrogen bond helices in the initial configuration of a BTA stack were left handed. Also, the dipoles in each molecule were in the 3:0 (or, in the language of this chapter, UUU) configuration. During the relaxation of the dipole to the more stable 2:1 (or UUD) state, the helical sense of the hydrogen bond chain of the stack changes to right handedness; however, soon enough the stack was seen to shuttle back to left-handed sense. The facile change in the handedness of the BTA stack at equilibrium along with the dipole configuration change (3:0 to 2:1) can be explained by the lower $\mathrm{C_{ar}}$-$\mathrm{C_{ar}}$-$\mathrm{C_a}$-O dihedral barrier in BTA than in PCA. Quantum DFT calculation at M06-2x/6-311+g(d,p) level of theory (relaxed scan) yields a value of around 1.0 kcal/mol for the dihedral barrier in BTA monomer. However, the same in the case of MPCA molecule is higher (3-4 kcal/mol) and thus its dipole flip, once occurred, is permanent. The same can be understood from

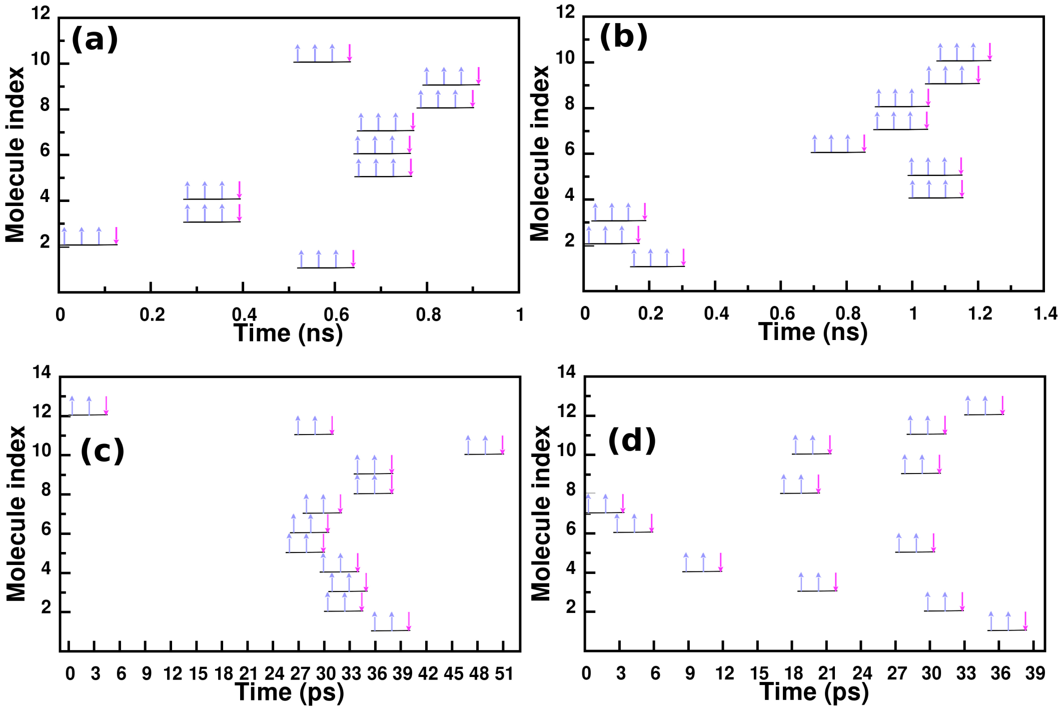

Figure 3.16: Non-sequential flipping of amide dipoles during simulations of PCA and BTA systems, initiated from the UUUU and symmetric (UUU) configurations in the LC phase. An external electric field is applied in a direction opposite to the amide dipoles. Events in two arbitrarily chosen stacks in each system are shown. **(a)**-**(b)**: Two stacks of PCA at 393 K. **(c)**-**(d)**: Two stacks of BTA at 460 K.

the potential energy surfaces for this dihedral angle in MPCA and BTA with methyl tail as shown in Figure 3.17. The geometry of the molecules at important angles are also depicted. In the case of PCA, all the molecules in the stack were in the UUUU configuration with four left handed hydrogen bonded helices. Although we could not observe the full relaxation of a stack to the more stable UDUD state due to the need for very long simulation trajectories, in the intermediate UUUD state, all the four h-bond helices continue to be left handed at zero field.

To summarise, at zero field, PCA stacks in UUUU configuration were observed to relax to a UUUD one and the process of dipole flip was sequential. However, BTA stacks in the UUU configuration relaxed to UUD one in a non-sequential manner. The reason for this difference lies in differences in the in-plane symmetry of arrangement of amide dipoles between PCA and BTA. The former has C_2 symmetry, while the latter is C_3 symmetric. When a dipole in BTA stack flips and intends to form a hydrogen bond with another molecule in the stack, it can easily form one by rotating the C_{ar}-C_{ar}-C_a-O dihedral towards either of its amide neighbours, which also reverses the handedness of the hydrogen bond chain. The same is not possible in the case of PCA, as one of the edges is quite long and the bond rotation towards this edge is sterically hindered

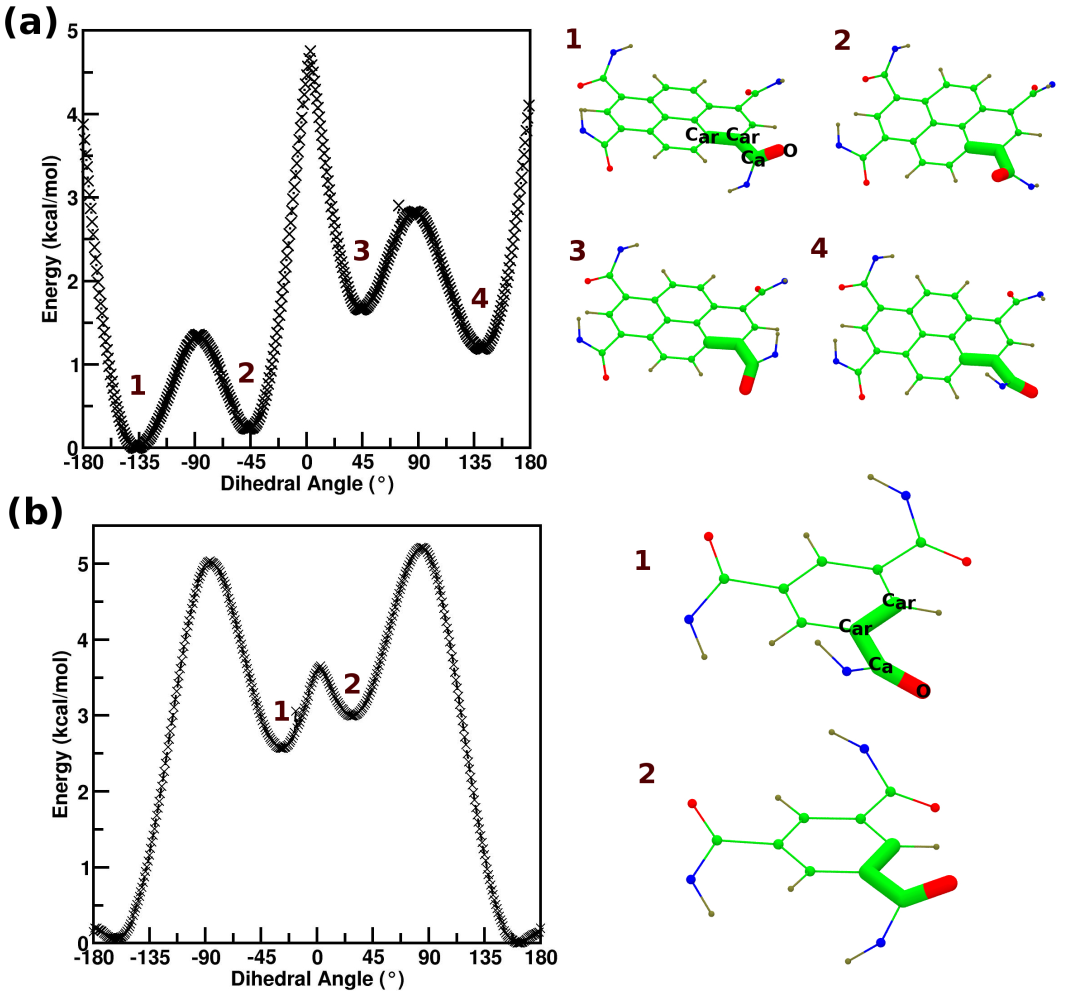

Figure 3.17: Potential energy surface (PES) of C_{ar}-C_{ar}-C_a-O dihedral angle, obtained from relaxed scan at M06-2x/6-311+g(d,p) level of theory, for **(a)** MPCA **(b)** BTA. The conformation of the molecules at important points on the PES are depicted on the right panels. Alkyl groups are not shown for clarity and the colour scheme is same as in Figure 3.2.

by a hydrogen attached to C_{ar}. Thus, only the bond rotation towards the short edge is possible. The same is observed in MD simulations of PCA and BTA stacks in their LC phases. Figure 3.18 exhibits the process of dipole relaxation in both these stacks, zooming in on a pair of molecules for better clarity. In PCA, as an intermediate state which is metastable, a bifurcated hydrogen bond is formed Figure 3.18**(b)**. A stable state is achieved via a dipole flip of the top molecule (see Figure 3.18**(c)**) Thus, the transformation of a PCA stack from UUUU to UUUD configuration at equilibrium is accompanied by sequential dipole flips, which is a consequence of the C_2 symmetry of the amide locations in the PCA molecule. In BTA, the dipole reversal happens non-sequentially, via reversal of the hydrogen bond sense, as seen from MD simulations of its LC phase shown in Figure 3.18**(d)**-**(f)**.

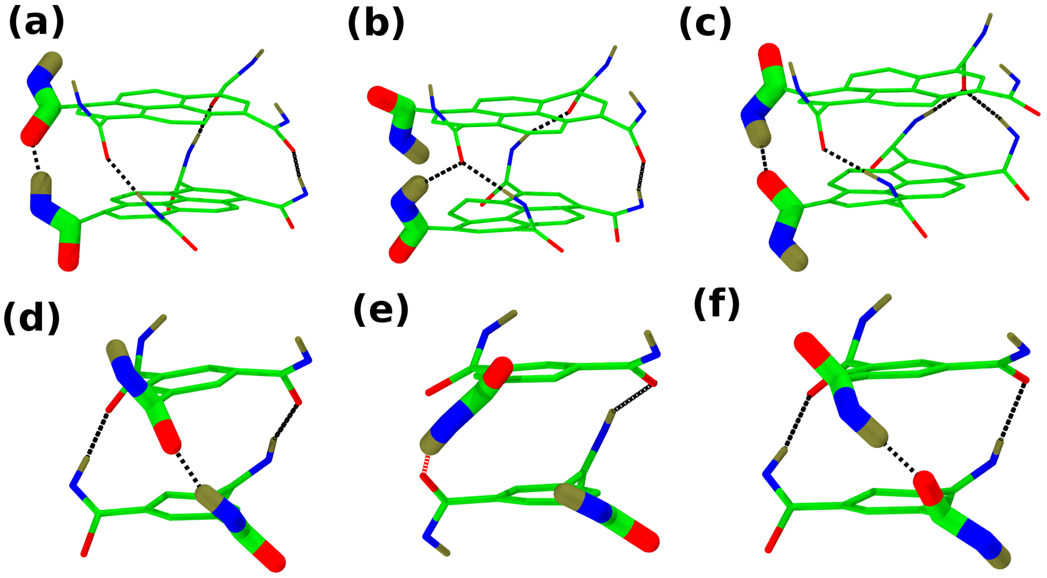

Figure 3.18: Results from equilibrium MD simulations of PCA (**a-c**) and BTA (**d- f**) stacks in their respective liquid crystalline phases. Only two molecules are shown fot clarity. Alkyl groups are not shown for clarity. The rotation of an amide group in the bottom molecule (highlighted with thicker bonds) causes a dipole flip in the molecule on the top as well. (**a**)-(**c**): Stages of dipole flip in PCA. (**d**)-(**f**): Stages of dipole flip in BTA. The dotted lines represents hydrogen bonds. Black (left handed) and red (right handed).

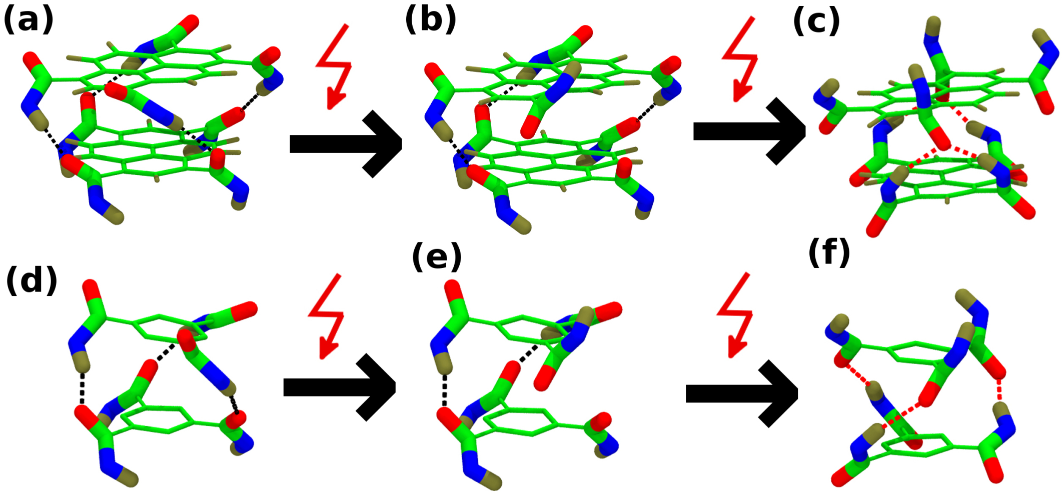

Figure 3.19: Schematic representation of the mechanism of handedness reversal in the LC phase upon application of electric field. (**a**)-(**c**) are for PCA while (**d**)-(**f**) are for BTA. (**a**) Starting geometry, (**b**) metastable, (**c**) final structure and (**d**) starting geometry, (**e**) metastable and (**f**) final structure. Black (left handed) and red (right handed) dotted lines are hydrogen bonds. Red arrow represents the E-field. While the helical sense of the hydrogen bonds in BTA are reversed, those in PCA do not exhibit a clear sense (handedness), post the reversal of the amide dipole vector.

In our earlier work [62], we showed that the process of polarisation switching in a BTA supramolecular stack upon reversal of the external E-field is associated with a reversal of handedness of the hydrogen bond helices which run along the stack. The same phenomenon is not observed in the PCA system, due to the fact that the amide groups in the latter are arranged in a C_2 symmetric fashion rather than with C_3 symmetry as in BTA. In the latter, neighbouring amide groups in a molecule are equidistant from a given amide, whereas in PCA, they are not. Moreover, the twist angle between the aromatic cores of adjacent molecules in a stack of BTA is 60^o, while it is 38^o in PCA. Thus, an amide group in BTA which has 'lost' its hydrogen bond (due to the E-field) can form another one with the amide of the neighbouring molecule in the opposite 'sense', in a rather facile manner. The same is not possible in the case of PCA (due to unequal amide-amide distances) and one ends up with bifurcated intermolecular hydrogen bonds as illustrated in Figure 3.19.

We followed the polarisation switching of PCA in its LC phase, mimicking the ferroelectric experiment. One half of the P-E (Polarization Vs. E-field) hysteresis loop was studied. Starting from the UUUU configuration in the LC phase at 393 K, we observed a polarisation of 1.9 μC/cm^2 at a field of 0.0004 V/Å. [65] Turning off the field resulted in a 'remnant' polarisation of 1.35 μC/cm^2. Upon reversal of the E-field, the polarisation did not get reversed completely within the time scale of our simulations and the same is shown in Figure. 3.14. The polarisation reversal is a result of rotation of the amide group. Intermolecular hydrogen bonds in the original configuration are broken and new ones are formed in this process.

3.4 Conclusions

Several characteristics of the supramolecular polymerization of a carboxamide functionalized pyrene core based molecule (PCA) have been determined using gas phase quantum chemical calculations and force field based molecular dynamics simulations. The molecule exhibits a rich configurational landscape, the richness arising from the varied relative orientations of dipoles of its four amide groups. The same is enhanced upon oligomerisation. While the UDUD configuration in which all the four inter-dipole interactions are optimal is the ground state of the single molecule, other dipole configurations are not much higher than $k_B T$, making them thermally accessible. The energy difference between the UDUD ground state and the first excited state increases with increasing oligomer size. Neither the UDUD monomer nor the oligomers exhibit a dipole moment, suggesting an isodesmic pathway for the self-assembly of this molecule in solution [36, 54].

PCA molecules self assemble in non-polar solvents via the formation of four intermolecular (amide-amide) hydrogen bonds. The one-dimensional stacks contain four hydrogen bond helices. Adjacent molecules in a PCA stack do not exhibit any lateral slip, just as in the well studied benzene-1,3,5-tricarboxamide system. Yet, the twist angles between molecules in both the systems are different, around 40^o in a PCA stack versus 60^o in the C_3 symmetric BTA system.

Force field based optimised geometries and energies of short oligomers were benchmarked against the quantum data and were found to fare rather well. MD simulations of a preformed PCA stack in solution showed that it was stable at ambient conditions. Simulations of self-assembly of molecules from a dispersed configuration were also performed and within the time scales accessible, short oligomers, primarily but not exclusively in the UDUD configuration were observed to form. The richness of the dipole configurational landscape and the diversity in the equilibrium population of monomers among such configurations makes the interplay of dipole interactions and self-assembly a challenging but interesting task, the characterisation of which we plan to undertake in the near future.

In the liquid crystalline phase of PCA, dipolar relaxation of molecules to the most stable UDUD state proceeds via a sequential mechanism of dipole flips – one molecule's amide dipole flips, followed by that of the adjacent one and so on. However, the same proceeds via a non-sequential fashion in the case of BTA stack, primarily due to the much smaller dihedral barrier for the C_{ar}-C_{ar}-C_{a}-O bond rotation than in the case of PCA. Yet, the presence of an external electric field makes the dipole flip to be non-sequential both in PCA as well as in BTA stacks in their respective LC phases.

A crucial difference in the behaviour of PCA and BTA stacks upon the application of an external field can be ascribed to differences in their molecular symmetry. When the E-field is applied in a direction opposite to the dipole moment vector of a hydrogen bond helix in a PCA or BTA stack, the amide dipole flips, the original intermolecular hydrogen bond is broken and a new one with another neighbour is formed. In the case of BTA, this process results in a reversal of handedness (helical sense), while in PCA, the process results in no preferred handedness. This difference too can be attributed to the easy access of the dihedral minimum with an opposite sense in the case of BTA and its absence in the case of PCA. The primary cause of this difference lies in the C_3 symmetry of the BTA molecule and the C_2 symmetry of the PCA molecule which result in different twist angles in their respective oligomers and consequent differences in hydrogen bond reformation ease.

While the electric field can in principle be employed for chiral enhancement [62], the current work points to the importance of molecular symmetry in determining if such enhancements are possible or not. In the case of C_2 symmetric PCA aromatic core, the enhancement is not possible. However, for a C_4 symmetric system, the process should be possible. We plan to investigate the crucial role of molecular symmetry on electric field induced changes in the helical sense of supramolecular stacks in the future.

Bibliography

[1] Tayi, A. S.; Kaeser, A.; Matsumoto, M.; Aida, T.; Stupp, S. I. Supramolecular Ferroelectrics. *Nat. Chem.* **2015**, *7*, 281–294.

[2] Patel, S.; Chauhan, A.; Vaish, R. Analysis of High-Field Energy Harvesting using Ferroelectric Materials. *Energy Technol.* **2014**, *2*, 480–485.

[3] García-Iglesias, M.; de Waal, B. F.; Gorbunov, A. V.; Palmans, A. R.; Kemerink, M.; Meijer, E. A Versatile Method for the Preparation of Ferroelectric Supramolecular Materials via Radical End-Functionalization of Vinylidene Fluoride Oligomers. *J. Am. Chem. Soc.* **2016**, *138*, 6217–6223.

[4] Anetai, H.; Wada, Y.; Takeda, T.; Hoshino, N.; Yamamoto, S.; Mitsuishi, M.; Takenobu, T.; Akutagawa, T. Fluorescent Ferroelectrics of Hydrogen-Bonded Pyrene Derivatives. *J. Phys. Chem. Lett.* **2015**, *6*, 1813–1818.

[5] Horiuchi, S.; Kumai, R.; Tokura, Y. Room-Temperature Ferroelectricity and Gigantic Dielectric Susceptibility on a Supramolecular Architecture of Phenazine and Deuterated Chloranilic Acid. *J. Am. Chem. Soc.* **2005**, *127*, 5010–5011.

[6] others,, et al. Towards Supramolecular Electronics. *Synth. Met.* **2004**, *147*, 43–48.

[7] Schemberg, J.; Schneider, K.; Demmer, U.; Warkentin, E.; Müller, A.; Ermler, U. Towards Biological Supramolecular Chemistry: A Variety of Pocket-Templated, Individual Metal Oxide Cluster Nucleations in the Cavity of a Mo/W-Storage Protein. *Angew. Chem. Int. Ed.* **2007**, *46*, 2408–2413.

[8] Borsenberger, P.; Chowdry, A.; Hoesterey, D.; Mey, W. An Aggregate Organic Photoconductor. II. Photoconduction Properties. *J. Appl. Phys.* **1978**, *49*, 5555–5564.

[9] Schierbaum, K.; Gerlach, A.; Haug, M.; Göpel, W. Selective Detection of Organic Molecules with Polymers and Supramolecular Compounds: Application of Capacitance, Quartz Microbalance and Calorimetric Transducers. *Sens. Actutors, A* **1992**, *31*, 130–137.

[10] Muraoka, T.; Kinbara, K. Development of Photoresponsive Supramolecular Machines Inspired by Biological Molecular Systems. *J. Photochem. Photobiol., C* **2012**, *13*, 136–147.

[11] others,, et al. Simple Mechanical Molecular and Supramolecular Machines: Photochemical and Electrochemical Control of Switching Processes. *Chem. Eur. J.* **1997**, *3*, 152–170.

[12] Xie, L.-H.; Ling, Q.-D.; Hou, X.-Y.; Huang, W. An Effective Friedel-Crafts Postfunctionalization of poly (N-vinylcarbazole) to Tune Carrier Transportation of Supramolecular Organic Semiconductors based on π-stacked Polymers for Nonvolatile Flash Memory Cell. *J. Am. Chem. Soc.* **2008**, *130*, 2120–2121.

[13] Mogera, U.; Gedda, M.; George, S. J.; Kulkarni, G. U. A Supramolecular Nanofibre Based Passive Memory Device for Remembering Past Humidity. *ACS Appl. Mater. Interfaces* **2017**,

[14] Gole, B.; Shanmugaraju, S.; Bar, A. K.; Mukherjee, P. S. Supramolecular Polymer for Explosives Sensing: Role of H-bonding in Enhancement of Sensitivity in the Solid State. *Chem. Commun.* **2011**, *47*, 10046–10048.

[15] Wang, K.; Yang, X.; Yang, R. Optical Chemical Sensors Based on Supramolecular Chemistry. *Sens. Actuators, B* **2000**, *66*, 263–265.

[16] Srinivasan, S.; Babu, P. A.; Mahesh, S.; Ajayaghosh, A. Reversible Self-Assembly of Entrapped Fluorescent Gelators in Polymerized Styrene Gel Matrix: Erasable Thermal Imaging via Recreation of Supramolecular Architectures. *J. Am. Chem. Soc.* **2009**, *131*, 15122–15123.

[17] Dong, R.; Zhou, Y.; Huang, X.; Zhu, X.; Lu, Y.; Shen, J. Functional Supramolecular Polymers for Biomedical Applications. *Adv. Mater.* **2015**, *27*, 498–526.

[18] Ma, X.; Zhao, Y. Biomedical Applications of Supramolecular Systems based on Host–Guest Interactions. *Chem. Rev.* **2014**, *115*, 7794–7839.

[19] Zhang, P.; Qian, X.; Zhang, Z.; Li, C.; Xie, C.; Wu, W.; Jiang, X. Supramolecular Amphiphilic Polymer-Based Micelles with Seven-Armed Polyoxazoline Coating for Drug Delivery. *ACS Appl. Mater. Interfaces* **2017**, *9*, 5768–5777.

[20] Bakker, M. H.; Lee, C. C.; Meijer, E.; Dankers, P. Y.; Albertazzi, L. Multicomponent Supramolecular Polymers as a Modular Platform for Intracellular Delivery. *ACS Nano* **2016**, *10*, 1845–1852.

[21] Kumar, M.; Brocorens, P.; Tonnelé, C.; Beljonne, D.; Surin, M.; George, S. J. A Dynamic Supramolecular Polymer with Stimuli-Responsive Handedness for in Situ Probing of Enzymatic ATP Hydrolysis. *Nat. Commun.* **2014**, *5*, 5793.

[22] Molla, M. R.; Rangadurai, P.; Pavan, G. M.; Thayumanavan, S. Experimental and Theoretical Investigations in Stimuli Responsive dendrimer-based Assemblies. *Nanoscale* **2015**, *7*, 3817–3837.

[23] Bochicchio, D.; Salvalaglio, M.; Pavan, G. M. Into the Dynamics of a Supramolecular Polymer at Submolecular Resolution. *Nat. Commun.* **2017**, *8*.

[24] Whitesides, G. M.; Boncheva, M. Beyond Molecules: Self-assembly of Mesoscopic and Macroscopic Components. *Proc. Natl. Acad. Sci.* **2002**, *99*, 4769–4774.

[25] Mes, T.; Smulders, M. M.; Palmans, A. R.; Meijer, E. Hydrogen-bond Engineering in Supramolecular Polymers: Polarity Influence on the Self-assembly of benzene-1, 3, 5-tricarboxamides. *Macromolecules* **2010**, *43*, 1981–1991.

[26] Kasimova, A. O.; Pavan, G. M.; Danani, A.; Mondon, K.; Cristiani, A.; Scapozza, L.; Gurny, R.; MoÌĹller, M. Validation of a Novel Molecular Dynamics Simulation Approach for Lipophilic Drug Incorporation into Polymer Micelles. *J. Phys. Chem. B* **2012**, *116*, 4338–4345.

[27] Petkau-Milroy, K.; Sonntag, M. H.; van Onzen, A. H.; Brunsveld, L. Supramolecular Polymers as Dynamic Multicomponent Cellular Uptake Carriers. *J. Am. Chem. Soc.* **2012**, *134*, 8086–8089.

[28] González-Rodríguez, D.; Schenning, A. P. Hydrogen-bonded Supramolecular π-functional Materials. *Chem. Mater.* **2010**, *23*, 310–325.

[29] Kang, J.; Miyajima, D.; Mori, T.; Inoue, Y.; Itoh, Y.; Aida, T. A Rational Strategy for the Realization of Chain-Growth Supramolecular Polymerization. *Science* **2015**, *347*, 646–651.

[30] Pal, D. S.; Kar, H.; Ghosh, S. Phototriggered Supramolecular Polymerization. *Chem. Eur. J.* **2016**, *22*, 16872–16877.

[31] others,, et al. Tuning The Nature and Stability of Self-Assemblies formed by ester benzene 1, 3, 5-tricarboxamides: The Crucial Role Played by the Substituents. *Soft Matter* **2016**, *12*, 7824–7838.

[32] Buendía, J.; Calbo, J.; García, F.; Aragó, J.; Viruela, P. M.; Ortí, E.; Sánchez, L. Helical Supramolecular Polymerization of C_3-Symmetric Amides and Retroamides: On the Origin of Cooperativity and Handedness. *Chem. Commun.* **2016**, *52*, 6907–6910.

[33] Yagai, S.; Monma, Y.; Kawauchi, N.; Karatsu, T.; Kitamura, A. Supramolecular Nanoribbons and Nanoropes Generated from Hydrogen-bonded Supramolecular Polymers Containing Perylene Bisimide Chromophores. *Org. Lett.* **2007**, *9*, 1137–1140.

[34] Nasyrov, D.; Vereshchagin, A. Polarity and Polarizability of the Amide Group. *Russ. Chem. Bull.* **1981**, *30*, 414–417.

[35] Fagnani, D. E.; Meese, M. J.; Abboud, K. A.; Castellano, R. K. Homochiral [2.2] Paracyclophane Self-Assembly Promoted by Transannular Hydrogen Bonding. *Angew. Chem. Int. Ed.* **2016**, *55*, 10726–10731.

[36] Kulkarni, C.; Balasubramanian, S.; George, S. J. What Molecular Features Govern the Mechanism of Supramolecular Polymerization? *ChemPhysChem* **2013**, *14*, 661–673.

[37] Filot, I. A.; Palmans, A. R.; Hilbers, P. A.; van Santen, R. A.; Pidko, E. A.; de Greef, T. F. Understanding Cooperativity in Hydrogen-bond-induced Supramolecular Polymerization: A Density Functional Theory Study. *J. Phys. Chem. B* **2010**, *114*, 13667–13674.

[38] Mayo, S. L.; Olafson, B. D.; Goddard, W. A. DREIDING: A Generic Force Field for Molecular Simulations. *J. Phys. Chem.* **1990**, *94*, 8897–8909.

[39] Keasler, S. J.; Charan, S. M.; Wick, C. D.; Economou, I. G.; Siepmann, J. I. Transferable Potentials for Phase Equilibria–United Atom Description of Five- and Six-Membered Cyclic Alkanes and Ethers. *J. Phys. Chem. B* **2012**, *116*, 11234–11246.

[40] Manz, T. A.; Sholl, D. S. Chemically Meaningful Atomic Charges that Reproduce the Electrostatic Potential in Periodic and Nonperiodic Materials. *J. Chem. Theory Comput.* **2010**, *6*, 2455–2468.

[41] Manz, T. A.; Sholl, D. S. Improved Atoms-in-molecule Charge Partitioning Functional for Simultaneously Reproducing the Electrostatic Potential and Chemical States in Periodic and Nonperiodic Materials. *J. Chem. Theory Comput.* **2012**, *8*, 2844–2867.

[42] Dennington, R.; Keith, T.; Millam, J.; Eppinnett, K.; Hovell, W. L.; Gilliland, R. GaussView. 2009.

[43] Plimpton, S. Fast Parallel Algorithms for Short-Range Molecular Dynamics. *J. Comput. Phys.* **1995**, *117*, 1–19.

[44] Martyna, G. J.; Klein, M. L.; Tuckerman, M. Nosé–Hoover chains: The Canonical Ensemble via Continuous Dynamics. *J. Chem. Phys.* **1992**, *97*, 2635–2643.

[45] Hoover, W. G. Constant-Pressure Equations of Motion. *Phys. Rev. A* **1986**, *34*, 2499.

[46] Hockney, R. W.; Eastwood, J. W. *Computer Simulation Using Particles*; CRC Press, 1988.

[47] Humphrey, W.; Dalke, A.; Schulten, K. VMD: Visual Molecular Dynamics. *J. Mol. Graph.* **1996**, *14*, 33–38.

[48] others,, et al. Gaussian 09, Revision D. 01. 2009.

[49] Hutter, J.; Iannuzzi, M.; Schiffmann, F.; VandeVondele, J. CP2K: Atomistic Simulations of Condensed Matter Systems. *WIREs Comput Mol Sci* **2014**, *4*, 15–25.

[50] Goedecker, S.; Teter, M.; Hutter, J. Separable Dual-Space Gaussian Pseudopotentials. *Phys. Rev. B* **1996**, *54*, 1703.

[51] Perdew, J. P.; Burke, K.; Ernzerhof, M. Generalized Gradient Approximation Made Simple. *Phys. Rev. Lett.* **1996**, *77*, 3865.

[52] Grimme, S.; Antony, J.; Ehrlich, S.; Krieg, H. A Consistent and Accurate ab initio Parametrization of Density Functional Dispersion Correction (DFT-D) for the 94 Elements H-Pu. *J. Chem. Phys.* **2010**, *132*, 154104.

[53] Kulkarni, C.; Reddy, S. K.; George, S. J.; Balasubramanian, S. Cooperativity in the Stacking of benzene-1, 3, 5-tricarboxamide: The Role of Dispersion. *Chem. Phys. Lett.* **2011**, *515*, 226–230.

[54] Kulkarni, C.; Bejagam, K. K.; Senanayak, S. P.; Narayan, K.; Balasubramanian, S.; George, S. J. Dipole-moment-driven Cooperative Supramolecular Polymerization. *J. Am. Chem. Soc.* **2015**, *137*, 3924–3932.

[55] Ikeda, T.; Iijima, T.; Sekiya, R.; Takahashi, O.; Haino, T. Cooperative Self-Assembly of Carbazole Derivatives Driven by Multiple Dipole–Dipole Interactions. *J. Org. Chem.* **2016**, *81*, 6832–6837.

[56] Tuckerman, M.; Berne, B. J.; Martyna, G. J. Reversible Multiple Time Scale Molecular Dynamics. *J. Chem. Phys.* **1992**, *97*, 1990–2001.

[57] Mahfud, R.; Lacks, D.; Ishida, H.; Qutubuddin, S. Molecular Dynamic Simulations of Self-Assembly of Amphiphilic Comb-like Anionic Polybenzoxazines. *Langmuir* **2014**, *30*, 11858–11865.

[58] Garzoni, M.; Baker, M. B.; Leenders, C. M.; Voets, I. K.; Albertazzi, L.; Palmans, A. R.; Meijer, E.; Pavan, G. M. Effect of H-bonding on Order Amplification in the growth of a Supramolecular Polymer in Water. *J. Am. Chem. Soc.* **2016**, *138*, 13985–13995.

[59] Martínez, L.; Andrade, R.; Birgin, E. G.; Martínez, J. M. PACKMOL: A Package for Building Initial Configurations for Molecular Dynamics Simulations. *J. Comput. Chem.* **2009**, *30*, 2157–2164.

[60] Shishido, Y.; Anetai, H.; Takeda, T.; Hoshino, N.; Noro, S.-i.; Nakamura, T.; Akutagawa, T. Molecular Assembly and Ferroelectric Response of benzenecarboxamides Bearing Multiple– CONHC14H29 Chains. *J. Phys. Chem. C* **2014**, *118*, 21204–21214.

[61] Urbanaviciute, I.; Meng, X.; Cornelissen, T. D.; Gorbunov, A. V.; Bhattacharjee, S.; Sijbesma, R. P.; Kemerink, M. Tuning the Ferroelectric Properties of Trialkylbenzene-1, 3, 5-tricarboxamide (BTA). *Adv. Electron. Mater.* **2017**,

[62] Bejagam, K. K.; Kulkarni, C.; George, S. J.; Balasubramanian, S. External Electric Field Reverses Helical Handedness of a Supramolecular Columnar Stack. *Chem. Commun.* **2015**, *51*, 16049–16052.

[63] Fitié, C. F.; Roelofs, W. C.; Magusin, P. C.; Wübbenhorst, M.; Kemerink, M.; Sijbesma, R. P. Polar Switching in trialkylbenzene-1, 3, 5-tricarboxamides. *J. Phys. Chem. B* **2012**, *116*, 3928–3937.

[64] Bejagam, K. K.; Fiorin, G.; Klein, M. L.; Balasubramanian, S. Supramolecular Polymerization of Benzene-1, 3, 5-tricarboxamide: A Molecular Dynamics Simulation Study. *J. Phys. Chem. B* **2014**, *118*, 5218–5228.

[65] The field value in simulations is around 100 times that applied experimentally. E-field values comparable to experiments would necessitate extremely long MD simulations.

Chapter 4

Dipolar Relaxation in Thin Films of Benzenecarboxamides

4.1 Introduction

Organic ferroelectric materials with large remnant polarisation and depolarisation times hold great promise for application as nonvolatile memory devices. [1, 2] Ferroelectric columnar liquid crystals (LCs) are one class of materials with switchable polarisation along the columns. In recent years, LC phases of supramolecular polymers have received attention due to their easy processability and tunable properties. [3] An external electric field switches the polarisation of such materials between two states with equal and opposite values +P_z and -P_z. These two states are global minima in the free-energy landscape of the ferroelectric phase. [4] The potential of ferroelectric materials for use in memory applications is realized through these bistable states.

Recent experiments have studied the ferroelectric response in N,N′,N″-tri(tetradecyl)-1,3,5-benzenetricarboxamide **(3BC)**, N,N′,N″,N‴,N⁗-penta(tetradecyl)benzenepentacarboxamide **(5BC)**. [5–7] Polar switching in these ferroelectric materials was realized through the rotation of the amide group dipole in response to the applied electric field. A recently discovered class of amide-based dipolar columnar discotic liquid crystals offers the intriguing opportunity to tune key ferroelectric parameters by side chain modification. [6] Shishido *et. al.,* synthesized derivatives of benzenecarboxamide (BC) bearing multiple $-CONHC_{14}H_{29}$ chains — N,N′-bis(tetradecyl)-1,4--benzenedicarboxamide **(2BC)**, N,N′,N″-tri(tetradecyl)-1,3,5-benzenetricarboxamide **(3BC)**, N,N′,N″,N‴-tetra(tetradecyl)-1,2,4,5-benzenetetracarboxamide **(4BC)**, N,N′,-N″,N‴,N⁗-penta(tetradecyl)benzenepentaca -rboxamide **(5BC)**, and N,N′,N″,N‴,-N⁗,N‴‴-hexa(tetradecyl)benzenehexacarboxamide **(6BC)**. They have studied these BCs both in solution, and liquid crystalline (LC) phases. The P-E hysteresis characteristics in the LC phase were measured and they found that 2BC, 3BC, and 5BC show ferroelectric behaviour while the other two compounds — 4BC and 6BC were paraelectric. [7]

In the present chapter, we examined all these variants of BCs both in solution phase. Dipole relaxation were studied in great detail in the case of 3BC and 5BC in their liquid crystalline phases. The chemical structure of the molecules are shown in Figure. 4.1. The homologues of the 3BC molecule with different alkyl chain lengths — hexyl **(3BC-C6)**, decyl **(3BC-C10)**, and tetradecyl **(3BC-C14)** were examined in liquid crystalline (LC) phase with an aim to identify molecular level reasons for differences in their dipole relaxation and thus the time scales for depolarisation in thin film samples. Methods to improve the retention times and remnant polarisation are suggested via computational studies of **(5BC-C14)** in its LC phase.

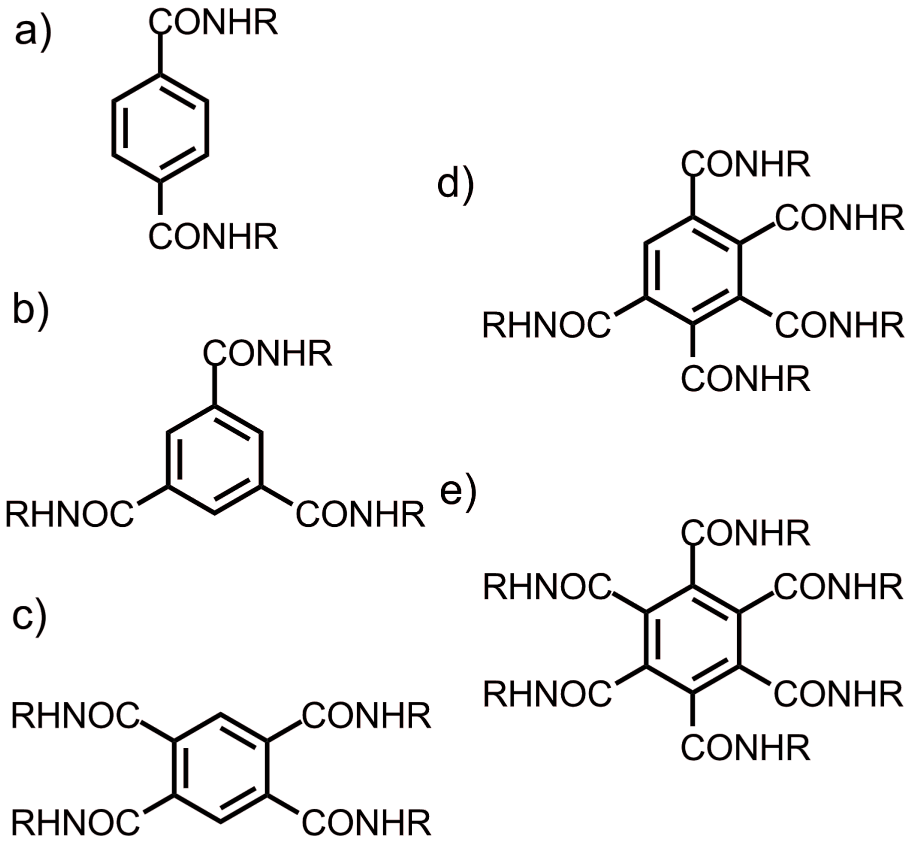

Figure 4.1: Chemical structure of molecules (a) N,N′-bis(tetradecyl)-1,4-benzenedicarboxamide (2BC), (b) N,N′,N″-tri(tetradecyl)-1,3,5-benzenetricarboxamide (3BC), (c) N,N′,N″,N‴-tetra(tetradecyl)-1,2,4,5-benzenetetracarboxamide (4BC), (d) N,N′,-N″,N‴,N⁗-penta(tetradecyl)benzenepentacarboxamide (5BC), (e) N,N′,N″,N‴,N⁗,-N′′′′′-hexa(tetradecyl)benzenehexacarboxamide (6BC)

4.2 Computational Details:

4.2.1 Charge Calculations:

The partial charges on the atoms of all the molecules used in force-field calculations were obtained, as before, from the quantum optimized structures using Density Derived Electrostatic and Chemical method (DDEC/c3). [8, 9] The molecules were placed in a cubic box of edge dimension 100 Å. Structures of the molecules were optimized using density functional theory (DFT) using the Quickstep method (QS) in CP2K software. [10] The Perdew-Burke-Ernzerhof (PBE) functional [11] with double ζ single polarisation basis set and an energy cutoff of 280 Ry was used. The Goedecker-Tetter-Hutter (GTH) [12] pseudopotentials described the interaction of the valence electrons with the nuclei and core electrons. Empirical DFT-D3 [13] corrections were used to include van der Waals interactions.

4.2.2 MD simulations:

Molecules were modelled in all-atom representation and the interaction potentials were taken from the DREIDING force field. [14]

$$
\begin{aligned}
E = \sum^{\text{bond}} K_r(r-r_o)^2 + \sum^{\text{angle}} K_\theta(\theta-\theta_0)^2 + \sum^{\text{dihedral}} K_\phi[1+dcos(n\phi)] \\
+ \sum^{\text{improper}} (1/2)K_\omega \left[\frac{1+cos(\omega_0)}{sin(\omega_0)}\right]^2 [cos(\omega)-cos(\omega_0)] + E_{nb}
\end{aligned}
\tag{4.1}
$$

$$
\begin{aligned}
E_{nb} &= E_{vdW} + E_Q + E_{hb} \\
\text{where,} \quad E_{vdW} &= Aexp(-Cr_{ij}) - \frac{B}{r_{ij}^6} \\
E_{hb} &= \begin{cases} L(r) & r < r_{in} \\ S(r) * LJ(r) & r_{in} < r < r_{out} \\ 0 & r > r_{out} \end{cases} \\
\text{Where,} \quad LJ(r) &= D_{hb}\left[5\left(\frac{R_{hb}}{R_{DA}}\right)^{12} - 6\left(\frac{R_{hb}}{R_{DA}}\right)^{10}\right] cos^4(\theta_{DHA}) \\
S(r) &= \frac{[r_{out}^2 - r^2]^2[r_{out}^2 + 2r^2 - 3r_{in}^2]}{[r_{out}^2 - r_{in}^2]^3} \\
E_Q &= \frac{q_i q_j}{4\pi\varepsilon_0 r_{ij}}
\end{aligned}
\tag{4.2}
$$

MD simulations were performed using the LAMMPS package. [15] Temperature was maintained through the use of a Nóse-Hoover chain thermostat [16] with a coupling constant of 0.5 ps and the pressure was maintained through Nóse-Hoover barostat. [17] Three-dimensional periodic boundary conditions were applied. Non-bonded interactions were truncated at 12 Å. Long range corrections to energy and pressure were applied. Full scaling of 1-4 interactions was employed. Long-range Coulombic interactions were treated using the particle-particle particle-mesh (PPPM) method with an accuracy of 0.00001. [18] The cross interactions between solute and solvent molecules were taken care through DREIDING mixing rules. The positions and velocities at each time step were updated by using velocity Verlet integration scheme with a time step of 0.5 fs. The coordinates of atoms were stored for post-processing at every 2.5 ps and the trajectory was visualized using VMD. [19]

4.3 Results and Discussions:

4.3.1 Solution Phase:

Decamers of all benzenecarboxamides (BCs) — (2BC, 3BC, 4BC, 5BC, 6BC) were constructed. These preformed structures were constructed from a monomer by rotating the amide group with respect to the plane of the central benzene core, so as to aid the formation of hydrogen bonds in the preformed stacks. However, the amide groups in the monomers of 4BC, 5BC and 6BC stay out-of-plane due to the steric hinderance. [7] The dipole of the amide group in BCs can orient in either up or down directions with respect to the phenyl core. To gain dipole-dipole interactions, we considered the initial structures of the molecules in such a manner that the neighbouring dipoles within a molecule orient in opposite directions. The alternative up, down arrangement of dipoles around the π-core has already been shown to be the ground state in several supramolecular monomers and was also discussed in Chapter 3. [20–23] These preformed decamers of BCs were soaked in a cubic box of linear dimension 50 Å, consisting of 940 carbon tetrachloride (CCl_4) molecules. The simulations were carried out at ambient conditions in the NPT ensemble, followed by 5 ns equilibration in NVT ensemble. Equilibrated trajectories were used to determine the twist angle, centroid-centroid distance between π cores of the neighbouring molecules, and their distributions are shown in Figure. 4.2, and the angle made by the amide group with the benzene core are tabulated in Table. 4.1.

Table 4.1: Geometry parameters of equilibrated structures of decamer

System	**centroid-centroid distance (Å)**	**Twist angle** (°)	**$C_{ar}-C_{ar}-C_a-O$ dihedral** (°)
2BC	3.68	54.0	42.0
3BC	3.64	56.0	42.0[a]
4BC	3.67	55.0	48.0
5BC	4.10	47.0	53.0
6BC	4.40	85.0	60.0

[a] The angle made by the amide bond with the central benzene core in 3BC as reported from experiments is 40°. [5]

In both 2BC and 3BC molecules, the amide groups have ample space to rotate, and equilibrated structures of these molecules' decamer show similar characteristics. Increasing the number of $-CONHC_{14}H_{25}$ chains attached to the phenyl core increases steric hindrance. In 4BC and 5BC, the amide groups have to make larger angles than

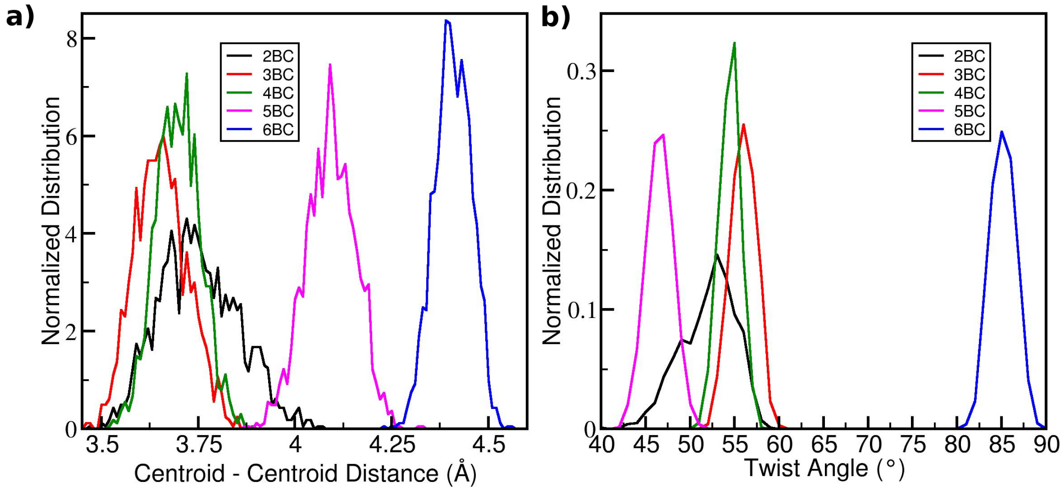

Figure 4.2: Results from MD simulations of preformed decamer of nBCs in solution at 298.15 K (a) Normalized distribution of centroid-centroid distance and (b) Normalized distribution of twist angle.

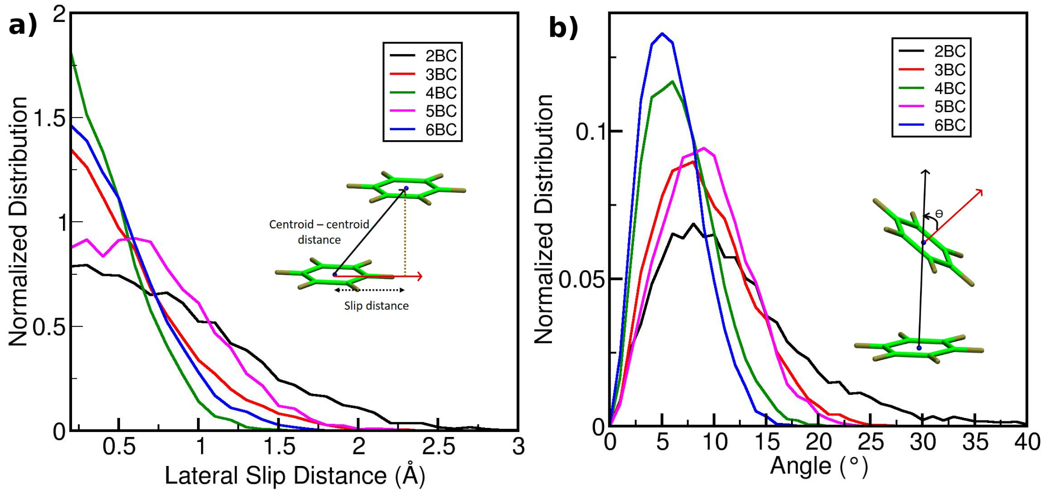

Figure 4.3: Probability density of (a) lateral displacement and (b) angle between the normals of phenyl cores of successive molecules in the stack. Results are obtained from MD simulations of preformed decamers of nBCs in solution at 298.15 K

in the 2BC and 3BC as can be seen from the values tabulated in Table. 4.1. The centroid-centroid distance increases with number of side chains attached to the phenyl core, which is in good agreement with experimental observations. [7]

In addition, the broad nature of the centroid-centroid distance distribution of the 2BC decamer is indicative of disorder in the stack. The disorder can be due to lateral slip and the splay angle (see schematic in Figure. 4.3b) between neighbouring molecules in the stack. Figure. 4.3a shows non-zero probability density at large slip distance and high splay angle for the 2BC stack, thereby confirming its loose packing relative to stacks of other compounds.

4.3.2 Liquid Crystalline (LC) Phase:

Table 4.2: Initial (at 50 K) and final (at 460 K) dimensions of the simulation box of nBC compounds in their LC phases, all the dipoles were oriented in the same direction with respect to the π plane in the initial configurations.

System	**Side chain length**	**a (Å)**	**b (Å)**	**c (Å)**	$\alpha(^\circ)$	$\beta(^\circ)$	$\gamma(^\circ)$
Initial Cell Parameters							
3BC	6	67.50	67.50	43.00	90	90	120
	10	90.00	90.00	43.00	90	90	120
	14	97.50	97.50	43.00	90	90	120
5BC	14	129.00	129.00	53.20	90	90	120
Final Cell Parameters							
3BC	6	51.06	45.07	42.96	90	90	102.00
	10	61.93	61.32	42.78	90	90	58.00
	14	66.44	70.48	42.82	90	90	63.96
5BC	14	75.69	74.71	65.05	90	90	102.00

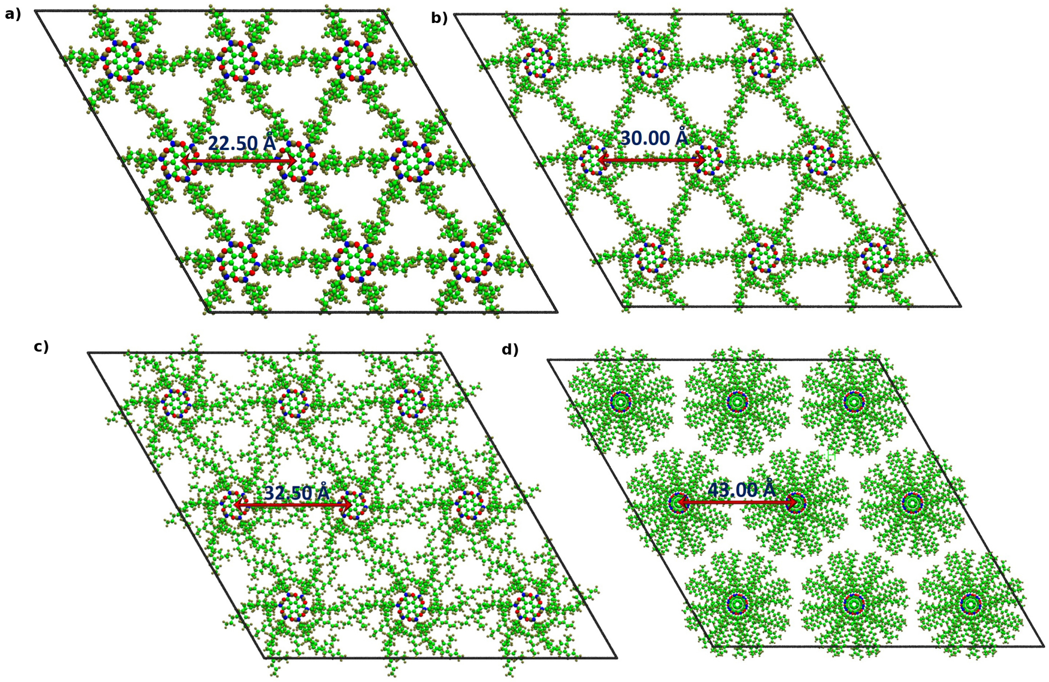

Figure 4.4: The initial structures of the systems in liquid crystalline (LC) phase. All amide dipoles are oriented in the same direction. (a) N,N′,N″-tri(hexyl)-1,3,5-benzenetricarboxamide (3BC-C6), (b) N,N′,N″-tri(decyl)-1,3,5-benzenetricarboxamide (3BC-C10), (c) N,N′,N″-tri(tetradecyl)-1,3,5-benzenetricarboxamide (3BC-C14), and (d) N,N′,N″,N‴,N⁗-penta(tetradecyl)benzenepentacarboxamide (5BC-C14) . Color Scheme: Green - Carbon, Tan - hydrogen, Red - Oxygen, Blue - Nitrogen.

Homologues of 3BCs are known to form columnar hexagonal liquid crystalline (LC) phase over a wide temperature range of 334-582 K. [24] These compounds are of interest for applications as ferroelectric materials with high retention times and remnant polarisation. [6] Polarisation retention is the ability of the ferroelectric material to remain electrically polarized even after the polarizing electric field is removed, and the time at which the depolarisation happens in the sample is defined as retention time. Polar switching in supramolecular ferroelectric materials is realized through the amide group rotation in response to the external electric field. [5] To understand polar retention in 3BC, we started with a fully poled (3:0) system in the LC phase for 3BC homologues with 14, 10 and 6 carbons long alkyl chains (3BC-C14, 3BC-C10, and 3BC-C6 respectively), the cell parameters used to construct the initial structures are given in Table. 4.2 and the structures are shown in Figure. 4.4a-c respectively. The retention time and depolarisation of ferroelectric materials are highly dependent on the packing of the molecules. [6, 25] In order to get neatly packed structures, we performed MD simulations starting from a low temperature of 50 K which was ramped to the target temperature of 460 K at which the molecules exist in LC phase over 2.5 ns in the NPT ensemble. The final structures from these runs have nice packing and all the molecules are found to be in the 3:0 configuration. The final configurations are shown in Figure. 4.5, 4.6 and 4.7 respectively. Saturation polarisation was calculated for each of the 3BC homologues. An obvious increase in saturation polarisation is seen with a decrease in the alkyl tail length, as seen in experiments. [26] This increase can be rationalized due to a decrease in the intercolumnar distance, which increases the dipole density. The values are tabulated in Table. 4.3.

Table 4.3: Saturation polarisation values for 3BCs and 5BC compounds.

System	Experiments		Our simulations	
	Temperature (K)	Polarisation (μC/cm^2)	Temperature (K)	Polarisation (μC/cm^2)
3BC-C6	323	6.7 [26]	460	1.63
3BC-C10	328	4.5 [26]	460	1.13
3BC-C14	– – –	– – –	460	0.88
5BC-C14	453	3.2 [7]	460	2.88

Later, these thin films of 3BC-C6, 3BC-C10 and 3BC-C14 were relaxed at 460 K temperature in the NPT ensemble. Intercolumnar distances were calculated from these equilibrium simulations and were found to be 16.07, 19.20 and 22.20 Å respectively, which are in good agreement with the experimentally observed values of 16.20, [6] 20.80 [6] and 22.40 Å respectively. [7] As the initial configurations were in the 3:0 dipolar configuration (i.e., all the three amide dipoles in any molecule were oriented in the same direction), the dipoles attempted to flip to 2:1 configurations, so as to attain anti-parallel orientation of dipole pairs within a molecule, which is the thermodynamic ground state. Consequent to the molecular dipole flips within a stack, the macrodipoles

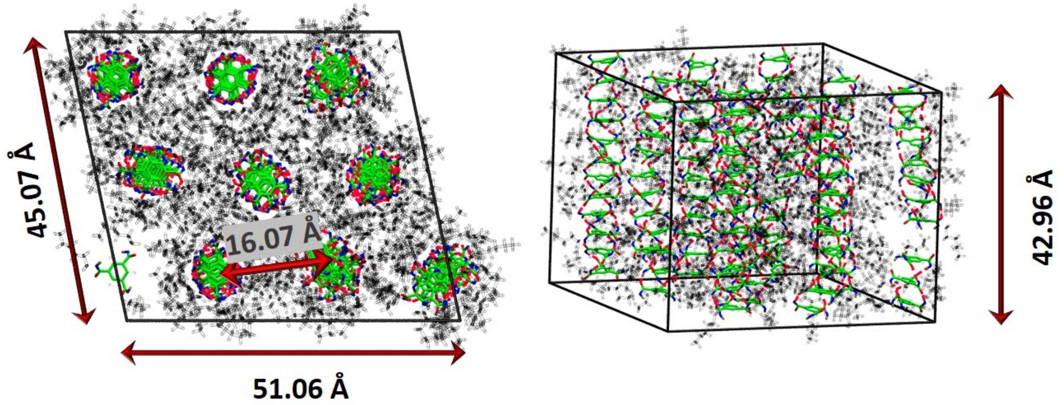
45.07 Å
16.07 Å
51.06 Å
42.96 Å

Figure 4.5: The final structure of 3BC-C6 from equilibrium simulations at 460 K. (a) side view and (b) top view. The colour scheme is same as in Figure. 4.4.

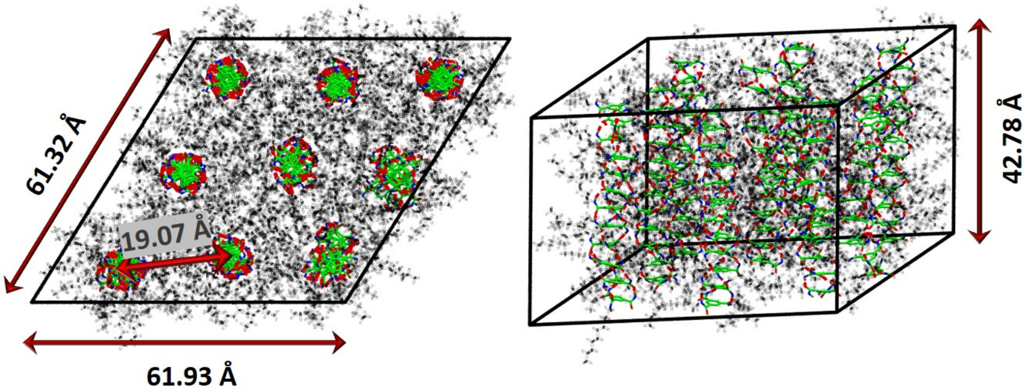
61.32 Å
19.07 Å
61.93 Å
42.78 Å

Figure 4.6: The final structure of 3BC-C10 from equilibrium simulations at 460 K. (a) side view and (b) top view. The colour scheme is same as in Figure. 4.4.

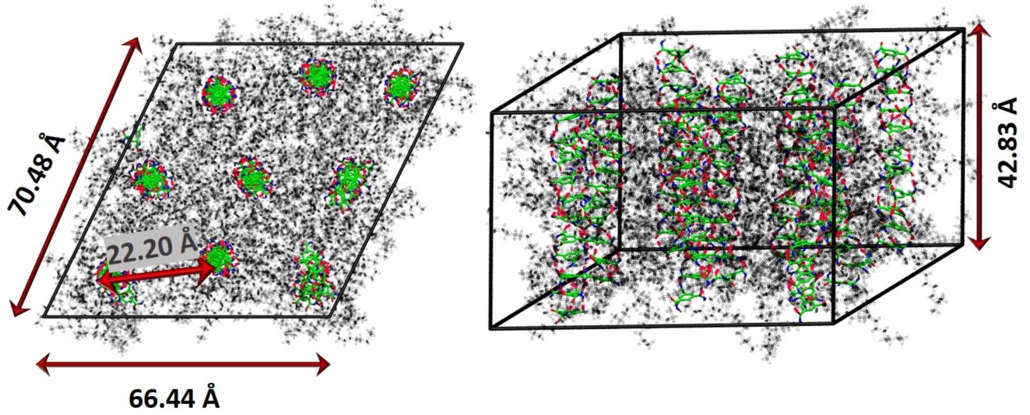
70.48 Å
22.20 Å
66.44 Å
42.83 Å

Figure 4.7: The final structure of 3BC-C14 from equilibrium simulations at 460 K. (a) side view and (b) top view. The colour scheme is same as in Figure. 4.4.

of each stack were also aligned so as to stabilise dipolar interactions and their ordering at 25 ns is shown schematically in Figure. 4.8. Thus, we attribute the depolarisation

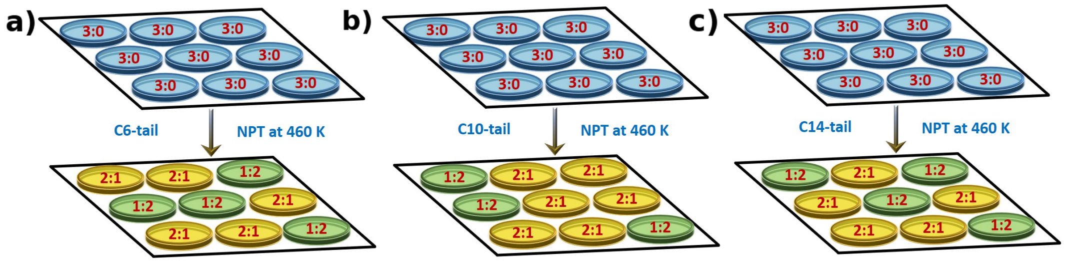
a)
3:0 3:0 3:0
3:0 3:0 3:0
3:0 3:0 3:0
C6-tail
NPT at 460 K
2:1 2:1 1:2
1:2 1:2 2:1
2:1 2:1 1:2
b)
3:0 3:0 3:0
3:0 3:0 3:0
3:0 3:0 3:0
C10-tail
NPT at 460 K
1:2 2:1 2:1
1:2 2:1 2:1
2:1 2:1 1:2
c)
3:0 3:0 3:0
3:0 3:0 3:0
3:0 3:0 3:0
C14-tail
NPT at 460 K
1:2 2:1 1:2
2:1 1:2 2:1
2:1 2:1 1:2

Figure 4.8: The configurations of each stack after 25 ns of equilibration in the NPT ensemble for (a) 3BC-C6, (b) 3BC-C10, and (c) 3BC-C14. The dipole configuration of each stack is labeled.

in homologues of 3BCs as not only to due to molecular dipole rotation but also from macrodipole interactions as well. The depolarisation curves are shown in Figure. 4.9 suggests that inter-stack macrodipole interactions, being stronger in the 3BC-C6 system due to shorter inter-stack distances is responsible for its slower depolarisation than those of 3BC-C10 and 3BC-C14.

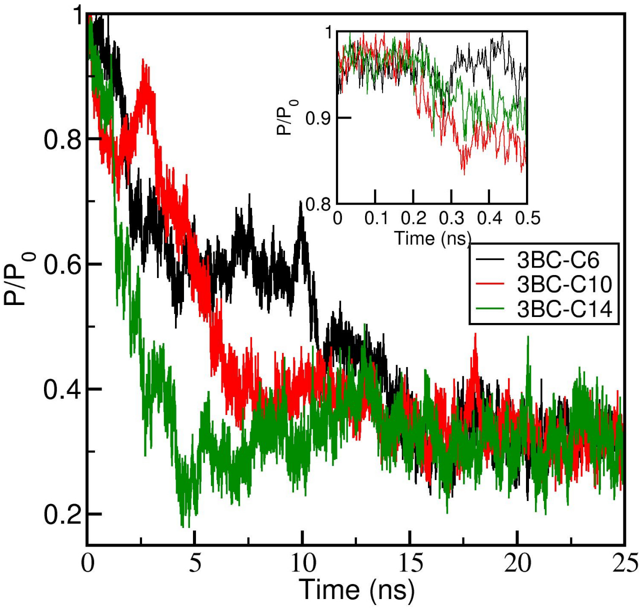

Figure 4.9: Depolarisation curves of 3BC homologues at 460 K. The inset shows the faster decay of polarisation in 3BC-C10 and 3BC-C14. P_0 is the polarisation of the sample in the fully poled state.

In the process of dipole relaxation, the hydrogen bonds between the amide groups of consecutive molecules within the same stacks break which creates disorder in the stack. Depolarisation starts at such disordered regions of the sample. Retention times can be increased through the suppression of such disorder and the same can be achieved by improving the molecular packing in the thin films. Tighter columnar packing was observed in 3BC-C6 molecule due to increased dipole density. Thus, the 3BC-C6 system is a potential candidate for practical applications when compared to 3BC-C10 and 3BC-C14. Urbanaviciute *et al.* studied polarisation retention of 3BC-C6 at two different temperatures, 22 and 80 °C, and found that at the higher temperature, the materials show lower retention time. [6]

For potential applications, materials with higher retention time even at high temperatures have to be engineered. Depolarisation in thin films is realized through dipole rotations, thus dipole rotation barriers have a prominent role in improving polarisation retention timings. Homologues of 3BC are associated with the same rotation barriers, which is independent of alkyl chain length. A recent study on branched-tailed 3BC homologues showed increased retention times. [26] Either in linear 3BC or in branched 3BC homologues, the dipolar density is tuned by engineering the tail length alone. Herein, we focus on the microscopic behaviour of a 5BC molecule, which has improved dipolar density, and which shows ferroelectric behaviour over a range of temperature, 299-470 K. [7]

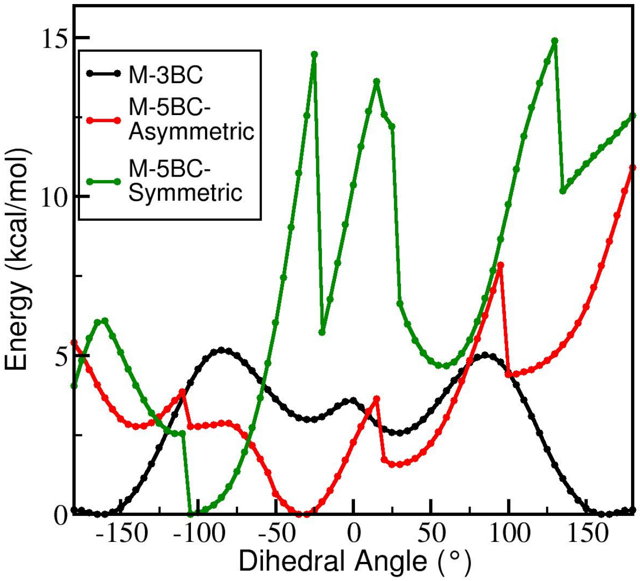

Figure 4.10: Potential energy surface (PES) of $C_{ar}-C_{ar}-C_a-O$ dihedral angle, obtained from relaxed scan at M06-2x/6-311+g(d,p) level of theory. The dihedral definitions are given in Figure. 4.11.

Dihedral barriers were estimated for methyl substituted 3BC and 5BC monomers — referred to as M-3BC and M-5BC respectively, and are shown in Figure. 4.10. These relaxed dihedral scans were performed in steps of 5° at M06-2x/6-311+g(d,p) level of theory using Gaussian package. [27]

Unlike M-3BC, the M-5BC molecule has two dihedral types depending on its location as shown in Figure. 4.11(b),(c). A dihedral with similar environment on its both sides is termed as symmetric dipole, while the one different surroundings is named

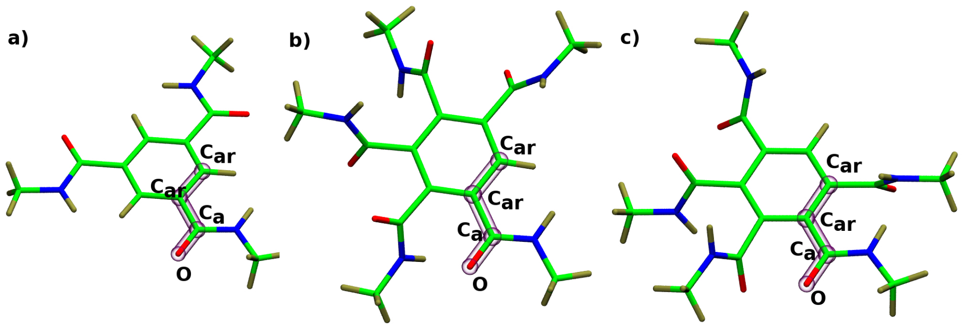

Figure 4.11: Atoms considered for relaxed dihedral scan runs are highlighted in magneta (a) N,N′,N″-tri(methyl)-1,3,5-benzenetricarboxamide (M-3BC), (b) Asymmetric dihedral of N,N′,N″,N‴,N⁗-penta(methyl)benzenepentacarboxamide (M-5BC), and (c) Symmetric dihedral of N,N′,N″,N‴,N⁗-penta(methyl)benzenepentacarboxamide (M-5BC). Color Scheme is same as in Figure. 4.4.

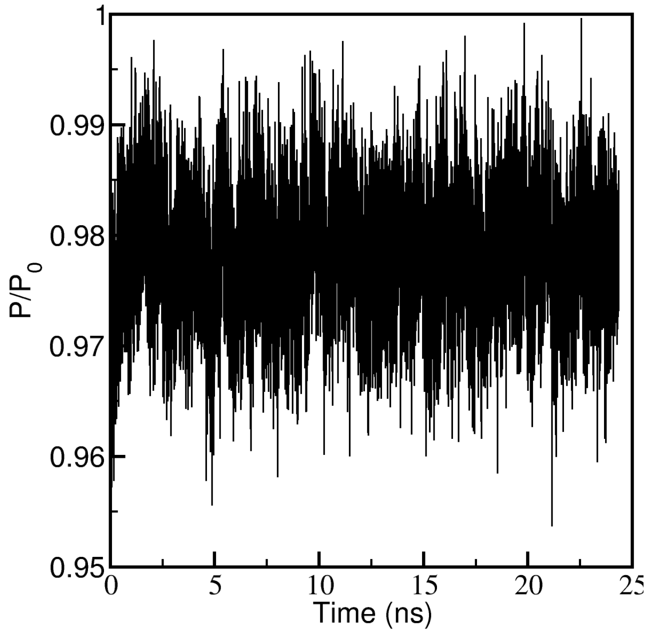

Figure 4.12: Depolarisation curve of 5BC system in its LC phase at 460 K. P_0 is the polarisation of the sample in fully poled state.

as asymmetric dipole. Dipole flipping in M-5BC is associated with very high barriers when compared to that in M-3BC molecule. To understand the effect of enhanced dipole rotation barriers and increased dipole density in 5BC molecule on depolarisation times, we constructed a LC phase of 5BC molecules, where the stacks were arranged in hexagonal lattice. The initial and final equilibrated simulation cell parameters are provided in Table. 4.2 The twist angle between the neighbouring molecules in 5BC was calculated from solution phase study and was found to be $\sim$ 47°, thus, to complete a pitch, we need to consider 7.6 molecules per stack. To preserve the continuity in the hydrogen bonding along the stacking direction (across the periodic boundary in the z direction), we considered 16 molecules per stack.

Similar to the liquid crystalline phase simulations of 3BC, the 5BC system was also relaxed from 50 to 460 K to improve the packing. The fully poled sample was equilibrated at 460 K for 25 ns in the NPT ensemble. The final configuration is shown in Figure. 4.13. The intercolumnar distance was measured from the equilibrated structures and was found to be 24.67 Å, in good agreement with experimentally observed value 25.40 Å. [7] The calculated saturation polarisation value of 2.88 μC/cm^2 too is in good agreement with the experimental value of 3.2 μC/cm^2 (see Table. 4.3). The depolarisation curve for this 5BC sample is shown in Figure. 4.12 The polarisation remained nearly time invariant over the entire simulation trajectory of 25ns, which suggests that the increased dipole rotation barrier and dipole density in 5BC are superior to those in 3BC, making the former an attractive choice for ferroelectric applications.

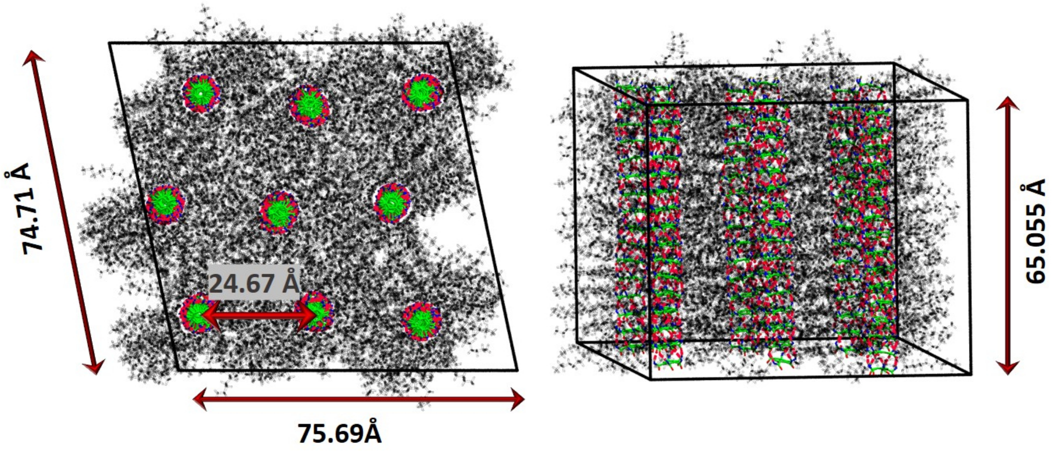

Figure 4.13: The final structure of 5BC-C14 from equilibrium simulations at 460 K. (a) side view and (b) top view. The colour scheme is same as in Figure. 4.4.

4.4 Conclusions:

Geometrical parameters such as centroid-centroid distance and twist angle between the neighbouring molecules in self-assembled structures of 2BC, 3BC, 4BC, 5BC and 6BC were calculated from solution phase MD simulations. The angle made by the amide group with the central phenyl core was measured for all these BCs, and it was found to increase from 3BC to 6BC, monotonically, due to increasing steric hindrance. Further, this angle also affects the packing parameters of the self-assembled structures, which is evident from the increase in centroid-centroid distance.

The effect of alkyl chain length on the retention time was studied from liquid crystalline phase studies of 3BC homologues at 460 K. Macrodipole rearrangements were observed in thin films to gain dipolar interactions during the process of depolarisation.

The intercolumnar distance in 3BC-C6, 3BC-C10 and 3BC-C14 were measured and validated against experimentally reported values. The depolarisation time in 5BC is rather large, which was attributed to an increase in dipole density and higher dipole rotation barrier. The high dihedral barrier for $\mathrm{C}_{ar}{-}\mathrm{C}_{ar}{-}\mathrm{C}_{a}{-}\mathrm{O}$ bond rotation in 5BC enables high retention times. Herein, we propose that depolarisation times can be tuned by increasing the dipole density and dihedral rotation barriers. With this, we believe 5BC molecule can be a promising candidate to use as a ferroelectric material with two desirable features i.e., high polarisation values as well as high retention times and is thus suitable for memory applications at modestly high operating temperature.

Bibliography

[1] Scott, J. F. Applications of modern ferroelectrics. *Science* **2007**, *315*, 954–959.

[2] Scott, J. C.; Bozano, L. D. Nonvolatile memory elements based on organic materials. *Advanced Materials* **2007**, *19*, 1452–1463.

[3] Goor, O. J.; Hendrikse, S. I.; Dankers, P. Y.; Meijer, E. From supramolecular polymers to multi-component biomaterials. *Chem. Soc. Rev.* **2017**, *46*, 6621–6637.

[4] Chandra, P.; Littlewood, P. B. *Physics of ferroelectrics*; Springer, 2007; pp 69–116.

[5] Fitié, C. F.; Roelofs, W. C.; Magusin, P. C.; Wübbenhorst, M.; Kemerink, M.; Sijbesma, R. P. Polar switching in trialkylbenzene-1, 3, 5-tricarboxamides. *J. Phys. Chemistry B* **2012**, *116*, 3928–3937.

[6] Urbanaviciute, I.; Meng, X.; Cornelissen, T. D.; Gorbunov, A. V.; Bhattacharjee, S.; Sijbesma, R. P.; Kemerink, M. Tuning the Ferroelectric Properties of Trialkylbenzene-1, 3, 5-tricarboxamide (BTA). *Advanced Electronic Materials* **2017**, *3*, 1600530.

[7] Shishido, Y.; Anetai, H.; Takeda, T.; Hoshino, N.; Noro, S.-i.; Nakamura, T.; Akutagawa, T. Molecular assembly and ferroelectric response of benzenecarboxamides bearing multiple- CONHC14H29 chains. *J. Phys. Chem. C* **2014**, *118*, 21204–21214.

[8] Manz, T. A.; Sholl, D. S. Chemically Meaningful Atomic Charges that Reproduce the Electrostatic Potential in Periodic and Nonperiodic Materials. *J. Chem. Theory Comput.* **2010**, *6*, 2455–2468.

[9] Manz, T. A.; Sholl, D. S. Improved Atoms-in-molecule Charge Partitioning Functional for Simultaneously Reproducing the Electrostatic Potential and Chemical States in Periodic and Nonperiodic Materials. *J. Chem. Theory Comput.* **2012**, *8*, 2844–2867.

[10] Hutter, J.; Iannuzzi, M.; Schiffmann, F.; VandeVo ndele, J. CP2K: Atomistic Simulations of Condensed Matter Systems. *WIREs Comput Mol Sci* **2014**, *4*, 15–25.

[11] Perdew, J. P.; Burke, K.; Ernzerhof, M. Generalized Gradient Approximation Made Simple. *Phys. Rev. Lett.* **1996**, *77*, 3865.

[12] Goedecker, S.; Teter, M.; Hutter, J. Separable Dual-Space Gaussian Pseudopotentials. *Phys. Rev. B* **1996**, *54*, 1703.

[13] Grimme, S.; Antony, J.; Ehrlich, S.; Krieg, H. A Consistent and Accurate ab initio Parametrization of Density Functional Dispersion Correction (DFT-D) for the 94 Elements H-Pu. *J. Chem. Phys.* **2010**, *132*, 154104.

[14] Mayo, S. L.; Olafson, B. D.; Goddard, W. A. DREIDING: A Generic Force Field for Molecular Simulations. *J. Phys. Chem.* **1990**, *94*, 8897–8909.

[15] Plimpton, S. Fast Parallel Algorithms for Short-Range Molecular Dynamics. *J. Comput. Phys.* **1995**, *117*, 1–19.

[16] Martyna, G. J.; Klein, M. L.; Tuckerman, M. Nosé–Hoover chains: The Canonical Ensemble via Continuous Dynamics. *J. Chem. Phys.* **1992**, *97*, 2635–2643.

[17] Hoover, W. G. Constant-Pressure Equations of Motion. *Phys. Rev. A* **1986**, *34*, 2499.

[18] Hockney, R. W.; Eastwood, J. W. *Computer Simulation Using Particles*; CRC Press, 1988.

[19] Humphrey, W.; Dalke, A.; Schulten, K. VMD: Visual Molecular Dynamics. *J. Mol. Graph.* **1996**, *14*, 33–38.

[20] Korlepara, D. B.; Henderson, W. R.; Castellano, R. K.; Balasubramanian, S. Differentiating the mechanism of self-assembly in supramolecular polymers through computation. *Chem. Commun.* **2019**, *55*, 3773–3776.

[21] Korlepara, D. B.; Balasubramanian, S. Molecular modelling of supramolecular one dimensional polymers. *RSC advances* **2018**, *8*, 22659–22669.

[22] Korlepara, D. B.; Bejagam, K. K.; Balasubramanian, S. Supramolecular polymerization of N, N$'$, N$''$, N$'''$-tetra-(tetradecyl)-1, 3, 6, 8-pyrenetetracarboxamide: a computational study. *The Journal of Physical Chemistry B* **2017**, *121*, 11492–11503.

[23] Bejagam, K. K.; Fiorin, G.; Klein, M. L.; Balasubramanian, S. Supramolecular polymerization of benzene-1, 3, 5-tricarboxamide: a molecular dynamics simulation study. *The Journal of Physical Chemistry B* **2014**, *118*, 5218–5228.

[24] Matsunaga, Y.; Miyajima, N.; Nakayasu, Y.; Sakai, S.; Yonenaga, M. Design of novel mesomorphic compounds: N, N$'$, N$''$-Trialkyl-1, 3, 5-benzenetricarboxamides. *Bulletin of the Chemical Society of Japan* **1988**, *61*, 207–210.

[25] Cornelissen, T. D.; Biler, M.; Urbanaviciute, I.; Norman, P.; Linares, M.; Kemerink, M. Kinetic Monte Carlo simulations of organic ferroelectrics. *Physical Chemistry Chemical Physics* **2019**, *21*, 1375–1383.

[26] Urbanaviciute, I.; Bhattacharjee, S.; Biler, M.; Lugger, J. A.; Cornelissen, T. D.; Norman, P.; Linares, M.; Sijbesma, R. P.; Kemerink, M. Suppressing depolarization by tail substitution in an organic supramolecular ferroelectric. *Physical Chemistry Chemical Physics* **2019**, *21*, 2069–2079.

[27] others,, et al. Gaussian 09, Revision D. 01, Gaussian. *Inc.: Wallingford, CT* **2009**,

Chapter 5

Computational Studies to Understand Self-assembly Selectively in the presence of ATP and Structural Rearrangments Therein

Chapter 5 discusses computational studies carried out to study the self-assembly of monomers selective to the presence of adenosine triphosphate (ATP) and to explain the time lags in observed spectroscopic measurements. It consists of two subchapters namely, Chapter 5A and Chapter 5B. In chapter 5A, the selective self-assembly of oligo(*p*-phenylenevinylene) (OPV) functionalized with dipicolylethylenediamine-zinc complex (DPA-Zn) — (OPV-DPA) — **1** molecules in the presence of adenosine triphosphate (ATP) is studied through molecular dynamics simulations at 298.15 K. The simulation studies provide paramount insights into its selectivity and also explains the time lags during the self-assembly process.

In Chapter 5B, Zero Kelvin DFT calculations have been performed to investigate the lag times observed in spectroscopic measurements during the self-assembly process of amphiphilic naphthalene diimide (NDI) derivative appended with guanidium receptors (NDG) in the presence of triphosphates namely, adenosine triphosphate (ATP) and guanosine triphosphate (GTP).

Chapter 5A

Modelling Biomimetic Temporal Self-assembly via Fuel-driven Controlled Supramolecular Polymerization

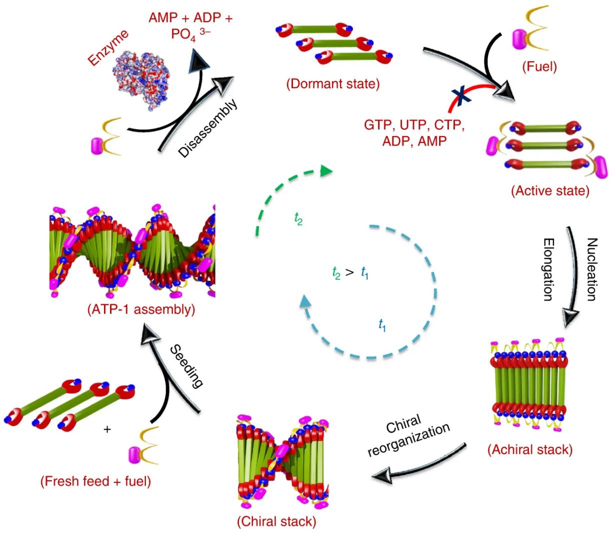
Enzyme
AMP + ADP + PO$_4^{3-}$
Disassembly
(Dormant state)
(Fuel)
GTP, UTP, CTP, ADP, AMP
(Active state)
Nucleation
Elongation
t_2
$t_2 > t_1$
t_1
(ATP-1 assembly)
Seeding
+
(Fresh feed + fuel)
(Chiral stack)
Chiral reorganization
(Achiral stack)

Reprinted with permission from "Biomimetic temporal self-assembly via fuel-driven controlled supramolecular polymerization" *Nat. Comm.* **2018**, *9*, 1–9. © 2018, Nature Publishing Group, https://www.nature.com/articles/s41467-018-03542-z. Experiments were carried by Dr. Ananya Mishra in Prof. Subi George's group at JNCASR.

5A.1 Introduction

In general, supramolecular polymers possess specific structural properties, but their dynamic nature enable them to undergo structural changes in response to external stimuli. By combining these reversible structures with tailor-made functionalities, functional supramolecular polymers have been discovered. Functional supramolecular polymers have been studied extensively over past two decades, [1–3] and their applications in biomedical field have been reported. [4] To gain control over these functional materials in terms of dispersity and structure is a prime challenge in the field of supramolecular polymerisation. Spatial and temporal control over the assembled structures have been seen in natural assemblies. Biological systems use self-assembly of proteins, controlled via various molecular cues, as a functional motif. [5] For example, actin monomers polymerise kinetically in the presence of ATP in cells via a nucleation-elongation mechanism, resulting in monodisperse self-assembled structures.

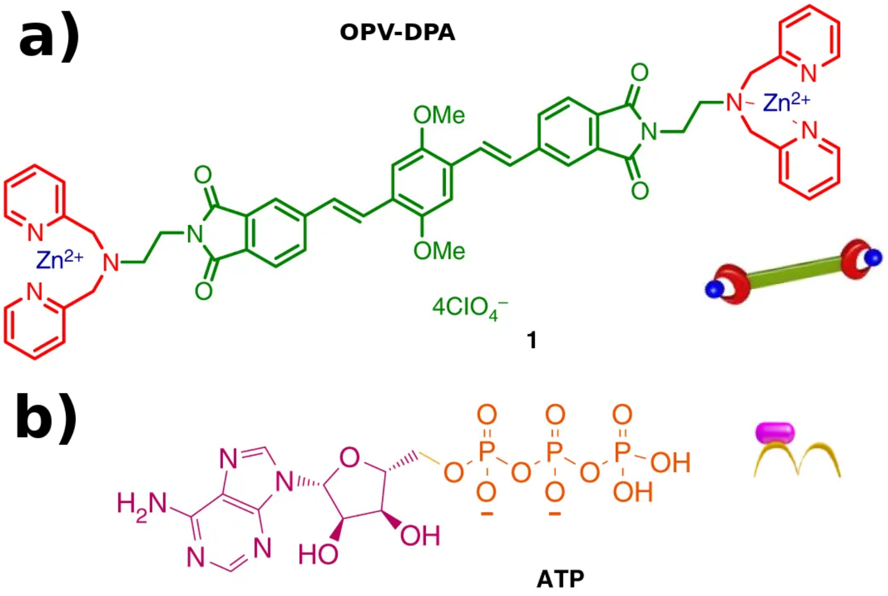

Figure 5A.1: Structure of **(a)** oligo(*p*-phenylenevinylene) (OPV) functionalized with dipicolylethylenediamine-zinc complex (DPA-Zn) (OPV-DPA) , **(b)** adenosine triphosphate (ATP).

In the present chapter, a synthetic system has been synthesised in the research group of Prof. Subi George at JNCASR, which can undergo a fuel-driven temporal supramolecular polymerisation with structural control. The structure of the molecules are shown in Figure. 5A.1 Experimental studies reveal that molecule OPV-DPA (**1**) reports a nucleation-growth and seeded supramolecular polymerisation, which can be temporally controlled by a specific biological co-factor, ATP, which is confirmed through spectroscopic studies such as CD and absorbance.

The growth mechanism was studied by the experimental group using several spectroscopic measurements as provided in Figure. 5A.2, both for the sake of completenenss and to aid further discussion. Time-dependent kinetics (monitored at 500 nm) showed the presence of a CD silent state of about 280 s (red plot, Figure. 5A.2). After this time lag, the CD signal increased sharply with time in a nonlinear manner, indicating a cooperative self-assembly, which finally saturates at around 1000 s. This time-delayed self-assembly was also reflected in the absorbance (blue plot, Figure. 5A.2). But interestingly, the time lag observed in absorbance ($t_{lag}(Abs_{500nm})$ = 203 s) was lesser than the CD time lag ($t_{lag}(CD_{500nm})$ = 280 s). [6]

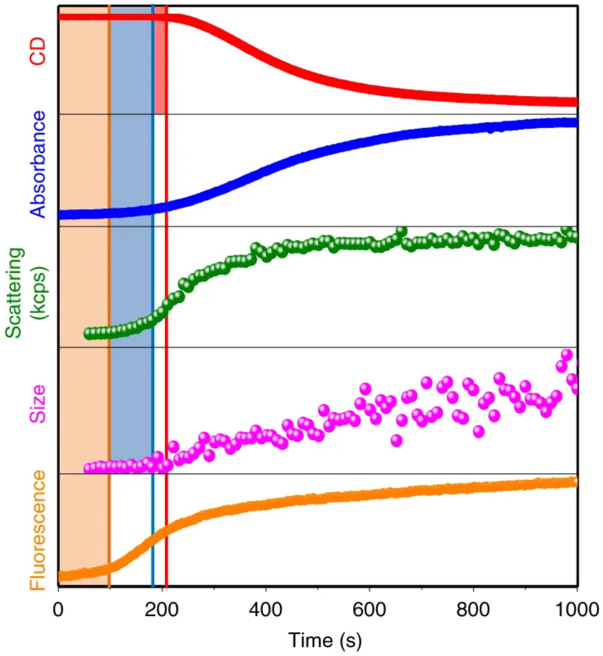

Figure 5A.2: Experimentally determined, growth kinetics and lag phases of ATP-driven nucleation growth of **1** monitored by CD (mdeg), absorbance, scattering in kcps (kilo counts per second), size (nm) obtained from dynamic light scattering (DLS) and fluorescence. Absorbance, CD, and emission were monitored at 500 nm (c=$2X10^{-5}$M, HEPES/CH_3CN, 90/10, v/v, 0.9 equiv. ATP, 30 °C). Data from experimental collaborators.

The origin of selective self-assembly and the observed time lags in spectroscopic measurements were unclear from the experimental studies. Herein, Molecular Dynamics (MD) simulations have been performed to gain insights into the selectivity of fuel-driven self-assembly and the time lags. To start with, the daunting task is to identify how the molecules of **1** organised to form 1D structures in presence of ATP. To determine the model structure, the following salient points are taken from experimental observations: (a) the ends of the supramolecular polymer has free receptor sites to drive a "living" growth in presence of additional ATP and (b) the ATP to **1** mole ratio is between 0.9 and unity.

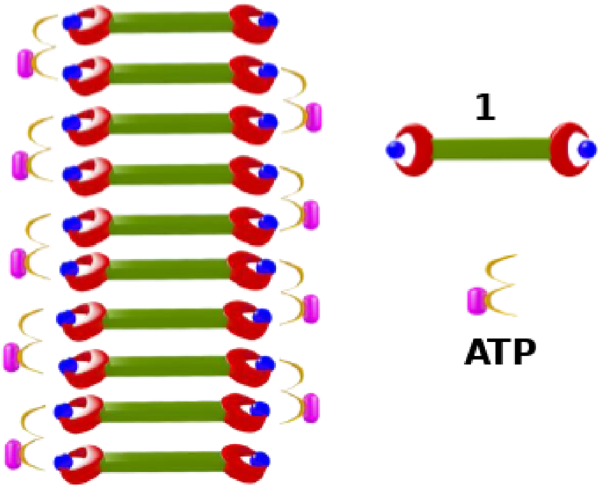

Figure 5A.3: Schematic model of ATP-**1** employed in MD simulations.

A schematic of such a model used for the MM/MD simulations is illustrated in Figure. 5A.3. In MD simulations, we considered the preformed stacks of ATP-**1** and GTP-**1** systems to determine the selectivity and showed that the intermolecular hydrogen bond between the ATP molecules is the primary cause of selectivity in supramolecular polymerisation. Further, we studied the structural changes in the oligomers of ATP-**1** and explained that the structural re-arrangements during the elongation of small oligomer is responsible for the lag time in the spectroscopic measurements.

5A.2 Computational Details

5A.2.1 Charge Calculations

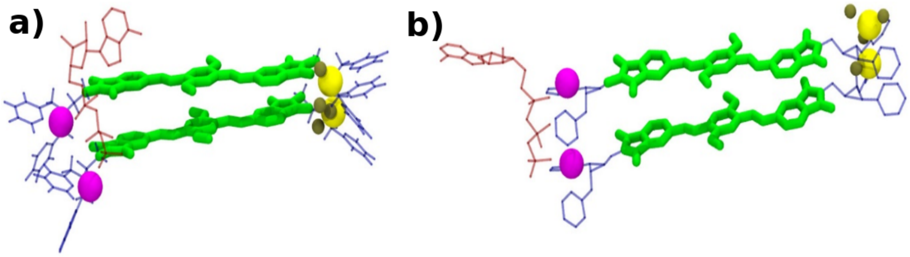

Figure 5A.4: Gas phase DFT calculations of the ATP-**1** dimer, **(a)** Initial and **(b)** final configurations of ATP-1 dimer. Colour Scheme: Green - OPV, Blue - DPA, Red - ATP/GTP. Zinc atoms are represented as spheres in two different colours (yellow and magenta) to emphasize helicity and the counter ions (Cl^-) shown in tan colour.

For charge calculation, we consider a dimer configuration (a total of 291 atoms) constructed using GaussView software [7] as shown in Figure. 5A.4(a). Density functional theory (DFT) calculations were performed using the QUICKSTEP module in CP2K software. [8] All valence electrons were treated in a mixed basis set with an energy cutoff of 280 Ry. The short-range version of the double zeta single polarization basis set was used. The effect of core electrons was taken through pseudopotentials of Goedecker-Tetter-Hutter (GTH). [9] The Perdew-Burke-Ernzerhof (PBE) exchange and correlation functional [10] was employed. DFT-D3 [11] corrections were used to take van der Waals interactions into account and the dimer geometry was optimised in gas phase. The initial and final configurations of this gas phase dimer are shown in Figure. 5A.4, respectively. A dimer of ATP-**1** has three parts: the OPV region, the DPA region, and the ATP. The phosphates of one ATP molecule can bind to two zinc atoms of two different molecules of **1**. Out of the four DPA receptor moieties in ATP-1dimer, two are bound to one ATP molecule, while the other two are free. Thus, the atomic site charges on either ends of ATP-**1** dimer will differ. Thus ATP-(or GTP-) oligomer will have both ATP-bound DPA ends as well as free (unbound) DPA receptor ends. Hence the forcefield has to have different charges on the backbone of **1** to take into account these structural differences. Figure. 5A.6(a) displays these different segments in ATP-**1** dimer, using which higher oligomers can be constructed. The segments of trimer, hexamer are shown in Figure. 5A.6(b),(c) respectively. The partial charges on the atoms in dimer are tabulated (See table. 5A.1, 5A.2, 5A.3, 5A.4 and 5A.6) for each segment and atom mapping scheme in the ATP-**1** dimer shown in Figure. 5A.5.

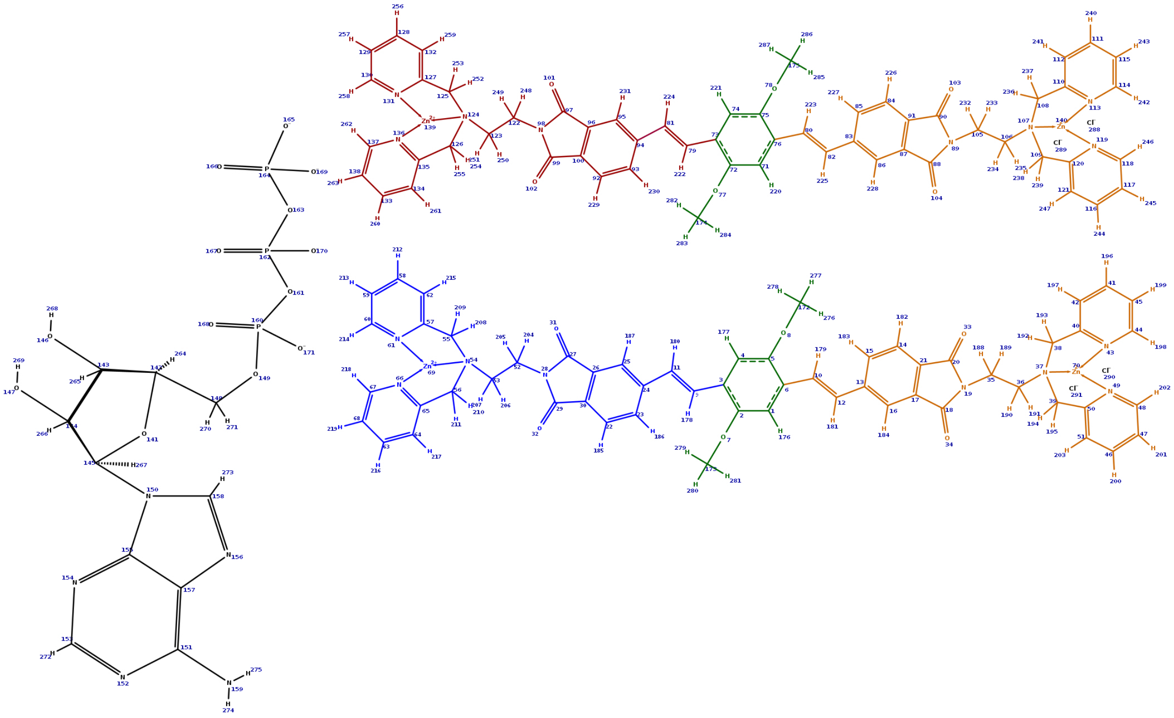

Figure 5A.5: Atom mapping scheme in the ATP-**1** dimer.

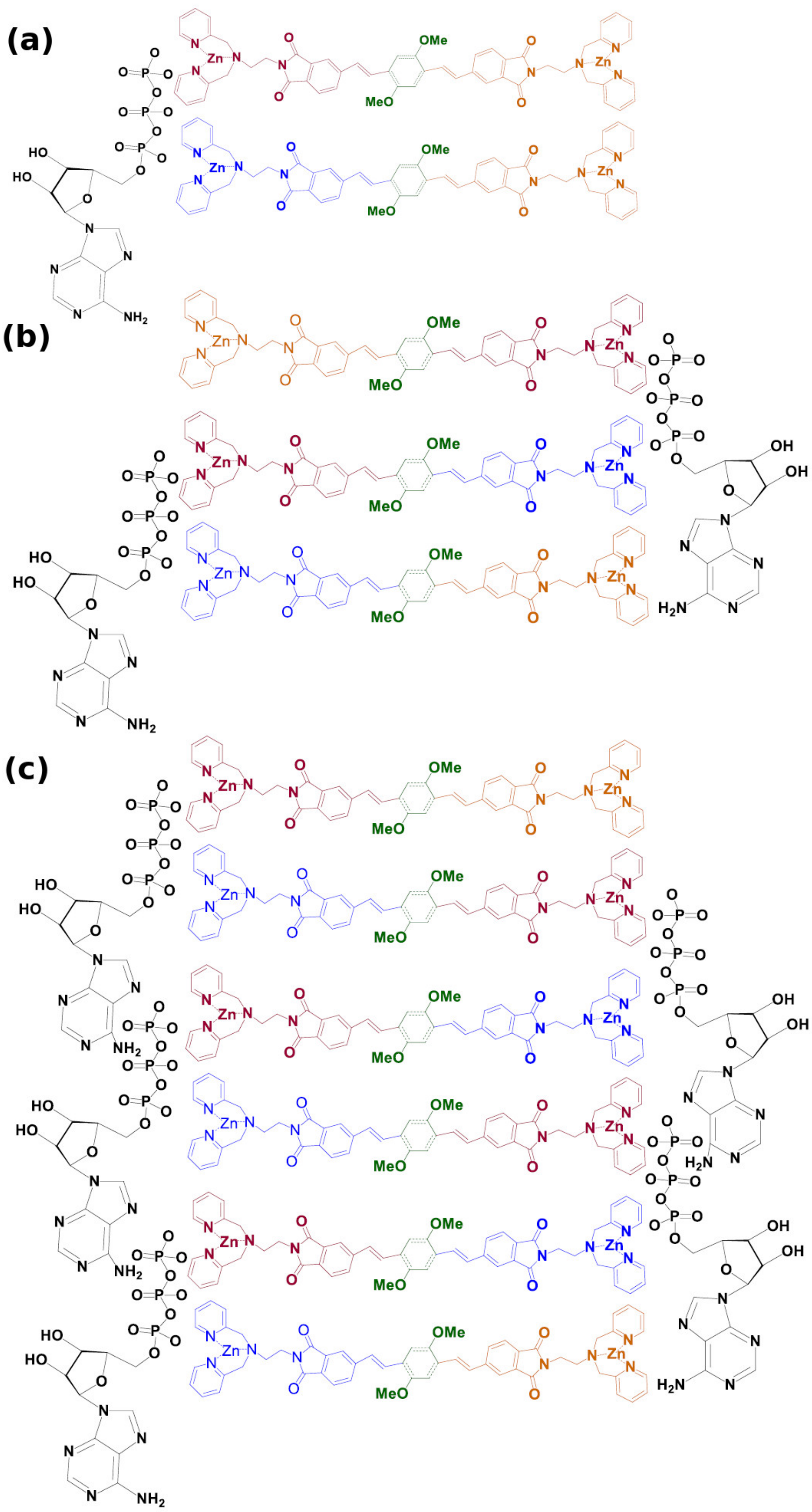

Figure 5A.6: Segment-wise representaion of ATP-**1** oligomers. (a). Dimer, (b). trimer and (c). hexamer. Segments with the same colour code have the same atomic site charges across different oligomers. The site charges themselves are determined for the dimer via gas phase DFT calculations.

Table 5A.1: Partial charges on atoms coloured green (Segment 1).

Atom Index	Charge (e)	Atom Index	Charge (e)
1	0.2001260	172	0.4697920
2	-0.2822740	173	0.4752950
3	0.0245920	276	0.3735670
4	0.2152150	277	0.3724460
5	-0.2780810	278	0.1301210
6	0.0378690	279	0.0718660
7	0.1232810	280	0.3300760
8	0.1331140	281	0.3962770

Table 5A.2: Partial charges on atoms coloured blue (Segment 2).

Atom Index	Charge (e)	Atom Index	Charge (e)	Atom Index	Charge (e)	Atom Index	Charge (e)
9	-0.2266090	53	-0.4241250	66	0.0911470	208	-0.2895450
11	-0.1069550	54	-0.2513020	67	0.1311690	209	-0.2902530
23	-0.1495710	55	-0.0327050	68	0.2510930	210	-0.0505850
24	0.1124240	56	0.1005830	69	-0.2545910	211	-0.0460950
25	-0.1623110	57	0.0947900	178	0.1139980	212	0.1126610
26	0.1044030	58	-0.1192450	180	-0.0710940	213	0.0797540
27	0.0991130	59	0.0821550	185	0.1159320	214	0.0565160
28	-0.1166080	60	0.1120950	186	0.1088430	215	-0.1599560
29	-0.1371350	61	-0.0661520	187	-0.1589540	216	-0.1746060
30	-0.0875030	62	-0.1720780	204	-0.2143040	217	-0.1557470
31	0.1357640	63	0.1302860	205	0.1001020	218	0.1549310
32	-0.0604140	64	0.0969930	206	0.1099340	219	0.0836320
52	-0.4596130	65	-0.1779110	207	0.1451300		

Table 5A.3: Partial charges on atoms coloured brown (Segment 3).

Atom Index	Charge (e)	Atom Index	Charge (e)	Atom Index	Charge (e)	Atom Index	Charge (e)
79	0.1207740	122	0.8612990	135	0.0799680	251	-0.3487000
81	0.1389940	123	0.2186420	136	0.0894010	252	0.2304780
92	0.0817870	124	-0.2735670	137	-0.1068700	253	-0.0958370
93	-0.2580400	125	0.0221610	138	0.0997350	254	0.1642070
94	-0.0616500	126	0.2122020	139	0.1155400	255	-0.4311570
95	-0.1170080	127	-0.2968420	222	0.1219070	256	-0.0399050
96	0.0764660	128	0.0323720	224	-0.2251400	257	0.5057720
97	0.0907790	129	0.1224910	229	0.1150890	258	-0.7468710
98	0.2525670	130	0.1260280	230	0.1696170	259	-0.5403430
99	0.0919510	131	-0.2272900	231	0.0013040	260	0.3320840
100	0.1242300	132	-0.2285050	248	-0.5495240	261	-0.4552300
101	0.2771600	133	-0.0951440	249	0.0223980	262	0.2389500
102	-0.2398790	134	0.1120180	250	0.1608390	263	0.1360720

Table 5A.4: Partial charges on atoms coloured orange (Segment 4).

Atom Index	Charge (e)	Atom Index	Charge (e)	Atom Index	Charge (e)	Atom Index	Charge (e)
10	-0.2268170	37	-0.1168010	50	0.4761820	194	0.1192220
12	0.1124760	38	-0.1477280	51	0.4783470	195	-0.2135850
13	0.0949340	39	-0.0743680	179	0.1074420	196	0.1120080
14	0.0836820	40	0.1436270	181	0.1025960	197	0.1115810
15	-0.1052880	41	-0.0629300	182	0.0717880	198	0.1393250
16	0.0797580	42	0.1201170	183	-0.1122140	199	0.2666950
17	0.1136890	43	-0.1210500	184	-0.1793490	200	-0.2491500
18	0.0944590	44	0.1315040	188	0.0923560	201	0.1404980
19	-0.1022510	45	0.4780740	189	0.1268300	202	0.0008720
20	0.1112070	46	0.4716750	190	0.2632420	203	0.1438200
21	-0.0942390	47	-0.4204660	191	-0.2086070		
35	0.1333100	48	-0.4554930	192	0.1243500		
36	0.1064510	49	-0.2208780	193	0.0078360		

Table 5A.5: Partial charges on atoms coloured black (Segment 5).

Atom Index	Charge (e)	Atom Index	Charge (e)	Atom Index	Charge (e)	Atom Index	Charge (e)
141	-0.1094850	152	-0.0798950	163	-0.0596450	265	-0.5511750
142	0.1222890	153	0.1396250	164	0.1230850	266	-0.5628490
143	-0.0810360	154	-0.0715840	165	-0.1186920	267	-0.6710930
144	0.1164130	155	0.1166360	166	0.1313450	268	1.5806230
145	-0.1572180	156	-0.1019970	167	0.4713770	269	-0.6466810
146	0.1035350	157	0.1390820	168	0.4650240	270	1.5442340
147	-0.1763640	158	0.1161540	169	-0.4359130	271	-0.8383400
148	0.1158830	159	-0.1198090	170	-0.4310800	272	-0.7795030
149	0.0935130	160	-0.1614720	171	-0.2107810	273	-0.7676080
150	-0.1244410	161	-0.0814980	172	0.4697920	274	-0.8010060
151	-0.1526800	162	0.1366790	264	0.1005910	275	-0.8466240

Table 5A.6: Partial charges on counter ion (Cl^-).

Atom Index	Charge (e)
288	-0.4678910
289	-0.4933320
290	-0.5463590
291	-0.5266740

5A.2.2 MD simulations

As in chapters 2 & 3, the solute molecules 1, ATP, GTP and counter ions were modelled using DREIDING [12] force field with DDEC/c3 charges on atomic sites. Water (solvent) molecules were represented in all atom model using TIP3P [13] parameters. Cross interactions between the solute and solvent molecules were considered using DREIDING's mixing rules. A pseudo bond between Zinc and sp^3-hybridised nitrogen atom of DPA was created, with equilibrium bond length 2.2 Å, which was chosen from studying crystal structure of similar compounds. [14] MD simulations were performed using LAMMPS package [15] at 298.15 K in the constant temperature and constant pressure ensemble. The Nosé-Hoover chain thermostat was used to maintain a constant temperature and Nosé-Hoover barostat used to maintain constant pressure with a coupling constant of 1 ps. Three-dimensional periodic boundary conditions were employed. Non-bonded interactions were truncated at distance of 12 Å. Particle-particle particle-mesh (PPPM) solver was used to consider the long-range interactions. The equations of motion were integrated using the velocity Verlet integrator with a timestep of 0.5 fs. The coordinates of the molecules were stored for post-processing every 2.5 ps and the trajectory was visualised using VMD. [16] In every simulation, the preformed oligomer was solvated in water using Packmol. [17]

5A.3 Results and Discussions

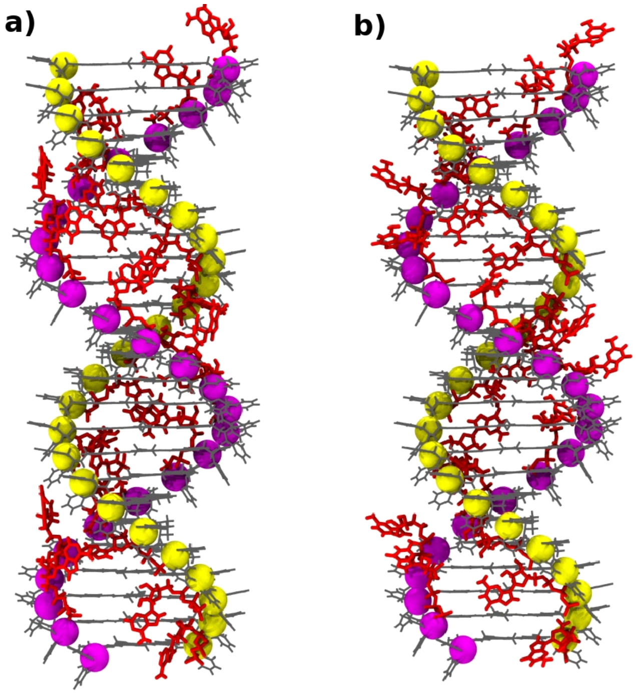

Figure 5A.7: Snapshots of initial structures of preformed (a). ATP-**1** and (b). GTP-**1** 25-mer. Zinc atoms have been depicted as spheres of two different colours (magenta and yellow) to demonstrate the helicity in the oligomers of the initial configurations in either of the stacks. Molecules of **1** are depicted in gray sticks (in a and b) and ATP and GTP have been shown in red.

ATP selectivity: To understand the selectivity of self-assembly of **1** molecules to ATP, we constructed 25-mer of ATP-**1** and GTP-**1** with a twist angle of 25° and the structures are shown in Figure. 5A.7, were solvated in water in a cubic box of dimension {66.88, 66.88, 140.6} Å. To maintain the charge neutrality in the system, we added counter ions (Cl^-). MD simulations are performed in NPT ensemble for 60 ns. While the first 5 ns of the trajectory was used for equilibration, the structural analyses reported

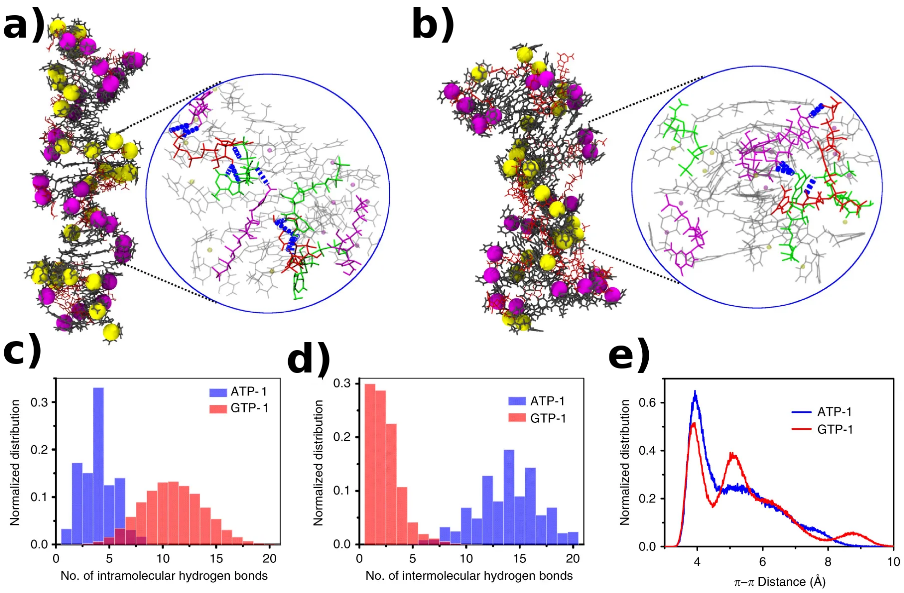

Figure 5A.8: Snapshots of final structures of 25-mer (a). ATP-**1** and (b). GTP-**1** obatined from MD simulations. Zoomed images in (a) and (b) show intermolecular H-bonding between the triphosphates. Zinc atoms have been depicted as balls of two different colours (magenta and yellow) for easy identification of the helicity in the oligomer. Molecules of **1** are depicted as grey sticks (in (a) and (b)), while ATP and GTP are in red. In zoomed images of (a) and (b), intermolecular H-bonds are shown as dashed light blue lines. Each ATP/GTP molecule is depicted in a distinct colour to make it obvious that the hydrogen bonds are intermolecular in character. Comparison between (c). intramolecular H-bonds, (d). intermolecular H-bonds and (e). π-π distance between two adjacent molecules of **1** in ATP-**1** and GTP-**1** simulated assemblies.

here were obtained from last 55 ns. The simulations suggest that ATP-**1** stack is more stable than the GTP-**1** stack due to a large number of intermolecular hydrogen bonds in former shown in Figure. 5A.8(a),(b). Although the mean number of intramolecular hydrogen bonds in GTP-**1** is more than that in ATP-**1** as seen from the normalized distributions (Figure. 5A.8(c)), such hydrogen bonds do not contribute to stack stability. In contrast, the average number of intermolecular hydrogen bonds in ATP-**1** is much larger than that in GTP-**1** (13 and 2 respectively, see Figure. 5A.8(d)). We envisage that intermolecular hydrogen bonds in ATP-bound stacks bring the molecules of **1** closer to each other to increase π-π interaction and which stabilizes the stacks. Mean values of π-π distances for ATP-**1** and GTP-**1** stacks were found out to be 3.8 Å and 5.2 Å, respectively (Figure. 5A.8(e)). The bimodal distribution of the π-π distance is due to molecules present in the periphery of the stack, which are relatively more labile than the ones in its core. On the other hand, in the case of the GTP-**1** assembly, the molecules in stack are not well packed, which gives rise to a multimodal distribution. Hence, MD simulations strongly suggest that the propensity of intermolecular H-bonding in

ATP-bound stacks than in GTP ones is responsible for the observed selectivity in the growth. From the equilibrated structure of ATP-**1**, we calculated the width and found it to be 3.2 nm which in good agreement with experimentally measured width of the fibres found from TEM.

Lagtime: To gain insights into the experimentally observed lag time (Figure. 5A.2), we simulated oligomers of ATP-**1** of various length (2-,3-,4-,6-,10-,15-mer: for 30 ns and 25-mer for 60 ns) and the system sizes are tabulated in Table. 5A.7.

Table 5A.7: System information over the oligomers of MD simulations.

Size of Oligomer (n)	**Number of '1'**	**Number of ATPs**	**Number of counter ions (Cl^-)**	**Number of solvent molecules (H_2O)**	**Box dimensions (Å)**
2	2	1	4	6075	(60,60,60)
3	3	2	4	5932	(60,60,60)
4	4	3	4	5765	(60,60,60)
6	6	5	6	5448	(60,60,60)
10	10	9	4	4929	(60,60,60)
15	15	14	4	5295	(60,60,80)
25	25	24	9	18551	(66.88,66.88,140.6)

A simulation of a dimer with initial structure as shown in Figure. 5A.10(a) was performed. **1** has a unique acceptor-donor-acceptor (A-D-A) electronic structure (Figure. 5A.9(a)) where the central dimethoxy phenyl ring acts as the donor and the phthallic imides are the acceptor moieties. [18, 19] As a result, in HEPES/CH_3CN (90/10, v/v), these molecules exist in a pre-associated slip-stacked conformation due to intermolecular charge transfer interactions is shown in Figure. 5A.9(b). Due to this pre-organised, slip-stacked native state of **1**, an allosteric re-arrangement of monomers would be essential to re-enforce the binding with the ATP molecules. However, in a dimer, the ends of molecule **1** which are not bound to ATPs are fluxional. In order to gain donor-acceptor interaction, molecule **1** slides over another. To quantify the magnitude of this slide, a slip distance defined as the lateral displacement of the central moiety in molecule **1** as shown Figure. 5A.10(c) is employed. The dimer shows a slip distance between adjacently placed **1** to be 5.2 Å and the same is shown in Figure. 5A.10(b).

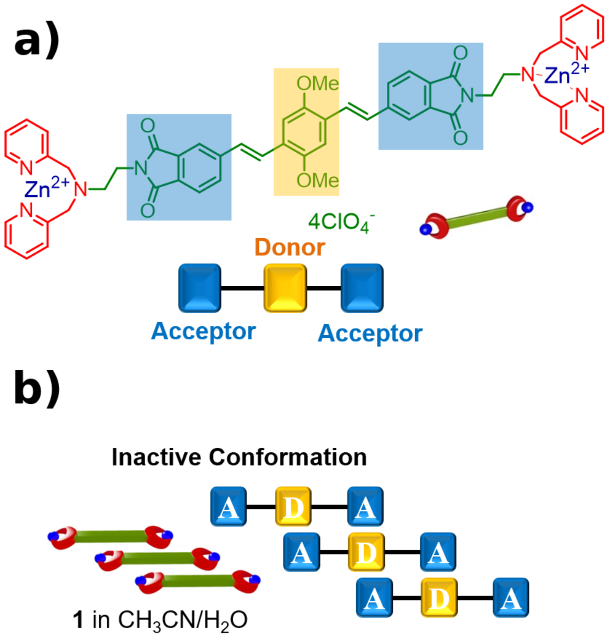
a)
OMe
OMe
O
O
N
N
Zn2+
4ClO4-
Donor
Acceptor
Acceptor
b)
Inactive Conformation
A D A
1 in CH3CN/H2O

Figure 5A.9: (a). Molecular structure of **1** and schematic depicting its A-D-A electronic configuration and (b). schematic showing inactive slipped supramolecular conformation of **1** in the absence of ATP.

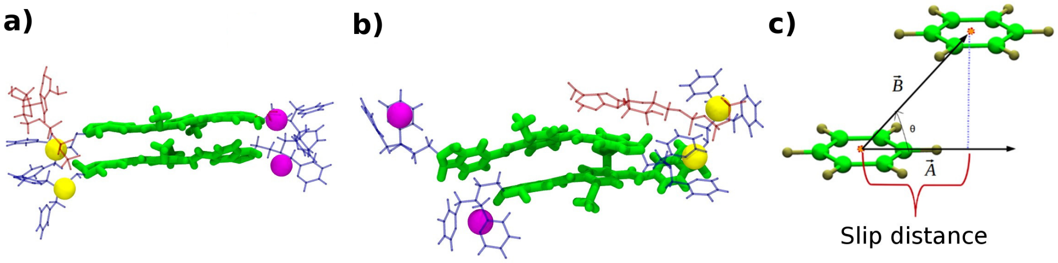
a)
b)
c)
B
θ
A
Slip distance

Figure 5A.10: Simulated Dimer (a). Initial configuration, (b). Final snapshot and (c). Definition of slip distance. The colour scheme is same as Figure. 5A.4

Table 5A.8: Slip distances in various oligomers

Oligomer size	Slip distance (Å)
2	5.20
3	3.55
4	4.42
6	3.25
10	2.07
15	2.37
25	1.35

Moving to higher oligomers, we found that ATPs bound to **1** re-enforces to form organised stacks as the slip distance decreases from 5.2 Å for a dimer to 1.35 Å for a 25-mer and the values are tabulated in Table 5A.8. The final shapshots of oligomers are shown in Figure 5A.11(c). From Figure 5A.11(a), it is clear that the normalized distribution of slip distance varies rapidly with oligomer size and the position of the peak shifts toward lower values with increasing oligomer size. Thus, the allosteric-binding-induced supramolecular reorganisation converts the inactive conformation of the monomers to an active conformation, which is the first chronological event en route to the nucleation process. To understand the structural evolution of various oligomers (all the oligomers constructed by considering a twist angle of 25°) with time, we defined an inverse order parameter (IOP) as

$$IOP(n) = \frac{RMSD}{(n-1)(\pi - \pi\ distance)} \tag{5A.1}$$

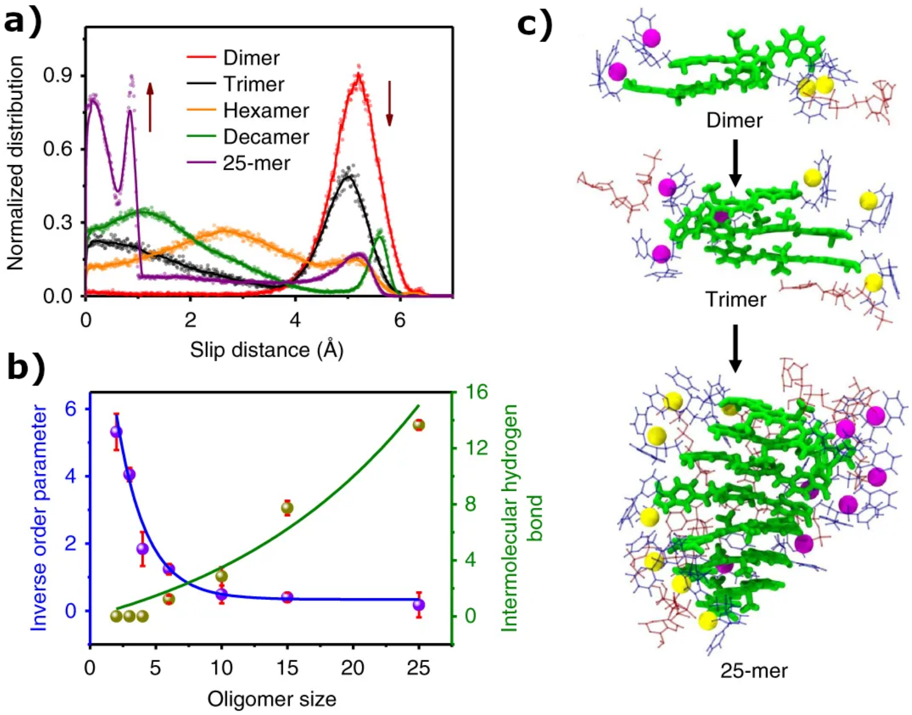

Figure 5A.11: (a). Slip distance distribution, (b). inverse order parameter (blue curve) and intermolecular H-bonds (green curve) per ATP for various oligomers extracted from MD simulations of ATP-**1** stacks and (c). Snapshots from MD simulations of ATP-1 oligomers showing decrease in slip distance with extent of polymerisation. The colour scheme is same as Figure. 5A.4

where n is oligomer size and the π-π distance was taken to be 3.8 Å. In the calculation of RMSD, only the coordinated of the OPV segments of the stack were used. RMSD, thus calculated, was averaged over all the frames for a given oligomer. Figure. 5A.11(b) provides the IOP calculated using the oligomer coordinated at 30

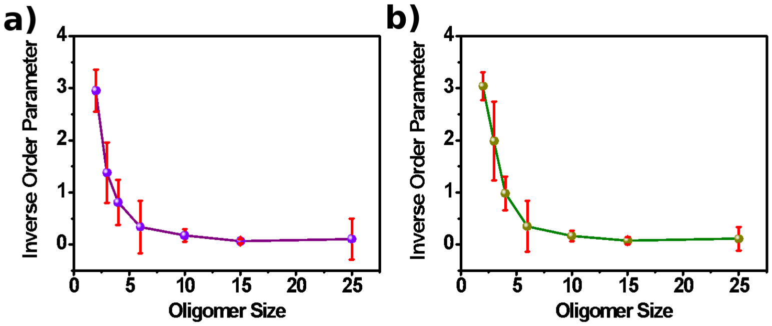

Figure 5A.12: Inverse order parameter (IOP) of various oligomers of ATP-**1** stacks with reference frame chosen for the calculation of RMSD. (a). 28 ns and (b). 29 ns.

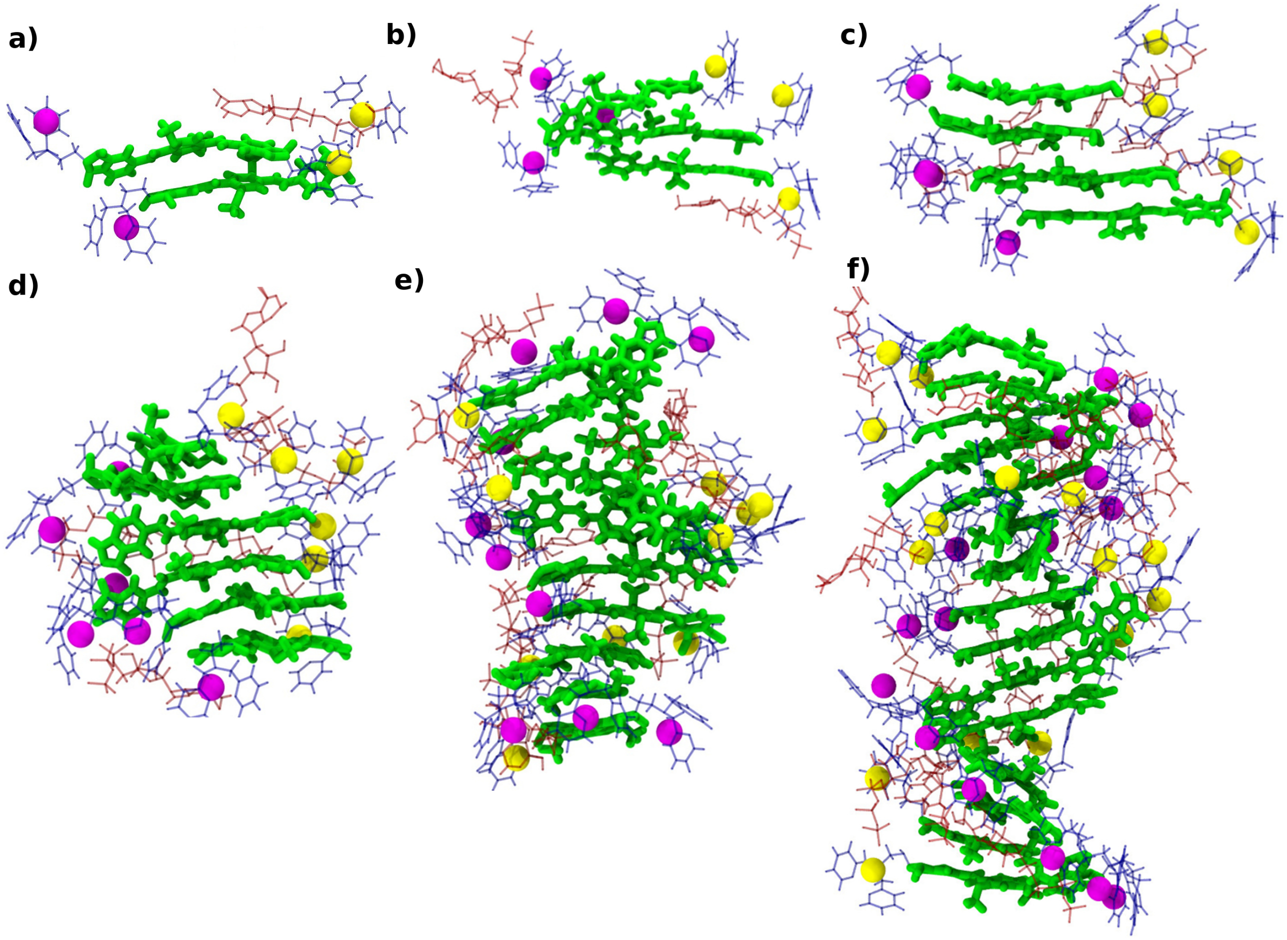

Figure 5A.13: Final snapshots of the simulated oligomers of (a) dimer, (b) trimer, (c) tetramer, (d) hexamer, (e) decamer and (f) pentadecamer. OPV core is depicted by thick green sticks, DPA and ATP have been represented by thin blue and red sticks, Zn atoms are depicted in spheres, with yellow on one side and magenta on the opposite, to clearly bring about the chirality of the assembly.

ns as reference. In Figure. 5A.11(a),(b) we show the same quantity calculated with the structure at 28 ns and 29 ns as reference respectively. The near invariance in

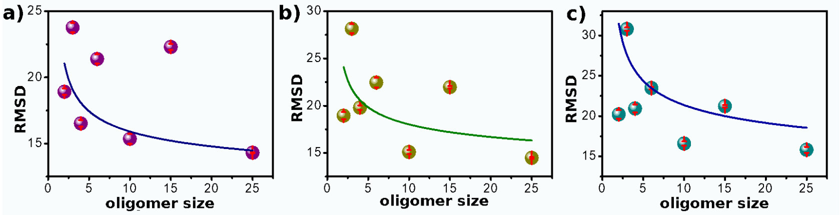

Figure 5A.14: RMSD of various oligomers of ATP-**1** with different reference frame chosen for the calculation of RMSD: (a). 28 ns, (b). 29 ns and (c). 30 ns. The error bars were calculated using the standard error formalism, by considering the RMSD data over time as blocks.

the behaviour of IOP confirms that the results are independent of the choice of the reference frame. The IOP tells us about the arrangement of (consecutive molecules in an oligomer) with respect to a free dimer. In the case a free dimer we observed a very large lateral slip and almost no twist when compared to an initial configuration which leads to a high IOP. As molecules in longer stacks exhibit a significant twist angle, their lower values of IOP imply lower fluxionality and greater stability of the stack implying chirality.

While performing simulation on systems with various oligomer sizes, we observed that the molecules in shorter oligomers exhibit structural differences with this initial configuration such as deviation in the twist angle along with a slip between the consecutive molecules. The fluxionality of the oligomers is estimated using RMSD, which is calculated with reference to a configuration, chosen arbitrarily, from a well-equilibrated run. The RMSD helps us in investigating the deviation of the twist angle as well as the slip distance from such reference structures. RMSD itself shows a weak decreasing dependence on oligomer size is shown in Figure. 5A.14. Remarkably, this is in line with the increase in number of intermolecular H-bonds per ATP with the increase in oligomer size, seen in the simulated assemblies (Figure. 5A.11(b), green curve). Further, the lesser RMSD in the higher oligomers ensures the enhanced chirality (See Figure. 5A.13) in the stacks, which explains the lag time between the absorbance and CD spectra shown in Figure. 5A.2.

5A.4 Conclusions

In conclusion, we have provided a model for the self-assembled structure and showed that the proposed model is in agreement with many experimental observations, including the mole ratio of monomer to fuel for the self-assembly process. With the help of this proposed model, we performed MD simulations and successfully explained the supramolecular polymerisation of molecules in the exclusive presence of fuel, ATP. The polymerisation is realised through intermolecular hydrogen bonds between adjacent ATPs in the self-assembled structures. The difference in lag times observed in various spectroscopic and scattering techniques have been explained by simulating oligomers of ATP-**1**. The considerable slip distance between the adjacent molecules in the shorter oligomers lead to the formation of stable nuclei that elongate further to form a chiral stack in which the slip distances are reduced, leading to a compact stack.

Bibliography

[1] Aida, T.; Meijer, E.; Stupp, S. I. Functional supramolecular polymers. *Science* **2012**, *335*, 813–817.

[2] Teunissen, A. J.; van der Haas, R. J.; Vekemans, J. A.; Palmans, A. R.; Meijer, E. Scope and limitations of supramolecular autoregulation. *B CHEM SOC JPN* **2016**, *89*, 308–314.

[3] Praveen, V. K.; Ranjith, C.; Bandini, E.; Ajayaghosh, A.; Armaroli, N. Oligo (phenylenevinylene) hybrids and self-assemblies: versatile materials for excitation energy transfer. *Chem. Soc. Rev.* **2014**, *43*, 4222–4242.

[4] Dong, R.; Zhou, Y.; Huang, X.; Zhu, X.; Lu, Y.; Shen, J. Functional supramolecular polymers for biomedical applications. *Adv. Mater.* **2015**, *27*, 498–526.

[5] Morris, A. M.; Watzky, M. A.; Finke, R. G. Protein aggregation kinetics, mechanism, and curve-fitting: a review of the literature. *Biochimica et Biophysica Acta (BBA)-Proteins and Proteomics* **2009**, *1794*, 375–397.

[6] Shoffner, S. K.; Schnell, S. Estimation of the lag time in a subsequent monomer addition model for fibril elongation. *Phys. Chem. Chem. Phys.* **2016**, *18*, 21259–21268.

[7] Dennington, R.; Keith, T.; Millam, J. Semichem Inc. *Shawnee Mission KS, GaussView, Version* **2009**, *5*.

[8] Hutter, J.; Iannuzzi, M.; Schiffmann, F.; VandeVondele, J. cp2k: atomistic simulations of condensed matter systems. *WIREs Comput Mol Sci* **2014**, *4*, 15–25.

[9] Goedecker, S.; Teter, M.; Hutter, J. Separable dual-space Gaussian pseudopotentials. *Phys. Rev. B* **1996**, *54*, 1703.

[10] Perdew, J. P.; Burke, K.; Ernzerhof, M. Generalized gradient approximation made simple. *Phys. Rev. Lett.* **1996**, *77*, 3865.

[11] Grimme, S.; Antony, J.; Ehrlich, S.; Krieg, H. A consistent and accurate ab initio parametrization of density functional dispersion correction (DFT-D) for the 94 elements H-Pu. *J. Chem. Phys.* **2010**, *132*, 154104.

[12] Mayo, S. L.; Olafson, B. D.; Goddard, W. A. DREIDING: a generic force field for molecular simulations. *J. Phys. Chem.* **1990**, *94*, 8897–8909.

[13] Jorgensen, W. L.; Chandrasekhar, J.; Madura, J. D.; Impey, R. W.; Klein, M. L. Comparison of simple potential functions for simulating liquid water. *J. Chem. Phys.* **1983**, *79*, 926–935.

[14] Mikata, Y.; Ugai, A.; Ohnishi, R.; Konno, H. Quantitative fluorescent detection of pyrophosphate with quinoline-ligated dinuclear zinc complexes. *Inorg. Chem.* **2013**, *52*, 10223–10225.

[15] Plimpton, S. Fast parallel algorithms for short-range molecular dynamics. *J. Comput. Phys.* **1995**, *117*, 1–19.

[16] Humphrey, W.; Dalke, A.; Schulten, K. VMD: visual molecular dynamics. *J. Mol. Graphics* **1996**, *14*, 33–38.

[17] Martínez, L.; Andrade, R.; Birgin, E. G.; Martínez, J. M. PACKMOL: a package for building initial configurations for molecular dynamics simulations. *J. Comput. Chem.* **2009**, *30*, 2157–2164.

[18] Dautel, O. J.; Wantz, G.; Almairac, R.; Flot, D.; Hirsch, L.; Lere-Porte, J.-P.; Parneix, J.-P.; Serein-Spirau, F.; Vignau, L.; Moreau, J. J. Nanostructuration of phenylenevinylenediimide-bridged silsesquioxane: from electroluminescent molecular J-aggregates to photoresponsive polymeric H-aggregates. *J. Am. Chem. Soc.* **2006**, *128*, 4892–4901.

[19] Delbosc, N.; Reynes, M.; Dautel, O. J.; Wantz, G.; Lère-Porte, J.-P.; Moreau, J. J. Control of the aggregation of a phenylenevinylenediimide chromophore by use of supramolecular chemistry: enhanced electroluminescence in supramolecular organic devices. *Chem. Mater.* **2010**, *22*, 5258–5270.

Chapter 5B

Microscopic Insights from Quantum Chemical Calculations to Explore Lagtime in Spectroscopic Measurements

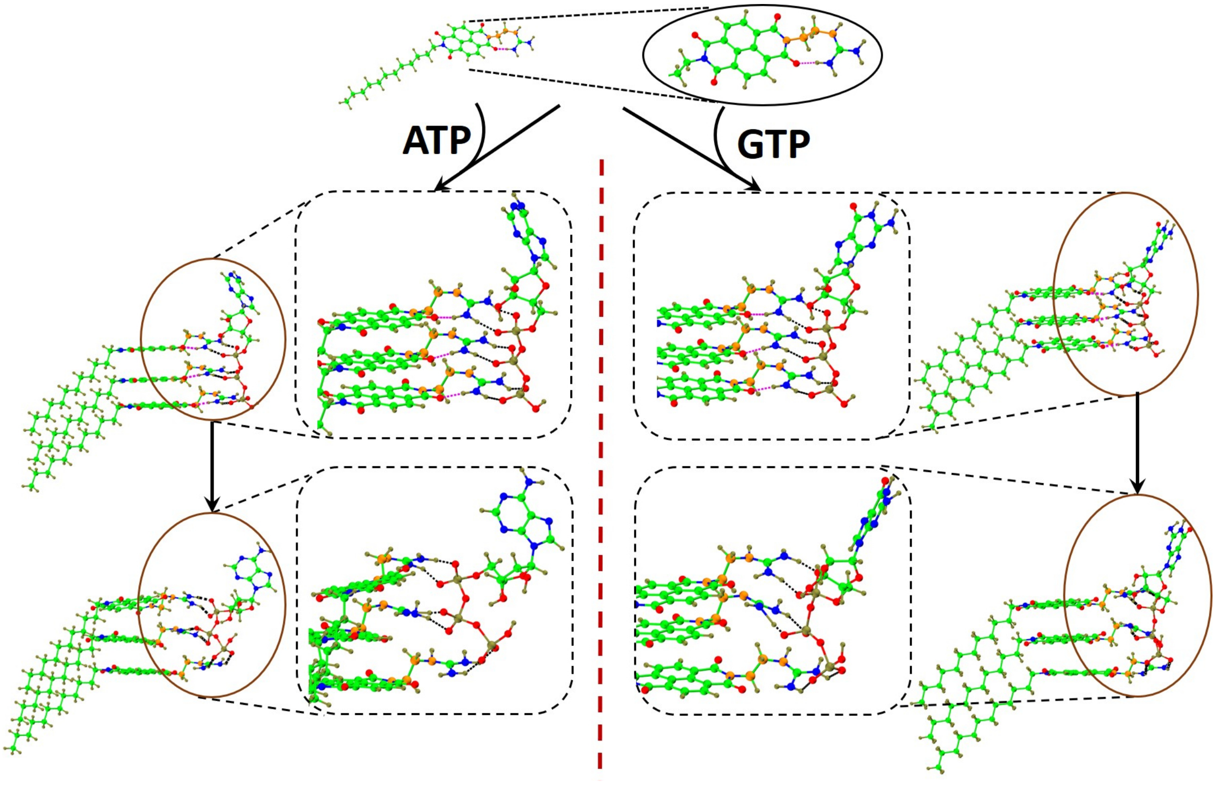

5B.1 Introduction

In the recent past, the field of supramolecular polymerisation focused on strategies to achieve control over the length and dispersity of supramolecular polymers. In order to fulfil this goal, nucleated- or seeded- self-assembly, or chain-growth mechanism have been employed in several studies. [1–5] In nucleated- and seeded self-assemblies, monomers undergo polymerisation on nuclei and pre-existing seeds, respectively, rather than forming new nuclei. In chain-growth mechanism, monomers polymerise on the initiator. An alternative approach towards realising the same objective is fuel-driven supramolecular polymerisation, [6] inspired by biological systems having spatial and temporal control over the self-assembly. [7] In this approach, the fuel modifies the non-covalent interactions between the monomers and drives the system towards self-assembly. However, how the interactions among the molecules in the self-assembled structures are altered was not well understood from the spectral changes observed experimentally. In Chapter 4A, we discussed ATP-driven self-assembly of OPV-DPA molecules, where we elucidated the spectral changes corresponding to the binding of ATP to OPV-DPA molecules.

In the present chapter, DFT calculations have been performed to find out the structural changes occurring in the self-assembling moiety **Amph-NDG** (naphthalene diimide appended with guanidinium receptor) upon binding with ATP (NDG-ATP) or GTP (NDG-GTP). The chemical structures of **Amph-NDG**, ATP, and GTP are shown in Figure. 5B.1. The growth mechanisms of NDG-ATP and NDG-GTP were studied through spectroscopic measurements by George and co-workers at 0.35 equiv. of ATP and GTP respectively. They found that the self-assembly of **Amph-NDG** proceeds in the presence of either ATP or GTP, the signatures of which are seen in the corresponding spectra provided in Figure. 5B.2.

5B.2 Quantum Chemical Calculations

The structures of **Amph-NDG** along with ATP and GTP were optimised using Gaussian Plane Waves (GPW) method, as implemented in the QUICKSTEP [8] module of CP2K. [9] The gaussians were mapped onto five grid levels, and the planewave cut-off is set to be 280 Ry. The exchange-correlation term was treated with the generalized gradient approximation parameterized by the spin-polarized Perdew-Burke-Ernzerhof (PBE) functional. [10] The Goedecker-Teter-Hutter (GTH) pseudopotentials [11, 12]

Reprinted with permission from “Bioinspired, ATP-driven co-operative supramolecular polymerization and its pathway dependence” *Chem. Comm.* **2020**, *56*, 1505-1508. © 2020, Royal Society of Chemistry, https://doi.org/10.1039/C9CC08790G.

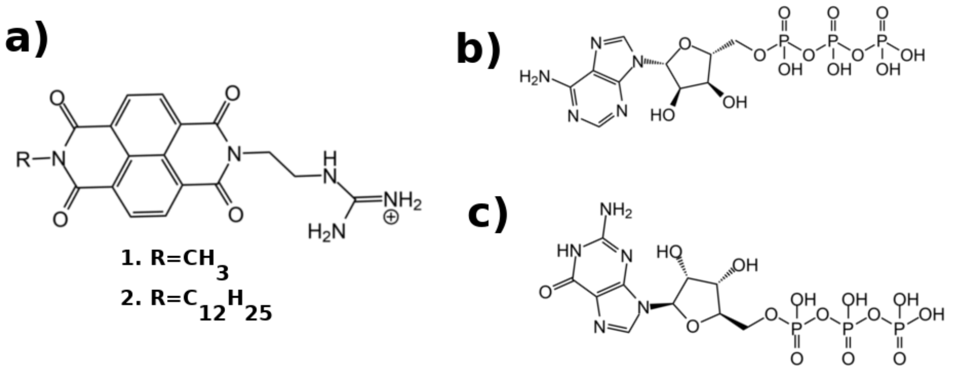

Figure 5B.1: Molecular structures (a) **Amph-NDG**, (b) adenosine triphosphate (ATP) and (c) guanosine triphosphate (GTP)

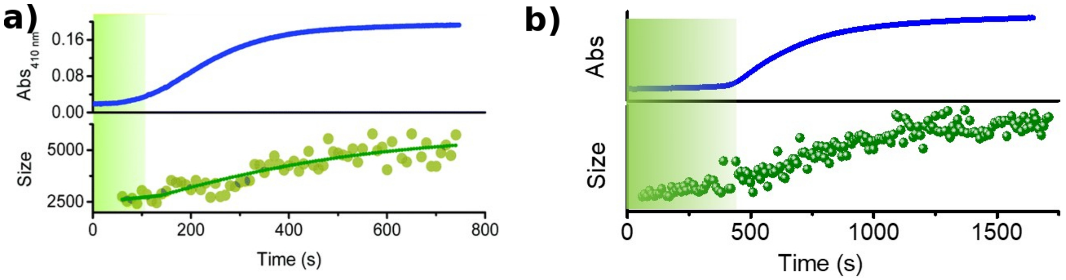

Figure 5B.2: Experimentally determined, growth kinetics and lag phases of (a) ATP-driven, and (b) GTP-driven nucleation growth of **Amph-NDG** monitored by absorbance spectra. Data from experimental collaborators.

were used to represent the effective potential from the nucleus and core electrons of an atom. The dispersion corrections were taken care by the Grimme [13] DFT-D3 method. DZVP-MOLOPT-SR-GTH basis set was used to represent the electronic wavefunctions in the density-functional theory (DFT). The preformed trimer was kept in an orthogonal box of dimensions {30, 50, 40} Å and the stacks were oriented along Z-axis.

A relaxed dihedral scan has been performed on **Amph-NDG** (Figure. 5B.1a1) using Gaussian package [14] at M06-2x/6-311g level of theory in steps of 5°.

5B.3 Modelling of self-assembled structures

We proposed a model structure which has three **Amph-NDG** bound to ATP as shown in Figure. 5B.3a. A trimer of **Amph-NDG** was constructed with an initial π-π distance of 4.0 Å along with a twist angle of 2.5° between the cores of neighbouring **Amph-NDG** molecules. In order to construct a trimer of NDG-ATP, ATP was placed such that each of its phosphate groups can interact with an imide (phosphate receptor) of one **Amph-NDG**. A trimer of NDG-GTP was built in the same way. The proposed model has been validated by comparing the computed width of a bilayer of NDG-ATP with that measured from experiments. The bilayer was constructed as follows:

- A bilayer of NDG-ATP trimer was constructed from a preformed trimer of NDG-ATP, and its mirror image with respect to Z-axis translated in XY-plane by the vector (-1.0, 10.0) Å.
- The bilayer 18-mer was constructed from six bilayer trimer units such that the neighbouring units have a twist angle of 6° and are separated by 11.7 Å along the z-direction.

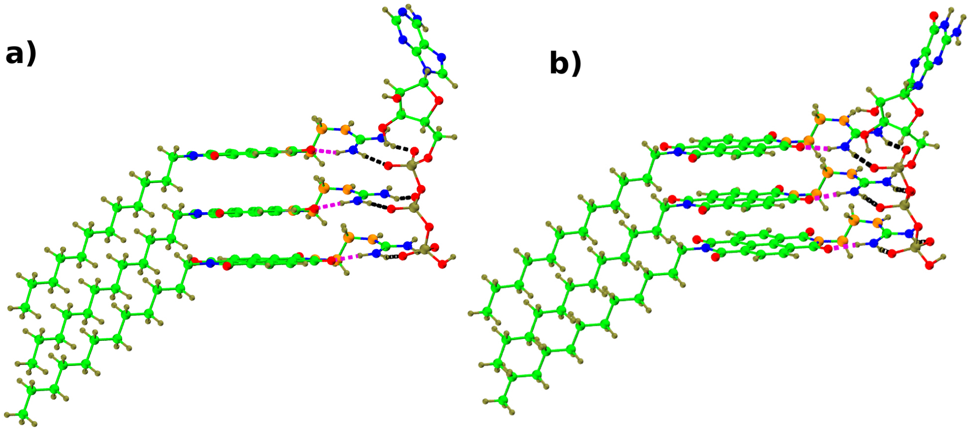

Figure 5B.3: Model structures of **Amph-NDG** bound to (a) adenosine triphosphate (ATP) and (b) guanosine triphosphate (GTP). Colour scheme: Green and orange - Carbon, Red - oxygen, Blue - Nitrogen, Tan - Hydrogen and the dotted lines (Magenta - inter and black -intra) represent hydrogen bonds.

5B.4 Results and discussion

Amph-NDG has the ability to form an intramolecular hydrogen bond between the guanidinium N−H and C=O group in **Amph-NDG**, similar to the molecule reported by Würthner and co-workers earlier. [5, 15] The intramolecular hydrogen bond enforces the molecule to present in a dormant state and its stability was confirmed from the geometry optimisation at M06-2x/6-311g level of theory using Gaussian package. [14] The initial and final structures of monomer (with the dodecyl chain replaced by a methyl group to decrease computational cost) of the geometry optimisation are shown in Figure. 5B.4. The stability of intramolecular hydrogen bond is further supported by a relaxed dihedral scan at M06-2x/6-311g level of theory, as seen from the corresponding potential energy surface shown in Figure. 5B.4d. The structure of the molecule at the global minimum of potential energy surface is shown in Figure. 5B.4c.

Experimentally, the dormant conformation of the monomer was found to be stable until ATP/GTP binding induces the activation of the monomers, thus triggering the

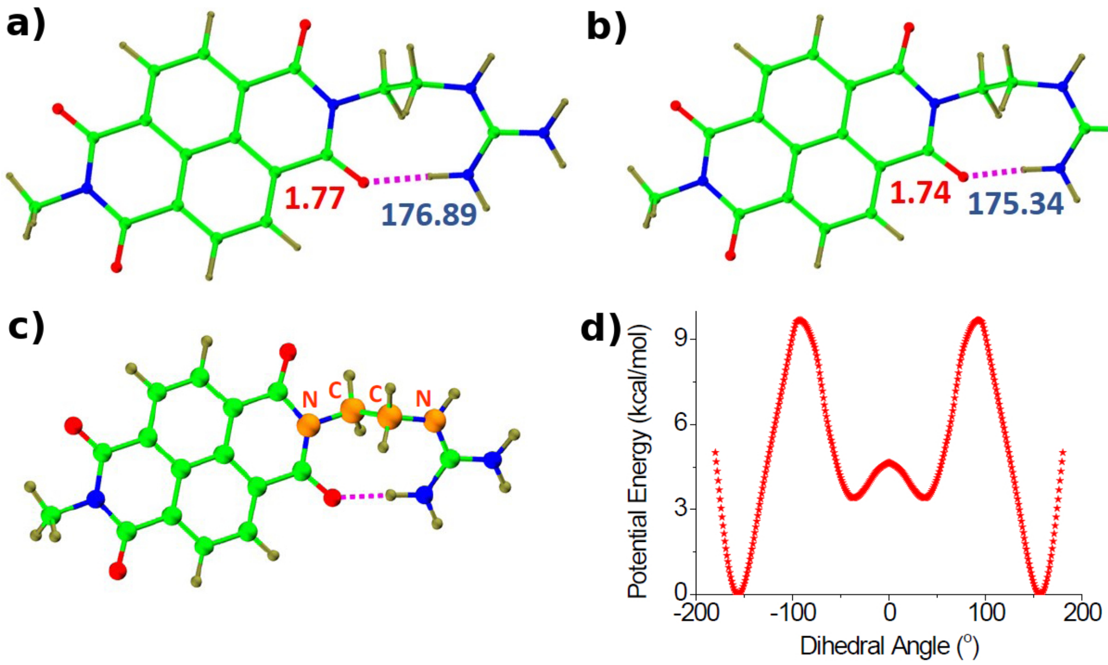
a)
1.77
176.89
b)
1.74
175.34
c)
N
C
C
N
d)
Potential Energy (kcal/mol)
0
3
6
9
-200
-100
0
100
200
Dihedral Angle (°)

Figure 5B.4: Quantum chemical calculations at M06-2x/6-311g level of theory (a) Initial, (b) final conformation of **Amph-NDG**, the intramolecular hydrogen bond distance is shown in magenta and the O−H−N (acceptor-hydrogen-donor) angle is shown in blue. (c) structure of **Amph-NDG** at global minimum on the potential energy surface for N−C−C−N dihedral angle, and the atoms corresponding to dihedral scan are shown in orange and (d) potential energy surface. Colour scheme is same as Figure. 5B.3.

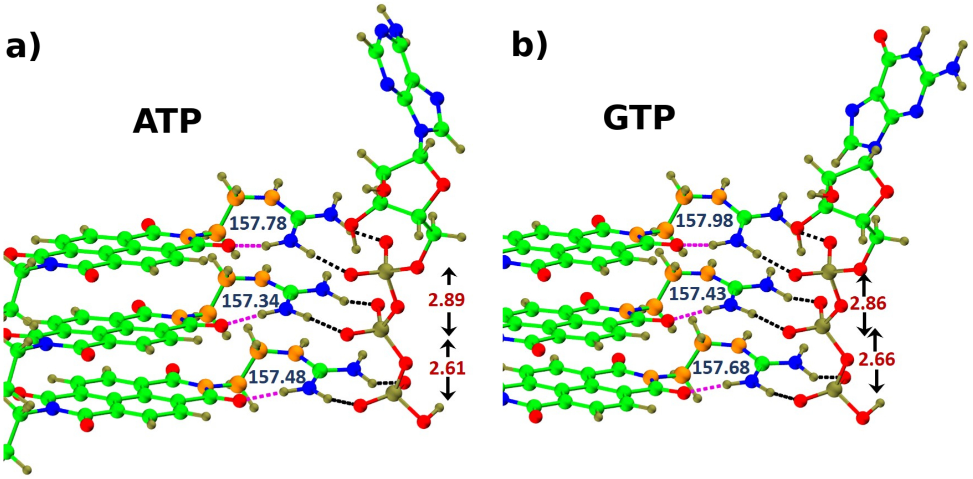
a)
ATP
157.78
157.34
157.48
2.89
2.61
b)
GTP
157.98
157.43
157.68
2.86
2.66

Figure 5B.5: Initial configurations of a trimer of (a) NDG-ATP and (b) NDG-GTP. The intramolecular hydrogen bond distance is shown in red and the O−H−N (acceptor-hydrogen-donor) angle is shown in blue. Colour scheme is same as Figure. 5B.3

growth process. In order to understand this, the constructed trimers of NDG-ATP and NDG-GTP were optimised at PBE-D3 level of theory in an orthogonal box of

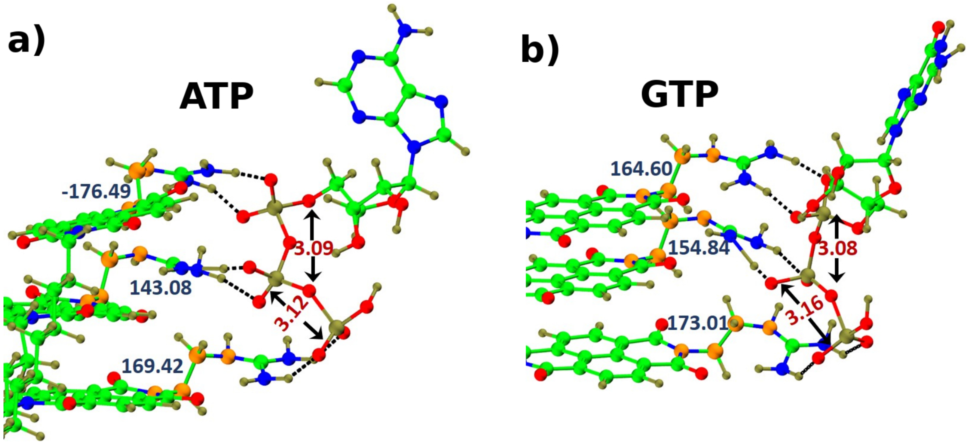

Figure 5B.6: Final configurations of trimer of (a) NDG-ATP and (b) NDG-GTP from geometry optimisations performed at PBE-D3 level of theory. The intramolecular hydrogen bond distance is shown in red and the O−H−N (acceptor-hydrogen-donor) angle is shown in blue. Colour scheme is same as Figure. 5B.3

dimension {30, 40, 50} Å. In the initial configuration of NDG-ATP trimer, the P−P (from PO_4^{3-}) distances are 2.61 and 2.89 Å respectively (Figure. 5B.5a), whereas in the case of NDG-GTP trimer (Figure. 5B.5b), they are 2.66 and 2.86 Å. Upon geometry optimisation, it was found that the intramolecular hydrogen bond between guanidinium N−H and imide C=O breaks by rotation of the N−C−C−N bond, so as to render a P−P distance of 3.09 Å which is close to the value reported in the crystal structure of ATP. [16] The increase in P−P distance, in turn, increases the distance between the guanidinium units of two adjacent **Amph-NDG** in NDG-ATP trimer from 3.9 Å to 4.8 Å. Consequently, the centroid-centroid distance between the π rings also changes (Figure. 5B.6a). A similar trend is seen in the case of NDG-GTP trimer as well, as seen from the values tabulated in Table. 5B.1.

Table 5B.1: Structural properties of optimised geometries of trimers of NDG-ATP and NDG-GTP at PBE-D3 level of theory

Parameters	**NDG-ATP**	**NDG-GTP**
gaunidinium-guanidinium distance (Å)	4.8	4.8
centroid-centroid distance (Å)	4.4	4.4
	4.2	3.8
P−P distance (Å)	3.09	3.08
	3.12	3.16

The addition of ATP or GTP brought about a structural rearrangement that requires bond rotation leading to the rupture of the intramolecular hydrogen bonds, the time taken for which is observed as lag time in self-assembly (See Figure 5B.2). These results are further supported by variable temperature ^{1}H NMR experiments of Amph-NDG dissolved in DMSO (molecularly dissolved state) which showed a broad N$-$H proton peak around 7.15 ppm value which evolved into a sharp peak on increasing the temperature from 25 °C to 70 °C, indicating the breakage of the intramolecular hydrogen bond between guanidinium N$-$H and imide C$=$O $\cdot$ Further, we performed geometry optimisation on the bilayer 18-mer of NDG-ATP using semi-empirical PM6 method. The measured width of the geometry optimised bilayer is $\sim$ 6.6 nm, which is in good agreement with bilayer height $\sim$ 7 nm, as measured from AFM images.

5B.5 Conclusions

The fuel-driven self-assembly of **Amph-NDG** and the associated lag time were studied using UV-Vis absorption spectroscopy. The possible model structures for NDG-ATP and NDG-GTP systems have been proposed, and the model structure for NDG-ATP system was substantiated with height profiles of NDG-ATP from atomic force microscopy and the monomer to ATP molar ratio in the self-assembly. Zero Kelvin DFT calculations have been performed to identify the viable changes in self-assembled structures. The dormant state of **Amph-NDG** monomer was found to have an intramolecular hydrogen bond between guanidinium N$-$H and C$=$O group, from geometry optimisation and relaxed dihedral scan. The existence of the dormant state precludes self-assembly. Upon addition of triphosphates (either ATP or GTP), the interaction between the imide group of guanidinium and phosphate group of triphosphate (from either ATP or GTP) triggers the dihedral rotation in **Amph-NDG**, as a consequence of which, the intramolecular hydrogen bond breaks. The time spent in undergoing this structural rearrangement has been ascribed to the experimentally observed lag time.

Bibliography

[1] Besenius, P. Controlling supramolecular polymerization through multicomponent self-assembly. *J. Polym. Sci., Part A: Polym. Chem.* **2017**, *55*, 34–78.

[2] Pal, A.; Malakoutikhah, M.; Leonetti, G.; Tezcan, M.; Colomb-Delsuc, M.; Nguyen, V. D.; van der Gucht, J.; Otto, S. Controlling the structure and length of self-synthesizing supramolecular polymers through nucleated growth and disassembly. *Angew. Chem. Int. Ed.* **2015**, *54*, 7852–7856.

[3] Robinson, M. E.; Lunn, D. J.; Nazemi, A.; Whittell, G. R.; De Cola, L.; Manners, I. Length control of supramolecular polymeric nanofibers based on stacked planar platinum (II) complexes by seeded-growth. *Chem. Commun.* **2015**, *51*, 15921–15924.

[4] Fukui, T.; Sasaki, N.; Takeuchi, M.; Sugiyasu, K. Living supramolecular polymerization based on reversible deactivation of a monomer by using a 'dummy' monomer. *Chem. Sci.* **2019**, *10*, 6770–6776.

[5] Kang, J.; Miyajima, D.; Mori, T.; Inoue, Y.; Itoh, Y.; Aida, T. A rational strategy for the realization of chain-growth supramolecular polymerization. *Science* **2015**, *347*, 646–651.

[6] Dhiman, S.; George, S. J. Temporally controlled supramolecular polymerization. *B CHEM SOC JPN* **2018**, *91*, 687–699.

[7] not listed, A. Spatiotemporal mechanisms of life. *Nat. Chem. Biol.* **2007**, *3*, 593.

[8] VandeVondele, J.; Krack, M.; Mohamed, F.; Parrinello, M.; Chassaing, T.; Hutter, J. Quickstep: Fast and accurate density functional calculations using a mixed Gaussian and plane waves approach. *Comput. Phys. Commun.* **2005**, *167*, 103–128.

[9] Hutter, J.; Iannuzzi, M.; Schiffmann, F.; VandeVondele, J. cp2k: atomistic simulations of condensed matter systems. *WIREs Comput Mol Sci* **2014**, *4*, 15–25.

[10] Perdew, J. P.; Ruzsinszky, A.; Tao, J.; Staroverov, V. N.; Scuseria, G. E.; Csonka, G. I. Prescription for the design and selection of density functional approximations: More constraint satisfaction with fewer fits. *J. Chem. Phys.* **2005**, *123*, 062201.

[11] Hartwigsen, C.; Gœdecker, S.; Hutter, J. Relativistic separable dual-space Gaussian pseudopotentials from H to Rn. *Phys. Rev. B* **1998**, *58*, 3641.

[12] Goedecker, S.; Teter, M.; Hutter, J. Separable dual-space Gaussian pseudopotentials. *Phys. Rev. B* **1996**, *54*, 1703.

[13] Grimme, S.; Antony, J.; Ehrlich, S.; Krieg, H. A consistent and accurate ab initio parametrization of density functional dispersion correction (DFT-D) for the 94 elements H-Pu. *J. Chem. Phys.* **2010**, *132*, 154104.

[14] others,, et al. Gaussian 09 Revision D. 01, 2009, Gaussian Inc. *Wallingford CT* **2009**, *93*.

[15] Ogi, S.; Stepanenko, V.; Sugiyasu, K.; Takeuchi, M.; WuÌĹrthner, F. Mechanism of self-assembly process and seeded supramolecular polymerization of perylene bisimide organogelator. *J. Am. Chem. Soc.* **2015**, *137*, 3300–3307.

[16] Kennard, O.; Isaacs, N. W.; Motherwell, W.; Coppola, J.; Wampler, D.; Larson, A. t.; Watson, D. The crystal and molecular structure of adenosine triphosphate. *Proceedings of the Royal Society of London. A. Mathematical and Physical Sciences* **1971**, *325*, 401–436.

Chapter 6

Exploring the lag phase and lag times of supramolecular polymers: Free Energy Simulations

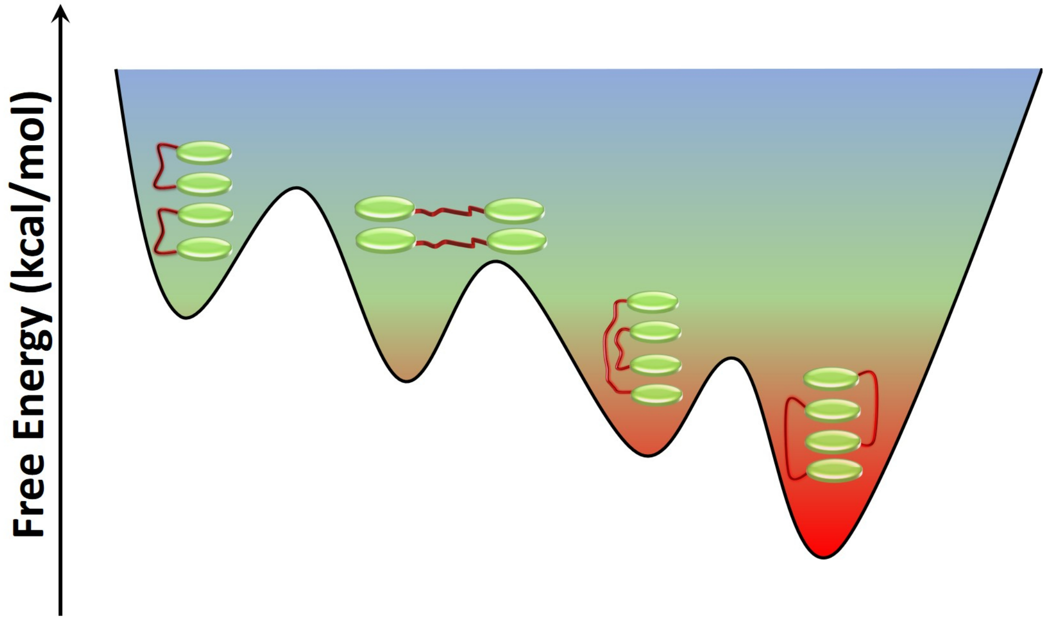
Free Energy (kcal/mol)

6.1 Introduction

Supramolecular polymers are formed through non-covalent interactions between the monomers units. [1] Since non-covalent interactions are weak (with interaction energies lesser than 20 kcal/mol), such polymers in solution can break and reform. Many of the supramolecular polymers are formed under thermodynamic control. Hence supramolecular polymerisation is focused predominantly on equilibrium structures. However, the performance of polymeric materials is highly dependent on the morphology and order in these materials. [2] Over the last decade, it has been shown that thermodynamically metastable aggregates can be formed under kinetic control by exploiting the complexity in the pathways of polymerisation. [3–7] The outcomes of such processes are dictated by the pathway of self-assembly rather than the free energy of the final state. Herein, the systems (monomers or short oligomers) trapped in a local minimum of the free energy landscape lead to the formation of non-equilibrium structures. In a complex free energy surface, many different non-equilibrium states can exist, and each of these states can impart a unique set of functional properties to the polymer — different from those of the equilibrium state.

The free energy landscape for the oligomerization of a given molecule depends on several parameters such as temperature, solvent composition, and salt concentration. [8] Depending on the relative orientations of the monomers, the aggregates can be either H-aggregates or J-aggregates. Formation of H- and J-aggregates of molecule follow different mechanisms of self-assembly, thus influencing its supramolecular packing motifs and finally, the properties of self-assembled structures. [9–11] While the morphology of the supramolecular polymer is largely determined by the structure of the monomer, recent studies show that tuning the experimental conditions employed during the polymerisation can affect the morphology of the aggregate. [12–17]

In non-dissipative polymerisation, there are three possible states namely, thermodynamically stable state (global minimum), metastable state and kinetically trapped state as shown in the free energy landscape in Figure. 6.1 Depending on the free energy barrier ΔG that separates the kinetic product from the thermodynamically stable product, the former can be formed from metastable ($\Delta G \sim k_B T$) or kinetically trapped state ($\Delta G \gg k_B T$).

Decades ago, proteins were shown to follow the nucleation-elongation mechanism to reach the kinetically controlled assembled structures. [18–20] However, independent studies on supramolecular polymers by Korevaar *et al.*, [7] bridged the gap between the natural protein fibrils and synthetic nanofibres, to explore the pathway complexity. Natural systems show advanced functionality through the kinetic self-assembly

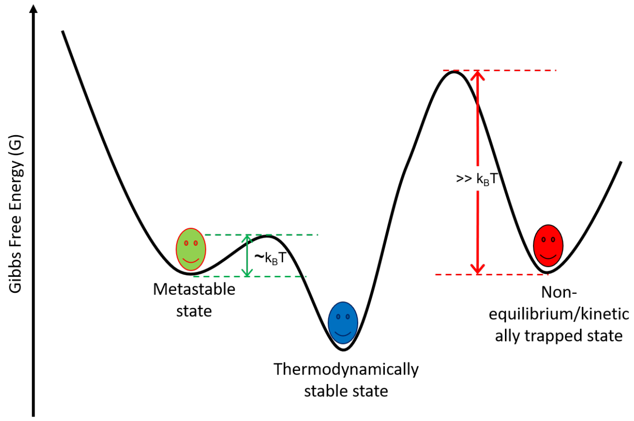
Gibbs Free Energy (G)
~k$_B$T
>> k$_B$T
Metastable state
Thermodynamically stable state
Non-equilibrium/kinetically trapped state

Figure 6.1: Schematic representation of the free-energy landscape of pathway complexity in supramolecular polymer.

process. [21, 22] The morphology, chirality, and polydispersity of kinetically controlled supramolecular aggregates depend on preparation methods such as the cooling rates, [7, 23–26] solvent processing, [27–34] external stimuli, [35–37] and photochemical conditions. [38] Polymers formed via such routes find many applications. [39]

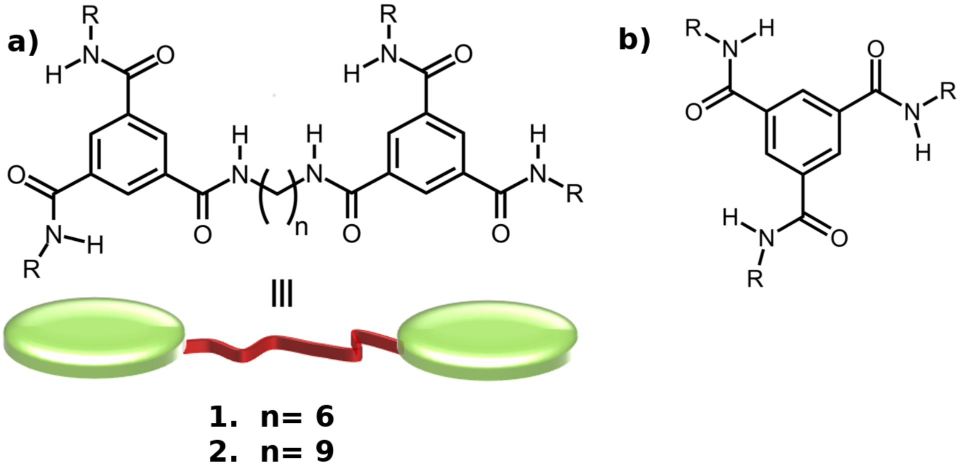

Figure 6.2: Structure of the molecules studied here. (a) N1,N1-(n-alkane-1,n-diyl)bis(N3,N5-dialkylbenzene-1,3,5-tricarboxamide), R=$C_{12}H_{25}$ — BnB and (b) N,N′,N″-1,3,5,benzene tricarboxamide (BTA).

Several experimental works and reviews on non-equilibrium self-assembly have been reported. [40–42] In this chapter, we focus on identifying conformationally and configurationally locked monomers and dimers, and obtain their relative stabilities. Furthermore, we obtain the minimum free energy pathways that connects these states and identifying the transition states. Such investigation allows one to understand the emergence of pathway complexity in a pedagogical system. Towards this aim, we chose a molecule, which is made up of two N,N′,N″-1,3,5-benzene tricarboxamide

(BTA) (shown in Figure. 6.2b) units, connected by an n-alkane-1,n-diyl linker with varying lengths (n). The molecule under study is N1,N1-(n-alkane-1,n-diyl)bis(N3,N5-dialkylbenzene-1,3,5-tricarboxamide) (shown in Figure 6.2a), and its relationship to BTA is obvious from its structure shown in Figure. 6.2b.

6.2 Computational Details:

6.2.1 Quantum Chemical Calculations:

Charge Calculations:

The partial charges on the atoms of the molecule were calculated from the valence electron density using Density Derived Electrostatic and Chemical (DDEC/c3) [43] approach. The valence electron density of an optimised monomer from DFT calculations at PBE-D3 level theory using the CP2K [44] software. Cube files of electron density thus generated were used as inputs to the DDEC/c3 [45] code to obtain atomic site charges.

Geometry Optimization:

Molecular structures were optimized using Gaussian and plane waves (GPW) method, wherein the Gaussians are mapped onto five grid levels. The finest level of the multigrid plane-wave cutoff is set to be 280 Ry, as implemented in the QUICKSTEP [46] module of CP2K package. [44] The exchange-correlation potential was treated with the generalized gradient approximation parametrized by the spin-polarized Perdew-Burke-Ernzerhof functional (PBE). [47] The Goedecker-Teter-Hutter (GTH) pseudopotentials [48, 49] are used to represent the effective potential from core electrons of an atom along with its nucleus. Dispersion corrections are taken care of by the Grimme [50] DFT-D3 method. DZVP-MOLOPT-SR-GTH basis set is used to represent the electronic wave function in density functional theory (DFT).

6.2.2 Force field based Molecular Dynamics (MD) Simulations:

Molecular Modelling:

The solute molecules were represented in an all-atom model, with the atoms considered as point particles carrying the charges obtained as mentioned earlier. The initial structures were constructed using GaussView. [51] General AMBER force field (GAFF) [52] is used to model the intermolecular interactions. The general potential term with atomic Cartesian coordinate vector $\vec{r_i}$ can be written as:

$$\begin{aligned} V_{solute}(r) = \sum_{bonds} K_r(r-r_{eq})^2 + \sum_{angles} K_\theta(\theta-\theta_{eq})^2 + \\ \sum_{dihedrals} \frac{K_n}{2}[1+cos(n\phi-\gamma)] + \\ \sum_{i<j} 4\epsilon_{ij}\left[\left(\frac{\sigma_{ij}}{r_{ij}}\right)^{12} - \left(\frac{\sigma_{ij}}{r_{ij}}\right)^{6} + \frac{q_i q_j}{r_{ij}}\right] \end{aligned} \tag{6.1}$$

n-nonane is considered as the solvent and these molecules are represented in united atom model with forcefield parameters taken from transferable potentials for phase equilibria (TraPPE) force field. [53] The potential form is:

$$\begin{aligned} V_{solvent}(r) = \sum_{bonds} K_r(r-r_{eq})^2 + \sum_{angles} K_\theta(\theta-\theta_{eq})^2 \\ + \sum_{dihedrals} [c_1(1+cos(\phi)) + c_2(1-cos(2\phi)) + \\ c_3(1+cos(3\phi))] + \sum_{i<j} 4\epsilon_{ij}\left[\left(\frac{\sigma_{ij}}{r_{ij}}\right)^{12} - \left(\frac{\sigma_{ij}}{r_{ij}}\right)^{6}\right] \end{aligned} \tag{6.2}$$

The interactions between unlike atoms are computed using the standard Lorentz-Berthelot combining rules. Thus, the system contains solute molecules in all-atom representation and solvent molecules in united atom representation. Such mixed approach was employed to reduce computational cost which would ensue had the solvent been treated at the all-atom level. In the current problem, the solvent is largely passive, and therefore, reducing the degrees of freedom would not affect the conclusions of this study.

Simulation Setup:

MD simulations were carried out using Gromacs-2018.3 [54] suite. The same suite patched with PLUMED-2.5.0 [55] was used for enhanced sampling calculations. All the energy minimizations were done using the conjugate gradient method. Verlet list was used to calculate non-bonded interaction energy within a cutoff of 1.5 nm. Long-range electrostatic interactions were calculated using particle mesh Ewald (PME) [56] approach. The atomic positions were updated once every 1 fs using a leap-frog integrator with all the bonds constrained using LINCS algorithm. [57] During the equilibration runs, the temperature was maintained at 298.15 K using v-rescale thermostat [58] with a coupling constant of 1 ps. The initial velocities were drawn from a Maxwell-Boltzmann distribution at 298.15 K. Pressure was maintained at 1 atm using Berendsen barostat [59] with a coupling constant of 1 ps. The atomic coordinates were stored once every 5 ps for post-processing.

6.3 Results and Discussions:

The molecules under study namely, B6B and B9B have two phenyl cores functionalized with amide groups which are connected by an n-alkane-1,n-diyl linker of varying lengths (n=6,9); corresponding chemical structures are shown in Figure 6.2a.

6.3.1 Gas Phase:

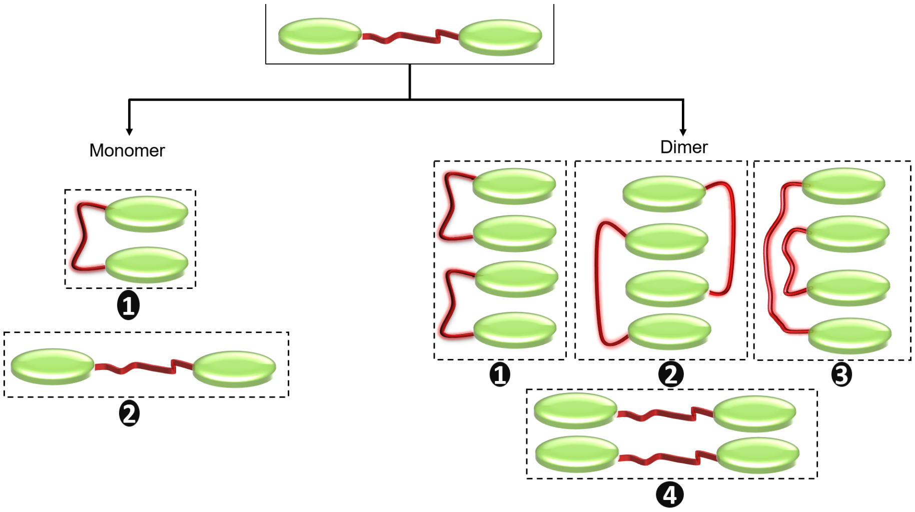

Figure 6.3: Schematic representation of possible monomer conformations and dimer configurations. Each configuration is labelled with a number for easy readability.

Monomer: Molecules B6B and B9B have three amide groups on each of their phenyl cores, which have the ability to form hydrogen bonds. Their monomers can exist in two conformations, folded and extended. The folded conformer can have three intramolecular hydrogen bonds, whereas the extended form cannot have any hydrogen bonds. A variety of other conformations with fewer than three hydrogen bonds and different relative orientations and positions of the two phenyl cores are also possible but are not discussed here. Furthermore, the amide groups on either phenyl cores can independently rotate about the $C_{aromatic}-C_{amide}$ bond, which allows for the possibility of the respective amide dipoles to be oriented either parallel or anti-parallel to each other. [60]. Herein, we consider them to be in 2:1 configuration of amide dipoles, as that would be the geometric ground state on electrostatic grounds. A brief discussion on these configuration was provided in Chapters 2 and 3. To estimate the relative stabilities of folded and extended conformations, we performed their gas phase geometry optimizations at PBE-D3 level of theory in a cubic box of linear dimension of 50 Å. In order to reduce the computational cost of these quantum calculations, we replaced the dodecyl side chains in B6B-, and B9B with methyl groups, and correspondingly the molecules are referred to as M-B6B, and M-B9B respectively. Further, the relative energies of these optimized structures were also evaluated from the force field, for a comparison against the quantum chemical results. The relative stabilities are tabulated (See Table 6.1) and a decent agreement (across the two methodologies, the signs of ΔE are the same, and the reduction in ΔE while going from n=6 to n=9 is also reproduced) between the values calculated from quantum and classical approaches validates the force field used in the present study.

Table 6.1: Energy difference between conformations of M-B*n*B monomer

ΔE = E_{ex}-E_{fold} (kcal/mol)		
Linker Length (*n*)	**Quantum**	**Forcefield**
6	36.27	23.35
9	23.30	18.84

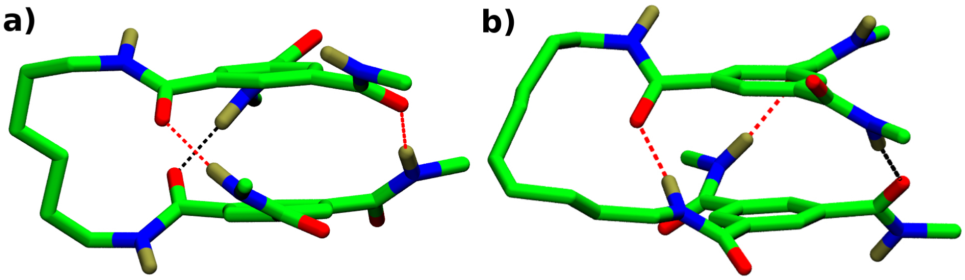

Figure 6.4: Optimized geometries of monomers from quantum chemical calculations. (a) M-B6B, and (b) M-B9B. Color Scheme: Green - Carbon, Red - Oxygen, Blue - Nitrogen and Tan - Hydrogen. The dotted lines represent the hydrogen bonds: Red - dipoles pointing above the phenyl core, Black - dipoles pointing down the phenyl core. The hydrogens which are not part of hydrogen bonding are not shown for clarity.

The geometry of folded conformations (shown in Figure 6.4) have three-fold hydrogen bonds similar to that of a BTA dimer. [61–64] The stability of the folded conformation is realised through π-π interaction between the phenyl cores and the formation of three intramolecular hydrogen bonds. Further, we calculated the dipole moments along the stacking direction of B6B and B9B from quantum chemical calculations and found it to be 4.5 Debye — independent of the linker length and comparable to the 5.04 Debye of a BTA dimer. [65]

Dimer: A dimer can exist in several configurations, and one can enumerate at least four distinct structures. One of these is the unfolded configuration, while the other three are in folded configuration, as shown in Figure 6.3. The construction of configuration 3 with all the hydrogen bonds intact is difficult due to short linker length. As expected, geometry optimizations of dimers of M-B6B, and M-B9B show that the folded configurations are stable when compared to the unfolded ones. The energy differences with respect to the geometric ground state are tabulated in Table 6.2.

Table 6.2: Energy difference between configurations of M-BnB dimer

ΔE = E_{config}-E_{ground} (kcal/mol)								
	Config 1		**Config 2**		**Config 3**		**Unfolded**	
Linker Length (n)	Quantum	Forcefield	Quantum	Forcefield	Quantum	Forcefield	Quantum	Forcefield
6	0.00	0.49	1.01	0.00	− − −	− − −	41.26	31.25
9	19.54	25.45	0.00	0.00	− − −	− − −	39.39	32.39

The folded configurations have 9 hydrogen bonds each, which includes both inter- and intra- molecular hydrogen bonds, whereas the unfolded dimer has 6 intermolecular hydrogen bonds. Among the possible folded dimer configurations, configuration 2 is energetically the most stable. In order to obtain insights into different pathways and the transition barriers en route these dimer configurations to the thermodynamically stable configuration, we generated the configurational free energy landscape at 298.15 K for both B6B and B9B.

6.3.2 Free energy calculations:

The free energy calculations were performed for B6B and B9B soaked in n-nonane at ambient conditions. A brief discussion of free energy methods employed in the present chapter was provided in chapter 1.

Monomer: The free-energy differences between the folded and extended conformations of a monomer of both B6B and B9B were estimated via umbrella sampling (US) approach. [66] For monomer free energy simulations, a monomer placed in a cubic box of side 7.5 nm, having 1150 molecules of n-nonane was considered. Systems were equilibrated for 5 ns in the NVT ensemble followed by equilibration in NPT ensemble for 10 ns.

The conformational space of a monomer has been explored by considering the radius of gyration (RG) as the reaction coordinate (RC) to characterize the transition between the folded and extended conformation of BnB (n=6 and 9). RG was defined based on atoms of all the carbons in the two phenyl rings. The RG values of the quantum chemical geometry optimized structures of folded and extended conformations are 0.23, and 0.78 nm respectively. In US, a series of windows were evenly located along the RC and the sampling of these windows was achieved by enforcing an external biasing harmonic potential with a spring constant 10000 kJ/mol/nm^2. Each window was sampled for 50 ns in the NVT ensemble at 298.15 K. After ensuring that there is adequate overlap between the RG probability distributions of the adjacent windows (Figure. 6.5) the free energy profiles were constructed using weighted histogram analysis method (WHAM). [67]

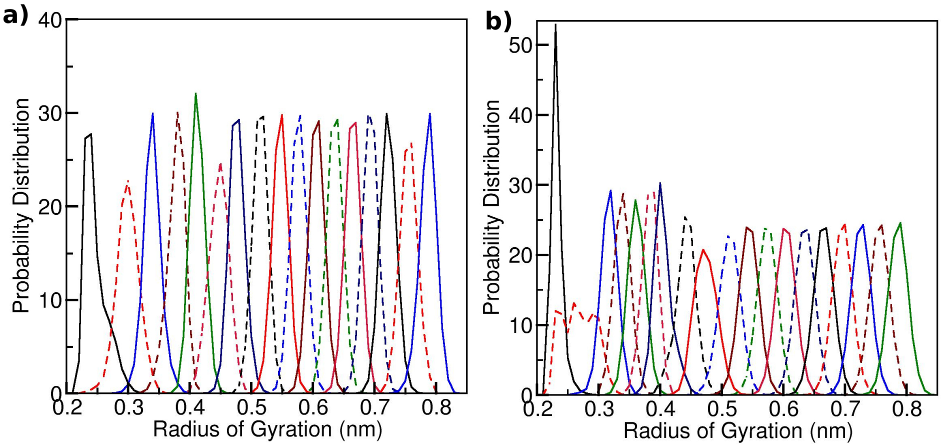

Figure 6.5: Probability distributions of reaction coordinate (RG) for all the windows from umbrella sampling simulations at 298.15 K. (a) for B6B and (b) for B9B.

For WHAM, we used the code written by Grossfield *et al.* [68] The upper and lower boundaries were set to 0.2 to 0.8 nm respectively. The number of bins was equal to 180, and the convergence tolerance was set to 10^{-10}. The free energy profiles along with schematic structures at important locations of RG are shown in Figure. 6.6a. The free energy differences (ΔF) between the extended and folded conformations for B6B and B9B are 4.98 and 5.49 kcal/mol, respectively, favoring the folded conformations. The free energy profiles with actual chemical structures obtained from cluster analyses for B6B and B9B are shown in Figure. 6.6b,c respectively.

Despite the folded monomer being structurally similar to the BTA dimer, dimerization free energy of BTA is much higher ($\sim$13.5 kcal/mol). [60, 65, 69] This disparity between the free energy differences can be attributed to the number of hydrogen bonds in the respective global minima — one in BnB (Figure. 6.6b,c) as opposed to three in BTA. We anticipate that the fewer number of hydrogen bonds in the BnB folded conformation is due to the higher $C_{aromatic}{-}C_{amide}$ torsional freedom at 298.15 K, as justified by the higher free energy difference of 8 kcal/mol and the presence of two hydrogen bonds (Figure. 6.6d) at the ground state as observed from the free energy profile of the BnB monomer at 50 K. The suppressed dihedral rotations at low temperatures allow the formation of two hydrogen bonds.

Dimer: Self-assembly pathway associated with several supramolecular systems have non-equilibrium, kinetic states, which are exploited to control the polydispersity and molecular weights of supramolecular polymers. [70, 71] The presence of kinetic

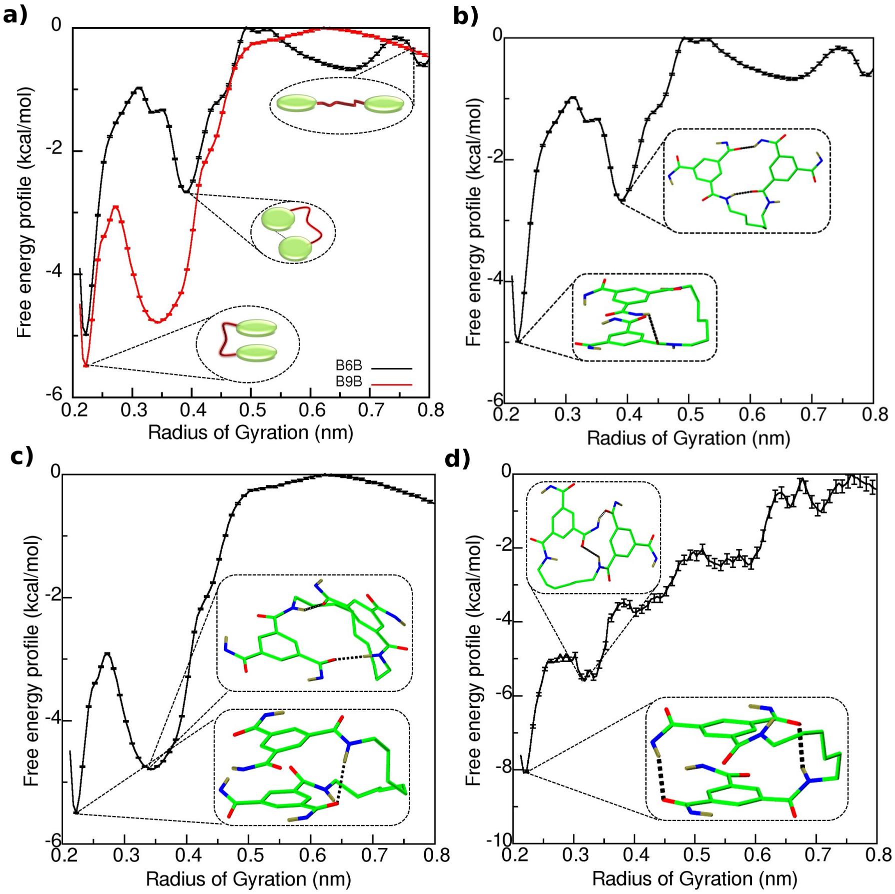

Figure 6.6: Free energy profiles of monomers in *n*-nonane. (a). For BnB molecules at 298.15 K, the schematics of structures contributing to various regions are shown. (b) for B6B, (c) for B9B with structures at 298.15 K and (d) for B6B at 50 K. The structures representing the different minima in the free energy profiles were obtained using cluster analysis as implemented in Gromacs *cluster* module.

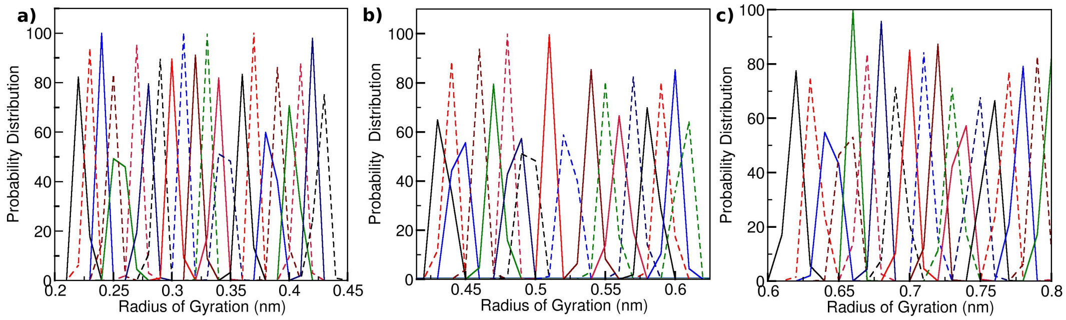

Figure 6.7: Probability distributions of reaction coordinate (RG) for all the windows of B6B free energy simulations at 50 K.

states can be experimentally found from thermal hysteresis in heating and cooling curves. [72] However, to the best of our knowledge, a detailed understanding of the non-equilibrium states and the transition barriers associated with them has not been reported till date. Towards this aim, we undertake a study of enumeration of several dimeric kinetically trapped states herein, obtain their relative free energies and also map out the lowest free energy pathways connecting them. Well-tempered metadynamics (WTM) simulations for both B6B and B9B systems were employed. The aim of these simulations is to estimate the free energy barriers for the transition from the non-equilibrium dimer configurations to the thermodynamically stable configuration. Therefore, the complete dissociation of dimers into monomers was prohibited by applying position restraints with a force constant of 10000 kJ/mol/nm^2 on the atoms of selected two phenyl rings of different molecules which were packed in such a way that they have π-π interactions.

Dimer Configuration	**Radius of Gyration (nm)**	**Inter molecular Coordination Number**	**Intra molecular Coordination Number**
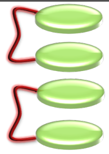	0.41	1	2
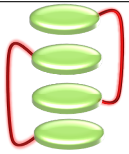	0.41	3	0
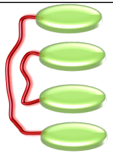	0.41	2	1
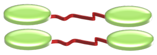	0.8 (B6B) 0.95 (B9B)	2	0

Table 6.3: Values of reaction coordinates to identify the configurations in the dimers.

The free energy landscape of the dimer was generated in the configurational space of the following reaction coordinates:

1. The radius of gyration of atoms present in the phenyl rings — RG.

2. The coordination number between the center of masses of each phenyl ring from different molecules — Inter-coordination number.

3. The coordination number between the center of masses of each phenyl ring with in the same molecule — Intra-coordination number.

The coordination number was calculated using rational switching function implemented in PLUMED package, [55]

$$\begin{aligned} s(r) &= \frac{1-(\frac{r-d_0}{r_0})^n}{1-(\frac{r-d_0}{r_0})^m} \\ &where, \\ d_0 = 0.155\,nm, r_0 &= 0.22\,nm, \\ n = 27, m &= 47. \end{aligned} \tag{6.3}$$

The values of RCs to identify the different configurations of dimer are tabulated in Table. 6.3. To perform WTM simulations, B6B and B9B systems were solvated in 1150 *n*-nonane molecules corresponding to an equilibrated box size of 7 nm. Gaussians with initial hill height of 20 kJ/mol and bias factor 30 were deposited once every 2 ps. The widths of these Gaussian along RG, Intra-coordination number, and Inter-coordination number are 0.01 nm, 0.1, and 0.1, respectively. The simulations of B6B and B9B were run for 2600 ns and 3300 ns respectively.

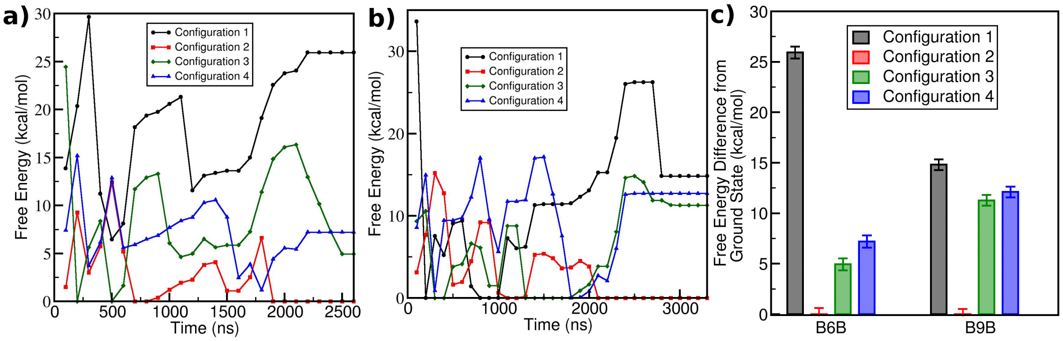

Figure 6.8: Time evolution of free-energy of various dimer configurations of (a) B6B, and (b) B9B. (c) Free energies of configurations **1**,**3**,**4** relative to the global minimum configuration **2**. The values were obtained from WTM simulations in solution at 298.15 K.

A home-built python code was used to estimate the free energies of the four dimer configurations over simulation time (Figure. 6.8a,b). The converged free energy calculations reveal that the thermodynamically stable state of the dimer is configuration 2. The free energy differences of other configurations with respect to configuration 2 are shown in Figure. 6.8c. The free energy surface was constructed using *sum_hills* module implemented in PLUMED, [55] and is shown in Figure. 6.9b,d for B6B and B9B respectively. A network diagram of dimer configurations is provided in Figure. 6.9a,b.

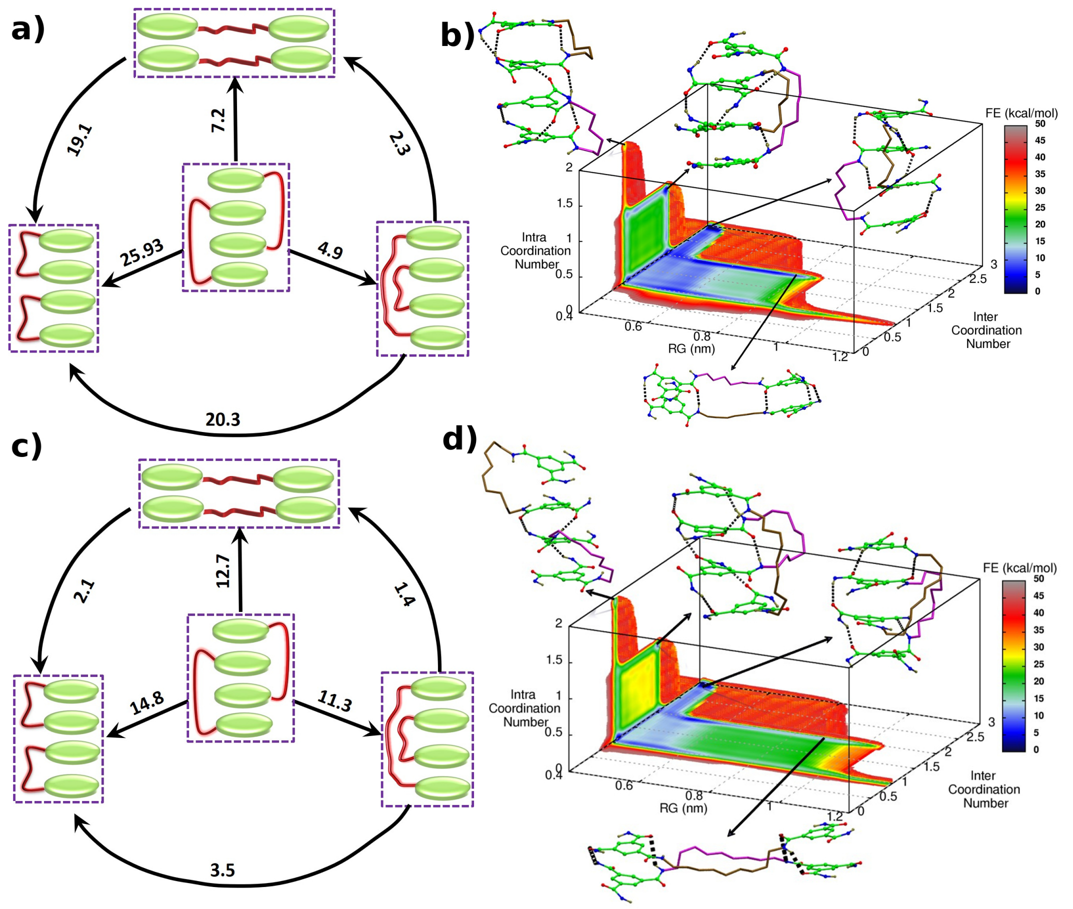

Figure 6.9: (a), (c) Network diagram of dimer configurations connecting the thermodynamically stable configuration (configuration 2) to the other configurations of B6B and B9B respectively. The arrows are drawn from low energy configurations to high energy configurations. The values on the arrows are the free energy differences between the connected nodes. The central node represents the global minimum. (b) and (d) The free energy landscape of B6B and B9B dimer respectively. Chemical structures shown in (b) and (d) are the most dominant clusters obtained from a cluster analysis of configurations contributing to the respective position in collective variable space.

The minimum free energy pathways connecting the kinetically trapped states to the thermodynamically stable configuration were obtained using a python code written by Macros-Alcalde *et al.* [73]. These pathways have multiple barriers and are shown in Figure. 6.10. Using transition state theory, we estimated the lag times associated with the transition from second most preferable state (Configuration 3) to the thermodynamically stable state (configuration 2), and the calculated values are 0.14, and 0.76 μs for B6B and B9B respectively. Experimentally observed lag times are in the order of ms or larger [3, 7, 74] which could arise from transition from larger kinetically trapped states to the ground state. The values obtained here are not inconsistent with these

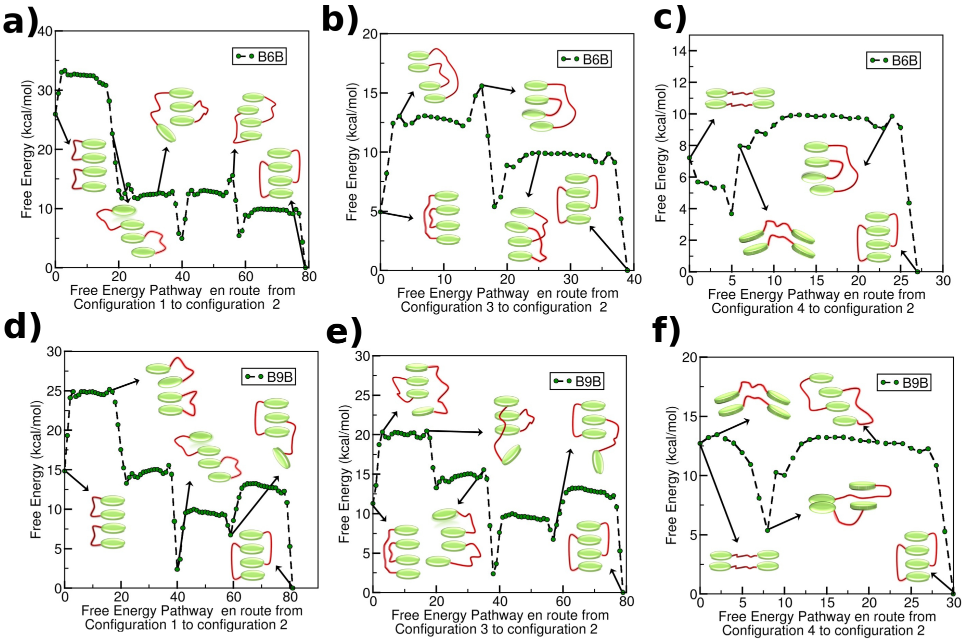

Figure 6.10: Minimum free energy path enroute configuration **2** from (a) **1**, (b) **3**, (c) **4** of B6B dimer and (d) **1**, (e) **3**, (f) **4** of B9B dimer. Structures corresponding to transition state and intermediate structures along the reaction pathway are shown via schematic representation.

experimental observations. We used the Gromacs *cluster* module to identify some intermediate structures along the minimum free energy paths. The most probable structures corresponding to configurations **1**, **2**, **3** and **4** of B6B dimer are shown in Figure. 6.11-6.14 and the percentage of population are tabulated in Table. 6.4. Similar analysis was done for B9B dimers as well and the structures are shown in Figure. 6.15- 6.18 and the population percentages are given in Table. 6.5.

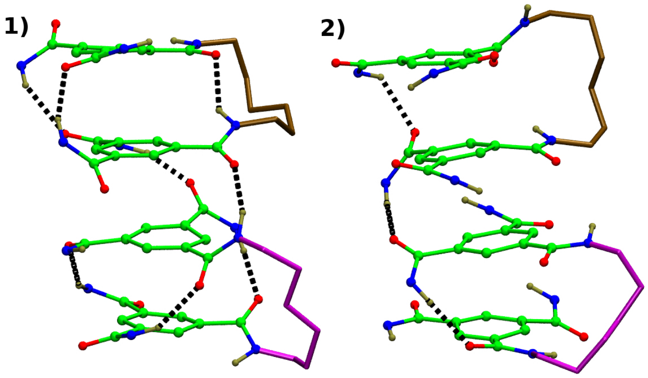

Figure 6.11: The representative structures (most probable ones from cluster analysis) of B6B dimer in configuration **1**. The colour scheme is same as in Figure. 6.4. The linkers are shown in magenta and ochre to differentiate the molecules.

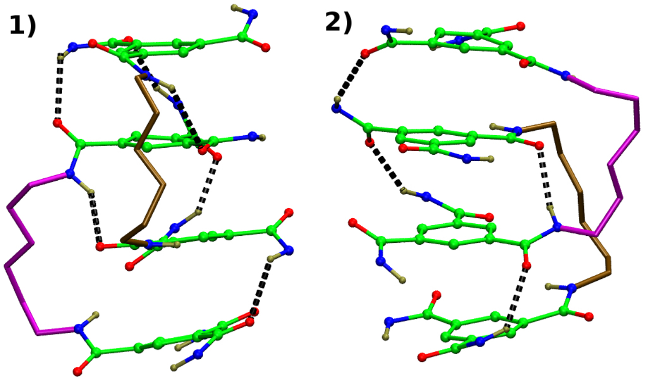

Figure 6.12: The representative structures (most probable ones from cluster analysis) of B6B dimer in configuration **2**. The colour scheme is same as in Figure. 6.4. The linkers are shown in magenta and ochre to differentiate the molecules.

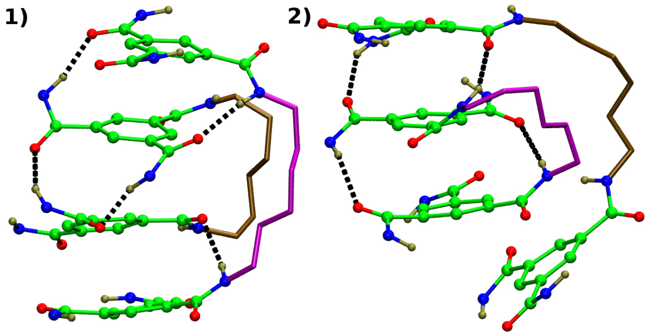

Figure 6.13: The representative structures (most probable ones from cluster analysis) of B6B dimer in configuration **3**. The colour scheme is same as in Figure. 6.4. The linkers are shown in magenta and ochre to differentiate the molecules.

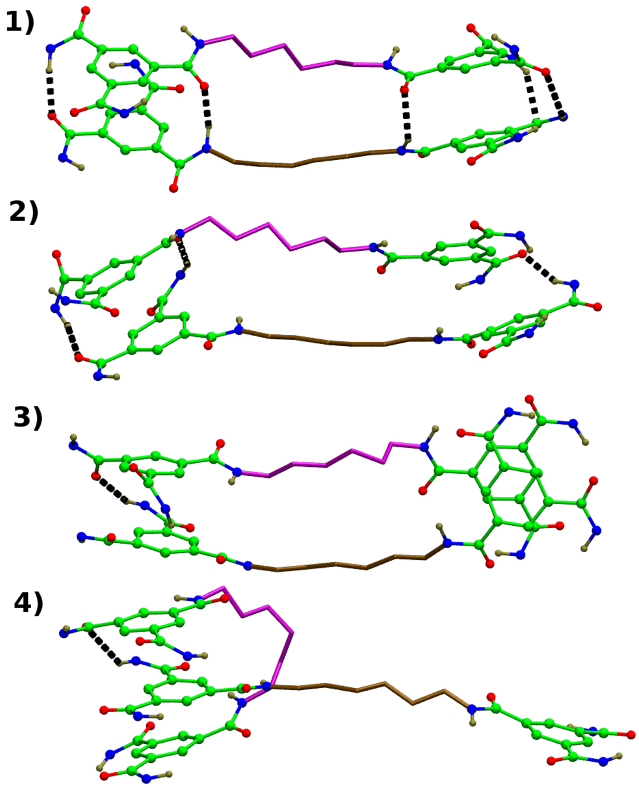

Figure 6.14: The representative structures (most probable ones from cluster analysis) of B6B dimer in configuration **4**. The colour scheme is same as in Figure. 6.4. The linkers are shown in magenta and ochre to differentiate the molecules.

Table 6.4: Percentage population of the most probable structures (obtained from cluster analysis) along with their figure indices of the four dimer configurations of B6B.

Configuration	**Index of structure**	**% of the structure**
1	1	81.26
	2	18.73
2	1	76.08
	2	23.91
3	1	95.09
	2	4.9
4	1	52.10
	2	31.09
	3	12.60
	4	3.36

Table 6.5: Percentage population of the most probable structures (obtained from cluster analysis) along with their figure indices of the four dimer configurations of B9B.

Configuration	Index of structure	% of the structure
1	1	66.78
	2	28.33
	3	3.30
	4	1.60
2	1	54.28
	2	40.91
	3	4.17
	4	0.63
3	1	50.00
	2	23.79
	3	17.20
	4	7.5
4	1	72.60
	2	13.69
	3	3.65
	4	3.65
	5	3.12
	6	3.12

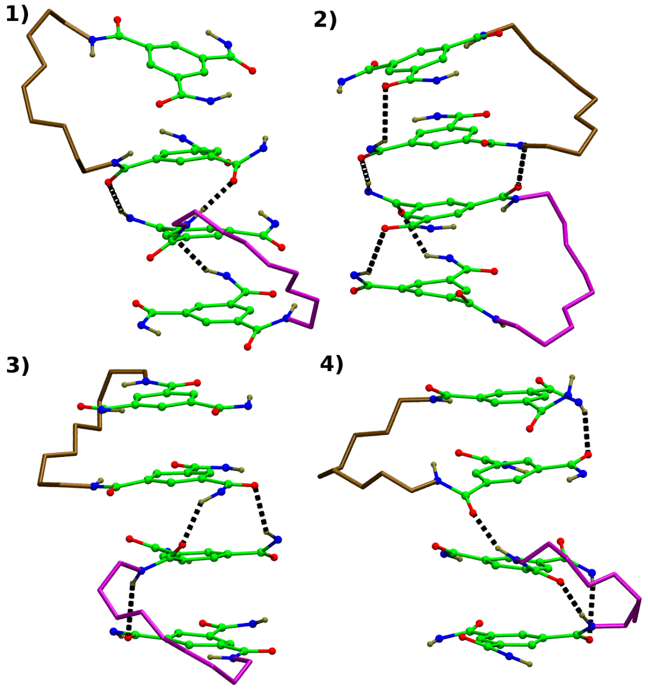

Figure 6.15: The representative structures (most probable ones from cluster analysis) of B9B dimer in configuration **1**. The colour scheme is same as in Figure. 6.4. The linkers are shown in magenta and ochre to differentiate the molecules.

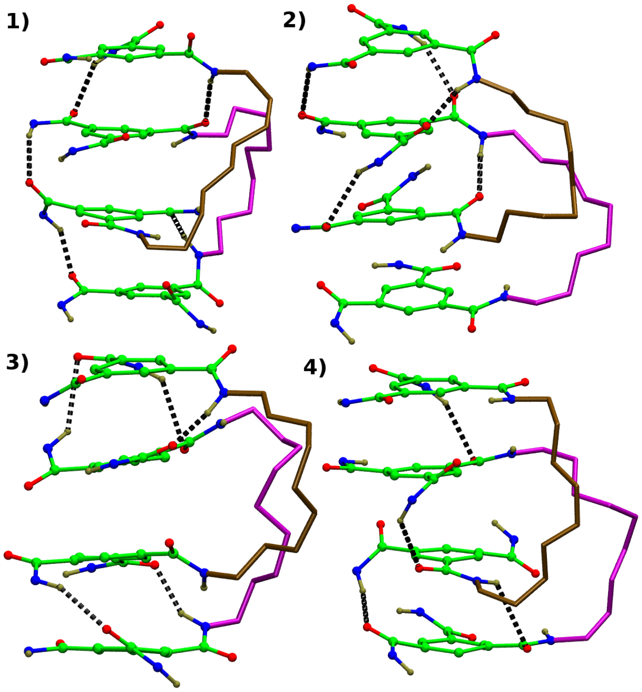

Figure 6.16: The representative structures (most probable ones from cluster analysis) of B9B dimer in configuration **2**. The colour scheme is same as in Figure. 6.4. The linkers are shown in magenta and ochre to differentiate the molecules.

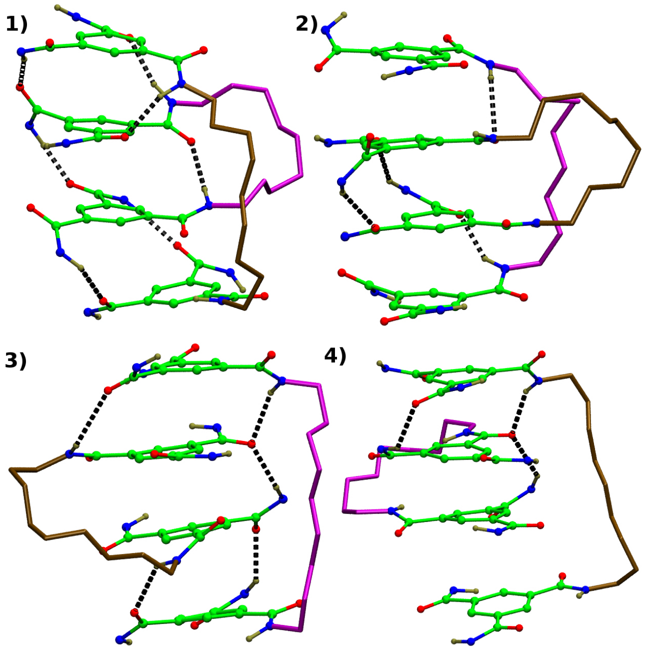

Figure 6.17: The representative structures (most probable ones from cluster analysis) of B9B dimer in configuration **3**. The colour scheme is same as in Figure. 6.4. The linkers are shown in magenta and ochre to differentiate the molecules.

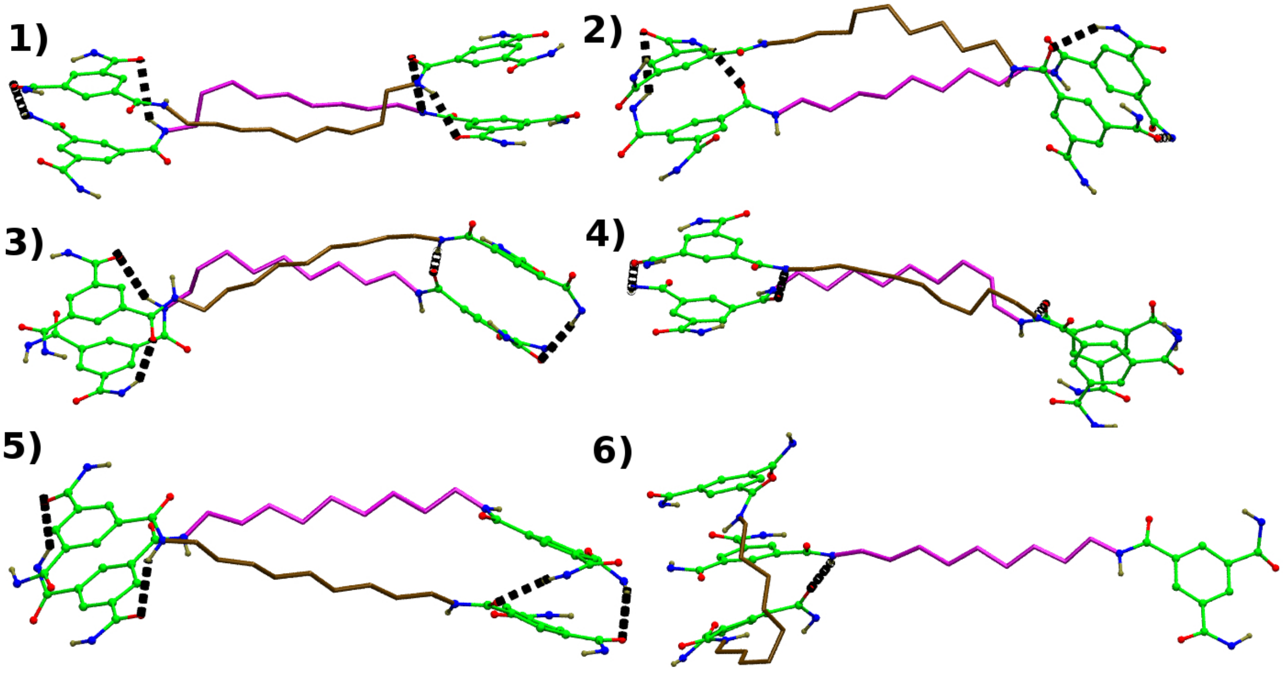

Figure 6.18: The representative structures (most probable ones from cluster analysis) of B9B dimer in configuration **4**. The colour scheme is same as in Figure. 6.4. The linkers are shown in magenta and ochre to differentiate the molecules.

6.3.3 Conclusions:

Conformations of monomer and dimer of prototypical molecules M-B6B, and M-B9B have been studied using gas phase quantum calculations and well tempered metadynamics simulations in solutions to understand the complexity of pathway in the oligomerisation process. Monomers of these molecules exist in two conformations namely, folded and extended. The monomer in folded conformation is energetically more stable than the extended form. Dipole moment of monomer along the stacking direction in folded conformation for each system was calculated from quantum chemical calculations and were compared against that of dimer of BTA. The dipole moments are independent of the linker length. Dimers of these molecules exhibit a rich configurational landscape, arising from the linker length. Force field based optimized geometries and energies of conformations of monomers and configurations of dimers were benchmarked against quantum data.

The free energy differences between these states as well as the pathways connecting them have been determined at ambient conditions in solution phase. The lag times associated with the transition of kinetically trapped dimer configurations to the ground state were estimated from free energy calculations of B6B, and B9B dimers. The work paves the way for the exploration of the transition pathways associated with experimentally observed lag phases of realistic systems under realistic thermodynamic conditions.

Bibliography

[1] Brunsveld, L.; Folmer, B.; Meijer, E. W.; Sijbesma, R. Supramolecular polymers. *Chem. Rev.* **2001**, *101*, 4071–4098.

[2] Liu, H.; Xu, J.; Li, Y.; Li, Y. Aggregate nanostructures of organic molecular materials. *Acc. Chem. Res.* **2010**, *43*, 1496–1508.

[3] Ogi, S.; Stepanenko, V.; Thein, J.; Würthner, F. Impact of alkyl spacer length on aggregation pathways in kinetically controlled supramolecular polymerization. *J. Am. Chem. Soc.* **2016**, *138*, 670–678.

[4] Frisch, H.; Fritz, E.-C.; Stricker, F.; Schmüser, L.; Spitzer, D.; Weidner, T.; Ravoo, B. J.; Besenius, P. Kinetically Controlled Sequential Growth of Surface-Grafted Chiral Supramolecular Copolymers. *Angew. Chem. Int. Ed.* **2016**, *55*, 7242–7246.

[5] Lü, B.; You, S.; Li, P.; Li, C.; Müllen, K.; Yin, M. Kinetically trapped supramolecular assembly of perylene dianhydride derivative in methanol: optical spectra, morphology, and mechanisms. *Chem.–Eur. J.* **2017**, *23*, 397–401.

[6] Choi, H.; Heo, S.; Lee, S.; Kim, K. Y.; Lim, J. H.; Jung, S. H.; Lee, S. S.; Miyake, H.; Lee, J. Y.; Jung, J. H. Kinetically controlled Ag+-coordinated chiral supramolecular polymerization accompanying a helical inversion. *Chem. Sci.* **2020**,

[7] Korevaar, P. A.; George, S. J.; Markvoort, A. J.; Smulders, M. M.; Hilbers, P. A.; Schenning, A. P.; De Greef, T. F.; Meijer, E. Pathway complexity in supramolecular polymerization. *Nature* **2012**, *481*, 492.

[8] Mattia, E.; Otto, S. Supramolecular systems chemistry. *Nat. Nanotechnol.* **2015**, *10*, 111.

[9] Ortony, J. H.; Newcomb, C. J.; Matson, J. B.; Palmer, L. C.; Doan, P. E.; Hoffman, B. M.; Stupp, S. I. Internal dynamics of a supramolecular nanofibre. *Nat. Mater.* **2014**, *13*, 812.

[10] Spano, F. C.; Silva, C. H-and J-aggregate behavior in polymeric semiconductors. *Annu. Rev. Phys. Chem.* **2014**, *65*, 477–500.

[11] Cai, K.; Xie, J.; Zhang, D.; Shi, W.; Yan, Q.; Zhao, D. Concurrent cooperative J-aggregates and anticooperative H-aggregates. *J. Am. Chem. Soc.* **2018**, *140*, 5764–5773.

[12] Bouteiller, L.; Colombani, O.; Lortie, F.; Terech, P. Thickness transition of a rigid supramolecular polymer. *J. Am. Chem. Soc.* **2005**, *127*, 8893–8898.

[13] Bellot, M.; Bouteiller, L. Thermodynamic description of bis-urea self-assembly: Competition between two supramolecular polymers. *Langmuir* **2008**, *24*, 14176–14182.

[14] others,, et al. Thermodynamic factors impacting the peptide-driven self-assembly of perylene diimide nanofibers. *J. Phys. Chem. B* **2014**, *118*, 8642–8651.

[15] Fennel, F.; Wolter, S.; Xie, Z.; Plötz, P.-A.; Kühn, O.; Würthner, F.; Lochbrunner, S. Biphasic self-assembly pathways and size-dependent photophysical properties of perylene bisimide dye aggregates. *J. Am. Chem. Soc.* **2013**, *135*, 18722–18725.

[16] van der Schoot, P.; Michels, M.; Brunsveld, L.; Sijbesma, R. P.; Ramzi, A. Helical transition and growth of supramolecular assemblies of chiral discotic molecules. *Langmuir* **2000**, *16*, 10076–10083.

[17] Baram, J.; Weissman, H.; Rybtchinski, B. Supramolecular polymer transformation: a kinetic study. *J. Phys. Chem. B* **2014**, *118*, 12068–12073.

[18] Oosawa, F.; Kasai, M. A theory of linear and helical aggregations of macromolecules. *J. Mol. Biol.* **1962**, *4*, 10–21.

[19] Powers, E. T.; Powers, D. L. The kinetics of nucleated polymerizations at high concentrations: amyloid fibril formation near and above the "supercritical concentration". *Biophys. J.* **2006**, *91*, 122–132.

[20] Goldstein, R. F.; Stryer, L. Cooperative polymerization reactions. Analytical approximations, numerical examples, and experimental strategy. *Biophys. J.* **1986**, *50*, 583–599.

[21] Mitchison, T.; Kirschner, M. Dynamic instability of microtubule growth. *Nature* **1984**, *312*, 237.

[22] Wu, H. Higher-order assemblies in a new paradigm of signal transduction. *Cell* **2013**, *153*, 287–292.

[23] Mabesoone, M. F.; Markvoort, A. J.; Banno, M.; Yamaguchi, T.; Helmich, F.; Naito, Y.; Yashima, E.; Palmans, A. R.; Meijer, E. Competing interactions in hierarchical porphyrin self-assembly introduce robustness in pathway complexity. *J. Am. Chem. Soc.* **2018**, *140*, 7810–7819.

[24] Haedler, A. T.; Meskers, S. C.; Zha, R. H.; Kivala, M.; Schmidt, H.-W.; Meijer, E. Pathway complexity in the enantioselective self-assembly of functional carbonyl-bridged triarylamine trisamides. *J. Am. Chem. Soc.* **2016**, *138*, 10539–10545.

[25] Yamamoto, T.; Fukushima, T.; Yamamoto, Y.; Kosaka, A.; Jin, W.; Ishii, N.; Aida, T. Stabilization of a Kinetically Favored Nanostructure: Surface ROMP of Self-Assembled Conductive Nanocoils from a Norbornene-Appended Hexa-peri-hexabenzocoronene. *J. Am. Chem. Soc.* **2006**, *128*, 14337–14340.

[26] Chen, Z.; Liu, Y.; Wagner, W.; Stepanenko, V.; Ren, X.; Ogi, S.; Würthner, F. Near-IR Absorbing J-Aggregate of an Amphiphilic BF2-Azadipyrromethene Dye by Kinetic Cooperative Self-Assembly. *Angew. Chem. Int. Ed.* **2017**, *56*, 5729–5733.

[27] Korevaar, P. A.; Newcomb, C. J.; Meijer, E.; Stupp, S. I. Pathway selection in peptide amphiphile assembly. *J. Am. Chem. Soc.* **2014**, *136*, 8540–8543.

[28] Cui, H.; Chen, Z.; Zhong, S.; Wooley, K. L.; Pochan, D. J. Block copolymer assembly via kinetic control. *Science* **2007**, *317*, 647–650.

[29] Hill, J. P.; Jin, W.; Kosaka, A.; Fukushima, T.; Ichihara, H.; Shimomura, T.; Ito, K.; Hashizume, T.; Ishii, N.; Aida, T. Self-assembled hexa-peri-hexabenzocoronene graphitic nanotube. *Science* **2004**, *304*, 1481–1483.

[30] Zang, L.; Che, Y.; Moore, J. S. One-dimensional self-assembly of planar π-conjugated molecules: adaptable building blocks for organic nanodevices. *Acc. Chem. Res.* **2008**, *41*, 1596–1608.

[31] Avinash, M.; Sandeepa, K. V.; Govindaraju, T. Emergent behaviors in kinetically controlled dynamic self-assembly of synthetic molecular systems. *ACS Omega* **2016**, *1*, 378–387.

[32] Lohr, A.; Würthner, F. Chiral Amplification, Kinetic Pathways, and Morphogenesis of Helical Nanorods upon Self-assembly of Dipolar Merocyanine Dyes. *Isr. J. Chem.* **2011**, *51*, 1052–1066.

[33] Korevaar, P. A.; Schaefer, C.; de Greef, T. F.; Meijer, E. Controlling chemical self-assembly by solvent-dependent dynamics. *J. Am. Chem. Soc.* **2012**, *134*, 13482–13491.

[34] Tidhar, Y.; Weissman, H.; Wolf, S. G.; Gulino, A.; Rybtchinski, B. Pathway-dependent self-assembly of perylene diimide/peptide conjugates in aqueous medium. *Chem.–Eur. J.* **2011**, *17*, 6068–6075.

[35] Komiya, N.; Muraoka, T.; Iida, M.; Miyanaga, M.; Takahashi, K.; Naota, T. Ultrasound-induced emission enhancement based on structure-dependent homo- and heterochiral aggregations of chiral binuclear platinum complexes. *J. Am. Chem. Soc.* **2011**, *133*, 16054–16061.

[36] others,, et al. Design amphiphilic dipolar π-systems for stimuli-responsive luminescent materials using metastable states. *Nat. Commun.* **2014**, *5*, 4013.

[37] Micali, N.; Engelkamp, H.; Van Rhee, P.; Christianen, P.; Scolaro, L. M.; Maan, J. Selection of supramolecular chirality by application of rotational and magnetic forces. *Nat. Chem.* **2012**, *4*, 201.

[38] Aliprandi, A.; Mauro, M.; De Cola, L. Controlling and imaging biomimetic self-assembly. *Nat. Chem.* **2016**, *8*, 10.

[39] Aida, T.; Meijer, E.; Stupp, S. I. Functional supramolecular polymers. *Science* **2012**, *335*, 813–817.

[40] Sorrenti, A.; Leira-Iglesias, J.; Markvoort, A. J.; de Greef, T. F.; Hermans, T. M. Non-equilibrium supramolecular polymerization. *Chem. Soc. Rev.* **2017**, *46*, 5476–5490.

[41] Wehner, M.; Würthner, F. Supramolecular polymerization through kinetic pathway control and living chain growth. *Nat. Rev. Chem.* **2019**, 1–16.

[42] Dhiman, S.; George, S. J. Temporally controlled supramolecular polymerization. *Bull. Chem. Soc. Jpn.* **2018**, *91*, 687–699.

[43] Manz, T. A.; Sholl, D. S. Improved atoms-in-molecule charge partitioning functional for simultaneously reproducing the electrostatic potential and chemical states in periodic and nonperiodic materials. *J. Chem. Theory Comput.* **2012**, *8*, 2844–2867.

[44] Hutter, J.; Iannuzzi, M.; Schiffmann, F.; VandeVondele, J. cp2k: atomistic simulations of condensed matter systems. *Wiley Interdiscip. Rev.: Comput. Mol. Sci.* **2014**, *4*, 15–25.

[45] Manz, T. A.; Limas, N. G. Introducing DDEC6 atomic population analysis: part 1. Charge partitioning theory and methodology. *RSC Adv.* **2016**, *6*, 47771–47801.

[46] VandeVondele, J.; Krack, M.; Mohamed, F.; Parrinello, M.; Chassaing, T.; Hutter, J. Quickstep: Fast and accurate density functional calculations using a mixed Gaussian and plane waves approach. *Comput. Phys. Commun.* **2005**, *167*, 103–128.

[47] Perdew, J. P.; Ruzsinszky, A.; Tao, J.; Staroverov, V. N.; Scuseria, G. E.; Csonka, G. I. Prescription for the design and selection of density functional approximations: More constraint satisfaction with fewer fits. *J. Chem. Phys.* **2005**, *123*, 062201.

[48] Goedecker, S.; Teter, M.; Hutter, J. Separable dual-space Gaussian pseudopotentials. *Phys. Rev. B* **1996**, *54*, 1703.

[49] Hartwigsen, C.; Gœdecker, S.; Hutter, J. Relativistic separable dual-space Gaussian pseudopotentials from H to Rn. *Phys. Rev. B* **1998**, *58*, 3641.

[50] Grimme, S.; Antony, J.; Ehrlich, S.; Krieg, H. A consistent and accurate ab initio parametrization of density functional dispersion correction (DFT-D) for the 94 elements H-Pu. *J. Chem. Phys.* **2010**, *132*, 154104.

[51] Dennington, R.; Keith, T.; Millam, J.; Eppinnett, K.; Hovell, W. L.; Gilliland, R. GaussView. 2009.

[52] Wang, J.; Wolf, R. M.; Caldwell, J. W.; Kollman, P. A.; Case, D. Erratum: Development and testing of a general amber force field (Journal of Computational Chemistry (2004) 25 (1157)). *J. Comput. Chem.* **2005**, *26*.

[53] Martin, M. G.; Siepmann, J. I. Transferable potentials for phase equilibria. 1. United-atom description of n-alkanes. *J. Phys. Chem. B* **1998**, *102*, 2569–2577.

[54] Abraham, M. J.; Murtola, T.; Schulz, R.; Páll, S.; Smith, J. C.; Hess, B.; Lindahl, E. GROMACS: High performance molecular simulations through multi-level parallelism from laptops to supercomputers. *SoftwareX* **2015**, *1*, 19–25.

[55] others,, et al. PLUMED: A portable plugin for free-energy calculations with molecular dynamics. *Comput. Phys. Commun.* **2009**, *180*, 1961–1972.

[56] Darden, T.; York, D.; Pedersen, L. Particle mesh Ewald: An Nlog(N) method for Ewald sums in large systems. *J. Chem. Phys.* **1993**, *98*, 10089–10092.

[57] Hess, B.; Bekker, H.; Berendsen, H. J.; Fraaije, J. G. LINCS: a linear constraint solver for molecular simulations. *J. Comput. Chem.* **1997**, *18*, 1463–1472.

[58] Bussi, G.; Donadio, D.; Parrinello, M. Canonical sampling through velocity rescaling. *J. Chem. Phys.* **2007**, *126*, 014101.

[59] Berendsen, H. J.; Postma, J. v.; van Gunsteren, W. F.; DiNola, A.; Haak, J. R. Molecular dynamics with coupling to an external bath. *J. Chem. Phys.* **1984**, *81*, 3684–3690.

[60] Bejagam, K. K.; Fiorin, G.; Klein, M. L.; Balasubramanian, S. Supramolecular polymerization of benzene-1, 3, 5-tricarboxamide: a molecular dynamics simulation study. *J. Phys. Chem. B* **2014**, *118*, 5218–5228.

[61] Kulkarni, C.; Meijer, E.; Palmans, A. R. Cooperativity scale: a structure–mechanism correlation in the self-assembly of benzene-1, 3, 5-tricarboxamides. *Acc. Chem. Res.* **2017**, *50*, 1928–1936.

[62] Kulkarni, C.; Balasubramanian, S.; George, S. J. What molecular features govern the mechanism of supramolecular polymerization? *ChemPhysChem* **2013**, *14*, 661–673.

[63] Garzoni, M.; Baker, M. B.; Leenders, C. M.; Voets, I. K.; Albertazzi, L.; Palmans, A. R.; Meijer, E.; Pavan, G. M. Effect of H-bonding on order amplification in the growth of a supramolecular polymer in water. *J. Am. Chem. Soc.* **2016**, *138*, 13985–13995.

[64] Korlepara, D. B.; Balasubramanian, S. Molecular modelling of supramolecular one dimensional polymers. *RSC Adv.* **2018**, *8*, 22659–22669.

[65] Korlepara, D. B.; Henderson, W. R.; Castellano, R. K.; Balasubramanian, S. Differentiating the mechanism of self-assembly in supramolecular polymers through computation. *Chem. Commun.* **2019**, *55*, 3773–3776.

[66] Torrie, G. M.; Valleau, J. P. Nonphysical sampling distributions in Monte Carlo free-energy estimation: Umbrella sampling. *J. Comput. Phys.* **1977**, *23*, 187–199.

[67] Kumar, S.; Rosenberg, J. M.; Bouzida, D.; Swendsen, R. H.; Kollman, P. A. The weighted histogram analysis method for free-energy calculations on biomolecules. I. The method. *J. Comput. Chem.* **1992**, *13*, 1011–1021.

[68] Grossfield, A. WHAM: the weighted histogram analysis method, version 2.0.9. *Available at membrane. urmc. rochester. edu/content/wham. Accessed November* **2013**, *15*, 2013.

[69] Bejagam, K. K.; Balasubramanian, S. Supramolecular polymerization: a coarse grained molecular dynamics study. *J. Phys. Chem. B* **2015**, *119*, 5738–5746.

[70] Valera, J. S.; Gómez, R.; Sánchez, L. Kinetic traps to activate stereomutation in supramolecular polymers. *Angew. Chem.* **2019**, *131*, 520–524.

[71] Chen, H.; Huang, Z.; Wu, H.; Xu, J.-F.; Zhang, X. Supramolecular polymerization controlled through kinetic trapping. *Angew. Chem. Int. Ed.* **2017**, *56*, 16575–16578.

[72] De Greef, T. F.; Smulders, M. M.; Wolffs, M.; Schenning, A. P.; Sijbesma, R. P.; Meijer, E. Supramolecular polymerization. *Chem. Rev.* **2009**, *109*, 5687–5754.

[73] Marcos-Alcalde, I.; Setoain, J.; Mendieta-Moreno, J. I.; Mendieta, J.; Gómez-Puertas, P. MEPSA: minimum energy pathway analysis for energy landscapes. *Bioinformatics* **2015**, *31*, 3853–3855.

[74] Ogi, S.; Matsumoto, K.; Yamaguchi, S. Seeded Polymerization through the Interplay of Folding and Aggregation of an Amino-Acid-based Diamide. *Angew. Chem. Int. Ed.* **2018**, *57*, 2339–2343.

Chapter 7

Summary and Future Outlook

The present thesis sheds light on the structural aspects, mechanisms and pathway complexity of supramolecular polymers.

In Chapter 1, free energy calculations based on atomistic MD simulations were performed on N,N′,N″-trialkylbenzene-1,3,5-tricarboxamide (BTA) and [2.2]para cyclophane-4,7,12,15-tetracarboxamide (pCpTA) to investigate the mechanism of self-assembly in non-polar solvents at ambient conditions.

Supramolecular aggregation has been demonstrated via atomistic models in Chapter 3. Due to the presence of large degrees of freedom in all-atom models, simulations at experimental concentration are expensive. This can be circumvented through dissipative particle dynamics (DPD) to enhance the self-assembly simulations. Dipole relaxations in the liquid crystalline phase of N,N′,N″,N‴-tetra-(Tetradecyl)-1,3,6,8-pyrenetetracarboxamide and N,N′,N″-trialkylbenzene-1,3,5-tricarboxamide were examined. The role of rotational symmetry - in the dipole arrangments around the molecule core - to observe the helical handedness reversal in presence of external electric field was elucidated. To generalize the phenomenon of handedness reversal, molecules having equidistant dipoles around the core have to be investigated.

In Chapter 4, the impact of alkyl chain length on dipole relaxations was demonstrated. Methods to improve the retention times and the magnitude of remnant polarization are suggested via studies of (5BC-C14) in its LC phase. A systematic study on other derivatives of pyrene, perylene bisimide can be done to rationalize the effect of structural modifications on their ferroelectric performance.

In Chapter 5, molecular level insights into the selective supramolecular polymerization of oligo(p-phenylenevinylene) (OPV) functionalized with the phosphate receptor dipicolylethylenediamine-zinc complex (DPA-Zn) - referred to as OPV-DPA to adenosine triphosphate (ATP) were presented. The experimentally observed lag times during the self-assembly process were explained.

In Chapter 6, conformations and configurations of monomer and dimer in the case of a prototypical molecule — N1,N1-(n-alkane-1,n-diyl)bis(N3,N5- dialkylbenzene-1,3,5-tricarboxamide) were explored. The relative free energy differences between the thermodynamically stable state and other configurations of the dimer were calculated via free energy calculations. To explore the complex self-assembly pathways in real systems, advanced free energy methods have to be adopt which are both computationally cheaper and have high efficiency in sampling.

To summarize, molecular dynamics simulations enable a microscopic understanding of several aspects of supramolecular polymers.

List of publications

- Supramolecular Polymerization of N,N′,N″,N‴-tetra-(Tetradecyl)-1,3,6,8-pyrenetetracarboxamide: A Computational Study
  Divya, B. Korlepara; Karteek K. Bejagam; Balasubramanian, S. *J. Phys. Chem. B* **2017**, 121, 11492-11503.
- Biomimetic temporal self-assembly via fuel-driven controlled supramolecular polymerization
  Ananya Mishra; **Divya, B. Korlepara**; Mohit Kumar; Ankit Jain; Narendra Jonnalagadda; Karteek K. Bejagam; Balasubramanian, S; Subi J. George. *Nat. Commun.* **2018**, 9, 1295.
- Differentiating the mechanism of self-assembly in supramolecular polymers through computation
  Divya, B. Korlepara; Will R. Henderson; Ronald K. Castellano; Balasubramanian, S. *Chem. Commun.* **2019**, 55, 3773-3776.
- Bioinspired, ATP-driven co-operative supramolecular polymerization and its pathway dependence
  Ananya Mishra; **Divya, B. Korlepara**; Balasubramanian, S; Subi J. George. *Chem. Commun.* **2020**, 56, 1505-1508.
- Molecular modelling of supramolecular one dimensional polymers
  Divya, B. Korlepara; Balasubramanian, S. *RSC Adv.* **2018**, 8, 22659-22669. (Not a part of this thesis.)
- Dipolar Relaxation in Thin Films of Benzenecarboxamides
  Divya, B. Korlepara; Srinath V. K. Kompella; Balasubramanian, S. (To be submitted.)
- Exploring the lag phase and lag times of supramolecular polymers: Free Energy Simulations
  Divya, B. Korlepara; Srinath V. K. Kompella; Balasubramanian, S. (To be submitted.)